

University of Nottingham
UK | CHINA | MALAYSIA

Risks to global water resources from geoengineering the climate with solar radiation management

THESIS

Lorna Burnell

supervised by:

Professor Ian Dryden (School of Mathematical Sciences)

Professor Markus Owen (School of Mathematical Sciences)

Professor Simon Gosling (School of Geography)

Dr Nick Mount (School of Geography)

September 2021

Abstract

Climate change, including global temperature rise, is one of the greatest threats facing humanity and the planet. The response of the collective human population to reduce greenhouse gas emissions, the driver of this change, has been far from adequate. To this end, methods of geoengineering the climate have been proposed, ranging from removal of carbon dioxide presently in the atmosphere (including Carbon Capture and Storage and Direct Air Capture) to methods of adjusting the amount of incoming solar radiation reaching the troposphere. Solar geoengineering (SG), also known as solar radiation management (SRM), is a proposed method of geoengineering which reflects a portion of incoming solar radiation back into space to slow or reverse global temperature rise. However, whilst simulations suggest that SG may be able to halt global mean temperature changes, it will not be able to counteract all aspects of climate change which threaten both society and ecosystems. One particularly well-known effect of current SG modelling experiments is that, when designed to offset a specific temperature rise under greenhouse gas forcing, precipitation values would be excessively offset and decrease below the baseline, reducing the overall intensity of the global hydrological cycle. A global-scale assessment is urgently needed to quantify the risks and opportunities SG poses to global water resources.

This project has examined how water resources (including drought and water scarcity) could be affected across the globe through deployment of SG. Throughout this work, the Geoengineering Large Ensemble Project (GLENS) modelling has been used as the scenario of SG; which aimed to reduce some of the negative outcomes of previous SG modelling results, including the negative changes in precipitation. Runoff directly output from the GLENS modelling was compared to simulated runoff generated by the Global Hydrology Model (GHM) Mac-PDM.17 using climate forcing from GLENS, in order to gain some understanding of intra-model variability. Aspects of both the hazard and risk solar geoengineering may pose, contrasted against those seen under unmitigated climate change, were examined through consideration of drought and water scarcity projections across the globe. The findings of this research help answer policy-relevant research questions such

as: which parts of the globe may benefit/suffer from SG; which regions may be better off with global warming than with a cooler climate achieved by SG; and how long may it take for such changes to occur; all within the context of global water resources.

To help answer the questions set out in this thesis a number of mathematical techniques have been employed. Extreme value theory was used to establish minimum monthly drought runoff return periods, whilst permutation tests were used to determine statistical significance between the solar geoengineering and climate change modelling ensembles. Further investigation of the permutation test revealed the importance of sample size on the power of the test. Summary statistics to summarise averages, variability and percentage change were used to interpret trends in the data. Mathematical methods were critical to model outputs, with the feedback algorithms governing the amount of stratospheric aerosol injection (and thus climate outcomes) and the probability distribution moisture method in Mac-PDM determining soil moisture across a gridcell (and thus saturation excess runoff). The importance of mathematical equations in controlling outputs, e.g. by the method used to calculate potential evapotranspiration, was also highlighted.

Under the specific scenarios of climate change and solar geoengineering used in this research, it has been seen that some areas may benefit from the amelioration of impacts from climate change through the implementation of solar geoengineering, namely many parts of the Americas, Europe, Australia and the Middle East. Other regions are projected to face greater water resource challenges under solar geoengineering, including parts of Southern Asia, Southeast Asia and many regions of Africa (Western, Middle and Eastern). This raises important questions around global equability of outcomes and equality for all nations, as well as the implications for future governance of any solar geoengineering deployment. A further important finding in the context of water scarcity was that the largest degree of future change often arose from future projected changes in population, with the climate scenario having a smaller overall impact. In addition to this, in some instances where solar geoengineering was projected to worsen conditions in comparison to climate change, this resulted from solar geoengineering maintaining conditions closer to the present-day climate, with climate change reducing future water scarcity when calculated at the annual scale. This demonstrates the complex interconnectedness of humans and the environment and advocates for more extensive research into possible impacts of solar geoengineering on global water resources. Future work into the affect of solar geoengineering on global water resources should particularly focus on using a wider range of modelling projections (including more realistic scenarios, i.e. not offsetting all warming) and greater consideration of variation in water availability throughout the year.

Acknowledgements

All of my supervisors have provided invaluable support, advice and guidance throughout this PhD and I am extremely grateful for this. I would like to thank Nick Mount for his excellent advice in directions and approaches to the research, Simon Gosling for his guidance and extensive understanding of global hydrology modelling, Ian Dryden for his great help in statistical approaches and Markus Owen for his help with coding practices and more particularly the ongoing support he has given all of us through leading the Modelling and Analytics for a Sustainable Society (MASS) Doctoral Scholarship programme. I must also give a huge thank you to the Leverhulme Trust for funding this PhD.

This thesis would not have been possible without the huge efforts of all the teams working to model solar geoengineering, in particular Simone Tilmes and those involved in the GLENS project. An enormous thank you must also be given to Ben Kravitz for so warmly welcoming me to visit Pacific Northwest National Laboratory, along with the team at Harvard's Solar Geoengineering Research Program, in particular Pete Irvine. I have learnt so much from both Ben and Pete and their enthusiasm is very inspiring. In addition to the climate model data, a big thank you is also owed to Simon Gosling and Katie Smith for their development of the hydrological model MacPDM.17, as well as to all who helped in collecting the observed river flow data in the GRDC repository.

My time at Nottingham would not have been the same without all of my fellow MASS students, whom I will forever be grateful to for their support and comradeship. An honourable mention must also go to the University of Nottingham Scuba Diving society and all of the wonderful people there who make it so special. I also want to thank all of the amazing friends I have made in Nottingham over my 7 years there, many will be lifelong friends and have kept me laughing through the PhD.

My Mum and partner Theo deserve a very special thank you for all the meals they've cooked for me over the final 6 months, without which I would have eaten many more

microwave meals! Both my Mum and Dad have always been so supportive and believed in me even when I don't believe in myself. My 3 siblings Owen, Helen and Isaac are simply the best siblings anyone could ask for and their encouragement has kept me going through the challenging times. I am also extremely grateful for their proof-reading of the various iterations of this work. Finally, I want to thank Theo for his amazing support, always wanting the best for me and for helping me keep everything in perspective.

Contents

1 Introduction **1**

1.1 Motivation . . . 2

1.2 Background to Climate Change and Governance . . . 3

1.2.1 The Climate System . . . 5

1.2.2 Scientific Evidence, Monitoring and Observations . . . 7

1.2.3 Modelling Climate Change . . . 8

1.2.4 Impacts . . . 9

1.2.5 Adaptation and Mitigation . . . 10

1.3 Background to Geoengineering . . . 11

1.3.1 Carbon Dioxide Removal . . . 12

1.3.2 Solar Geoengineering . . . 13

1.3.2.1 Stratospheric Aerosol Geoengineering . . . 15

1.3.3 Modelling of Solar Geoengineering . . . 20

1.3.3.1 GeoMIP . . . 22

1.3.3.2 GLENS . . . 24

1.3.3.3 Other modelling results . . . 26

1.3.4 Projected Hydrological Impacts . . . 28

1.4 Research questions . . . 32

1.5 Thesis Structure . . . 33

2 Comparison of Online and Offline Runoff **35**

2.1 Introduction . . . 36

2.1.1 MacPDM.17 . . . 40

2.1.2 CLM4.5 - Land Surface Model used in GLENS . . . 44

2.1.3 Summary of model differences . . . 48

2.2 Method . . . 50

2.2.1 Processing GLENS data . . . 51

2.2.2 Modifying MacPDM . . . 52
2.2.3 Formatting climate variables for input into MacPDM . . . 52
2.2.4 Selection of validation catchments . . . 53
2.3 Results . . . 56
2.3.1 Comparison with observed data . . . 56
2.3.2 Projected differences under SG and RCP8.5 . . . 65
2.3.2.1 38 catchments used in validation . . . 65
2.3.2.2 Global analysis using hydroregions . . . 71
2.4 Discussion . . . 79
2.5 Conclusion . . . 87

3 Drought Runoff under Solar Geoengineering 88
3.1 Introduction . . . 89
3.1.1 Types of drought and drought propagation . . . 90
3.1.2 Drought indices . . . 92
3.1.3 Threshold methods and low flow analysis . . . 94
3.1.4 Current studies of drought under solar geoengineering . . . 95
3.1.5 Chapter Outline . . . 98
3.2 Method . . . 99
3.2.1 Extreme value analysis of monthly minimum runoff . . . 99
3.2.2 Low flow statistics . . . 101
3.2.2.1 Seasonality in low flow . . . 102
3.3 Results . . . 103
3.3.1 Extreme Minimum Monthly Flow . . . 104
3.3.2 Analysis of gridcell level low flow . . . 106
3.4 Discussion . . . 114
3.5 Conclusion . . . 119

4 Water Scarcity under Solar Geoengineering 121
4.1 Introduction . . . 122
4.1.1 Global Water Scarcity . . . 122
4.1.2 Chapter Outline . . . 125
4.2 Materials and Methods . . . 126
4.2.1 Climate model and scenarios . . . 126
4.2.2 Population scenarios . . . 126
4.2.3 The WCI . . . 127
4.2.4 Statistical Analysis . . . 131

4.2.5 Comparison with only population changing in the future 133
4.3 Results 133
4.4 Discussion 142
4.5 Conclusions 148

5 Synthesis and Conclusion **150**
5.1 Research Questions 151
5.1.1 Road ahead for Solar Geoengineering? 155
5.2 Future work 158

Appendix A Hydrobelts and hydroregions **159**

Appendix B Catchment comparison graphs **161**

Appendix C Low flow quantile change maps - Q80 **200**

Appendix D Standard deviation of daily precipitation **203**

Appendix E Power of the permutation test **205**

Appendix F Water Scarcity projections by Sub-region **207**

List of Figures

1.1 The many interactions between components of the Earth system which drive climate. Radiation from the sun brings life to plants and warms our atmosphere, plants exchange CO_2 and water with the atmosphere, clouds transport water around the planet precipitating down over our land and oceans, the ocean helps regulate heat and CO_2 from the atmosphere and volcanic eruptions eject particles into the atmosphere which can have a cooling effect. Humans have had a hand in altering almost all aspects of this climate system. Reproduced from Lockwood (2009), after an original in Houghton (2005). 5

1.2 Radiative forcing estimates in 2011 relative to 1750 and aggregated uncertainties for the main drivers of climate change. Values are global average radiative forcing (RF), partitioned according to the emitted compounds or processes that result in a combination of drivers. The best estimates of the net radiative forcing are shown as black diamonds with corresponding uncertainty intervals; the numerical values are provided on the right of the figure, together with the confidence level in the net forcing (VH – very high, H – high, M – medium, L – low, VL – very low). Albedo forcing due to black carbon on snow and ice is included in the black carbon aerosol bar. Small forcings due to contrails (0.05 W m–2, including contrail induced cirrus), and HFCs, PFCs and SF6 (total 0.03 W m–2) are not shown. Concentration-based RFs for gases can be obtained by summing the like-coloured bars. Volcanic forcing is not included as its episodic nature makes it difficult to compare to other forcing mechanisms. Total anthropogenic radiative forcing is provided for three different years relative to 1750. Taken from Stocker (2014). 6

1.3 The eponymously named Keeling Curve depicts the carbon dioxide atmospheric concentrations recorded at Mauna Loa observatory since Charles David Keeling first recorded atmospheric CO_2 there in 1958. Concentrations fluctuate seasonally, but an alarming continual increase from 318ppm of CO_2 to over 400ppm has taken place over the last 60 years. Adapted from Scripps Institution of Oceanography (2021). 7

1.4 Radiative forcing and global mean temperature trajectories for 9 CMIP6 scenarios, with inclusion of 4 RCPs used in CMIP5 for comparison. From Gidden et al. (2019). 9

1.5 Three-part schema of the climate problem. The horizontal arrows in the top row show the causal chain in this version of the anthropogenic climate problem. The vertical arrows and the bottom row define the modes of intervention. From Keith (2000). 11

1.6 Preliminary overall evaluation of the main geoengineering techniques based on their effectiveness and affordability (as well as safety and timeliness). From Shepherd (2009). 11

1.7 A representation of various proposed geoengineering techniques. From New Scientist (2009). 12

1.8 Modelled and observed near-global (82.5°N–70°S) monthly mean temperature anomalies of the lower troposphere (TLT) before and after statistical removal of El Niño–Southern Oscillation (ENSO) and volcano signals. (a) The original TLT anomalies are departures from the climatological monthly means over January 1979–December 2012. (b) Removal of the estimated ENSO signal in TLT reduces the noise that partially obscures the temperature response to the eruptions of El Chichón and Pinatubo. (c) Temperature residuals derived from subtracting the ENSO, El Chichón, and Pinatubo signals from the original TLT data. Figure from Santer et al. (2014). The grey band (composing of many overlapping individual lines) shows the TLT anomaly range from 28 individual global climate models used in the Phase 5 Coupled Model Intercomparison Project (CMIP5) which contributed to the fifth IPCC assessment report; for example CanESM2, GISS-E2-R, HadGEM2-ES, MIROC5 and NorESM1-M. The black line depicts the multi-model mean TLT anomaly from all of these individual models. The red and blue lines show two independent remote sensing satellite products for observed TLT. 19

1.9 Situated on the Kuril Islands in the North Pacific, the image depicts the eruption of the Raikoke volcano on June 22^{nd} 2019, which was violent enough to reach into the stratosphere. Some volcanic eruptions can deliver enough material into the stratosphere to increase stratospheric aerosol levels and reduce radiative forcing. Figure from NASA (2019). 20

1.10 A schematic of the four experiments from GeoMIP Phase 1. G1 and G2 are solar dimming experiments in which incoming solar radiation is turned down in the model, whilst G3 and G4 use injection of SO_2 or sulphate aerosols into the tropical lower stratosphere. G3 approximately balances the RCP4.5 positive forcing, whilst G4 forces a negative radiative forcing from the beginning of the experiment through injection of 5 Tg of SO_2 per year. Figure adapted from Kravitz et al. (2011). 23

1.11 Global mean surface temperature (T0; top), the inter-hemispheric surface temperature gradient (T1; middle), and the equator-to-pole surface temperature gradient (T2; bottom) for RCP8.5 (grey for single ensemble members and black for the ensemble mean) and for the geoengineering simulations (light blue for single ensemble members and dark blue for the ensemble mean) as compared to 2015-2025 values for the RCP8.5 simulation. From Tilmes et al. (2018). 26

1.12 Through emissions reductions and CDR long-term stabilization of the climate is possible, but there is potential for significant overshoot of the desired maximum temperature increase. Limited and temporary solar geoengineering may be able to shave the peak off of this overshoot. From MacMartin et al. (2018). 27

1.13 All-model ensemble annual average hydrology differences (mm day^{-1}), averaged over simulation years 11-50. The stippling indicates where fewer than 75 percent of the models (9/12) agree on the sign of difference. Adapted from Figure 5 (Kravitz et al., 2013a). 29

2.1 A schematic overview of the model components and structure of MacPDM. 43

2.2 Location of the 38 catchments used in the study. 54

2.3 Difference in annual average total catchment discharge/runoff between GRDC observed data and 3 modelled/gridded outputs for 38 catchments around the globe. 57

2.4 Difference in monthly average total catchment discharge/runoff between GRDC observed data and GLENS and MacPDM modelled outputs for Yenisey river. 59
2.5 Difference in monthly average total catchment discharge/runoff between GRDC observed data and GLENS and MacPDM modelled outputs for Severnaya Dvina river. 59
2.6 Difference in monthly average total catchment discharge/runoff between GRDC observed data and GLENS and MacPDM modelled outputs for Rhine river. 60
2.7 Difference in monthly average total catchment discharge/runoff between GRDC observed data and GLENS and MacPDM modelled outputs for Elbe river. 60
2.8 Difference in monthly average total catchment discharge/runoff between GRDC observed data and GLENS and MacPDM modelled outputs for Fraser river. 61
2.9 Difference in monthly average total catchment discharge/runoff between GRDC observed data and GLENS and MacPDM modelled outputs for Columbia river. 61
2.10 Difference in monthly average total catchment discharge/runoff between GRDC observed data and GLENS and MacPDM modelled outputs for Mississippi river. 61
2.11 Difference in monthly average total catchment discharge/runoff between GRDC observed data and GLENS and MacPDM modelled outputs for Rio Santiago river. 62
2.12 Difference in monthly average total catchment discharge/runoff between GRDC observed data and GLENS and MacPDM modelled outputs for Irrawaddy river. 62
2.13 Difference in monthly average total catchment discharge/runoff between GRDC observed data and GLENS and MacPDM modelled outputs for Chao Phraya river. 62
2.14 Difference in monthly average total catchment discharge/runoff between GRDC observed data and GLENS and MacPDM modelled outputs for Xingu river. 63
2.15 Difference in monthly average total catchment discharge/runoff between GRDC observed data and GLENS and MacPDM modelled outputs for Zaire river. 63

2.16 Difference in monthly average total catchment discharge/runoff between GRDC observed data and GLENS and MacPDM modelled outputs for Sao Francisco river. 64
2.17 Difference in monthly average total catchment discharge/runoff between GRDC observed data and GLENS and MacPDM modelled outputs for Darling river. 64
2.18 Difference in monthly average total catchment discharge/runoff between GRDC observed data and GLENS and MacPDM modelled outputs for Fitzroy river. 65
2.19 Violin plots to display differences in model (MacPDM vs. GLENS) and scenario (RCP8.5 vs. SG) projections from control period for a number of different hydroregions - a) Boreal North America, b) Boreal Europe, c) Boreal Asia (West Siberia), d) Boreal Asia (East Siberia), e) Northern Mid Latitude North America, f) Northern Mid Latitude Europe, g) Northern Mid Latitude Asia. 73
2.20 Violin plots to display differences in model (MacPDM vs. GLENS) and scenario (RCP8.5 vs. SG) projections from control period for a number of different hydroregions - a) Northern Dry North America, b) Northern Dry Africa, c) Northern Dry Asia (Middle East), d) Northern Dry Asia (Central Asia), e) Northern Sub Tropical North America, f) Northern Sub Tropical Africa, g) Northern Sub Tropical Asia. 74
2.21 Violin plots to display differences in model (MacPDM vs. GLENS) and scenario (RCP8.5 vs. SG) projections from control period for a number of different hydroregions - a) Equatorial South America, b) Equatorial Africa, c) Equatorial Asia, d) Southern Sub Tropical South America, e) Southern Sub Tropical Africa, f) Southern Sub Tropical Australia and Oceania. . . . 75
2.22 Violin plots to display differences in model (MacPDM vs. GLENS) and scenario (RCP8.5 vs. SG) projections from control period for a number of different hydroregions - a) Southern Dry South America, b) Southern Dry Africa, c) Southern Dry Australia and Oceania, d) Southern Mid Latitude South America, e) Southern Mid Latitude Africa, f) Southern Mid Latitude Australia and Oceania. 76
2.23 Percentage changes in future mean annual runoff (2050-70) by gridcell for RCP8.5 and SG under MacPDM modelling for Northern Hemisphere hydroregions. 77

2.24 Percentage changes in future mean annual runoff (2050-70) by gridcell for RCP8.5 and SG under MacPDM modelling for Equatorial and Southern Hemisphere hydroregions. 77
2.25 Percentage changes in future mean annual runoff (2050-70) by gridcell for RCP8.5 and SG under GLENS modelling for Northern Hemisphere hydroregions. 78
2.26 Percentage changes in future mean annual runoff (2050-70) by gridcell for RCP8.5 and SG under GLENS modelling for Equatorial and Southern Hemisphere hydroregions. 78

3.1 Example of detrended timeseries of monthly minimum each year. 100
3.2 Results from the extreme value analysis showing the 20 year return level of monthly minimum runoff in each catchment, with comparison between baseline (BL) 2010-30 in black, RCP8.5 (CC) 2050-70 in red and Solar Geoengineering (SG) 2050-70 in blue. 105
3.3 Percentage difference in Q95 between SG 2050-70 and Baseline 2010-30 - (SG-BL)/BL x 100. 108
3.4 Percentage difference in Q95 between RCP8.5 2050-70 and Baseline 2010-30 - (RCP8.5-BL)/BL x 100. 108
3.5 Absolute (mm) difference in Q95 between SG 2050-70 and Baseline (2010-30) - SG-BL. 109
3.6 Absolute (mm) difference in Q95 between RCP8.5 2050-70 and Baseline (2010-30) - RCP8.5-BL. 109
3.7 The change in seasonality of months below the Q95 low flow runoff threshold (see methods) from baseline (2010-30) to future scenario (2050-70) per gridcell, grouped by hydroregion. 113
3.8 The change in seasonality of months below the Q80 low flow runoff threshold (see methods) from baseline (2010-30) to future scenario (2050-70) per gridcell, grouped by hydroregion. 114

4.1 Relative change in annual river discharge at 2°C compared with present-day, under RCP8.5. Colour hues show the multimodel mean change, and saturation shows the agreement on the sign of change across all GHM GCM combinations. From Schewe et al. (2014). 123
4.2 Future global population projections under the five SSPs. The population pathways SSP2, 3 and 5 are found to be compatible with a future where solar geoengineering may be implemented and so are used in this research. . 124

4.3 The effect of climate change only on exposure to water scarcity in 2050 under the SRES A1B scenario, using the WCI (1,000 m^3/capita/year; left panels) and the WSI (0.4; right panels). Top panels display the change in scarcity classes with the HadCM3 GCM only. The other panels show consistency across 21 simulations (with all CMIP3 models), in terms of the number of simulations out of 21 that show an increase in exposure (indicative of where there is an increase in scarcity or a watershed moves into water scarcity; middle panels), or decreases (a decrease in scarcity or move out of scarcity; bottom panels). From Gosling and Arnell (2016). 125
4.4 The Sub-regions of the globe as defined by the UN geoscheme (United Nations, 2019). 129
4.5 Schematic to show the data pre-processing required before calculation of water scarcity. 130
4.6 The number of people in water scarcity across the globe using the RCP8.5 and SG 20 ensemble members. The shaded area contains the 5th and 95th percentiles. The year the permutation test shows a pointwise statistically significant difference (p<=0.05) for the first time between the RCP8.5 and SG scenarios can be seen as a vertical line on the graph. 134
4.7 The number of people in water scarcity in each Sub-region using the RCP8.5 and SG 20 ensemble members . The shaded area contains the 5th and 95th percentiles. The year the permutation test shows a pointwise statistically significant difference (p<=0.05) for the first time between the RCP8.5 and SG scenarios can be seen as a vertical line on the graph. 135
4.8 The 3 cartograms (under a) SSP2, b) SSP3 and c) SSP5 population projections) show the proportional future change in people exposed to water scarcity when the solar geoengineering scenario is compared to RCP8.5 ((RCP8.5 - SG) / RCP8.5 *100). The distorted areas of each Sub-region represents the number of people in water scarcity, the colour represents the magnitude of proportional change and the shading gives the degree of certainty in the signal of water scarcity through the total number of years across the ensembles for which the difference between the scenarios is statistically significant. 137
4.9 Percentage change in water scarcity from baseline (2010-30) under 3 population pathways (SSP2, 3 and 5) and 3 future (2050-70) scenarios (only change in population, RCP8.5 and SG). The bars show the ensemble mean, with the range being the maximum and minimum values across the ensemble. 138

4.10 Percentage change in water scarcity from baseline (2010-30) under 3 population pathways (SSP2, 3 and 5) and 3 future (2050-70) scenarios (only change in population, RCP8.5 and SG). The bars show the ensemble mean, with the range being the maximum and minimum values across the ensemble. 139

5.1 Year of "solar geoengineering" or "solar radiation management" publications from Web of Science search, February 2021. 156

A.1 Location of the 8 global hydrobelts (excluding Greenland) and 26 hydroregions as defined by Meybeck et al. (2013). 160

B.1 Catchment comparison graphs for Kolyma catchment under Observed, GLENS and MacPDM results. Graphs show the ensemble mean modelled (2015-2025) and observed runoff distributions for a) annual, DJF and JJA and b) seasonal cycle and well as c) projected future (2050-70) runoff differences by model (MacPDM vs. GLENS) and scenario (RCP8.5 vs. SG). 162

B.2 Catchment comparison graphs for Lena catchment under Observed, GLENS and MacPDM results. Graphs show the ensemble mean modelled (2015-2025) and observed runoff distributions for a) annual, DJF and JJA and b) seasonal cycle and well as c) projected future (2050-70) runoff differences by model (MacPDM vs. GLENS) and scenario (RCP8.5 vs. SG). 163

B.3 Catchment comparison graphs for Amur catchment under Observed, GLENS and MacPDM results. Graphs show the ensemble mean modelled (2015-2025) and observed runoff distributions for a) annual, DJF and JJA and b) seasonal cycle and well as c) projected future (2050-70) runoff differences by model (MacPDM vs. GLENS) and scenario (RCP8.5 vs. SG). 164

B.4 Catchment comparison graphs for Yenisey catchment under Observed, GLENS and MacPDM results. Graphs show the ensemble mean modelled (2015-2025) and observed runoff distributions for a) annual, DJF and JJA and b) seasonal cycle and well as c) projected future (2050-70) runoff differences by model (MacPDM vs. GLENS) and scenario (RCP8.5 vs. SG). 165

B.5 Catchment comparison graphs for Olenek catchment under Observed, GLENS and MacPDM results. Graphs show the ensemble mean modelled (2015-2025) and observed runoff distributions for a) annual, DJF and JJA and b) seasonal cycle and well as c) projected future (2050-70) runoff differences by model (MacPDM vs. GLENS) and scenario (RCP8.5 vs. SG). 166

B.6 Catchment comparison graphs for Severnaya Dvina catchment under Observed, GLENS and MacPDM results. Graphs show the ensemble mean modelled (2015-2025) and observed runoff distributions for a) annual, DJF and JJA and b) seasonal cycle and well as c) projected future (2050-70) runoff differences by model (MacPDM vs. GLENS) and scenario (RCP8.5 vs. SG). 167
B.7 Catchment comparison graphs for MacKenzie catchment under Observed, GLENS and MacPDM results. Graphs show the ensemble mean modelled (2015-2025) and observed runoff distributions for a) annual, DJF and JJA and b) seasonal cycle and well as c) projected future (2050-70) runoff differences by model (MacPDM vs. GLENS) and scenario (RCP8.5 vs. SG). . 168
B.8 Catchment comparison graphs for Saskatchewan catchment under Observed, GLENS and MacPDM results. Graphs show the ensemble mean modelled (2015-2025) and observed runoff distributions for a) annual, DJF and JJA and b) seasonal cycle and well as c) projected future (2050-70) runoff differences by model (MacPDM vs. GLENS) and scenario (RCP8.5 vs. SG). . 169
B.9 Catchment comparison graphs for Assiniboine catchment under Observed, GLENS and MacPDM results. Graphs show the ensemble mean modelled (2015-2025) and observed runoff distributions for a) annual, DJF and JJA and b) seasonal cycle and well as c) projected future (2050-70) runoff differences by model (MacPDM vs. GLENS) and scenario (RCP8.5 vs. SG). . 170
B.10 Catchment comparison graphs for Red catchment under Observed, GLENS and MacPDM results. Graphs show the ensemble mean modelled (2015-2025) and observed runoff distributions for a) annual, DJF and JJA and b) seasonal cycle and well as c) projected future (2050-70) runoff differences by model (MacPDM vs. GLENS) and scenario (RCP8.5 vs. SG). 171
B.11 Catchment comparison graphs for Winnipeg catchment under Observed, GLENS and MacPDM results. Graphs show the ensemble mean modelled (2015-2025) and observed runoff distributions for a) annual, DJF and JJA and b) seasonal cycle and well as c) projected future (2050-70) runoff differences by model (MacPDM vs. GLENS) and scenario (RCP8.5 vs. SG). . 172
B.12 Catchment comparison graphs for Churchill catchment under Observed, GLENS and MacPDM results. Graphs show the ensemble mean modelled (2015-2025) and observed runoff distributions for a) annual, DJF and JJA and b) seasonal cycle and well as c) projected future (2050-70) runoff differences by model (MacPDM vs. GLENS) and scenario (RCP8.5 vs. SG). . 173

B.13 Catchment comparison graphs for Albany catchment under Observed, GLENS and MacPDM results. Graphs show the ensemble mean modelled (2015-2025) and observed runoff distributions for a) annual, DJF and JJA and b) seasonal cycle and well as c) projected future (2050-70) runoff differences by model (MacPDM vs. GLENS) and scenario (RCP8.5 vs. SG). 174
B.14 Catchment comparison graphs for Yangtze catchment under Observed, GLENS and MacPDM results. Graphs show the ensemble mean modelled (2015-2025) and observed runoff distributions for a) annual, DJF and JJA and b) seasonal cycle and well as c) projected future (2050-70) runoff differences by model (MacPDM vs. GLENS) and scenario (RCP8.5 vs. SG). 175
B.15 Catchment comparison graphs for Elbe catchment under Observed, GLENS and MacPDM results. Graphs show the ensemble mean modelled (2015-2025) and observed runoff distributions for a) annual, DJF and JJA and b) seasonal cycle and well as c) projected future (2050-70) runoff differences by model (MacPDM vs. GLENS) and scenario (RCP8.5 vs. SG). 176
B.16 Catchment comparison graphs for Rhine catchment under Observed, GLENS and MacPDM results. Graphs show the ensemble mean modelled (2015-2025) and observed runoff distributions for a) annual, DJF and JJA and b) seasonal cycle and well as c) projected future (2050-70) runoff differences by model (MacPDM vs. GLENS) and scenario (RCP8.5 vs. SG). 177
B.17 Catchment comparison graphs for Danube catchment under Observed, GLENS and MacPDM results. Graphs show the ensemble mean modelled (2015-2025) and observed runoff distributions for a) annual, DJF and JJA and b) seasonal cycle and well as c) projected future (2050-70) runoff differences by model (MacPDM vs. GLENS) and scenario (RCP8.5 vs. SG). 178
B.18 Catchment comparison graphs for Neva catchment under Observed, GLENS and MacPDM results. Graphs show the ensemble mean modelled (2015-2025) and observed runoff distributions for a) annual, DJF and JJA and b) seasonal cycle and well as c) projected future (2050-70) runoff differences by model (MacPDM vs. GLENS) and scenario (RCP8.5 vs. SG). 179
B.19 Catchment comparison graphs for Volga catchment under Observed, GLENS and MacPDM results. Graphs show the ensemble mean modelled (2015-2025) and observed runoff distributions for a) annual, DJF and JJA and b) seasonal cycle and well as c) projected future (2050-70) runoff differences by model (MacPDM vs. GLENS) and scenario (RCP8.5 vs. SG). 180

B.20 Catchment comparison graphs for Don catchment under Observed, GLENS and MacPDM results. Graphs show the ensemble mean modelled (2015-2025) and observed runoff distributions for a) annual, DJF and JJA and b) seasonal cycle and well as c) projected future (2050-70) runoff differences by model (MacPDM vs. GLENS) and scenario (RCP8.5 vs. SG). 181
B.21 Catchment comparison graphs for Columbia catchment under Observed, GLENS and MacPDM results. Graphs show the ensemble mean modelled (2015-2025) and observed runoff distributions for a) annual, DJF and JJA and b) seasonal cycle and well as c) projected future (2050-70) runoff differences by model (MacPDM vs. GLENS) and scenario (RCP8.5 vs. SG). . 182
B.22 Catchment comparison graphs for Mississippi catchment under Observed, GLENS and MacPDM results. Graphs show the ensemble mean modelled (2015-2025) and observed runoff distributions for a) annual, DJF and JJA and b) seasonal cycle and well as c) projected future (2050-70) runoff differences by model (MacPDM vs. GLENS) and scenario (RCP8.5 vs. SG). . 183
B.23 Catchment comparison graphs for St. Lawrence catchment under Observed, GLENS and MacPDM results. Graphs show the ensemble mean modelled (2015-2025) and observed runoff distributions for a) annual, DJF and JJA and b) seasonal cycle and well as c) projected future (2050-70) runoff differences by model (MacPDM vs. GLENS) and scenario (RCP8.5 vs. SG). . 184
B.24 Catchment comparison graphs for Fraser catchment under Observed, GLENS and MacPDM results. Graphs show the ensemble mean modelled (2015-2025) and observed runoff distributions for a) annual, DJF and JJA and b) seasonal cycle and well as c) projected future (2050-70) runoff differences by model (MacPDM vs. GLENS) and scenario (RCP8.5 vs. SG). 185
B.25 Catchment comparison graphs for Colorado catchment under Observed, GLENS and MacPDM results. Graphs show the ensemble mean modelled (2015-2025) and observed runoff distributions for a) annual, DJF and JJA and b) seasonal cycle and well as c) projected future (2050-70) runoff differences by model (MacPDM vs. GLENS) and scenario (RCP8.5 vs. SG). . 186
B.26 Catchment comparison graphs for Rio Santiago catchment under Observed, GLENS and MacPDM results. Graphs show the ensemble mean modelled (2015-2025) and observed runoff distributions for a) annual, DJF and JJA and b) seasonal cycle and well as c) projected future (2050-70) runoff differences by model (MacPDM vs. GLENS) and scenario (RCP8.5 vs. SG). . 187

B.27 Catchment comparison graphs for Irrawaddy catchment under Observed, GLENS and MacPDM results. Graphs show the ensemble mean modelled (2015-2025) and observed runoff distributions for a) annual, DJF and JJA and b) seasonal cycle and well as c) projected future (2050-70) runoff differences by model (MacPDM vs. GLENS) and scenario (RCP8.5 vs. SG). . 188
B.28 Catchment comparison graphs for Chao Phraya catchment under Observed, GLENS and MacPDM results. Graphs show the ensemble mean modelled (2015-2025) and observed runoff distributions for a) annual, DJF and JJA and b) seasonal cycle and well as c) projected future (2050-70) runoff differences by model (MacPDM vs. GLENS) and scenario (RCP8.5 vs. SG). . 189
B.29 Catchment comparison graphs for Zaire catchment under Observed, GLENS and MacPDM results. Graphs show the ensemble mean modelled (2015-2025) and observed runoff distributions for a) annual, DJF and JJA and b) seasonal cycle and well as c) projected future (2050-70) runoff differences by model (MacPDM vs. GLENS) and scenario (RCP8.5 vs. SG). 190
B.30 Catchment comparison graphs for Amazonas catchment under Observed, GLENS and MacPDM results. Graphs show the ensemble mean modelled (2015-2025) and observed runoff distributions for a) annual, DJF and JJA and b) seasonal cycle and well as c) projected future (2050-70) runoff differences by model (MacPDM vs. GLENS) and scenario (RCP8.5 vs. SG). . 191
B.31 Catchment comparison graphs for Xingu catchment under Observed, GLENS and MacPDM results. Graphs show the ensemble mean modelled (2015-2025) and observed runoff distributions for a) annual, DJF and JJA and b) seasonal cycle and well as c) projected future (2050-70) runoff differences by model (MacPDM vs. GLENS) and scenario (RCP8.5 vs. SG). 192
B.32 Catchment comparison graphs for Burdekin catchment under Observed, GLENS and MacPDM results. Graphs show the ensemble mean modelled (2015-2025) and observed runoff distributions for a) annual, DJF and JJA and b) seasonal cycle and well as c) projected future (2050-70) runoff differences by model (MacPDM vs. GLENS) and scenario (RCP8.5 vs. SG). . 193
B.33 Catchment comparison graphs for Rio Parnaiba catchment under Observed, GLENS and MacPDM results. Graphs show the ensemble mean modelled (2015-2025) and observed runoff distributions for a) annual, DJF and JJA and b) seasonal cycle and well as c) projected future (2050-70) runoff differences by model (MacPDM vs. GLENS) and scenario (RCP8.5 vs. SG). . 194

B.34 Catchment comparison graphs for Sao Francisco catchment under Observed, GLENS and MacPDM results. Graphs show the ensemble mean modelled (2015-2025) and observed runoff distributions for a) annual, DJF and JJA and b) seasonal cycle and well as c) projected future (2050-70) runoff differences by model (MacPDM vs. GLENS) and scenario (RCP8.5 vs. SG). . 195
B.35 Catchment comparison graphs for Cooper Creek catchment under Observed, GLENS and MacPDM results. Graphs show the ensemble mean modelled (2015-2025) and observed runoff distributions for a) annual, DJF and JJA and b) seasonal cycle and well as c) projected future (2050-70) runoff differences by model (MacPDM vs. GLENS) and scenario (RCP8.5 vs. SG). . 196
B.36 Catchment comparison graphs for Orange catchment under Observed, GLENS and MacPDM results. Graphs show the ensemble mean modelled (2015-2025) and observed runoff distributions for a) annual, DJF and JJA and b) seasonal cycle and well as c) projected future (2050-70) runoff differences by model (MacPDM vs. GLENS) and scenario (RCP8.5 vs. SG). 197
B.37 Catchment comparison graphs for Fitzroy catchment under Observed, GLENS and MacPDM results. Graphs show the ensemble mean modelled (2015-2025) and observed runoff distributions for a) annual, DJF and JJA and b) seasonal cycle and well as c) projected future (2050-70) runoff differences by model (MacPDM vs. GLENS) and scenario (RCP8.5 vs. SG). 198
B.38 Catchment comparison graphs for Darling catchment under Observed, GLENS and MacPDM results. Graphs show the ensemble mean modelled (2015-2025) and observed runoff distributions for a) annual, DJF and JJA and b) seasonal cycle and well as c) projected future (2050-70) runoff differences by model (MacPDM vs. GLENS) and scenario (RCP8.5 vs. SG). 199

C.1 Percentage difference in Q80 between SG 2050-70 and Baseline (2010-30) - (SG-BL)/BL x 100). 201
C.2 Percentage difference in Q80 between RCP8.5 2050-70 and Baseline (2010-30) - (RCP8.5-BL)/BL x 100). 201
C.3 Absolute (mm) difference in Q80 between SG 2050-70 and Baseline (2010-30) - SG-BL. 202
C.4 Absolute (mm) difference in Q80 between RCP8.5 2050-70 and Baseline (2010-30) - RCP8.5-BL. 202

D.1 Graph to show the standard deviation for each year in the daily total land precipitation for each of the 3 RCP8.5 and 20 SG ensemble members. . . . 204

F.1 Graph shows the percentage change in water scarcity for each Sub-region in the future (2050-70) under three scenarios (only change in population, scenario for RCP8.5 and scenario for SG) in comparison to the present day (2010-30). 208
F.2 Graph shows the percentage change in water scarcity for each Sub-region in the future (2050-70) under three scenarios (only change in population, scenario for RCP8.5 and scenario for SG) in comparison to the present day (2010-30). 209
F.3 Graph shows the percentage change in water scarcity for each Sub-region in the future (2050-70) under three scenarios (only change in population, scenario for RCP8.5 and scenario for SG) in comparison to the present day (2010-30). 210
F.4 Graph shows the percentage change in water scarcity for each Sub-region in the future (2050-70) under three scenarios (only change in population, scenario for RCP8.5 and scenario for SG) in comparison to the present day (2010-30). 211
F.5 Graph shows the percentage change in water scarcity for each Sub-region in the future (2050-70) under three scenarios (only change in population, scenario for RCP8.5 and scenario for SG) in comparison to the present day (2010-30). 212

List of Tables

1.1 The four RCPs following different emissions scenarios which lead to set Radiative Forcing and degrees of climate change by the end of the century. From Moss et al. (2010). 8

1.2 Some of the main impacts of climate change. 10

2.1 A number of popular models used for global hydrology study 39

2.2 Structural model comparison between MacPDM and CLM4.5 49

2.3 Percentage differences ((modelled - observed)/observed *100) between gridded (GLENS, MacPDM, GRUN) and observed streamflow data for 38 global catchments (range in brackets). 58

2.4 Differences in time shift (in plus or minus months) of Monthly Peak and Minimum runoff between model (MacPDM and GLENS) and scenario (RCP8.5 and SG) for 38 global catchments, from mid century (2050-70) to baseline (2015-2030). 68

2.5 Percentage differences in Annual Change and Seasonal Amplitude of runoff between model (MacPDM and GLENS) and scenario (RCP8.5 and SG) for 38 global catchments, from mid century (2050-70) to baseline (2015-2030). . 70

2.6 General trends across the hydroregions for percentage change from the baseline in future (2050-70) mean annual runoff under RCP8.5 and SG. . . 78

3.1 Median (across the gridcells in each hydroregion) of the maximum length of consecutive months at or below Q95 and Q80, with the respective interquartile ranges in brackets. 112

3.2 Median (across the gridcells in each hydroregion) of the maximum length of consecutive months at or below Q95 and Q80, with the respective interquartile ranges in brackets. Using baseline 2010-30 thresholds. 112

4.1 The SSP scenarios (O'Neill et al., 2014). 127

E.1 Investigating the power of the permutation test, using a sample size of 20, 10 and 3 for the solar geoengineering group, including the median (minimum & maximum) of the 30 random sample sets of the 20 ensemble members for sample sizes of 10 and 3. The number of the 30 sample sets which were actually statistically significantly different are also shown to demonstrate how the power of the test and ability to find signifcant differences decreases with decreasing sample size. 206

List of Abbreviations

AR5/6 ..... IPCC Fifth/Sixth Assessment Report

BDC ..... Brewer-Dobson Circulation

BECS ..... Bio-energy with Carbon Storage

BVOC ..... Biogenic Volatile Organic Compound

CCS ..... Carbon Capture and Storage

CCT ..... Cirrus Cloud Thinning

CDO ..... Climate Data Operators

CDR ..... Carbon Dioxide Removal

CESM ..... Community Earth System Model

CIMP5/6 ..... Phase 5/6 Coupled Model Intercomparison Project

CLM ..... Community Land Model

COP ..... UN Conference of the Parties

DAC ..... Direct Air Capture

DGVM ..... Dynamic Global Vegetation Model

ENSO ..... El Niño-Southern Oscillation

ESM ..... Earth System Model

ET ..... Evapotranspiration

GAW ..... Global Atmospheric Watch

GCM ..... General Circulation Model

GCM ..... Global Climate Model

GeoMIP ..... Geonengineering Model Intercomparison Project

GHG ..... Greenhouse Gas

GHM ..... Global Hydrological Model

GHWM ..... Global Hydrology and Water Resources Model

GLENS ..... Geoengineering Large Ensemble project

GLUE ..... Generalised Likelihood Uncertainty Estimation

GRDC ..... Global Runoff Data Centre

GRUN ..... Global Grided Runoff dataset

IPCC ..... Intergovernmental Panel of Climate Change

ISIMIP ..... Inter-Sectoral Impact Model Intercomparison Project

JULES ..... Joint UK Land Environment Simulator

LAI ..... Leaf Area Index

LSM ..... Land Surface Model

MCB ..... Marine Cloud Brightening

MODIS ..... Moderate Resolution Imaging Spectroradiometer

NOA ..... North Atlantic Oscillation

NDCs ..... Nationally Determined Contributions

ORCHIDEE ..... ORganizing Carbon and Hydrology in Dynamic EcosystEms

PDSI ..... Palmer Drought Severity Index

PDM ..... Probability Distributed Model

PET ..... Potential Evapotranspiration

PFT ..... Plant Functional Type

RCP ..... Relative Concentration Pathway

RF ..... Radiative Forcing

RTM ..... River Transport Model

SAG ..... Stratospheric Aerosol Geoengineering

SAI ..... Stem Area Index

SG ..... Solar Geoengineering

SPEI ..... Standardized Precipitation Evapotranspiration Index

SPI ..... Standardized Precipitation Index

SRI ..... Standardized Runoff Index

SRM ..... Solar Radiation Management

SSP ..... Shared Socioeconomic Pathway

TOA ..... Top Of Atmosphere

UN ..... United Nations

UNFCCC ..... United Nations Framework Convention on Climate Change

USDA ..... United States Department of Agriculture

VOCs ..... Volatile Organic Compounds

WACCM ..... Whole Atmosphere Community Climate Model

WCI ..... Water Crowding Index

WMO ..... World Meteorological Organization

WSI ..... Water Stress Index

WS ..... Water Scarcity

Chapter 1

Introduction

1.1 Motivation

Climate change poses a significant and unremitting global threat which, if left without abatement, will result in catastrophic effects on our planet. The Intergovernmental Panel on Climate Change (IPCC), the main source of information on climate change, state that "Warming of the climate system is unequivocal, and since the 1950s, many of the observed changes are unprecedented over decades to millennia. The atmosphere and ocean have warmed, the amounts of snow and ice have diminished, sea level has risen, and the concentrations of greenhouse gases have increased" (Stocker, 2014). The solution is to stop our emissions of greenhouse gases now. However, it is becoming increasingly clear, particularly over the last decade, that current action is far too slow. Despite growing appreciation of the magnitude of this threat amongst policy makers, business owners and the general public, there still remains a global inertia which is holding back the rapid emissions reductions necessary to avoid the worst effects of climate change.

Amongst the scientific community there is growing credibility in the concept of geoengineering as an option to help address this dangerous climate change. Many feel more comfortable with methods of carbon capture and storage due to their relative safety and reduced interference in climate processes (Shepherd, 2009), with much progress having been made in increasing the efficiency and affordability of these methods (Keith et al., 2018). However, others argue that this approach is still too slow and small scale to make an appreciable difference quickly enough (Fuss et al., 2014, Rockström et al., 2016, Field and Mach, 2017), with many advocating for research into methods of solar geoengineering to help avoid the worst impacts of climate change (Wigley, 2006, Long and Shepherd, 2014, MacMartin et al., 2018). If solar geoengineering were to be a viable option, then much research is necessary in order to evaluate any and all of the risks and benefits. One well recognised effect of current terrestrial solar geoengineering approaches is that global temperature and global precipitation cannot both be perfectly corrected for at the same time (Irvine and Keith, 2020). Warming of the global climate is cited as leading to a "strengthening of the hydrological cycle" along with enhancing existing trends such that wet areas become wetter and dry areas drier (Held and Soden, 2006). Returning global temperature to a set value through solar geoengineering is widely understood to overcompensate the reduction in precipitation when compared to a world unimpeded by climate change, therefore resulting in a "weakening of the hydrological cycle". However, these impacts are very dependent on the scenario of solar geoengineering being considered, they are not intrinsically linked to solar geoengineering and need not occur, per se.

It is critical that the impacts of solar geoengineering are studied well ahead of a time when it may possibly be used, in an effort to avoid unintended consequences and ensure some comprehension of any trade-offs involved. Climate model outputs are, of course, just projections of possible modelled futures, but they are the best way for us to glean insight into global scale effects from solar geoengineering scenarios. Small scale field studies could also be extremely valuable for gaining better understanding of some of the fine scale processes involved; which for the stratosphere are not particularly well understood. Whilst much research has been conducted on the climate impacts of possible solar geoengineering scenarios, there has been little, if any, use of these model projections to gain an understanding of the direct risk to humanity, in particular no example of the risk of water scarcity from solar geoengineering can be found. Moving beyond the necessary baseline understanding of physical climate changes, this research looks to improve awareness of how a specific solar geoengineering scenario may affect future global water resources.

1.2 Background to Climate Change and Governance

Over the last 300 million years, plants and small organisms have trapped carbon from the atmosphere under the earth as coal, oil and natural gas. When humanity realised these reserves could be used as fuels we began to deplete them at ever increasing rates, releasing the carbon stored in them back to the atmosphere. We have known for more than a century now, when Nobel prize winner Svante Arrhenius (amongst others) first theorised the impact of atmospheric carbon dioxide on global temperature (Arrhenius, 1896), that this release of greenhouse gases will result in a warming of the climate. Through satellite observations and measurements taken at the surface, this effect has been substantiated and the warming observed since 1950 has been shown to be overwhelmingly anthropogenic in nature, with only a very small portion attributed to natural forcing (Huber and Knutti, 2012). "Fingerprinting" is a technique that has been employed to discern differences in temperature signals brought about by external natural solar variability and volcanic eruptions or anthropogenic influences of greenhouse gas concentrations and aerosols. The use of such techniques to study observed global temperature change concluded that multidecadal warming of the troposphere and cooling of the lower stratosphere, which is evident in all satellite datasets and simulations of forced climate change examined here, "cannot be explained by solar or volcanic forcing, or by any known mode of internal variability" (Santer et al., 2013). Cooling of the lower stratosphere is a result of human released aerosols, whilst the warming of the troposphere a result of human released greenhouse gases. This clear dominance of an anthropogenic signal in climate variability has also been detected

at the seasonal scale for tropospheric temperature (Santer et al., 2018).

As far back as 1965 (Tukey, 1965), with this understanding that carbon dioxide emissions over the coming decades would dramatically alter the climate and global surface temperatures, the US president's Science Advisory Committee warned of the predicted impacts resulting from this temperature rise, including rising sea levels, melting ice caps and biological changes. Interestingly, however, instead of encouraging changes in behaviour and use of fossil fuels, they hypothesised how this warming could be counteracted through alteration of surface albedo; more specifically through floating small reflective particles across large areas of ocean. This may be the earliest reference to geoengineering. Thanks to the efforts of fossil fuel industry lobbyists to create doubt about the human-induced nature and severity of climate change (in the same way the tobacco industry had previously done for smoking and cancer), this early warning failed to gain immediate widespread mainstream acceptance (Oreskes and Conway, 2011).

Under mounting concern in the 1980s about the impact of carbon dioxide and other greenhouse gases, the United Nations Environment Programme (UNEP) along with the World Meterological Organization (WMO) started to examine anthropogenic climate change and in 1988 formed the Intergovernmental Panel on Climate Change (IPCC) (IPCC, 2020). The IPCC released their Fifth Assessment Report (AR5) in 2013/2014, with contributions from three Working Groups: Working Group I covers the physical science basis of climate change; Working Group II investigates impacts, adaptation and vulnerability; Working Group III looks at mitigation of climate change (Stocker, 2014). The next report (AR6) will be released in stages through 2021 to 2022, with a special report on global warming of 1.5°C having been finalised in September 2018 (IPCC, 2020).

In order to address climate change, global action is required. Since 1995, there has been an annual meeting (except in 2020) entitled Conference of the Parties (COP) organised by the United Nations (UN) (UNFCCC, 2020a). COP21 was held in Paris in 2015 and was a significant step towards global agreement on the dangers of climate change and the action which must be taken. Here the Paris Agreement was drawn up, binding all countries, once ratified, to devise nationally determined contributions (NDCs) setting out each nations efforts to reduce their emissions and adapt to climate change. The main aim of the Paris Agreement is to limit global temperature increase during this century to well below 2°C, and if possible below 1.5°C, above pre-industrial levels (UNFCCC, 2020b).

It is interesting to note that, despite the extreme alteration in day-to-day human activities during 2020 in response to the Covid-19 outbreak, at the time of greatest reduction in daily

global CO_2 emissions (down 17% in early April when compared to the 2019 average) these emissions values correspond to levels seen in 2006 (Le Quéré et al., 2020) - highlighting just how rapid the global increase in CO_2 emissions has become, alongside demonstrating that changes in individual's behaviour alone will unlikely be enough to change our trajectory, we need system level change.

1.2.1 The Climate System

The Earth's climate is driven by interaction between the atmosphere, biosphere, hydrosphere, cryosphere and lithosphere (Lockwood, 2009), Figure 1.1. Atmospheric dynamics drive changes in precipitation, and many other variables, across the globe.

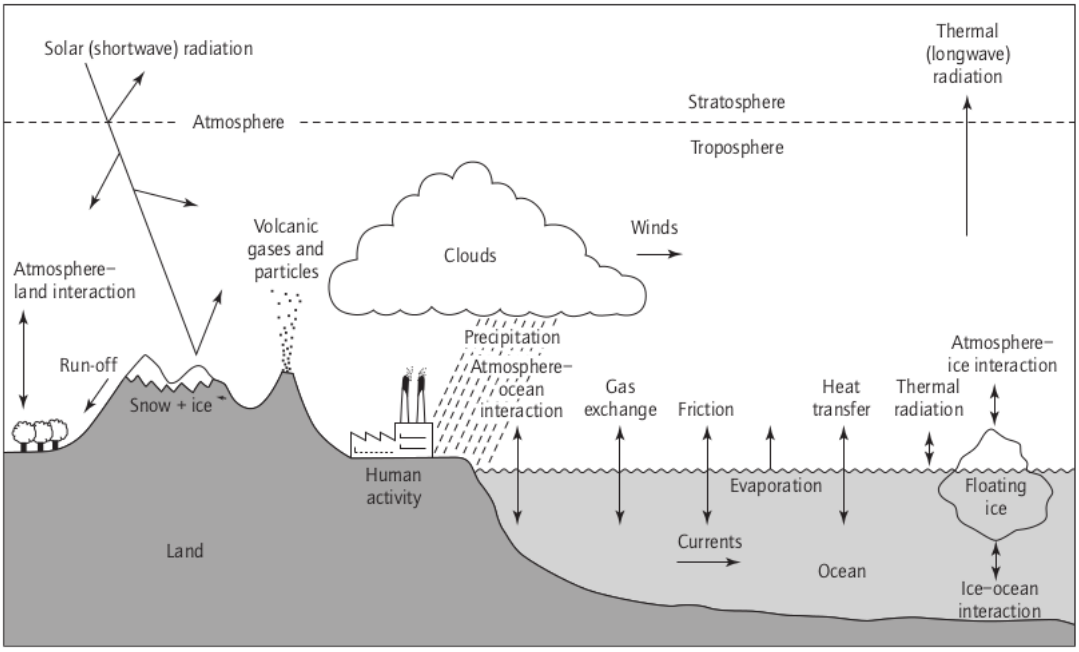


Figure 1.1: The many interactions between components of the Earth system which drive climate. Radiation from the sun brings life to plants and warms our atmosphere, plants exchange CO_2 and water with the atmosphere, clouds transport water around the planet precipitating down over our land and oceans, the ocean helps regulate heat and CO_2 from the atmosphere and volcanic eruptions eject particles into the atmosphere which can have a cooling effect. Humans have had a hand in altering almost all aspects of this climate system. Reproduced from Lockwood (2009), after an original in Houghton (2005).

One integral part of the climate system, and which keeps the planet habitable, are greenhouse gases (GHGs). Absorbing and emitting longwave radiation from the surface, GHGs prevent thermal radiation from travelling back out to space, trapping the heat close to the Earth's surface. It is our understanding of the different effects that various gases and aerosols have on the atmosphere which drives our appreciation of anthropogenic influences on the system and cultivated the idea that solar geoengineering could help us balance out these human induced effects. Radiative Forcing (RF) can act as a quantitative meas-

ure of the impact some imposed agents (e.g. GHGs) have on the climate response (in particular the mean global temperature). RF is normally measured in Watts/m^2 and is the net change in the Earth's energy balance between two points in time (usually from pre-industrial to present or a given future date) (Stocker, 2014). The RF of CO_2 was calculated in the latest IPCC report (Stocker, 2014) to be 1.82 (1.63 to 2.01)W/m^2 for the period from 1750 to 2011; by far the largest RF of any of the GHGs. Most aerosols (excluding Black carbon) have a cooling effect, however the uncertainty in their exact RF is larger than for many gases and greenhouse gases. Figure 1.2 outlines a number of key radiative forcing contributors and their proportional role in driving climate change.

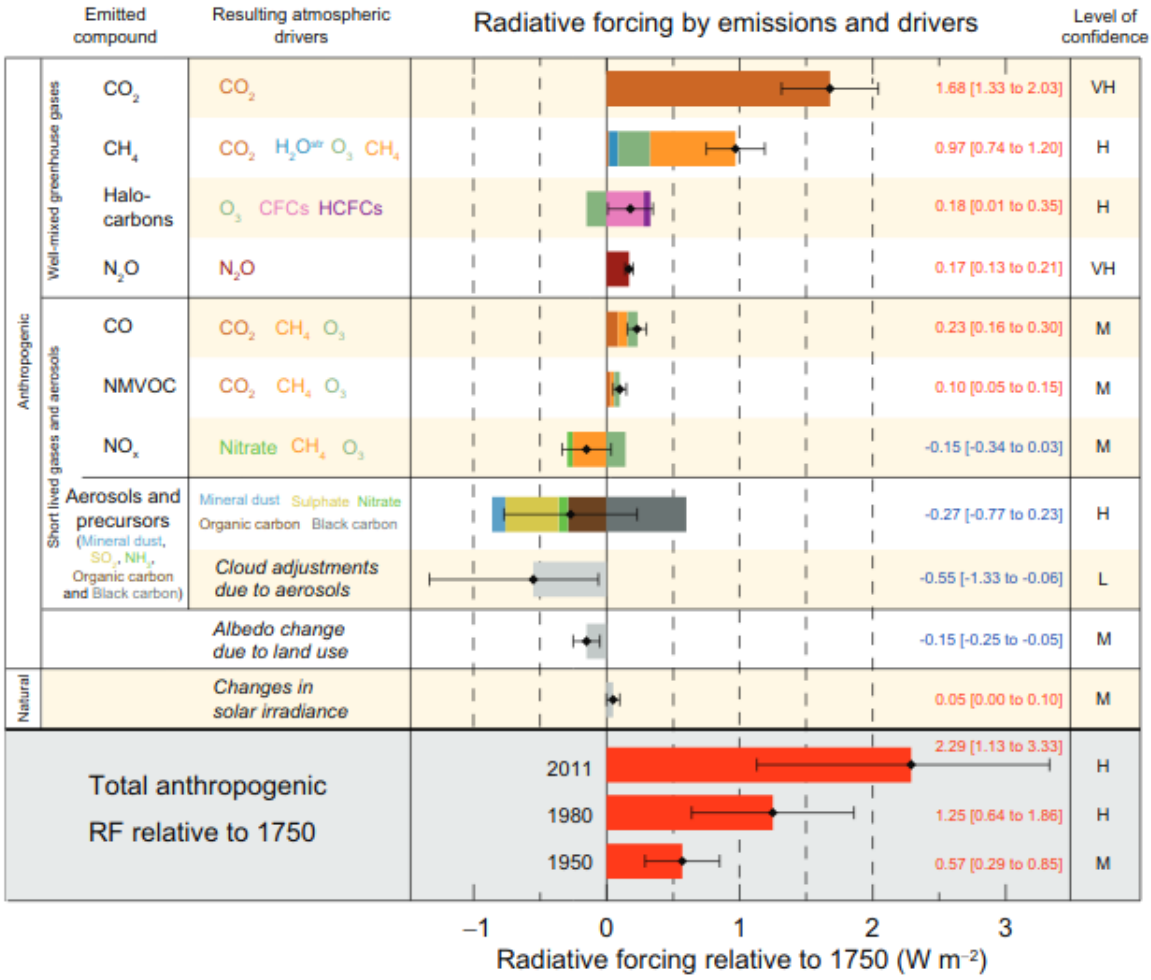


Figure 1.2: Radiative forcing estimates in 2011 relative to 1750 and aggregated uncertainties for the main drivers of climate change. Values are global average radiative forcing (RF), partitioned according to the emitted compounds or processes that result in a combination of drivers. The best estimates of the net radiative forcing are shown as black diamonds with corresponding uncertainty intervals; the numerical values are provided on the right of the figure, together with the confidence level in the net forcing (VH – very high, H – high, M – medium, L – low, VL – very low). Albedo forcing due to black carbon on snow and ice is included in the black carbon aerosol bar. Small forcings due to contrails (0.05 W m–2, including contrail induced cirrus), and HFCs, PFCs and SF6 (total 0.03 W m–2) are not shown. Concentration-based RFs for gases can be obtained by summing the like-coloured bars. Volcanic forcing is not included as its episodic nature makes it difficult to compare to other forcing mechanisms. Total anthropogenic radiative forcing is provided for three different years relative to 1750. Taken from Stocker (2014).

1.2.2 Scientific Evidence, Monitoring and Observations

The influence humankind has had on the planet since the industrial revolution has led to the last three centuries widely being considered its own epoch, the Anthropocene, seen to be distinctly different to the preceding 10-12 millennia of the warm Holocene epoch (Crutzen, 2002). Evidence, such as CO_2 and methane levels in the polar ice core records, show that greenhouse gas levels now surpass those seen in at least the last 800,000 years (Scripps Institution of Oceanography, 2021). In addition to the magnitude of change, the rate of CO_2 rise in the atmosphere in recent time has been shown to exceed instances of rapid CO_2 increases in the past, for example CO_2 jumps between 330,000 and 450,000 years ago were found to be nine times slower than present day rise in CO_2 (Nehrbass-Ahles et al., 2020).

In 1958 Charles David Keeling first officially recorded atmospheric CO_2 at Mauna Loa, Hawaii. Since then, recordings at Mauna Loa Observatory have been used to construct the famous Keeling Curve (Figure 1.3); a record of the increase in atmospheric CO_2 concentrations. This rapid rise in CO_2 concentration, from 280 parts per million (ppm) in pre-industrial times, to the most recent recording (24thth March 2021) of 416.16ppm (Scripps Institution of Oceanography, 2021) has been unrelenting. Before this PhD began in 2016 daily CO_2 levels were not yet consistently above 400ppm (due to seasonal fluctuations). This is now the case and the likely reality for many years to come.

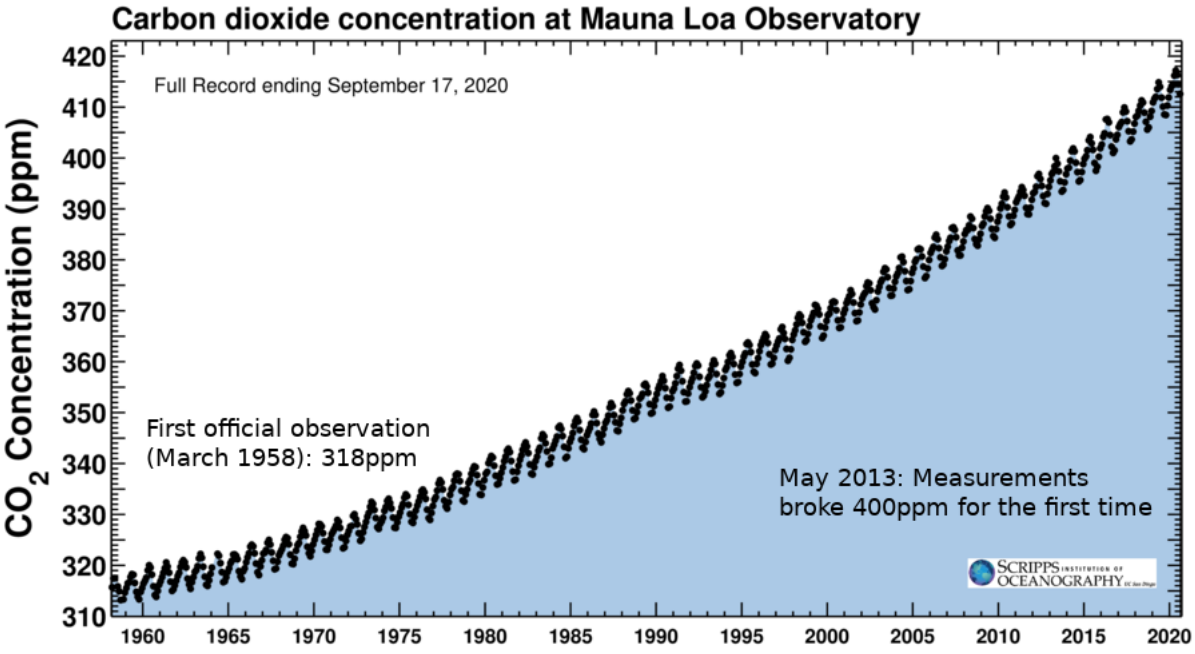


Figure 1.3: The eponymously named Keeling Curve depicts the carbon dioxide atmospheric concentrations recorded at Mauna Loa observatory since Charles David Keeling first recorded atmospheric CO_2 there in 1958. Concentrations fluctuate seasonally, but an alarming continual increase from 318ppm of CO_2 to over 400ppm has taken place over the last 60 years. Adapted from Scripps Institution of Oceanography (2021).

Other GHGs, in addition to CO_2, are being increasingly recognised for their importance in raising global temperature levels, perhaps most notably methane (CH_4) and black carbon (soot) (Van Renssen, 2012). Climate change is monitored through a global network of instrumental records and satellite imagery, with ground measurements disproportionately weighted in Northern Hemisphere mid and high latitudes (as well as these observations generally being of higher quality) (Schultz et al., 2015, Hansen and Cramer, 2015). Successive years and decades are now continually deemed the "warmest on record" or at least the second warmest. 2019 was determined to be the second warmest year in the 140 year climate record, just after 2016, with an average global temperature of 0.95 °C and is now the 43^{rd} consecutive year in which land and ocean global temperatures were at least some degree above the average. The years 2010-2019 were found to be the warmest decade on record (NOAA, 2020), which is unsurprising given that the last 5 years hold the 1^{st} to 5^{th} spots for warmest years. This unrelenting temperature rise and the associated impacts have motivated more serious consideration of solar geoengineering.

1.2.3 Modelling Climate Change

To better understand future impacts of climate change, projections of the future climate and environment are generated using Global Climate Models (GCMs) and Earth System Models; which include additional aspects of the environment, for example dynamic vegetation. Most climate modelling since 2013 now considers 4 representative concentration pathways (RCPs) for Radiative Forcing (as explained above) in the year 2100 of 2.6, 4.5, 6.0 and 8.5 W/m^2 (relative to pre-industrial values) (van Vuuren et al., 2011) for future climate change projections (RCP2.6 is wildly optimistic, RCP4.5 a favourable scenario, RCP6.0 a likely scenario and RCP8.5 a high emissions scenario which would lead to many negative impacts from climate change). Table 1.1 outlines more information on each of the RCPs.

Table 1.1: The four RCPs following different emissions scenarios which lead to set Radiative Forcing and degrees of climate change by the end of the century. From Moss et al. (2010).

Name	Radiative forcing	Concentration ppm	Pathway
RCP8.5	>8.5Wm^{-2} in 2100	>1,370 CO_2-equiv. in 2100	Rising
RCP6.0	~6Wm^{-2} at stabilization after 2100	~850 CO_2-equiv. (at stabilization after 2100)	Stabilization without overshoot
RCP4.5	~4.5Wm^{-2} at stabilization after 2100	~650 CO_2-equiv. (at stabilization after 2100)	Stabilization without overshoot
RCP2.6	Peak at ~3Wm^{-2} before 2100 and then declines	Peak at ~490 CO_2-equiv. before 2100 and then declines	Peak and decline

These 4 pathways formed the basis of the modelling undertaken as part of the Phase 5 Coupled Model Intercomparison Project (CMIP5) which contributed to the fifth IPCC assessment report (LLNL, 2013). A new generation of models and pathways have been used as part of the 6^{th} phase - CMIP6. Widespread reporting of these model results highlight the increased climate sensitivity of the CMIP6 over CMIP5 models (Meehl et al., 2020, Flynn and Mauritsen, 2020, Zelinka et al., 2020). The 9 new scenarios (outlined in Figure 1.4) combine both climate and socioeconomic projections, including such scenarios as an "overshoot" pathway, in which delay in mitigation leads to an emissions peak mid-century before actions are taken to limit and reduce atmospheric greenhouse gases (Gidden et al., 2019).

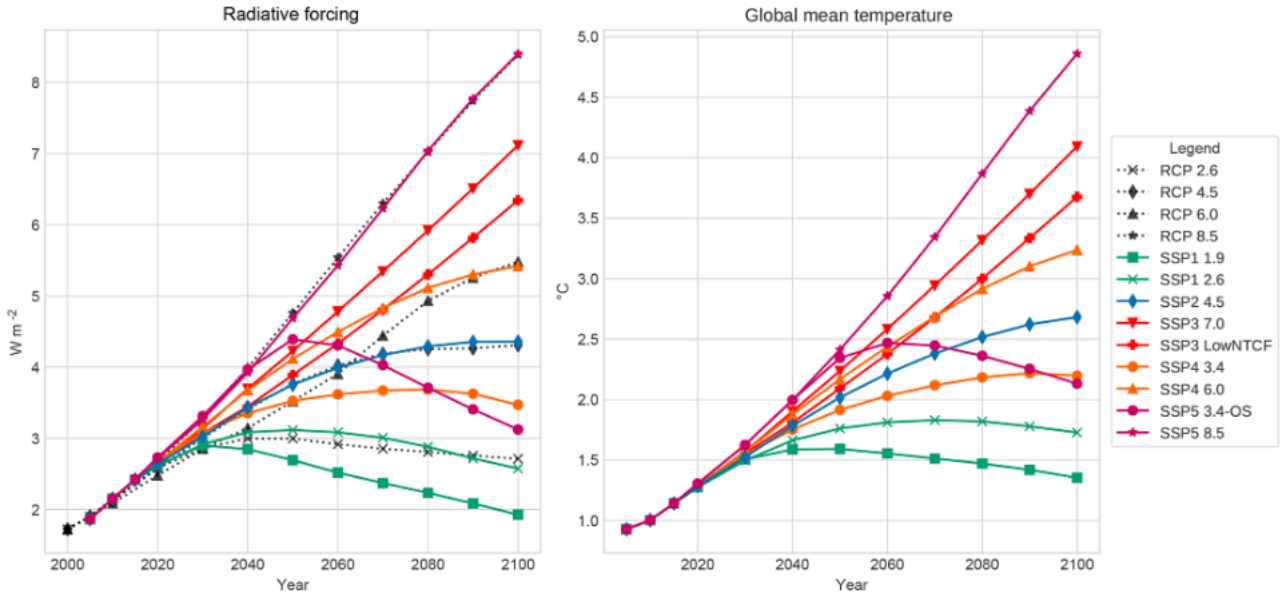


Figure 1.4: Radiative forcing and global mean temperature trajectories for 9 CMIP6 scenarios, with inclusion of 4 RCPs used in CMIP5 for comparison. From Gidden et al. (2019).

1.2.4 Impacts

The increase in atmospheric GHG concentrations has not only resulted in an increase in global temperatures, but it has also led to a large number of other impacts. These impacts will progressively worsen over the coming century if action is not taken. Some examples are outlined in Table 1.2. Not all of these impacts are directly linked to temperature rise, for example ocean acidification from increased CO_2. Therefore, solar geoengineering, acting to counter Radiative Forcing from GHGs, can only be a complementary method to emissions reductions (or CO_2 removal) in addressing these impacts.

Table 1.2: Some of the main impacts of climate change.

Types of Impacts	Examples
Hydrosphere Impacts	Sea level rise (Jevrejeva et al., 2014) (Marcos and Amores, 2014); potential changes to ocean circulation (Srokosz and Bryden, 2015); ocean acidification (Gattuso et al., 2013); changes to the hydrological cycle; likely impact on the intensity and even frequency of extreme events (hurricanes, floods, droughts).
Biosphere Impacts	Loss and degradation of ecosystems, including coral reefs (De'ath et al., 2012) Pandolfi et al. (2011); extinction and shifts in biodiversity through the need to adjust to changing habitats and altered climate patterns (Pacifici et al., 2015).
Cryosphere Impacts	Melting of the polar ice caps; glaciers receding.
Atmosphere Impacts	Change in the composition of the atmosphere.
Human Impacts	Air pollution; food shortage; changes to human migration (Black et al., 2011); potential risk for increased armed conflict (Solow, 2013) (Theisen et al., 2013); considerable economic costs.

1.2.5 Adaptation and Mitigation

In order to address the plethora of impacts resulting from an increase in GHGs, various adaptation and mitigation methods have been employed or considered. Adaptation strategies will not lead to a reduction in climate change, but they can reduce the impact that changes will have on the global population. Mitigation methods mainly focus on governmental level shifts to reduce GHG emissions and the rate of climate change, however action can also be taken by individuals, for example shifting to more sustainable vehicles (Howey, 2012), eating less meat (Ripple et al., 2014) and improved low-energy construction methods to reduce environmental impacts (Farese, 2012).

It is increasingly believed by those in the climate science community that this will not prove sufficient in keeping global GHG levels within "safe" limits. For this reason, momentum has gained in the topic of geoengineering the climate: "the deliberate large-scale intervention in the Earth's natural systems to counteract climate change" (UoOxford, 2017). As with any climate change mitigation strategy, it is of vital importance that any potential action on SG is thoroughly examined before being implemented (Gardiner, 2011). However, the fact that research into SG is even being considered could foster greater appreciation for the seriousness of the current situation and through discussion of the impacts of possible SG help focus society on the very real impacts that climate change will have (Long and Shepherd, 2014). Figure 1.5 depicts a simple consideration for how adaptation, mitigation and geoengineering (both SG and CO_2 removal) could collectively address the climate problem.

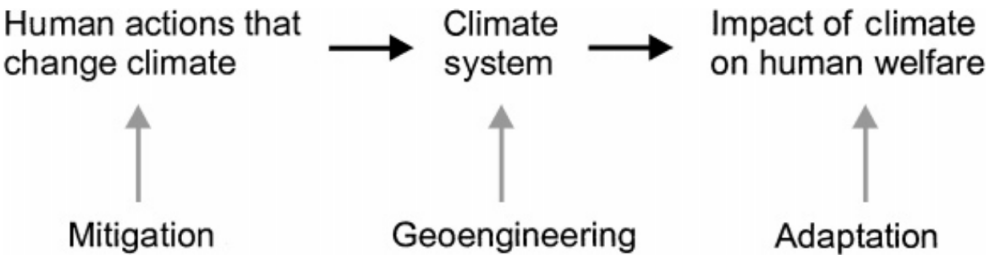


Figure 1.5: Three-part schema of the climate problem. The horizontal arrows in the top row show the causal chain in this version of the anthropogenic climate problem. The vertical arrows and the bottom row define the modes of intervention. From Keith (2000).

1.3 Background to Geoengineering

Two main categories of geoengineering have been considered: Carbon Dioxide Removal (CDR) and Solar Geoengineering (SG); a third smaller (and more recent) category is Cirrus Cloud Thinning (CCT) (Mitchell and Finnegan, 2009). Figure 1.6 outlines the trade-off to be had between effectiveness of a geoengineering method and its affordability and safety, with Figure 1.7 providing a visual representation of some of these geoengineering methods. One solar geoengineering technique, which centres around the concept of reflecting a portion of incoming solar radiation back into space through injection of sulphate aerosols into the stratosphere in order to cool global temperatures, is thought to be one of the most affordable and feasible choices (Shepherd, 2009).

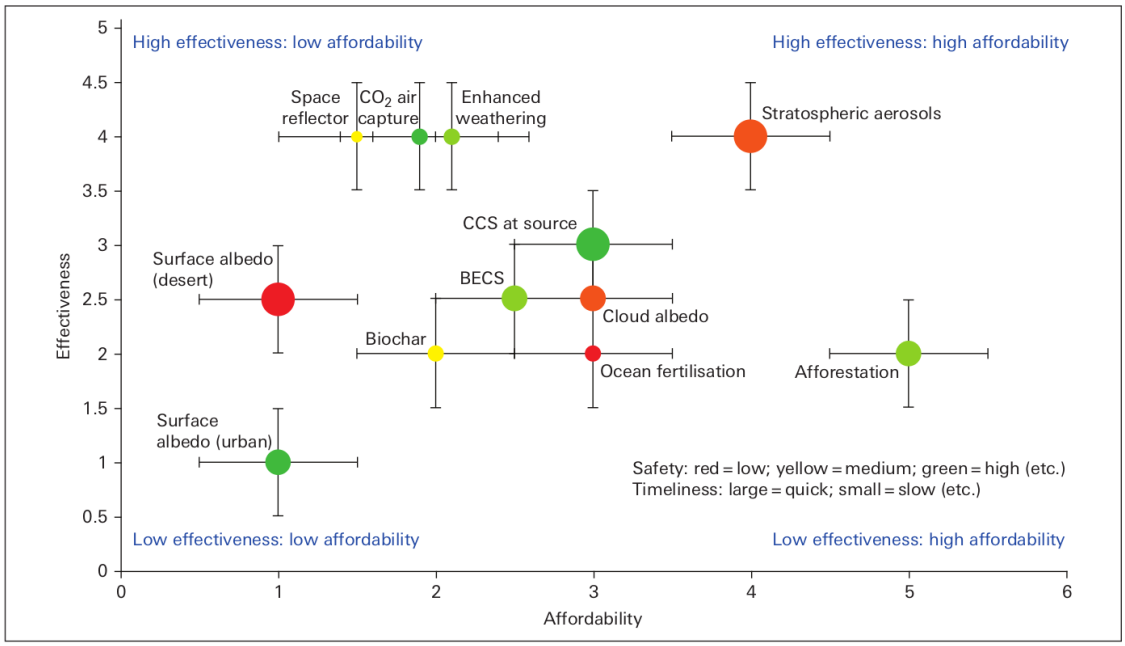


Figure 1.6: Preliminary overall evaluation of the main geoengineering techniques based on their effectiveness and affordability (as well as safety and timeliness). From Shepherd (2009).

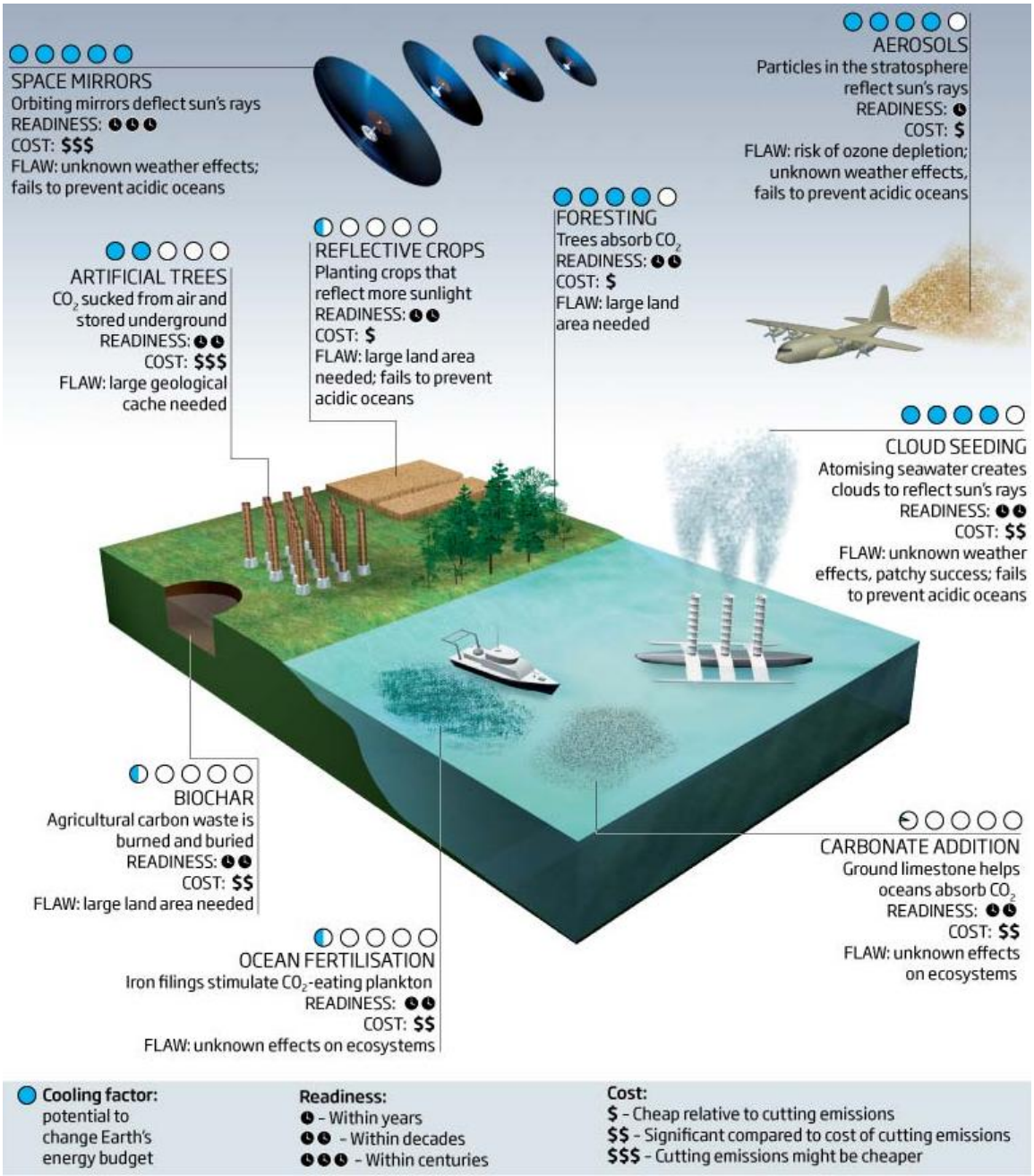


Figure 1.7: A representation of various proposed geoengineering techniques. From New Scientist (2009).

1.3.1 Carbon Dioxide Removal

Carbon Dioxide Removal (CDR), including Carbon Capture and Storage (CCS) and Direct Air Capture (DAC), can be seen largely as a mitigation strategy and is deemed fairly "safe, effective, sustainable and affordable" (Shepherd, 2009). These methods do not involve altering the climate system, other than to remove the GHGs which the human population has released into the atmosphere. Main concerns around their safety revolve around the storage aspect, with some plans utilising old oil and gas fields to store the captured carbon. CDR methods may prove increasingly popular with policy makers as

they would allow continued use of fossil fuels before transitioning to greener energy sources, with a capture mechanism on outlet pipes to prevent illegal emissions. Alongside this, the belief that future CDR will be sufficiently large scale enough for direct air capture to remove large quantities of CO_2, facilitates the ability of nations to pledge commitments to future removal of greenhouse gas emissions produced in the present day; deferring responsibility onto future societies. However, despite now increasingly being cited as a key component to meeting global temperature targets, the feasibility of rapid technological developments in CDR which would provide this sufficiently large-scale usage is uncertain (Field and Mach, 2017).

1.3.2 Solar Geoengineering

Mikhail Budyko first suggested in 1974 (English language translation 1977) that we could control rising global temperatures through addition of sulphate into the stratosphere, delivered by aeroplanes through the burning of sulphur containing fuels; which could be adjusted to fine-tune the amounts of resultant aerosol and thus the climate response (Budyko, 1977). He believed that if global warming were ever to reach excessive levels that it was a moral obligation to modify the climate in order to prevent changes in conditions brought about through anthropogenic activities and that we would have the technological proficiency to do this, reducing global temperatures by as much as several degrees. Whilst this topic can be very divisive when discussing morality and what action would be right or wrong to take, Budyko is well reasoned in thinking that it is morally just that we as humans look to alter the climate (and as a result the biosphere) as little as possible from its natural state; whether this be through remediation by climate modification or other means.

Since that time, little serious discussion surrounded solar geoengineering (SG). However, back in 2006 Paul Crutzen broke the taboo (Crutzen, 2006), encouraging consideration of this technology as a method to reduce the effects of climate change. Since then, considerable progress has been made in investigating the possible benefits and impacts of solar geoengineering, with the establishment of the Geoengineering Modelling Intercomparison Project (GeoMIP) whose aim is to collate and organise modelling experiments into the impact of geoengineering on the climate and environment. Boettcher and Schäfer (2017) outline the main developments in geoengineering research in the decade since the publication of Crutzen (Crutzen, 2006).

SG can reduce global temperatures by reflecting incoming solar radiation back out to space, but may have potentially devastating impacts on the climate system (Shepherd,

2009). A main limitation of SG is that it will not address all aspects of climate change, due to its inability to reduce the high levels of GHGs in the atmosphere, instead creating a novel scenario of elevated GHGs whilst maintaining a lower global temperature. Solar geoengineering should therefore only be implemented as a complementary strategy to reduce global temperatures and climate change impacts, with the main focus still being the reduction of GHG emissions and a shift to sustainable energy supply. There is risk that SG deployment could be used as a substitute for targeted emissions reductions, given that it would not require adjustments to lifestyle or industry. One particular example of SGs limitations is that it would not resolve the problem of ocean acidification, given the high levels of GHGs which would still persist in the atmosphere. The Royal Society (Shepherd, 2009) recommended, of SG, that these "methods should not be applied unless there is a need to rapidly limit or reduce global average temperatures". We are arguably at that point, but even so there is the potential that SG could be used as part of a number of measures to reduce the effect of climate change (MacMartin et al., 2018). It is likely that emissions reduction targets and a commitment to limit warming to 1.5 to 2°C above pre-industrial levels will not be met without the use of technologies such as CCS (Peters and Geden, 2017). However, the climate response to the removal of carbon and reduction in emissions is slow, with an amount of future warming already determined by the greenhouse gases currently present in the atmosphere. SG has thus been propounded as a way to rapidly cut temperature rise (resulting from greenhouse gases), allowing society and the environment to avoid the worst effects of climate change (MacMartin et al., 2018).

SG includes Marine Cloud Brightening (MCB) (Latham, 1990); spaced based approaches; stratospheric aerosol injection; increased surface albedo.

Geoengineering is far from a perfect method to combat climate change, and it could be argued that any human intervention to the climate system should be avoided. However, given the slow movement of countries to adopt significant emissions reductions and the fact that GHGs can have long atmospheric lifetimes, alternative action plans are being considered. As research and experiments into solar geoengineering progress, it is extremely important to properly engage and inform the public of what is being undertaken, as proceeding without this may lead to societal opposition; even to those whom it would likely benefit (Frumhoff and Stephens, 2018). Given this, it is extremely pertinent to try and assess what impacts (both positive and negative) geoengineering could have on the climate, environment, ecosystems and human civilisation. One area which has particular cause for assessment is the hydrological cycle (Kravitz et al., 2013c), as observation (Trenberth and Dai, 2007) and model (Robock et al., 2008) based research indicates a reduction in its

intensity as a result of some scenarios of geoengineering (more specifically stratospheric aerosol injection at the equator), particularly in monsoon regions, thus leading to a decrease in precipitation and runoff in many areas. If this were to occur then it would have significant implications for the global population, for example volcanic eruptions (often seen as an analog for sulphate aerosol injection) have contributed to famine in Africa, India and Japan (Laki fissure eruption in Iceland, 1783-84) (Robock, 2008). The impacts of any solar geoengineering, however, are entirely dependent on the means and design of the deployment. As well as uncertainty displayed in model projections of SG resulting both from the method of SG and from the inherent model uncertainty, there is also uncertainty in the impacts corresponding to any particular SG approach. MacMartin et al. (2019) acknowledge that no amount of research can completely eliminate the uncertainty of the effects of solar geoengineering on the climate and the subsequent impacts on the planet. This is in part what makes the notion of solar geoengineering so scary. But what is also scary is the prospect of unmitigated climate change.

1.3.2.1 Stratospheric Aerosol Geoengineering

A layer of aerosol called the Junge Layer exists in the lower stratosphere between around 15 and 25km altitude (Kremser et al., 2016), surrounding the planet and peaking in concentration around 5km above the tropopause (Mackenzie, 2009). This stratospheric aerosol is mostly composed of concentrated sulphuric acid (H_2SO_4) droplets, with smaller contributions from meteorites (mineral elements) and injection of other material from the troposphere (e.g. soot and soil dust) (Friberg et al., 2018), and is predominantly formed from the injection and oxidation of SO_2 following large volcanic eruptions (Mackenzie, 2009). Recently it has been discovered that large forest fires can also emit aerosols directly into the stratosphere through pyrocumulonimbus events, after detection of peaks in high levels of aerosols in the stratosphere, previously only thought explicable by volcanic eruptions, occurred without the incidence of a suitable eruption (Fromm et al., 2010). The huge fires in Australia at the beginning of 2020 lofted smoke more than 15km into the atmosphere (Seftor, 2020). However, these aerosols are very different in their composition and climate effect to sulphate aerosols.

The reaction of sulphur species ejected by volcanic eruptions (SO_2 and to a much smaller degree H_2S) with OH and H_2O over a period of weeks forms H_2SO_4 in the stratosphere (Robock, 2000). Because H_2SO_4 has a low vapour pressure, the oxidation of SO_2 will always form aerosol mass (rather than a mix of gas and aerosol) (Williams and Baltensperger, 2009). In addition, a constant, but small, background source of H_2SO_4 may

come from the oxidation by UV radiation at ∼25km of carbonyl sulphide (OCS) which are emitted by microbes and industrial sources and percolate into the lower stratosphere (Mackenzie, 2009, Crutzen, 1976).

Distribution and lifetime of stratospheric aerosol is controlled by transport as well as chemistry and microphysics (Kremser et al., 2016). Aerosol is transported in three main ways: by direct injection of sulphate precursor gases into the stratosphere during large volcanic eruptions; through exchange across the tropical tropopause layer (TTL) of tropospheric precursor gases and within the stratosphere through the Brewer-Dobson Circulation (BDC) (Kremser et al., 2016). The BDC is a global-scale mass circulation which chiefly transports tropospheric air from the equator, where it rises into the stratosphere, poleward until it sinks at mid- and high-latitudes (Butchart, 2014). There are two branches to the BDC, a shallow branch (which carries the majority of the air transported by the BDC) through the lowermost stratosphere which generally has transit times of one year or less and a deep branch (or tropical pipe (Friberg et al., 2018)) extending higher in the stratosphere through which air has a residency time of a few years (up to ∼5 years) (Birner and Bönisch, 2011). Whether emissions from volcanic eruptions reach the shallow or deep branch of the BDC determines the aerosols residency time and also their climatic impact.

SO_2 and OCS are two main precursor gases for stratospheric aerosol which are brought by the upwelling tropospheric air of the BDC in the tropics into the stratosphere, but there has been uncertainty surrounding which of these gases dominates aerosol contribution (Brühl et al., 2012, Sheng et al., 2015). It seems unlikely that a gas that is so water-soluble and reactive would not be scavenged during cloud processes (Crutzen, 1976) and it does indeed seem from recent research by Rollins et al. (2017) that little SO_2 reaches the upper troposphere in the tropics and there is insufficient concentrations to contribute significantly to background stratospheric aerosol. OCS (as described above) does, however, reach the stratosphere through upwelling tropospheric air and therefore constitutes a larger portion of the background aerosol in the Junge Layer.

Climate models which can resolve stratospheric chemistry and processes consistently produce projections in which the BDC speeds up as a result of climate change. However, there is large uncertainty surrounding the driving mechanisms for this speed up. Regardless, this acceleration of the BDC will have a large impact on the stratosphere, not least by altering removal of aerosols and transport of material across the tropopause, which will affect ozone column depth amongst other things (Butchart, 2014).

Stratospheric aerosol has an important role in increasing ozone depletion as their surfaces play host to heterogeneous chemical reactions; especially pertinent for ozone loss in the midlatitude layer (Mills et al., 1993). This ozone depletion has only become relevant in historically recent times however, because the presence of anthropogenically released gases such as chlorine are required for the reactions (Robock, 2000). It must therefore be acknowledged that changes to stratospheric aerosol concentrations will likely impact upon ozone column depth, in addition to any other influences it may have; be that desired and engineered or unintended.

Another significant role stratospheric aerosol plays is in its ability to alter radiative forcing - both by reflecting incoming shortwave radiation back out to space (leading to surface cooling) and by absorbing incoming near-infrared radiation and outgoing longwave radiation (leading to localised warming) (Kremser et al., 2016).

The principle of injecting sulphate aerosols into the stratosphere as a means to cool global temperatures is based on the observations of lower temperatures in the year following a large volcanic eruption in which sulphate aerosols ejected from the volcano enter the stratosphere. Sulphate aerosols are highly reflective and so their presence results in the reflection of incoming solar radiation back out to space, which in turns leads to cooler temperatures in the troposphere close to the Earth's surface. The injection of aerosols into the stratosphere (rather than another location in the atmosphere) is due to this layer being further from the surface and the longer residence time (around a year) of particles in the stratosphere as opposed to the troposphere (where they fall out in a matter of days). This means that fewer aerosols will be needed than if they were injected at a lower atmospheric level as well as there being a greater global dispersion when injected at these higher elevations (Rasch et al., 2008b). In addition to the effect of altitude of aerosol injection, the size of aerosol particles has also been shown to be important (Rasch et al., 2008a). Larger particles, of similar size to those emitted during volcanic eruptions, are poorer scatters of incoming radiation and absorb some of the outgoing radiation when compared to smaller particles and almost twice as large an injection amount may be needed for these larger particles to offset a doubling of carbon dioxide (Rasch et al., 2008a).

Volcanoes emit a number of gases into the atmosphere, most abundantly N_2, H_2O and CO_2, however despite H_2O and CO_2 being important greenhouse gases, their concentrations in the atmosphere are already far too high for a single eruption to lead to noticeable warming (Robock, 2000). The same cannot be said for the impact that volcanic release of sulphur species (predominantly SO_2 but also occasionally H_2S (Luhr et al., 1984)) into

the stratosphere can have on surface cooling. An estimate 20Tg and 7Tg of SO_2 was emitted during the eruptions of Mt Pinatubo (1991) and El Chichón (1982) respectively (Bluth et al., 1992); which translates to an estimated aerosol loading of 30Tg and 12Tg (McCormick et al., 1995). Robock and Mao (1995) found that subsequent to large volcanic eruptions an average global cooling of around 0.1 to 0.2°C occurs, peaking approximately 1 year after the eruption, but the climate cooling effect persists for several years. McCormick et al. (1995) detail how a drop in global mean temperature of ∼0.5°C was observed a year after the eruption of Mt. Pinatubo. The year following the largest known historical eruption (that of Tambora in 1815) became known as the "Year Without a Summer" and led to widespread crop failure (Oppenheimer, 2003). Further back in time, around 75,000 years ago, estimates for the super-volcanic eruption of Younger Toba Tuff suggest a far greater temperature reduction of between 3.2 and 4.5°C (Harris, 2008, Oppenheimer, 2002, Rampino and Self, 1992) (Rampino et al. (1988) estimate 1000Tg of stratospheric aerosol resulted from this eruption). The temperature reduction caused by the volcanic eruptions of El Chichón and Mt Pinatubo can be clearly seen in Figure 1.8 and both their clouds had circled around the globe within three weeks (El Chichón - Robock and Matson (1983), Mt. Pinatubo - Bluth et al. (1992)). When these large volcanic eruptions occur in tropical latitudes however, a winter warming is also seen in the Northern Hemisphere, this is due to a greater degree of stratospheric heating in the tropics compared to higher latitudes, which enhances the equator-to-pole temperature gradient and thus strengthens the polar vortex (Robock, 2000).

In addition to the clear surface cooling signal from large volcanic eruptions, smaller eruptions have also been seen to have an impact on the climate, moderating the rate of warming in the 21^{st} century (Santer et al., 2014). For the period 2006-2015, the impact of volcanic eruptions on stratospheric aerosol optical depth was to increase it globally by ∼40%; corresponding to a radiative forcing of -0.2 Wm^{-2} (Friberg et al., 2018).

Most recently, the eruption of Raikoke on the 22^{nd} June 2019 produced the strongest radiative forcing signal since that from Mt Pinatubo, analysis of this eruption is still ongoing but an estimated 1.5Tg of SO_2 was ejected into the stratosphere (UoL, 2019) and a sulphur layer 20 times thicker than normal was observed (Fox, 2019). The plume reached 17km, and with an indicated tropopause height of ∼11km at the time this is well into the stratosphere (NASA, 2019). Despite this however, the single event of the Raikoke eruption was not large enough to have a significant impact on Earth's climate (UoL, 2019), although there was a visible effect in the form of purple skies (Fox, 2019). Figure 1.9 shows the plume from the Raikoke eruption taken by astronauts on the morning

of the eruption.

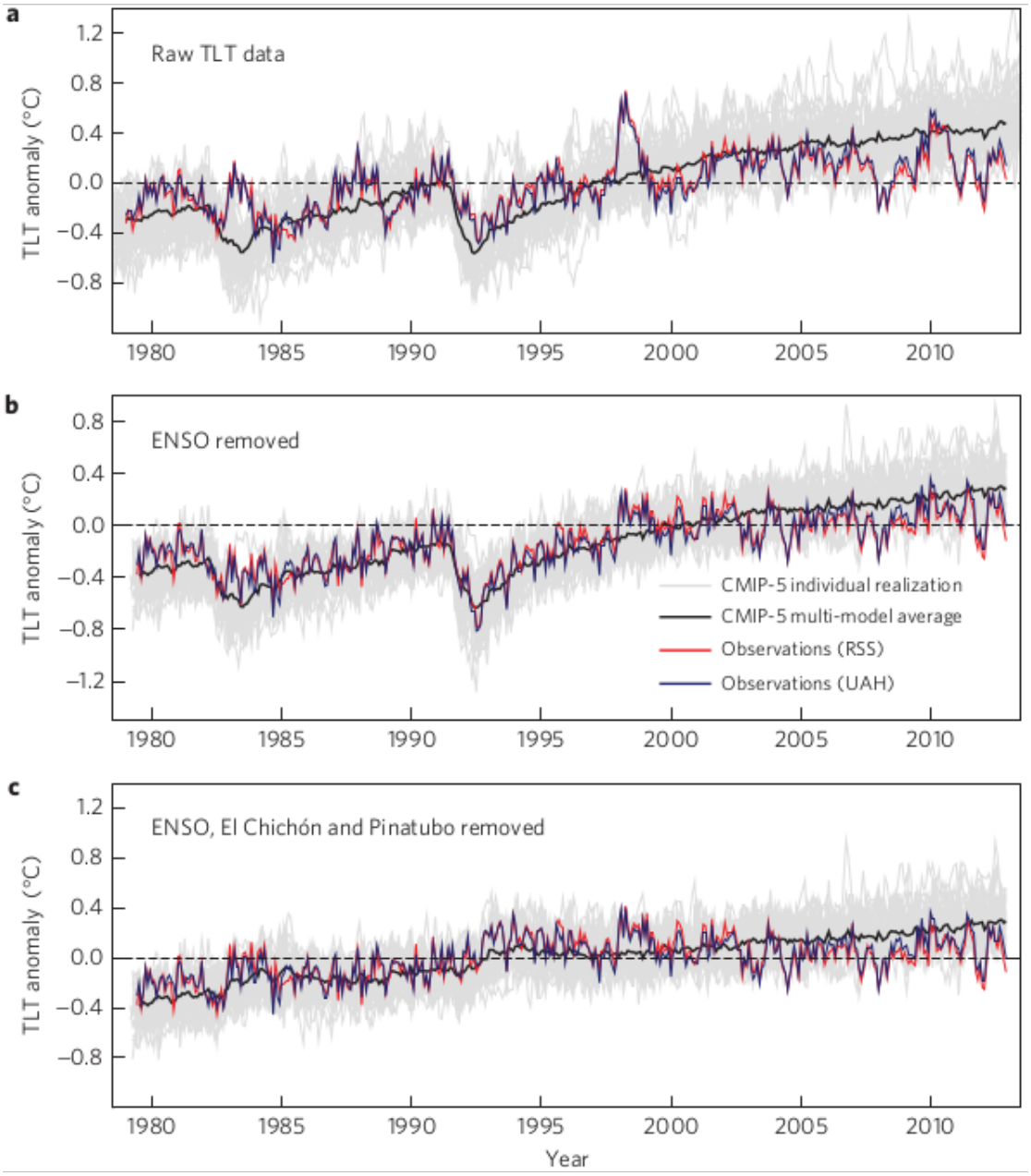


Figure 1.8: Modelled and observed near-global (82.5°N–70°S) monthly mean temperature anomalies of the lower troposphere (TLT) before and after statistical removal of El Niño–Southern Oscillation (ENSO) and volcano signals. (a) The original TLT anomalies are departures from the climatological monthly means over January 1979–December 2012. (b) Removal of the estimated ENSO signal in TLT reduces the noise that partially obscures the temperature response to the eruptions of El Chichón and Pinatubo. (c) Temperature residuals derived from subtracting the ENSO, El Chichón, and Pinatubo signals from the original TLT data. Figure from Santer et al. (2014). The grey band (composing of many overlapping individual lines) shows the TLT anomaly range from 28 individual global climate models used in the Phase 5 Coupled Model Intercomparison Project (CMIP5) which contributed to the fifth IPCC assessment report; for example CanESM2, GISS-E2-R, HadGEM2-ES, MIROC5 and NorESM1-M. The black line depicts the multi-model mean TLT anomaly from all of these individual models. The red and blue lines show two independent remote sensing satellite products for observed TLT.



Figure 1.9: Situated on the Kuril Islands in the North Pacific, the image depicts the eruption of the Raikoke volcano on June 22^{nd} 2019, which was violent enough to reach into the stratosphere. Some volcanic eruptions can deliver enough material into the stratosphere to increase stratospheric aerosol levels and reduce radiative forcing. Figure from NASA (2019).

There are risks and implications associated with stratospheric injection of sulphate aerosols, including ozone depletion (Heckendorn et al., 2009), drought, increased diffuse rather than direct sunlight (thought to be highly influential to plant development), an inability to reduce CO_2 levels (which in turn will result in the continuation of ocean acidification), the elimination of blue skies, potential conflict and militarisation of the technology (Robock et al., 2009). However, some risks, such as the increase in acid rain (sulphate aerosols consist of H_2SO_4 - sulphuric acid) have been considered to be only very small (Rasch et al., 2008b), given the small proportion of sulphur being introduced by geoengineering compared to the sulphur already active in the Earth's System.

Due to the imperfect nature of sulphate aerosol, consideration has also been given to using different stratospheric aerosols which may improve outcomes and reduce negative side effects (Dykema et al., 2016).

1.3.3 Modelling of Solar Geoengineering

There exist a number of ways to model solar geoengineering, largely dependent on the sophistication of the climate model involved. For models which do not include a detailed consideration of the stratosphere or stratospheric aerosol microphysics then so-called sun-

shade or solar dimming geoengineering can be simulated, in which incoming solar radiation is reduced in the model, effectively turning down the sun in order to mimic the reduction in incoming solar radiation resulting from sulphate aerosols reflecting a portion of it back to space. Solar dimming experiments, through insolation reduction, can work well as a proxy for stratospheric aerosol geoengineering, encapsulating the main features of the response, such as changes to the hydrological cycle and surface cooling (Niemeier et al., 2013, Kalidindi et al., 2015). These types of simulations have been demonstrating for a while now that we could cool the planet through solar geoengineering (Govindasamy and Caldeira, 2000).

Other, more complex, models which do include more thorough treatment of stratospheric processes can model solar geoengineering through injection of sulphate aerosols. Despite solar dimming experiments providing the broad signals from this injection of sulphate into the stratosphere, there are important features that are missed. For example, aerosols absorb outgoing longwave radiation, causing localised heating in the lower stratosphere, altering the heating gradient across the tropopause and shifting atmospheric circulation (Richter et al., 2017, Simpson et al., 2019). Further effects of sulphate geoengineering which solar dimming experiments cannot capture include effects on stratospheric ozone (Pitari et al., 2014) and an increased proportion of diffuse radiation (Madronich et al., 2018) - of particular importance for plants.

These aerosol modelling experiments can be further divided based upon injection location and timing. During the initial phases of solar geoengineering modelling, the majority of simulations involved injection solely at the equator; although some did consider the impacts from injecting in just one hemisphere or the other (Haywood et al., 2013). However, better climate moderation outcomes can be achieved through monitoring and adjustment of injection at multiple latitudes based on feedback to the model from climate signals. In more recent times, the effects from injecting during different seasons has been considered.

It is also important to note that predominantly modelling has adjusted for temperature, when it may be more effective to adjust for radiative forcing (Dykema et al., 2016).

What we have learnt from these efforts to represent the effect of various stratospheric aerosol injection approaches within global climate models, is that no method of solar geoengineering can so far perfectly offset climate change. There will be residual regional effects and it is much more challenging to ameliorate multiple impacts of climate change than simple adjustment to global temperature metrics.

Throughout this discussion if injection of sulphate aerosols is referred to, then this should be taken to mean injection of the precursor gas sulphur dioxide, which is then oxidised to sulphate aerosol in the atmosphere.

1.3.3.1 GeoMIP

GeoMIP (the Geoengineering Model Intercomparison Project) was formed to collate geoengineering modelling efforts, in order to ensure that the different GCMs were adhering to the same experimental design and thus be more directly comparable (allowing for greater consideration of uncertainty in model projections) GeoMIP (2020). This in turn helps to improve understanding of the impacts geoengineering may have and aid in the clarity of message. The limitation of this approach, however, is that more simplistic experiments are needed in order to allow as many modelling groups to participate as possible; in this case that means solar dimming rather than stratospheric aerosol injection. Simplistic does not necessarily mean worse, and some would even argue that our understanding of aerosol microphysics, cloud behaviour and other processes are too weak to warrant use of more sophisticated models and indeed that there is much insight to be had from studying more simple experiments.

Figure 1.10 shows the different experiments included in Phase 1 of the GeoMIP experiments; G1 and G2 consider solar dimming, whilst G3 and G4, carried out by fewer modelling groups, investigate stratospheric aerosol injections (Kravitz et al., 2011). The GeoMIP experiments also modelled future scenarios of highly elevated climate change ($4xCO_2$) and a pre-industrial control (piControl) (i.e. negating the impacts of modern climate change), to allow comparison of the impacts of SG and an imagined extreme scenario of climate change to control conditions.

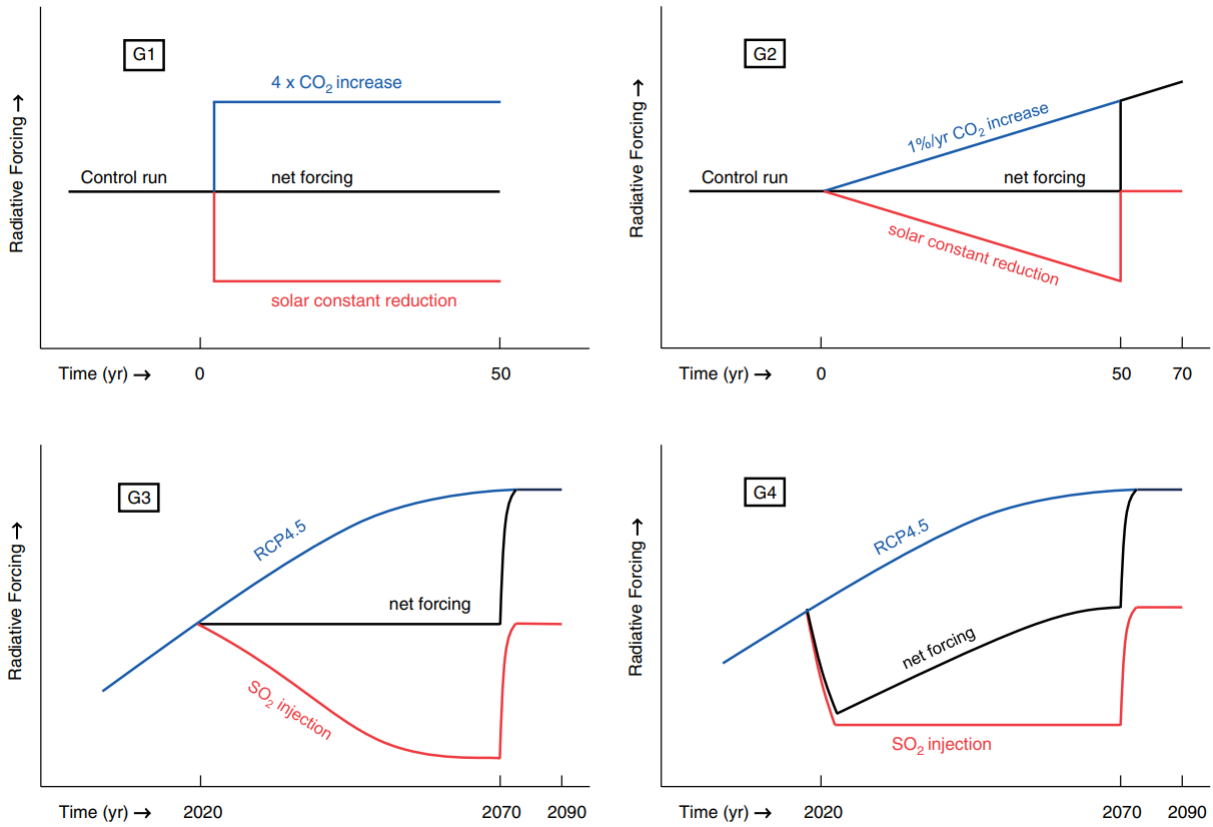


Figure 1.10: A schematic of the four experiments from GeoMIP Phase 1. G1 and G2 are solar dimming experiments in which incoming solar radiation is turned down in the model, whilst G3 and G4 use injection of SO_2 or sulphate aerosols into the tropical lower stratosphere. G3 approximately balances the RCP4.5 positive forcing, whilst G4 forces a negative radiative forcing from the beginning of the experiment through injection of 5 Tg of SO_2 per year. Figure adapted from Kravitz et al. (2011).

Further GeoMIP experiments followed. In Phase 2 three experiments were conducted, implementing difference idealized marine cloud brightening simulations (G1ocean-albedo, G4cdnc, and G4sea-salt) (Kravitz et al., 2013b). Phase 6 (numbered to match CMIP6) is the most recent modelling effort including four experiments: an extension of G1 (G1ext) to allow for better statistical analysis of impacts and better understanding of longer scale processes; G6solar and G6sulfur - designed to enable direct comparison of stratospheric aerosol vs. sunshade geoengineering within a multi-model setting; and G7 cirrus for investigation of cirrus cloud thinning - however, there is uncertainty about whether GCMs can correctly model upper tropospheric water and cirrus cloud (Kravitz et al., 2015). As well as this a number of testbed experiments were also produced by different modelling groups.

The GeoMIP studies have produced a wide range of results, highlighting how solar geoengineering may affect extreme events (Curry et al., 2014, Aswathy et al., 2015), the hydrological cycle and flooding (Wei et al., 2018), agriculture and vegetation (Xia et al., 2014,

Glienke et al., 2015), amongst many others.

Kravitz et al. (2020) have very recently examined differences between two generations of models (13 models from CMIP5 and 7 from CMIP6) participating in GeoMIP and undertaking the G1 solar reduction/dimming experiment, finding them to be statistically indistinguishable when considering changes in the hydrological cycle, temperature and energetics. They therefore conclude that model development in this newer generation (which primarily affects the climate sensitivity of the CMIP6 models - increasing it from CMIP5 models) has not altered the overarching global climate impacts projected from solar dimming in these experiments and provides confidence in the results. The G1 experiment is, however, an idealised experiment, ran to create large climate responses which are easier to decipher from noise, as well as simplified in approximating stratospheric aerosol geoengineering through solar dimming. Whilst there is value in being able to compare outputs from large numbers of models which are able to perform these more simplified experiments, this approach does fail to capture the complex microphysics needed to more completely model stratospheric aerosols and their impact on climate response.

1.3.3.2 GLENS

Modelling of solar geoengineering with sulphate aerosols has, until relatively recently, predominantly used an injection location of the equator. Despite the lowering of global temperatures that this leads to, an imbalance in the equator-to-pole temperature gradient has been seen in these simulations; with overcooling of the tropics and undercooling of the poles being observed. This has in turn impacted upon monsoonal precipitation and in general contributed towards a weakening of the hydrological cycle under these solar geoengineering scenarios. However, new work undertaken as part of the Stratospheric Aerosol Geoengineering Large Ensemble (GLENS) project (Tilmes et al., 2018) has tried to improve upon this, using four injection locations across the globe in order to preserve the equator-to-pole temperature gradient (amongst other aims). The GLENS project has simulated 20 control (RCP8.5) and 20 feedback (SG) runs where instead of injecting solely at the equator, there are four aerosol injection locations; at 15 degrees and 30 degrees north and south of the equator. There is also a feedback effect so that each year the amount of aerosols injected at each position is altered based on feedback from climate results in the previous year to achieve a lower global temperature but also maintain the temperature gradient from equator to pole. It can be seen in Figure 1.11 that these new solar geoengineering scenarios can indeed preserve both the global mean temperature and the equator-to-pole gradient at (or near to) 2010 values.

CESM1(WACCM) is an Earth System Model (ESM) which can be used to make future climate projections and was the model used here to project climate and surface responses to a solar geoengineering scenario. The main component of the model is the Community Earth System Model version 1 (CESM1) (Hurrell et al., 2013) which is coupled to sophisticated atmosphere model component, the Whole Atmosphere Community Climate Model (WACCM) (Tilmes et al., 2018). WACCM has a spatial resolution of 0.9° latitude by 1.25° longitude, with 70 vertical layers up to an altitude of 140km (Mills et al., 2017) and is able to model stratospheric chemistry and sulphate aerosols well, therefore providing a good environment to simulated scenarios of stratospheric aerosol solar geoengineering (Mills et al., 2016, 2017). CESM1(WACCM) simulates sulphate aerosol formation (resulting from injection of SO_2) through oxidation (Liu et al., 2012).

Tilmes et al. (2018) outlines the modelling approach undertaken to simulate solar geoengineering. To establish a baseline control, from which stratospheric aerosol injection can be implemented, CESM1-WACCM was used to generate 20 runs following the RCP8.5 emissions pathway (Representative Concentration Pathway 8.5 - an extreme level of climatic change with a radiative forcing of 8.5 W/m^2 in 2100 (van Vuuren et al., 2011)), 17 of these ran from 2010-2030, with a remaining 3 running from 2010-2097. The project simulated 20 control (climate change projections following RCP8.5) and 20 feedback (solar geoengineering with stratospheric aerosols) ensemble runs. The 20 runs all start from slightly different initial conditions and the use of this ensemble aids in understanding of how differences seen between the RCP8.5 and SG projections are a result of climatic variability. Each control ensemble member was used to initiate the corresponding 20 solar geoengineering runs (spanning the period 2020 to 2099), which were adjusted dependent on the feedback-control algorithm, in order to meet 3 temperature objectives of maintaining levels at the RCP8.5 2015-2025 average level. These temperature objectives (T0 - global mean surface temperature, T1 - inter-hemispheric surface temperature gradient and T2 - equator-to-pole surface temperature gradient) were obtained from RCP8.5 2015-2025 averaged values of the initial 13 ensemble members, with derived values of 288.21K for T0, 0.59K for T1 and -6.01K for T2. A feedback-control algorithm was then applied to the 20 SG ensemble members each year, from a starting point of 2020 in the respective RCP8.5 ensemble member, to adjust the amount of SO2 injected at each of the 4 injection locations ∼5km above the tropopause (15°N, 15°S, 30°N, 30°S) to meet T0, T1 and T2.

Whilst the more sophisticated GLENS scenarios make significant progress in improving the negative effects solar geoengineering, through stratospheric aerosol injection, can have on global temperature patterns (Tilmes et al., 2018), other climate implications, such as

regional precipitation change, can still not be completely ameliorated.

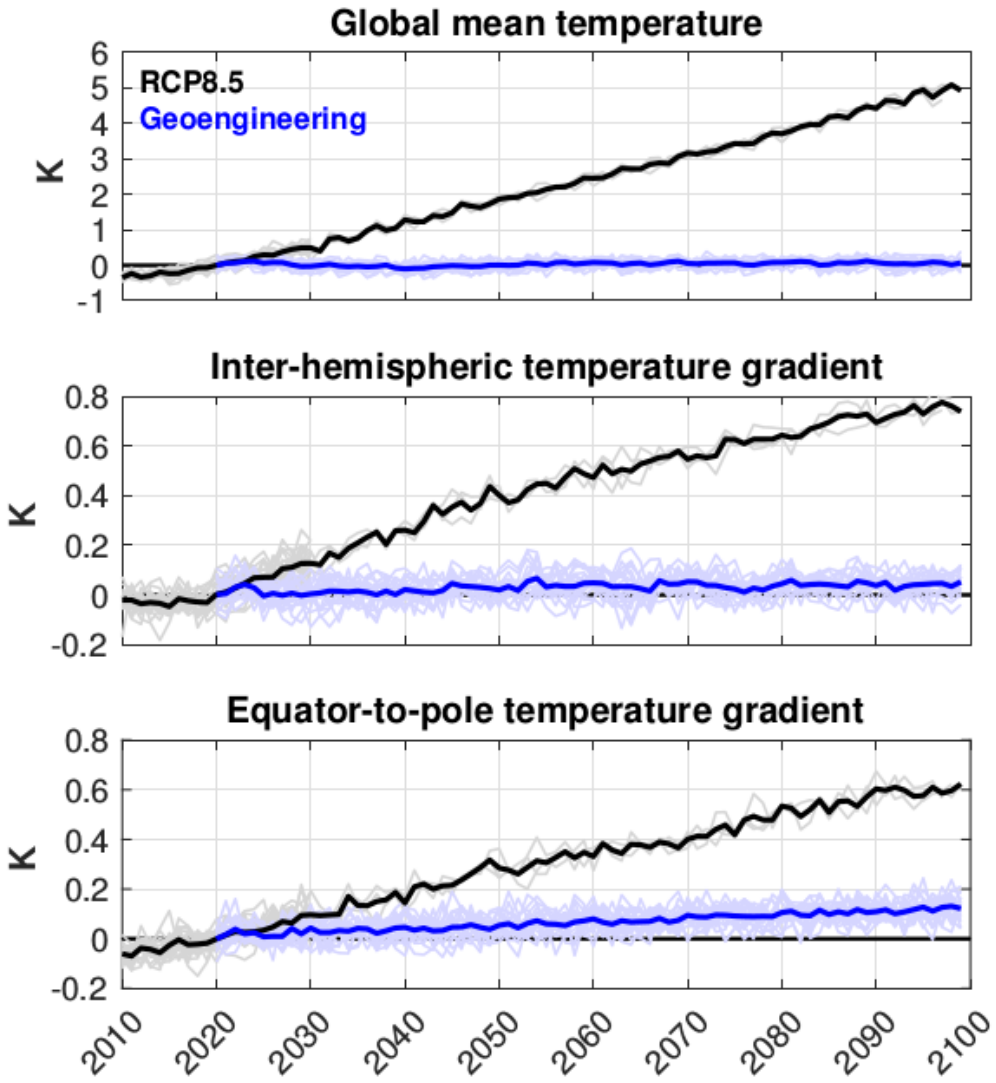


Figure 1.11: Global mean surface temperature (T0; top), the inter-hemispheric surface temperature gradient (T1; middle), and the equator-to-pole surface temperature gradient (T2; bottom) for RCP8.5 (grey for single ensemble members and black for the ensemble mean) and for the geoengineering simulations (light blue for single ensemble members and dark blue for the ensemble mean) as compared to 2015-2025 values for the RCP8.5 simulation. From Tilmes et al. (2018).

1.3.3.3 Other modelling results

MacMartin et al. (2018) consider the use of solar geoengineering to help limit global temperature rise to 1.5°C above pre-industrial levels. The possible use of solar geoengineering arises from an "overshoot" scenario where despite the use of CDR and emissions reductions, peak temperature still reaches 3°C above pre-industrial before coming down again. Figure 1.12 outlines how limited and temporary solar geoengineering may be deployed to shave off this peak and limit the maximum global temperature increase to 1.5°C. Through the use of climate emulators and simulated results from 12 GeoMIP models a projection for this use of solar geoengineering to limit warming to 1.5°C can be made. They show from

this analysis that "there are no regions where a majority of models project that this moderate level of geoengineering would produce a statistically significant shift in precipitation further away from preindustrial levels." (MacMartin et al., 2018).

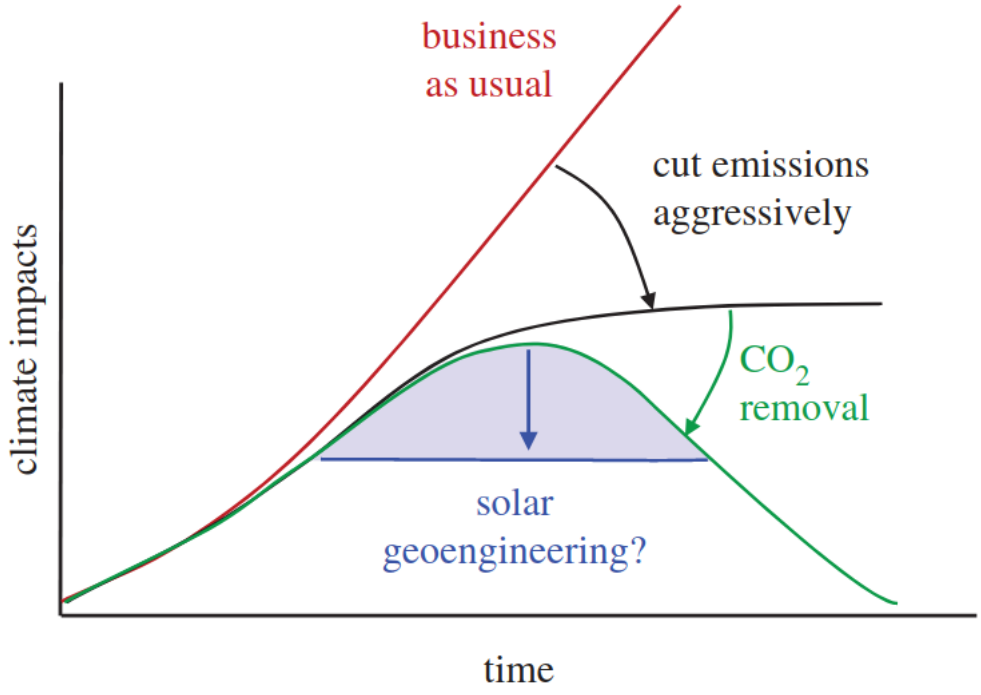


Figure 1.12: Through emissions reductions and CDR long-term stabilization of the climate is possible, but there is potential for significant overshoot of the desired maximum temperature increase. Limited and temporary solar geoengineering may be able to shave the peak off of this overshoot. From MacMartin et al. (2018).

Tilmes et al. (2020) conducted further assessment of the use of solar geoengineering in such "overshoot" projections to meet both 1.5 and 2°C maximum global temperature targets. Here, however, stratospheric aerosol injection was modelled within a climate model, rather than projected using a climate emulator. The Community Earth System Model version 2 (CESM2) coupled with the Whole Atmosphere Community Climate Model (WACCM6) was used to model the overshoot scenario (SSP5-34-OS) from CMIP6 as a baseline scenario. Similarly to the GLENS simulations, a feedback algorithm was used to adjust sulphur injection amounts at 15 and 30 degrees north and south of the equator to meet the same three temperature targets. They discover that changes to surface air temperature, ice sheet melting and the Atlantic Meridional Overturning Circulation are strongly determined by which temperature target is being met (1.5 or 2°C above pre-industrial). Whilst precipitation changes and ozone depletion are more strongly controlled by the amount of sulphate injected. They advocate for further multi-model assessments of scenarios in which emissions reductions, CDR and solar geoengineering are used in conjunction to limit global temperature rise, in order to ascertain agreement in potential

projected impacts.

Additional modelling has been carried out in order to gain greater understanding of some of the responses to sulphate aerosols seen in the stratosphere. Simpson et al. (2019) investigated the influence of localised stratospheric heating using model simulations similar in setup to GLENS and found that the dynamical response initiated by stratospheric heating has an important role in how solar geoengineering may alter precipitation.

With the knowledge that regional effects still persist, even with more sophisticated feedback solar geoengineering modelling (such as GLENS), Visioni et al. (2019) sought to simulate a first attempt at seasonally adjusted stratospheric aerosol geoengineering, in the hope that this would lead to better climate outcomes. Prior to this, most simulations have injected sulphate aerosols at a constant rate across the whole year. The motivation for exploring seasonal injection follows from the fact that sunlight and stratospheric circulation both vary seasonally, thus provide an opportunity to better tailor the injection scheme. The injection of sulphur dioxide was adjusted for four seasons and five locations (15°N, 15°S, 30°N, 30°S and the equator - 5km above the tropopause). They can conclude that through utilisation of seasonal injection, less total sulphur dioxide may be required to meet the same objectives as in annual injection, which could alleviate some degree of the negative impacts commonly associated with solar geoengineering.

Recent modelling using CESM1(WACCM) (Visioni et al., 2020) has revealed that the assumption of transport of aerosols injected into the stratosphere to high latitudes, essential to produce the climate outcomes such as in GLENS, may not hold true. They find that the localised stratospheric warming caused by the presence of sulphate aerosols can act to block aerosol access to high latitudes through strengthening of the stratospheric polar vortex. Without these aerosols reaching higher latitudes, they cannot produce the result of a more even equator to pole temperature gradient and thus cannot produce superior climate outcomes to equator-only injection.

1.3.4 Projected Hydrological Impacts

Many of the studies which inject aerosols at the equator have found simulations of solar geoengineering to reduce global mean precipitation. Tilmes et al. (2013) compared outputs of GeoMIP G1 experiments from 12 Global Climate Models (GCMs) and found that the precipitation changes in the models resulting from geoengineering indicate a "considerable weakening of the hydrological cycle" in a future world. They found that carbon dioxide induced initial reductions in evapotranspiration (soon reversed under climate change and

thus leading to increase global precipitation), persist in the solar geoengineering scenario to result in global mean precipitation reduction of 4.5%. They find a significant reduction in monsoon rain across South America (6%), North America (7%), South Africa (5%) and East Asia (6%). This is in contrast to the experiment of extreme global warming (under a 4xCO_2 scenario), which is shown to increase global precipitation by 0.10 mm day^{-1} on land and 0.22mm day^{-1} over the oceans. Recent research (Kleidon et al., 2015) also suggests that consideration of how the thermodynamically constrained surface energy balance responds to changes in radiative forcing, rather than the full modelling of the climate system (using GCMs), is a robust predictor of change in the hydrological cycle at the global scale. For example, the projected hydrological changes resulting from climate change and solar geoengineering, generated from this more simplistic method, produces comparable results to those from the GeoMIP experiments (generated using GCMs).

Weakening of the hydrological cycle has been interpreted from the difference between precipitation and evaporation (a basic proxy for runoff) and an example of this can be seen in Figure 1.13.

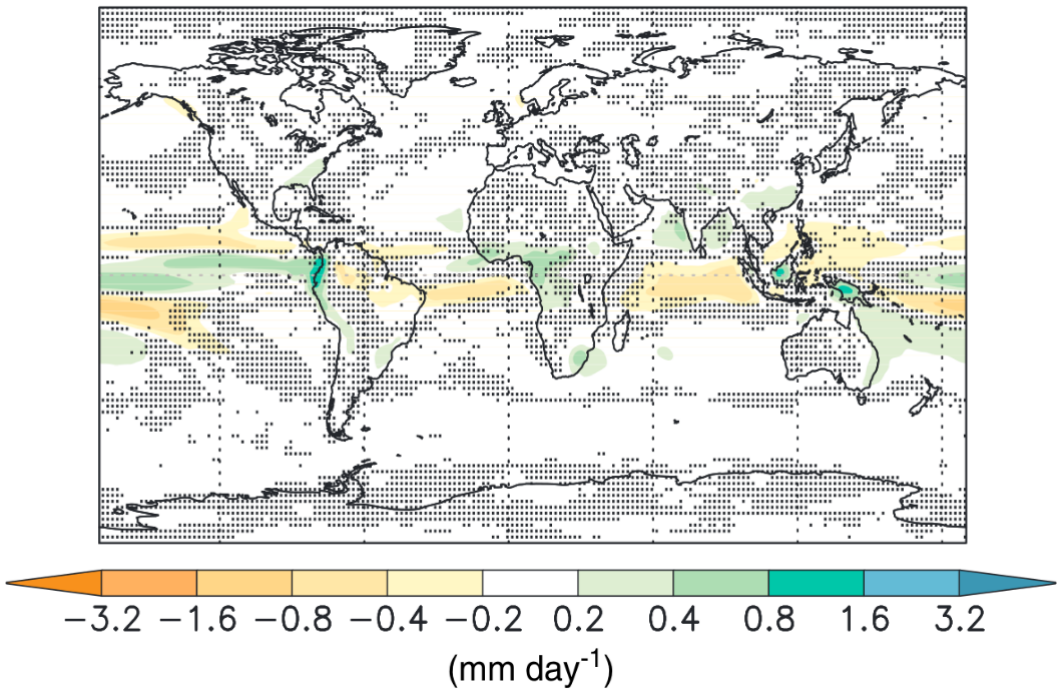


Figure 1.13: All-model ensemble annual average hydrology differences (mm day^{-1}), averaged over simulation years 11-50. The stippling indicates where fewer than 75 percent of the models (9/12) agree on the sign of difference. Adapted from Figure 5 (Kravitz et al., 2013a).

It has been shown that the hydrological cycle responds differently to forcing from solar radiation and carbon dioxide (Allen and Ingram, 2002, Andrews et al., 2009, Bala et al., 2008). Early studies of solar geoengineering found a "weakened" hydrological cycle in re-

sponse to solar geoengineering where global temperature had been reduced through solar reduction to compensate for increases in temperature from elevated carbon dioxide, when compared to an unaltered climate, i.e. one with a similar temperature but less atmospheric carbon dioxide present and no solar reduction (Lunt et al., 2008, Rasch et al., 2008a, Robock et al., 2008). Bala et al. (2008) explain how the offsetting of greenhouse gas temperature rise through incoming solar radiation reduction leads to a decrease in the global mean precipitation. When comparing the amount of change in global mean evaporation resulting from solar or carbon dioxide forcings of similar magnitudes, they conclude that solar forcing generates a greater change in evaporation, meaning the hydrological sensitivity (global mean precipitation percentage change per degree of warming) is larger for solar forcing than for carbon dioxide forcing. Bala et al. (2010) have attributed this difference in sensitivity to differences in a fast response of the hydrological cycle resulting from differences in tropospheric absorption of energy between solar and carbon dioxide forcings. The fast response results in the adjustment of the land, troposphere and stratosphere ahead of any mean temperature change. Whilst the slow response is in reaction to temperature changes (i.e. a feedback response). Both Bala et al. (2010) and Andrews et al. (2009) concluded that the slow hydrological response is similar for solar and carbon dioxide forcings. When combined, the fast and slow response represent the total climate change resulting from all forcings (Bala et al., 2010). A number of studies (Gregory and Webb, 2008, Andrews and Forster, 2008, Andrews et al., 2009) have found that increased concentrations of atmospheric carbon dioxide leads to rapid and significant adjustment in the troposphere which alters water vapour, ice, snow and cloud processes as well as reducing effective radiative forcing (ERF). However, when considering similar surface temperature changes driven by solar radiation or carbon dioxide forcing, the changes in surface net radiative fluxes arising from insolation changes are larger and to counteract this changes in combined sensible and latent heat fluxes are also larger (Bala et al., 2008). For this reason, the sensitivity of the hydrological cycle to temperature change is greater when that change is driven by alteration to incoming solar radiation as opposed to greenhouse gases (Bala et al., 2008). These findings support the broad conclusion that solar geoengineering cannot perfectly offset at the same time both global mean temperature and global mean precipitation changes arising from elevated greenhouse gas levels (Tilmes et al., 2013).

These findings have particular relevance for stratospheric aerosol geoengineering in that they can help to explain some of the hydrological response to such novel climate conditions; where temperature is reduced due to solar forcing changes resulting from additional sulph-

ate aerosols in the stratosphere, but elevated levels of carbon dioxide still persist and act as forcings in their own right. Kravitz et al. (2013c) use this energetic perspective to examine changes to the hydrological cycle in GeoMIP, concluding that a larger change in latent heat flux under G1 when compared to 4xCO2 indicates larger evaporation reductions and that this signal dominates the response in precipitation decrease under G1.

The GLENS project simulations reduce the global hydrological shifts seen under previous modelling of solar geoengineering (Tilmes et al., 2018), however regional changes remain. The GLENS simulations involve extreme amounts of stratospheric aerosol injection, in an effort to create a large signal-to-noise ratio which would make any climate signals clear to interpret. It is therefore not surprising that the outcome of this includes regional hydrological change. However, a recent study (MacMartin et al., 2018) found that when solar geoengineering is used in combination with emissions reduction and CDR and only in order to reach the 1.5°C Paris Agreement targets (rather than offset all warming) and not to lower temperatures beyond this, there was no region of the globe in which the majority of precipitation projections were statistically significantly different from pre-industrial values. This suggests a more limited effect on the hydrological cycle if more moderate solar geoengineering scenarios are considered.

It is also important to consider the location of any SG method to be implemented. For example, Haywood et al. (2013) found in their use of a globally coupled atmosphere-ocean model that stratospheric aerosol loadings in the Northern Hemisphere could exacerbate drought in the Sahel, whereas targeting the Southern Hemisphere may see a "greening of the Sahel".

Wei et al. (2018) considers global flood risk, using runoff from the GeoMIP G4 scenario routed into river discharge using the routing model CaMa-Flood. They conclude that solar geoengineering with sulphate aerosols is likely to reduce the increase in flood hazard seen under RCP4.5, back to levels closer to historical flood hazard.

Niemeier et al. (2013) conclude, from studying three solar geoengineering methods (sulphate aerosols, space mirrors and sea-salt aerosols to brighten marine clouds), that the hydrological response is heavily reliant on the technique used. By analysing the atmospheric heating imbalance (resulting from disparities in the radiative budget between the top of the atmosphere (TOA) and surface) differences between the three methods can be asserted. Both methods which employ aerosols result in a greenhouse effect from their absorption of longwave radiation, this must be balanced by a larger reduction of net downwelling shortwave radiation and thus a larger reduction in latent heat flux than is the case for the

space mirrors approach. Further differences in climate response arise from the methods' global (sulphate aerosols and space mirrors) or regional (sea-salt aerosol enhancement of marine cloud) scope.

An additional large influence on the hydrological response to solar geoengineering, albeit an area of considerable uncertainty, is the effect of vegetation. Dagon and Schrag (2016) attribute significant regional and global impacts to this climate-vegetation connection which are deeply affected by carbon dioxide levels and which cannot be avoided through reduction in solar radiation. They find that increased plant water use efficiency along with decreased stomatal conductance led to evapotranspiration decline under solar geoengineering. The changes to precipitation and evaporation will in turn alter runoff and soil moisture, with the influence varying depending on location and timing.

In their analysis of soil moisture change under the GLENS scenario, Cheng et al. (2019) find that despite global mean soil moisture being largely unaltered from present in the solar geoengineering case, there is still regional effects - namely significant decreases in soil moisture in India, the Amazon, N. Africa and northwest China. Similarly to other variables they find that less disparity in soil moisture arises from multiple injection locations vs equator only injection.

1.4 Research questions

A number of studies have now examined the impact of solar geoengineering on hydrologically important variables, for example precipitation, evapotranspiration and soil moisture. However, a comprehensive investigation into the direct effect of SG on water resources, in particular in relation to human impacts, cannot be found in the literature (Irvine et al., 2017). Although a few studies have considered the hazard associated with solar geoengineering, none have looked at the risk, explicitly considering the interconnection with the human population. This PhD aims to take the first steps to help address this knowledge gap through exploring both the physical hazard (drought) and the risk (water scarcity) a specific scenario of solar geoengineering may pose for global water resources. In addition, it will look to examine some of the uncertainty that arises in the projections of global runoff, which is at the root of any conclusions about the hazard or risk for water resources that arises from the scenario of solar geoengineering. This will be explored through comparison of the direct outputs of runoff from the climate model (CESM1(WACCM)) under the GLENS SG scenario with runoff generated by the hydrological model Mac-PDM.17 using the climate outputs of the GLENS modelling. The aim of this is to build an under-

standing of how the hydrological response will differ for SG and climate change between the two modelled outputs of runoff, considering the impact of offline (GHM - Mac-PDM) vs. online (GCM - CESM1(WACCM)) runoff generation. Throughout this thesis the GLENS modelling outputs from a specific solar geoengineering scenario will be used, comparing a future world following the RCP8.5 pathway of emissions and subsequent climate change with a solar geoengineering scenario designed to inject enough sulphate aerosols into the stratosphere to offset any of the warming from present day, maintaining temperatures at the average 2015-2025 levels. The questions this research looks to address can be summarised into 3 main questions, which will be addressed in each chapter in turn:

(1) How will implementation of online (within the GCM) or offline (generated from GHM using GCM climate inputs) simulation methods affect runoff across the globe under stratospheric aerosol solar geoengineering?
(2) How may solar geoengineering through stratospheric aerosol injection influence the future hazard of drought across the globe?
(3) How may solar geoengineering through stratospheric aerosol injection influence the future risk from water scarcity across the globe?

Research question (1) will be explored in Chapter 2, with research questions (2) and (3) addressed in Chapters 3 and 4, respectively. The findings of each of these chapters will be brought together and synthesised in Chapter 5.

1.5 Thesis Structure

This chapter has aimed to introduce the concepts of solar geoengineering and the underlying climate change challenges which may necessitate the need for this technology. The relevant literature and background needed for understanding of the further concepts explored in this thesis (e.g. hydrological modelling, drought and water scarcity) will accompany the corresponding chapter. The structure of the thesis will follow the research questions in a logical progression by first examining how models project future global runoff and the uncertainty that can be introduced at this stage; which then propagates throughout subsequent conclusions of impacts (Chapter 2). The relative hazards presented by these future projections of runoff changes under different climate scenarios (RCP8.5 or SG) will be examined in Chapter 3 through consideration of how drought (characterised by runoff which falls below a low flow threshold) patterns may be impacted across the globe. Finally, an appraisal of the relative risk solar geoengineering may pose to water resources is undertaken through examination of how water scarcity projections will change in the fu-

ture when the GLENS solar geoengineering scenario is compared to the projections under RCP8.5.

Chapter 5 will look to synthesise the finds of this research into a coherent picture of how water resources, when explored through specific climate scenarios and metrics, may be affected by the deployment of solar geoengineering. It will also discuss the complexities surrounding solar geoengineering including the science, limitations (including those resulting from the persistence of elevated carbon dioxide levels), safety, deployment and ethics, along with exploring what further research is needed before a more comprehensive understanding of the impacts of solar geoengineering on water resources can be drawn. By following the steps in the construction of a water scarcity assessment, from the underlying model projections, to the physical affects on the earth system, to then incorporating projections of population change (all of which influence the conclusions drawn about each climate scenario), it is hoped that a picture can be built up about how these conclusions may be influenced by their means of conception. Chapter 2 will allow us to gain an appreciation for how the runoff directly output from the GLENS scenario differs to another model output and therefore how this may affect results of Chapter 3 and 4. Whilst Chapter 3 will consider the natural aspect of the threat posed to water resources by a changing climate (be that through RCP8.5 or SG). The regions of the world most affected by the physical hazard can then be compared with those which see the largest risks when considering the human driven dimension to the water resource problem. Although different methods have been used and direct comparisons of concurrent and contrasting areas of threats or benefits from solar geoengineering cannot be made, it is important to consider how the potential outcomes inferred from the research in Chapters 3 and 4 are influenced by the parts of the risk-hazard space which are included. A further step in the analysis of Chapter 4 will also help to understand the human and physical dimensions of the challenges or benefits SG may present to water resources in the future. Alongside projecting water scarcity under SG and RCP8.5, the chapter will also examine how water scarcity would change if the climate were to remain at the present-day conditions. This will help to decipher how much of the driver of water scarcity projections would be from the human rather than the natural forcing and whether population change will alleviate or exacerbate the physical changes. Are the increases in population lain over areas which are put under pressure by SG, or do they not overlap?

Chapter 2

Comparison of Online and Offline Runoff

2.1 Introduction

Models of all kinds are continually becoming more detailed, more complex and more precise, with increasing computing power. The development of these models can create an illusion of being closer to the truth, however this is not necessarily the case, we might just be getting more precisely wrong. The only way to confirm or deny this is with really good observation data, which is not always available. It is, in fact, often seen as a main limiting factor in the development and progress of hydrological models. Beven (2012) argues that until we have better observations and measurements of the environment which can be built into models (through more informed choice of parameter values and used in calibration), we will ultimately be held back in improving our understanding of (particularly catchment level) hydrology and how to model water moving through the environment. However, alongside this need to advance our representation of hydrology in the modelled world, the further we move away from simple models which are easier to comprehend, the more we may lose sight of the fact that these models can only ever be representations of the real-world, unable to capture all of the features and characteristics. Despite this, models have a critical role in aiding our understanding of how the world may be altered by driving forces such as climate change and how we could adapt to and manage these changes, particularly at a global scale. It is important to understand how the use of different models will influence model outputs, as differences in model results will alter perceived outcome of impacts. Here we investigate the impact of whether the modelling is "online" (generated within an ESM (Earth System Model) with the Land Surface Model (LSM) coupled to the other model components e.g. atmosphere) or "offline" (derived using ESM climate outputs as inputs to a Global Hydrological Model (GHM)) on model projections of runoff under solar geoengineering and climate change scenarios.

Attempts to quantify hydrological processes date back to the mid 19th century (Mulvany, 1851). Large steps forward in our representation of hydrological processes were made by Sherman (1949) (unit hydrograph) and Horton (1945) (Hortonian overland flow/infiltration excess overland flow), but it was not until 1966 that a catchment model of the hydrological system emerged with Crawford and Linsley (1966). There are a large number of catchment scale models now in use for hydrological research around the globe, broadly divided into empirical and physically-based models (Beven, 2012).

Empirical models link inputs to outputs and are often "black box", with little concern for how this relation occurs, just that there is a good model fit to available data (with an obvious drawback of this type of modelling being the need for very high quality observa-

tion data). Other data-based models use "transfer functions" to relate model inputs to their outputs, with a simple example being the unit hydrograph. The unit hydrograph transforms actual rainfall into "effective" rainfall, often using infiltration equations or Φ-index (constant infiltration rate). This "effective" rainfall is equal to direct (also termed surface or storm) runoff. The unit hydrograph also requires separation into a storm runoff and baseflow component to streamflow. Limitations arising from non-linear relationships between rainfall and streamflow have led to the development of non-linear transfer functions (NARMAX models), as well as hydrograph separation issues leading to attempts to directly relate total actual rainfall and total streamflow e.g IHACRES model (Beven, 2012). The IHACRES model achieves this by making use of a rainfall filter (including a soil storage component) to generate an effective rainfall which through a quick flow and slow flow transfer function is related to total streamflow (Borzì et al., 2019).

The first three-dimensional physically-based catchment hydrology model was described by Freeze and Harlan (1969), bringing together a number of equations for surface and subsurface processes (e.g. Richards equations). However, the computation required to solve the set of nonlinear partial differential equations meant that it was not until a number of years later that the SHE model put this theory into practice (Abbott et al., 1986b,a). Many modern physically-based models are still based on the work of Freeze and Harlan (1969).

Many other important concepts (calibration and parameterisation) and divisions of catchment models (lumped vs. distributed, stochastic vs. deterministic) exist, and extensive summary of these can be found in the literature, e.g. Beven (2012).

Since 1989, when Vörösmarty et al. (1989) introduced the first macro-scale hydrological model, and particularly over the last two decades, many studies have employed Global Hydrology Models (GHMs) to gain insight into global water resource challenges, drought and flooding. There now exist a wide suite of GHMs with varying resolutions and complexity (see Table 2.1 for a number of the most commonly used models in global hydrology).

The basic model structure for GHMs includes a soil layer and subsurface processes, vegetation layer, evapotranspiration and snowmelt equations. A very important development came in the form of satellite data, which provided global coverage of soil and vegetation classifications and facilitated the use of this data in global scale models.

Modelling of global hydrology does not exclusively apply to GHMs however, and a whole variety of disciplines incorporate hydrology into global scale representation of systems

such as climate, carbon, ecology and other earth and human systems (Bierkens, 2015). Considered in this way global scale modelling of hydrology can be dated back to early land surface components of GCMs. Manabe (1969) presented one of the first simplistic representations of hydrology within a GCM, predicting atmospheric water vapour, snow cover and soil moisture, with soil water storage modelled through a series of boxes covering the land area possessing a finite storage capacity and which spill over to generate surface runoff - termed "Bucket" model. Further improvements to these early GCM land surface schemes saw development to soil processes added, along with canopy interception and a vegetation layer (Deardorff, 1978, Dickinson, 1984).

The models used to study global hydrology differ in both spatial and temporal resolution and complexity of structure (e.g. methods of parameterisation, numbers of layers, inclusion of energy as well as water balance). As discussed, not all of these models are strictly GHMs. Some models include routing of water into rivers, some incorporate human impacts (including reservoirs and abstraction) (Veldkamp et al., 2018), some allow for calibration (Hunger and Döll, 2008), whilst others have actively growing vegetation components. Rough divisions of these models can be made, those that are coupled to GCMs or Earth System Models (ESMs) are termed Land Surface Models (LSMs), models which include dynamic vegetation are aptly named Dynamic Global Vegetation Models (DGVMs) and GHMs which include consideration of human impacts and water use have been coined Global Hydrology and Water Resources Models (GHWMs). However, in reality most models can fall into multiple categories, with many LSMs now also having DGVM attributes and some GHMs' elements (e.g. VIC) being used in LSMs. It is also important to clarify differences between Earth System Models and GCMs. Whilst both couple together multiple model components to attempt to realistically represent the Earth and processes in the atmosphere, ocean, cryosphere and on land (both biotic and abiotic), ESMs go a step further through incorporation of interactive movement of carbon; linking the terrestrial and aquatic to the biochemical and considering human influences on the system (SOCCOM, 2020).

The differences that exist in model structure highlights the inherent uncertainty in global hydrology modelling. Sood and Smakhtin (2015) identify 4 sources of uncertainty: that arising from model inputs (e.g. precipitation - when recorded as point data at gauging stations interpolation is required to fill in between these points, in reality there may be much greater heterogeneity in precipitation across this area that cannot be capture by these spread out stations), model structure (e.g. bucket model for soil moisture scheme), parameter values (e.g. Leaf Area Index - LAI) and observed data (in the validation of

simulated river flow).

Table 2.1: A number of popular models used for global hydrology study

Model	Type	Reference(s)	Important Features
MacPDM	GHM	Gosling and Arnell (2011)	PDM, option of Penman, Penman-Monteith and Priestley-Taylor for PET, no routing, no human impacts
GWAVA	GHM	Meigh et al. (1999)	models reservoirs and irrigation, and as fine as 0.1° resolution, developed to model water scarcity
VIC	GHM	Liang et al. (1994)	uses Penman-Monteith to model PET and includes 2-3 soil layers and 13 landcover layers, employs the eponymous variable infiltration curve to model soil moisture
WaterGap	GHM	2 - Alcamo et al. (2003) 3 - Verzano et al. (2012)	Priestley-Taylor for PET calculation, human impacts included and water availability calculated
PCR -GLOBWB	GHM	Wada et al. (2014)	3 subterrain layers - 2 soil and 1 groundwater, includes crop modelling and reservoirs, uses Penman-Monteith for evapotranspiration
LPJmL	DGVM	Bondeau (2007)	Uses Priestley-Taylor for ET, has 2 soil layers, dynamic vegetation and human parameterisation
H08	GHM	Hanasaki et al. (2008)	Includes human impacts and crop model, as well as using energy balance to calculate ET, can be run at 3 hourly timestep
WBMplus	GHM	Vörösmarty et al. (1989)	uses a bucket model for soil moisture, includes irrigation and reservoirs and use thornthwaite/ hamon ET method
MATSIRO	LSM	Takata et al. (2003)	includes 5 soil layers over which the Richards equation is used to model subsurface processes, includes a simplified TOPMODEL for surface runoff
JULES	LSM	Best et al. (2011)	Models dynamic vegetation, the carbon cycle and energy balance
ORCHIDEE	LSM	Krinner et al. (2005)	Employs PFTs to describe vegetation with multiple PFTs existing in one gridcell, includes modelling of the energy balance, uses a double bucket model for hydrology, includes carbon cycling, and models vegetation dynamically.

This chapter focuses on examining the differences in simulated runoff when a relatively simplistic GHM (MacPDM) and more complex and integrated ESM (CESM-WACCM) are employed to investigate global responses to climate change and solar geoengineering. The data used for this research are from the GLENS project (Tilmes et al., 2018) and are described in more detail in Chapter 1. The runoff directly outputted from the GLENS project was generated "online" using the Land Surface Model CLM4.5 coupled to a sea ice (CICE4), ocean (POP2), atmosphere (WACCM), aerosol (MAM3) and biogenic emissions (MEAGAN2.1) model component (Tilmes et al., 2018). The "offline" runoff projections were generated by running a number of climate variables outputted from the GLENS simulations through the GHM MacPDM. A description of MacPDM and CLM4.5 is outlined below, in order to aid in the understanding of model structure and help identify why any differences in runoff output may have occurred.

Many studies have investigated the use of GHMs and LSMs in global hydrological modelling of climate change, in addition to work testing uncoupled (forced with observed data) and coupled (to the other model components of a ESM) LSMs' performance. Understandably, given the relative youth of the field and limited number of climate model simulations, much less research has been published on global hydrology under solar geoengineering, and no comparison of runoff produced from an "offline" GHM and "online" LSM can be found in the literature. Whether external calculation of runoff using prescribed daily inputs to a GHM produces significantly different outcomes to those directly outputted from an ESM and whether the coupled nature of the Earth System Model can produce "superior" results is of great interest, given the wide application of both of these modelling approaches. Confusingly the terms online and offline can also refer to modelling of LSMs either coupled or uncoupled to GCMs/ESMs, but from here on "offline" will specifically apply to a GHM (MacPDM) forced with climate outputs from an ESM, with "online" runoff generated from a LSM (CLM4.5) coupled to other ESM model components.

2.1.1 MacPDM.17

Arnell (1999) outlines how Macro-PDM (the earliest version of MacPDM), in common with many other water balance models, has a basic structure:

$$S_t = P_t - AE_t - D_t - Q_t + S_{t-1} \tag{2.1.1}$$

where P_t, AE_t, D_t and Q_t are precipitation, actual evaporation, delayed runoff and direct runoff during time interval t, respectively, and S_{t-1} and S_t are storage in soil, lakes and

wetlands at the beginning and end of the time interval. Inputs to the model, alongside model calculations, are used to determine the variables in Equation 2.1.1. The earlier version Mac-PDM.09 from 2010 required "monthly input data of precipitation, temperature, cloud cover, wind speed, vapour pressure and number of wet days (daily precipitation greater than 0.1mm) in a month" (Gosling et al., 2010). Whereas, the daily control setup used in this project for Mac-PDM.17 allows daily forcings, requiring precipitation (snow and rain; mm), temperature (°C), relative humidity (%), wind speed (ms^{-1}), net downwelling longwave radiation (Wm^{-2}) and incoming solar/shortwave radiation (Wm^{-2}) as the climate input variables. Precipitation input has an even distribution across each gridcell and the temperature is used to account for snowfall generation (when temperature falls below a threshold precipitation is as snow not rain) and snowmelt rates (a constant rate of melting per degree of warming above another set threshold).

The latest version of the model, MacPDM.17, was advanced from MacPDM.09 by Smith (2015) with the development of new vegetation and soil layers and the optimisation of some of the 123 parameters used in the model through a Generalised Likelihood Uncertainty Estimation (GLUE) assessment. Within hydrology, GLUE is a popular uncertainty analysis method used to investigate the problem of equifinality - where various combinations of parameter choices can give the same output. Through sampling of the parameter space many model runs are evaluated against observed data to find a set of behavioural models for which the parameter choices lead to acceptable model performance (Beven and Binley, 1992). A description of the model structure of MacPDM.17 can be found in Gosling and Arnell (2011) (as no fundamental model changes have been made since then) and is summarised below. An overview of the model structure can also be seen in Figure 2.1.

Parameters of vegetation characteristics (such as vegetation height, stomatal conductance and leaf area index) govern the amount of precipitation that is intercepted by the vegetation and along with inputs for climate condition (e.g. solar radiation and wind speed) control how much evaporation occurs, through calculation of potential evapotranspiration using the Penman-Monteith equation. The landcover type of each gridcell (which is used to characterise the vegetation, e.g. forest or grassland) is also important in determining the soil moisture storage capacity of the gridcell, through the rooting depth of plants and their influence on the storage capacity. Determination of the average soil moisture storage across the gridcell is used to linearly adjust the ratio of actual to potential evapotranspiration (as calculated by the Penman-Monteith equation).

The underlying principle of MacPDM.17 is based on the Probability Distributed Model (PDM) for rainfall-runoff of a kind first described by Moore (1985), and expanded upon in Moore (2007). The PDM is used to derive the probability distributed soil moisture subroutines of Mac-PDM such that the soil moisture across the gridcell varies statistically (unlike the fixed precipitation, and other, input value for the whole of the gridcell). This variability in soil moisture is carried out using a Pareto distribution (most widely employed in PDMs (Moore, 2007)), following Moore (2007), with distribution function and probability density function

$$F(c) = 1 - \left(1 - \frac{c}{c_{max}}\right)^{b} \qquad 0 \leqslant c \leqslant c_{max} \ , \tag{2.1.2}$$

$$f(c) = \frac{b}{c_{max}} \left(1 - \frac{c}{c_{max}}\right)^{b-1} \qquad 0 \leqslant c \leqslant c_{max} \ , \tag{2.1.3}$$

where parameters c_{max} and b are the maximum storage capacity and degree of spatial variability of the storage capacity respectively. The ability for soil moisture to vary across the gridcell means that at any time a proportion of the catchment is saturated (at maximum soil moisture storage capacity – determined by soil texture and vegetation rooting depth) and therefore generates quickflow runoff. This differs from more simplistic approaches that assume a constant soil moisture value across the gridcell and thus require the whole gridcell to be saturated before quickflow is generated, which is not reasonable, in the real world, due to varying topography and conditions across the area of the gridcell. The ability of the PDM to generate quickflow runoff in only a portion of the gridcell at any time means initialisation of runoff occurs more rapidly in response to precipitation events.

MacPDM.17 outputs quickflow and slowflow runoff (as well as a number of other variables) at each time step for every grid square across the globe. Runoff is routed within the gridcell (via two cascading linear reservoirs for quickflow and as a non-linear function of groundwater stores for slowflow) to account for losses and generate daily runoff at the outlet of the gridcell, but is not routed between gridcells.

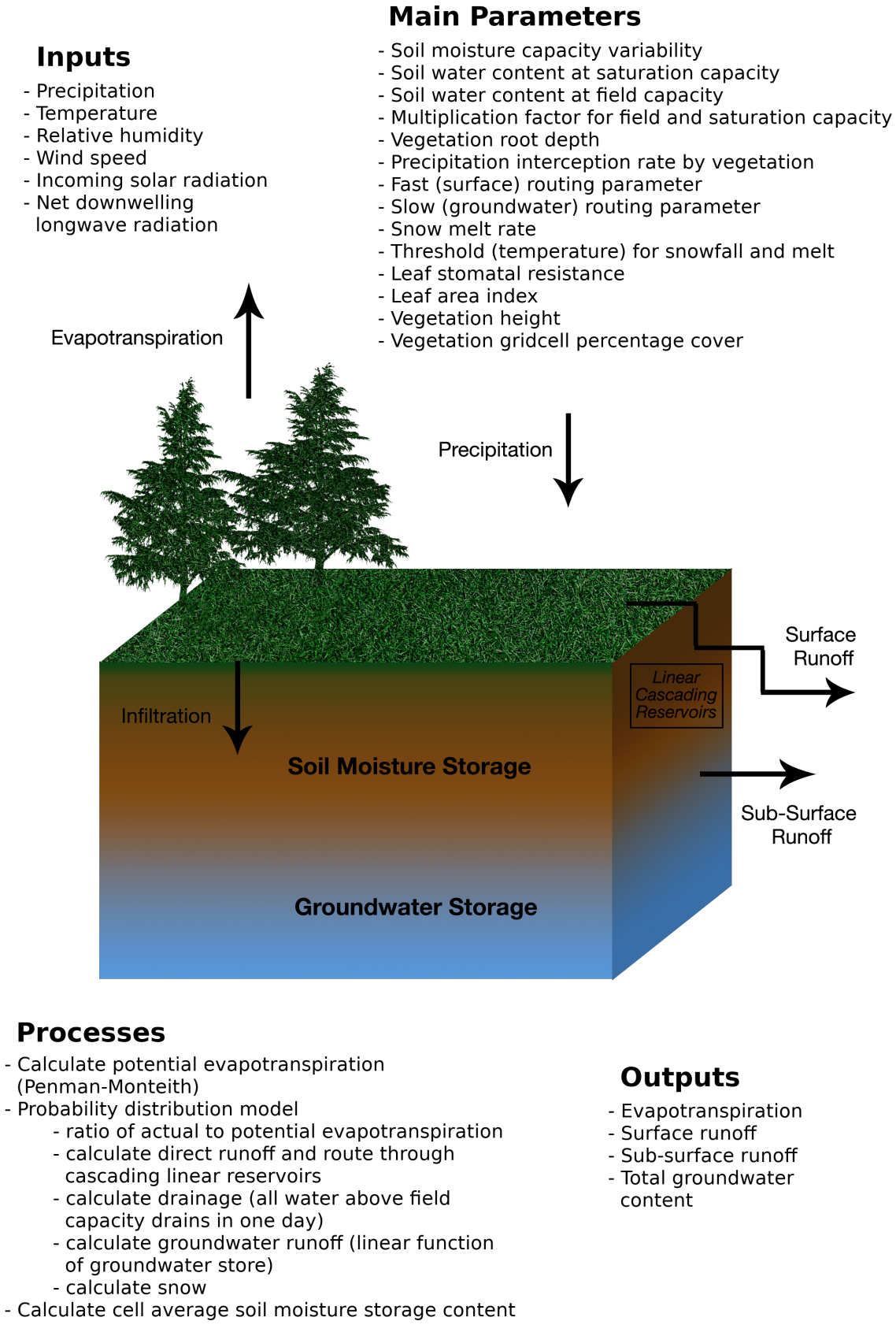


Figure 2.1: A schematic overview of the model components and structure of MacPDM.

Examples of the application of various versions of Mac-PDM can be seen in Arnell (2003, 2004), Gosling et al. (2010, 2011). Gosling and Arnell (2011) outlines the importance of the potential evapotranspiration (PET) method employed within MacPDM, finding the greatest model sensitivity resulting from the choice of PET method. Simulations using the Priestley-Taylor method of PET calculation produce greater runoff values (20-60%) in drier regions when compared to simulations using the Penman-Monteith method, with the reverse true for wetter regions. The disparities are seen to be a result of the Priestley-Taylor method lacking a humidity input (humid regions see some of the greatest differences in annual runoff) and the method being known to generally not perform well in arid and semi-arid regions.

MacPDM.17 has fixed vegetation and soil layers for the whole simulation length, at a resolution of 0.5 degrees. Smith (2015) developed new input layers with improved land-cover and soil classifications. The previous landcover input was rather out of date (being derived from 1984 AVHRR satellite imagery (De Fries et al., 1998)) and a combination of the GlobCover 2009 product from the MERIS spectrometer on the ENVISAT satellite (Arino et al., 2012) and the GLC2000 product from the SPOT4 satellite (Bartholomé and Belward, 2005) were used to update vegetation classes for each 0.5 degree gridcell. Importantly, this also allowed the inclusion of urban and permanently flooded categories to the map, which had been missing prior to this. Previous classification of soil texture had used a limited number of classes, which hinders the models' ability to characterise and differentiate between varying soil porosity and permeability. The USDA's well established soil texture classification (SCS, 1987), based upon relative silt, sand and clay percentages, was used to categorise each soil unit in the FAO Digital Soil Map of the World (which at the time had last been updated in 2007) into 1 of the 12 USDA texture classes; with the addition of Histosols (organic) and Lithosols (shallow or rocky).

MacPDM does not include modelling of dams, reservoirs and human interactions, instead outputting "naturalised" flow. The model also does not route runoff between gridcells into streamflow. Both of these factors mean a direct comparison between MacPDM and GLENS ESM runoff output, which does not include correction for land use change, is more easily interpretable.

2.1.2 CLM4.5 - Land Surface Model used in GLENS

The GLENS project simulated solar geoengineering using the ESM CESM1(WACCM) with CLM4.5 as its Land Surface Model. CLM4.5 is described in detail by Oleson et al. (2013).

CLM4.5 has been developed, with intermediate model versions, from CLM3, which was identified as requiring improved simulation of the hydrological cycle in order to better represent aspects of the climate. Development of the model since CLM3 has included updating the landcover distributions using MODIS satellite imagery, incorporation of urban processes (e.g. canyon model) and multiple different density classes, optional inclusion of a crop model, refining of canopy, soil, snow and groundwater parameterisations and modelling, use of Plant Functional Types (PFTs) rather than biome derived landcover classifications, better modelling of stomatal conductance and photosynthesis (Bonan et al., 2011, Sun et al., 2012), inclusion of TOPMODEL-based treatment of runoff (also with an alternative VIC-based method for runoff simulation (Li et al., 2011)) and the addition of interactive carbon (distinguishing between ^{13}C and ^{14}C) and nitrogen cycling, including nitrogen constraints to plant growth. This modification has improved representation of evapotranspiration, runoff and water storage in the model (Oleson et al., 2013).

Each of the $0.9 \times 1.25^{\circ}$ gridcells in the model can be divided up into 5 different land units (vegetated, crop (if crop model on - which it was not for GLENS simulations), lake, glacier and urban (which can be tall, high or medium density)). Each of these land units can be further divided into columns e.g. urban type - roof, impervious, pervious etc. and whether crop land unit is irrigated or unirrigated (vegetated, lake and glacier land units only have a single column at present). Finally, each of the columns (for vegetated and crop) can be further delineated into multiple PFTs. The energy and water balance is calculated for each land unit type and PFT (although only the weighted average of all PFTs in the column is used) and soil/snow processes are simulated at the column level. There are 15 soil layers, 10 lake layers and as many as 5 snow layers. Calculations for hydrology are conducted over the top 10 layers (3.8m), with the underlying 5 layers representing bedrock.

The division of vegetated land units into 15 possible PFTs (and bare ground) is intended to improve the representation of how different types of vegetation function and respond to external forcing. For each PFT, temperature, canopy water storage and surface fluxes (water vapour, transpiration, sensible heat - adjusted based on temperature) are modelled individually and parameter values for Leaf Area Index (LAI), Stem Area Index (SAI), top and bottom canopy heights are defined using MODIS satellite imagery (Lawrence and Chase, 2007, Zeng et al., 2002, Bonan et al., 2002)). The distribution of PFTs can vary with time across the column if run in transient mode (this was not the case for the GLENS simulations and the prescribed vegetation distributions are fixed for the whole time period). However, values of LAI, SAI and top and bottom canopy height can change with time if the biogeochemistry model has been turned on, in which case the prescribed values

are replaced with the model's predictions of LAI, SAI and top and bottom canopy heights. The GLENS simulations do include seasonal adjustment of LAI in response to climate change (Cheng et al., 2019). In addition to LAI and SAI responses to solar radiation, parameters for root distribution, nitrogen and water uptake by roots, canopy resistance, throughfall, canopy interception and drip, respiration, photosynthesis (in C3 (Farquhar et al., 1980)) and C4 (Collatz et al., 1992) plants), transpiration, carbon and nitrogen stores and stomatal conductance (under shaded and sunlit conditions using the Ball-Berry model (Collatz et al., 1991, Sellers et al., 1996)) are all included for each PFT. PFTs are also grouped by phenology response and the link with the carbon and nitrogen cycles; seasonal deciduous (temperature and day length dependent), stress deciduous (temperature and soil water dependent), evergreen. Modelling of carbon and nitrogen cycling through the system includes modelling of stores and processes within plants and soil and varies by PFT.

Evaporation from the ground and the canopy as well as plant transpiration are all modelled individually through consideration of latent heat fluxes. The partitioning of latent heat into soil evaporation, canopy evaporation and transpiration is hard to determine, but (Lawrence et al., 2007) suggest that previous versions of CLM underestimated the transpiration fraction, resulting in drier soils. Improvements to the parameterisation of hydrology and vegetation has allowed more realistic partitioning of ET through increasing soil moisture storage and availability to plants for transpiration and reduction in canopy interception (resulting in lower canopy evaporation and more water available at the ground for transpiration). Ground evaporation takes account of soil and litter resistance and is dependent on soil moisture. Transpiration is also a function of PFT, interacting with stomatal conductance and photosynthesis parameterisations.

Subsurface processes are modelled using Darcy's Law and the modified Richards equation (Zeng and Decker, 2009). For each column, soil colour, texture and organic matter are described, and the thermal conductivity, heat capacity and hydraulic properties are derived as a factor of these soil properties. The mineral (silt/sand - quartz and feldspar, clay - aluminosilicates) and organic composition of the soil, as well as the volume of soil water, determine hydraulic conductivity and soil matric potential (another way of measuring soil water availability - the difference between field capacity and the permanent wilting point). As variables for mineral and organic soil can vary greatly, a bulk hydraulic response is determined, where there is assumed to be a weighted response in the hydraulic parameters, based on the proportions of clay and sand (Clapp and Hornberger, 1978, Cosby et al., 1984) and organic material (Lawrence and Slater, 2008). An equation for the conservation

of mass is used to model soil water content, integrating down through the vertical soil layers using parameters for infiltration (upper boundary condition), gravity, diffusion, transpiration, surface and subsurface runoff and interactions with groundwater (lower boundary condition).

The phase change of water is modelled to assign volumes of snow, ice or water in the model and is determined by excess (or shortage) of energy required to adjust the current temperature to freezing. The mass of water and ice, thickness of snow and temperature is modelled, with snow coverage calculated using Swenson and Lawrence (2012) and snow volumes subsequent to snow melt computed using a depletion curve. Melt water is modelled as travelling down through the snow, with the excess after saturation contributing to runoff, either as liquid or solid. The impact of particles (such as black carbon) on melting (as well as albedo and longwave radiation) is also incorporated into the calculations.

SIMTOP (Niu et al., 2005), a simple model based off of Beven and Kirkby (1979)'s TOPMODEL, is used to simulate runoff. The method is characterised by the use of fractional saturated area, a function of both topography and soil moisture. The fraction of the gridcell that is saturated generates saturation excess surface runoff and the maximum saturated fraction is determined by the topography of the gridcell. Total moisture input is found by adding the liquid precipitation which reaches the ground and the snow melt. Infiltration excess (Hortonian) overland flow is modelled if the total moisture input exceeds maximum infiltration rates. Water is also stored at the surface, e.g. in wetlands, and defined by its temperature and mass of water.

The percentage cover of lakes in each gridcell is derived from the Global Lake and Wetland Database (Lehner and Döll, 2004) and lakes are modelled using the LISSS model (Subin et al., 2012). Hydrology is representative of impervious surfaces, all precipitation falls to the ground (with nothing to intercept it), water volume remains constant and the runoff term used can be negative.

Runoff from glaciers is modelled from the residual of the glacier water balance and similar to lake runoff is permitted to be negative. Some of the modelling is unrealistic however. Unlike the treatment of snow melt, which can contribute to runoff, glacier melt is assumed to stay where it has melted until it refreezes.

A River Transport Model (RTM) is included to allow routing of total runoff from each gridcell downstream to eventually flow into the ocean. This improves the coupling of land and ocean, the modelling of freshwater influence on ocean circulation and to close

the water cycle. The runoff is routed through the RTM via a liquid water and ice water stream to provide better model performance in terms of global energy conservation when run "online", coupled to the other CESM components. In order to allow comparison with MacPDM, which does not model routed runoff, the routed runoff has not been used here.

The resolution of CLM4.5 means urban areas have limited influence on overall climate beyond being able to determine the temperature changes in urban areas. The modelling is a reasonable comparison with MacPDM, which, whilst including an urban landcover, does not include human impacts such as reservoirs and dams.

CLM4.5 also includes elements that a hydrology model would not include, for example a fire model (Li et al., 2012), methane model (Riley et al., 2011), biogenic volatile organic compound (BVOC) model (Guenther et al., 2012), dust model (Zender et al., 2003).

Since the release of CLM4.5, further revisions have been made, with the most current version being CLM5 (Lawrence et al., 2019).

2.1.3 Summary of model differences

A summary of the main model differences between MacPDM and CLM4.5 can be seen in Table 2.2. A large difference between the two models is how they compute volumes of runoff based on the proportion of the gridcell area that is saturated and therefore generates fast runoff (this is often but not always overland flow). MacPDM uses the Pareto distribution to determine soil moisture capacity and the proportion of the gridcell which is saturated (when soil moisture is at maximum capacity). Conversely, CLM4.5 employs consideration of topographic variability in order to assign the part of the catchment which would become saturated (and thus generate fast runoff) subsequent to a precipitation event. The fact that MacPDM only considers one homogenous soil layer, whilst CLM4.5 includes 15 soil layers - with processes computed using more complex equations, is another important difference between the models. For any given gridcell MacPDM only allows for grassland and one other type of landcover to be present, however CLM4.5 permits any number of fractional vegetation types within a gridcell, allowing for a more complex vegetation interaction with precipitation and evapotranspiration. Vegetation characteristic parameters can change over time within CLM4.5, however they are fixed for the whole time period within MacPDM, this again leads to a more complex response to vegetation in CLM4.5. Finally, the method of potential evapotranspiration calculation (critical for determining the water balance and available water for runoff generation) differs between

the two models.

Table 2.2: Structural model comparison between MacPDM and CLM4.5

STRUCTURAL COMPONENT	MacPDM	CLM4.5
Energy balance	Not included	Included
Division of gridcell into vegetation proportions	Only fraction of grass plus another vegetation	Any number of fractional vegetation types
Number of soil layers	1	15
Prescribed or dynamic LAI	prescribed for each vegetation type	can change dynamically over time
Evapotranspiration	Penman-Monteith Priestley-Taylor	Latent heat fluxes resulting from vegetation and hydrology parameterisations
Snow melt	mm/day/°C	depletion curve
Vegetation Phenology	Not present	Seasonal change included
Surface Runoff	probability distributed model and linear cascading reservoirs	Maximum fractional saturated area
Subsurface processes	linear function of groundwater store	modified Richards equation
Carbon and Nitrogen cycling	not possible	included

The model structure of MacPDM and CLM4.5 are largely seen to differ through MacPDM's more simplistic treatment of many of the components vs. the more physically based, detailed and time varying nature of CLM4.5 model elements. That is not to say however, that this more complex representation of processes within CLM4.5 will lead to more accurate or robust projections.

It is likely that the utilization of dynamic plant responses and the modelling of ET (given the importance of ET method indicated by Gosling and Arnell (2011)) are important in determining overall model differences in simulated runoff. However, as with many comparison studies, the variation in model structure and parameter choices is extensive enough that deciphering the exact cause of differences in runoff output is very challenging. Future studies would benefit from more controlled conditions where only certain model components are changed at a given time, allowing greater understanding of how each elements influences the model outcomes and providing an increased insight into precisely which modelling choices more closely reflect real-world processes or in fact if any model setup can replicate these processes correctly (Clark et al., 2011). This, however, was beyond of the scope of the current research, which looked to understand differences in model output from online and offline computation.

Neither model has been calibrated for this study and so differences in the two model outputs cannot be attributed to presence of calibration in one model but not the other. Despite the lack of calibration, Smith (2015) showed how the current parameterisation of MacPDM produced reasonable results when compared to observed streamflow in a number of large catchments.

2.2 Method

To determine the impact of "online" vs. "offline" modelling on predictions of global runoff under a scenario of climate change and solar geoengineering, the GLENS data set was used (Tilmes et al., 2018). The GLENS project is described in more detail in Chapter 1 so only a brief outline will be included here. The project modelled a scenario of SG whereby feedback from climate signals in the model determined stratospheric sulphate aerosol amounts to be injected at four possible locations across the globe, to maintain 2010-30 climate conditions as best as possible, focusing on three objectives: global mean surface temperature, inter-hemispheric surface temperature gradient and equator-to-pole surface temperature gradient. 20 ensemble members were run, starting for slightly different initial climate conditions. The background climate scenario to this was RCP8.5, 20 ensemble members were run from 2010-30, with each of these used to initiate the corresponding SG ensemble member, three RCP8.5 ensembles were extended to the end of the century to allow comparison of climate impacts.

As detailed above, the ESM used to provide the required climate and surface variables was the Community Earth System Model version 1 (CESM1) (Hurrell et al., 2013) coupled to the Whole Atmosphere Community Climate Model (WACCM) (Tilmes et al., 2018). The atmospheric model used, WACCM, is able to model stratospheric chemistry and sulphate aerosols well and therefore provides a good environment to simulated scenarios of stratospheric aerosol solar geoengineering (Mills et al., 2016, 2017).

The "online" modelling results were generated using CLM4.5 as the Land Surface Model component of CESM1(WACCM). Total liquid runoff at a monthly temporal resolution was directly outputted from the model and is the variable used here for "online" projections (UCAR, 2020).

Some processing was required to attain the 6 input climate forcing variables for MacPDM "offline" projections (described below). MacPDM was run at a daily time step and daily data output from CESM1(WACCM) for precipitation, temperature, net downwelling long-wave radiation, incoming solar radiation, wind speed, specific humidity and surface pres-

sure were used to generate the model inputs. The model was run 40 times using the climate inputs for each of the 20 ensemble members of the RCP8.5 and SG scenario. Despite the modelling being run at a daily resolution, Gosling and Arnell (2011) explain how the generalised response of daily processes in the model mean that outputs should only be used to study runoff at the monthly scale; this is therefore the lowest temporal resolution used in this analysis.

Observed global gridded runoff at 0.5° (GRUN data, (Ghiggi et al., 2019)) and observed streamflow for 38 catchments across the globe (GRDC dataset, (GRDC, 2020)) were used for comparison with the catchment aggregated modelled results to ascertain how analogous they are to real-world measurements. These 38 catchments were chosen to achieve as comprehensive a coverage of the main global hydrobelts (Meybeck et al., 2013) as possible, whilst adhering to the additional selection criteria (area >100,000km^2, continuous and recent timeseries). The mean difference of each scenario from the observed, seasonal shift in peak and minimum monthly runoff from present day, as well as annual change and amplitude were all statistics used to examine the projected impacts of climate change and solar geoengineering on runoff. The hydroregions which subdivide the 8 main hydrobelts were also used to examine model differences at the grid cell resolution for future projections of the RCP8.5 and SG scenarios. The hydrobelts and hydroregions can be seen in Figure A.1.

Further detail of the method used in this analysis is outlined below.

2.2.1 Processing GLENS data

The modelling results directly outputted from the GLENS project were used as the "online" projections. The Land Surface Model component of the Earth System Model used in the GLENS project was CLM4.5 and total liquid runoff was output from the model at a monthly temporal resolution (UCAR, 2020).

Total liquid runoff was simulated by CESM1(WACCM) using CLM4.5 as the LSM for 20 climate change (RCP8.5) and 20 solar geoengineering (SG) ensemble members at a 0.9×1.25° spatial and monthly temporal resolution. In order to make direct comparisons between the MacPDM generated runoff and these runoff projections, a spatial downscaling to 0.5×0.5° (to match the output resolution of MacPDM) was required. This was conducted using CDO's mass conserving downscaling technique (Schulzweida, 2019).

2.2.2 Modifying MacPDM

Some modification was made to the original Fortran MacPDM.17 code for use in this research. The code had only previously permitted 35 years of model run, and so in order to allow the full timeseries to be simulated a number of adaptations to the matrix storage size and numbers of iterations was made. The code was also condensed to remove all model setup options except for the daily input (this was simply to improve readability for the user). Hydrological models include a "spin up" time at the beginning of the simulation, this can also be termed a "wetting up" period and permits the water in the model to reach equilibrium from an initial dry state void of any system water storage. The version MacPDM.17 included a 10 year spin, however this was an error in the code which essentially performed two sequential 5 year spin ups, with the first 5 years simply being emptied and only the second spin up having effect on the results. Due to the nature of this study and the need to preserve as much of the timeseries as possible for the comparison of near time runoff, the code was updated to remove the redundant first spin up, leaving a total 5 year spin up time for the model.

2.2.3 Formatting climate variables for input into MacPDM

To generate the "offline" runoff 6 climate variables are required for input into the hydrological model MacPDM.17: precipitation, temperature, relative humidity, wind speed, net down-welling longwave radiation and incoming shortwave radiation. All but one of these variables, relative humidity, was output for the GLENS runs at the daily scale. Equation 2.2.1 shows the method used to estimate daily relative humidity using three variables (specific humidity, temperature and pressure) (Casey, 2017):

$$RH = 100\frac{w}{w_s} \approx 0.263pq\left[\exp\left(\frac{17.67(T-T_0)}{T-29.65}\right)\right]^{-1} \tag{2.2.1}$$

where RH is relative humidity, w is mass mixing ratio of water vapour to dry air (dimensionless), w_s is mass mixing ratio of water vapour to dry air at equilibrium (dimensionless), p is pressure in units Pa, q is specific humidity (dimensionless), T is temperature in units K and T_0 is reference temperature (typically 273.16 K) in units K.

Two climate variables output from the ESM, PS (surface pressure) and QREFHT (reference height specific humidity), were in 6 hourly time units and so needed to be aggregated to daily data. TREFHT (reference height temperature) was already at the daily time scale.

The daily data was then spatially downscaled in order to meet the $0.5 \times 0.5^{\circ}$ scale MacPDM uses. A mass conserving downscaling technique was used for precipitation, with bilinear interpolation used for the other five variables (Schulzweida, 2019).

The data from these 6 variables were then correctly formatted from netcdf files to the specific text input files required for MacPDM and run through MacPDM to give daily output files for each grid cell.

In order to make comparisons between the "offline" and "online" runoff, the MacPDM daily output data and GLENS monthly runoff were temporally aggregated to annual and monthly totals. The data were also spatially aggregated to the catchment scale in units of m^3 for the comparison with observed streamflow data.

2.2.4 Selection of validation catchments

In order to assess the performance of the "online" and "offline" modelling, validation against observed catchment river discharge was required. The selection of validation catchments was based upon that used by Zaherpour et al. (2018): only "major" catchments, larger than 100,000 km^2, were deemed suitable (WMO, 2006); coverage of all 8 global hydrobelts (Meybeck et al., 2013) was desired and only recent and continuous timeseries were considered. This dramatically reduced the number of possible catchments that could be used for validation. After this selection process 38 global catchments remained, their locations can be seen in Figure 2.2.

The selection criteria, being quite restrictive, leave very few possible catchments for comparison with modelled results. In order to not exclude catchments unnecessarily, if only a few continuous days were absent, particularly given the lowest temporal resolution of study is monthly, then linear interpolation across the gap was used to fill these missing data.

Throughout this research global catchments are defined using the drainage direction map (DDM30, (Döll and Lehner, 2002)). In order to match the modelled catchment areas as best as possible to the observed GRDC reported areas, small alterations were made to the 0.5° DDM30 catchment boundaries. In addition to this, an area weighted adjustment was applied to the model results based on the proportional difference in area between the 0.5° gridded model results and the GRDC reported areas using Haddeland et al. (2011). The modelled runoff predictions from the "online" and "offline" simulations were then compared to the observed values to allow interpretation of the model results and which, if either, more closely matched the real-world measurements. An additional dataset (GRUN,



Figure 2.2: Location of the 38 catchments used in the study.

(Ghiggi et al., 2019)) was used in the comparison. This 0.5° gridded runoff was used to help determine whether any disparities in model fit to the observed data could be arising from the gridded nature of the model results and the representation of catchment streamflow through summing of catchment runoff.

As mentioned above, the earliest possible date from the MacPDM simulations was 2015, therefore to keep as realistic a comparison to the observed as possible (and to control for differences between the modelled results), the years 2015-2024 were used for MacPDM and GLENS simulations in the analysis with observed streamflow. To ensure the best possible agreement between observed and modelled results, the most recent decade for each of the 38 catchment GRDC observed datasets was used. However, this varied between catchments and in a few cases was a whole decade apart from the modelled time period. The most recent decade of the gridded GRUN observed runoff was also used and which spanned the years 2005-2014.

Modelled runoff was converted to a measurement comparable to observed data by converting runoff depths to volume per gridcell and then summing these gridcell values across the catchment to give an annual total volume of water in m^3. Then the mean annual discharge equivalent value across the decade and the 20 ensemble members was calculated. Catchment discharge in cumecs (m^3/s) was similarly converted to volume in m^3/year.

To examine future projected changes in runoff in these 38 catchments under the RCP8.5 and SG scenarios, a number of comparisons were made to the present day, using the time periods 2050-70 and 2015-30. Shifts in monthly peak and monthly minimum runoff from 2015-30 to 2050-70 were examined for each catchment in order to gauge how each of the climate scenarios impacted seasonal trends; this is reported as either a positive (later) or negative (earlier) number of months. Annual average change in runoff as well as the amplitude (maximum minus minimum monthly runoff) were also considered, allowing a deeper understanding of how future totals and extremes in runoff are projected to change.

To extend the comparison of future projections in runoff under the specific climate change and solar geoengineering scenarios used in this study, a gridcell level comparison was undertaken to allow full global analysis of change, beyond the 38 catchments, using the aforementioned hydroregions to summarise this spatially.

2.3 Results

All comparisons depict the mean scenario response unless a range is indicated, i.e. for Solar Geoengineering (SG) and Climate Change (RCP8.5) scenarios, 20 (or 3 for future RCP8.5) ensemble members were run, with the mean monthly, seasonal or annual values found for each scenario. The intra-model variability, seen in the boxplots shown in Appendix B, is often small in comparison to the difference between the two model sets of MacPDM and GLENS. However, the model ensemble variability is non-negligible and sometimes leads to reasonably large ranges in percentage differences from the observed data; as shown in Table 2.3. Variability between ensemble runs tends to increase with progression into the future, likely due to divergence in the climate responses from more similar initial conditions. Variability is also often higher under solar geoengineering than climate change and this may be related to the larger ensemble for solar geoengineering in the future, as well as the varying feedback adjustment of aerosol injection location and amount to climate conditions, which can differ between ensemble members.

2.3.1 Comparison with observed data

It can be seen from Figure 2.3 that, in general, GLENS mostly overestimates (even if only by a relatively small degree) observed catchment total discharge and MacPDM tends to underestimate discharge (modelled as the sum of runoff across the whole catchment). The observed GRUN dataset was included to allow an interpretation of how much the differences between modelled and GRDC observed results was arising from the gridded nature of the modelled dataset or the method of totalling catchment runoff to represent catchment discharge. It can be seen that in general the GRUN gridded runoff matches the observed runoff more closely than either of the modelled cases, however there are still instances where there is a large disparity between the gridded observed runoff and observed streamflow.

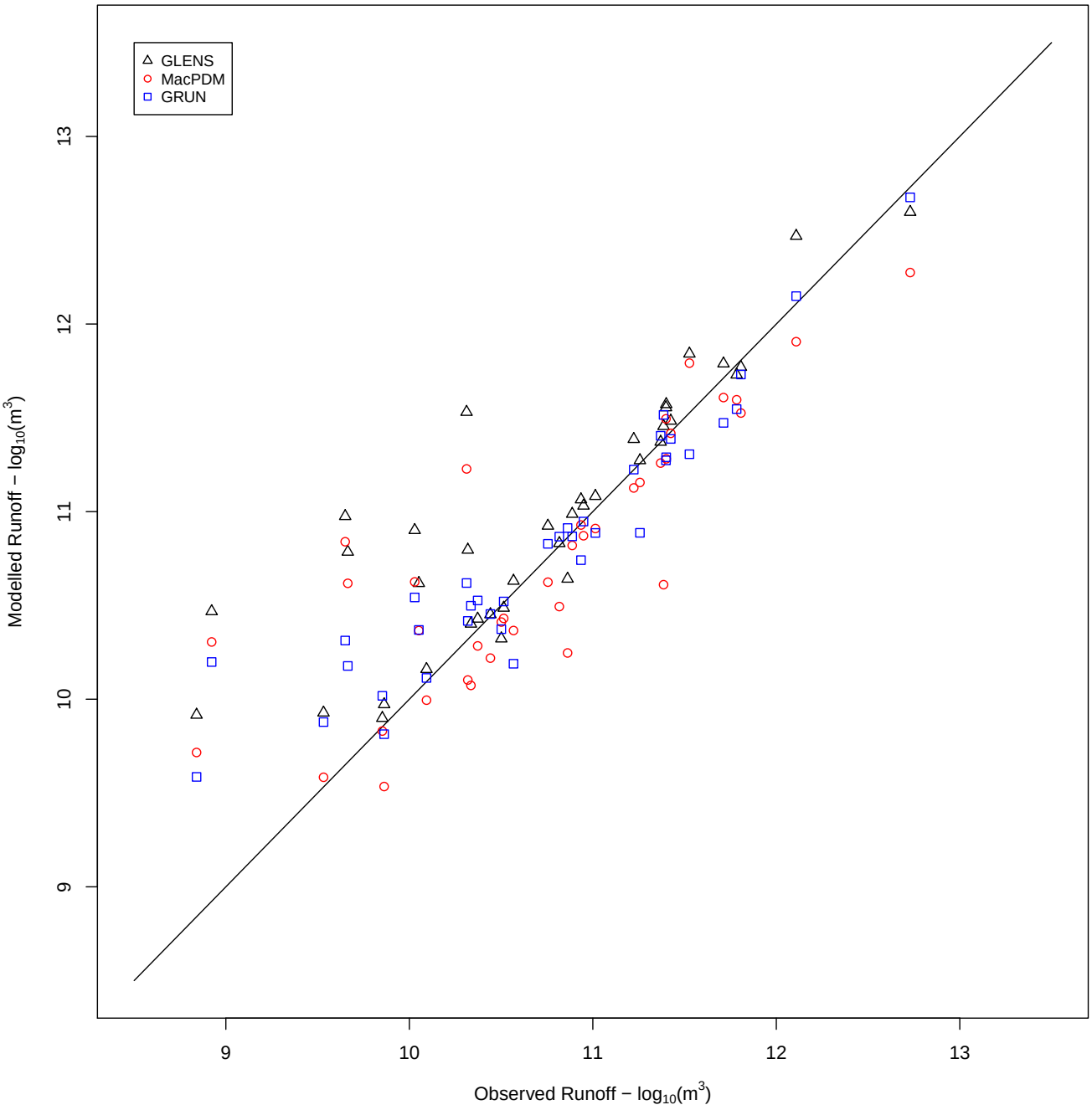


Figure 2.3: Difference in annual average total catchment discharge/runoff between GRDC observed data and 3 modelled/gridded outputs for 38 catchments around the globe.

Table 2.3 shows the differences between modelled and observed data for the 38 catchments as percentage differences of gridded runoff (GLENS, MacPDM, GRUN) from observed streamflow (GRDC), with the mean of the ensemble and range (in brackets) displayed for each of the modelled cases. The catchments are divided by hydrobelt, and it can be seen that in general Dry catchments have a poor fit to the observed, with some (but not all) Sub Tropical (Chao Phraya, Rio Parnaiba) and Mid Latitude (Darling) catchments also fitting rather poorly.

Table 2.3: Percentage differences ((modelled - observed)/observed *100) between gridded (GLENS, MacPDM, GRUN) and observed streamflow data for 38 global catchments (range in brackets).

River	GLENS	MacPDM	GRUN
Boreal			
KOLYMA	34.6 (20.1 - 48.9)	-1.5 (-11.8 - 8.4)	-36.0
LENA	19.4 (9.2 - 28.3)	-21.3 (-28.5 - -15.0)	-42.3
AMUR	43.4 (29.0 - 61.5)	24.7 (12.8 - 36.4)	-25.1
YENISEY	-11.7 (-19.3 - -5.8)	-35.0 (-40.1 - -29.9)	-42.1
OLENEK	15.6 (-10.5 - 29.2)	-37.1 (-54.7 - -26.9)	-58.2
SEVERNAYA DVINA	17.1 (2.4 - 31.3)	-21.3 (-32.9 - -12.6)	-25.4
MACKENZIE	14.6 (3.4 - 30.8)	-1.7 (-11.0 - 10.8)	-8.2
SASKATCHEWAN	13.8 (-17.0 - 52.8)	-18.3 (-43.9 - 21.8)	42.6
ASSINIBOINE	148.7 (79.3 - 223.2)	12.6 (-53.0 - 92.8)	121.8
RED	28.8 (-9.3 - 88.2)	-53.0 (-71.3 - -22.1)	-10.6
WINNIPEG	-33.7 (-53.0 - -9.3)	-18.7 (-39.9 - 7.3)	-25.5
CHURCHILL	2.4 (-22.0 - 26.3)	-40.1 (-53.5 - -28.8)	2.9
ALBANY	-6.1 (-27.1 - 12.4)	-17.5 (-33.0 - -2.5)	1.6
N. Mid Latitude			
YANGTZE	106.6 (87.4 - 122.1)	84.2 (67.8 - 98.4)	-39.8
ELBE	16.5 (-9.2 - 36.1)	-45.3 (-60.2 - -32.8)	45.4
RHINE	3.2 (-13.7 - 15.7)	-52.5 (-62.0 - -45.2)	12.0
DANUBE	-39.9 (-52.9 - -27.0)	-75.8 (-81.5 - -68.3)	12.3
NEVA	25.8 (12.5 - 44.5)	-14.5 (-23.6 - 0.3)	-4.4
VOLGA	48.6 (31.5 - 64.6)	-23.9 (-33.3 - -13.9)	-22.4
DON	200.3 (137.1 - 259.4)	-39.2 (-62.0 - -13.0)	25.5
COLUMBIA	45.6 (28.1 - 56.8)	-20.0 (-31.5 - -10.9)	0.2
MISSISSIPPI	-8.1 (-21.3 - 8.4)	-47.7 (-56.3 - -29.2)	-16.1
ST. LAWRENCE	0.5 (-18.2 - 14.6)	-22.5 (-39.6 - -6.9)	8.3
FRASER	20.7 (12.8 - 30.1)	-16.4 (-24.1 - -10.4)	-0.4
N. Dry			
COLORADO	268.7 (202.1 - 318.8)	106.2 (47.7 - 159.4)	107.7
RIO SANTIAGO	1220.7 (1077.8 - 1412.1)	798.1 (657.1 - 936.5)	225.7
N. Sub Tropical			
IRRAWADDY	3.8 (-9.1 - 15.1)	-20.8 (-32.2 - -10.7)	-57.3
CHAO PHRAYA	644.5 (521.7 - 808.7)	294.7 (210.0 - 410.7)	226.1
Equatorial			
ZAIRE	129.5 (114.6 - 145.3)	-37.2 (-44.0 - -26.2)	9.8
AMAZONAS	-26.3 (-31.1 - -22.8)	-64.9 (-66.3 - -63.6)	-11.8
XINGU	17.5 (-8.2 - 33.6)	-83.2 (-87.6 - -79.2)	35.0
S. Sub Tropical			
BURDEKIN	16.6 (-35.0 - 68.2)	-20.3 (-58.4 - 22.7)	4.7
RIO PARNAIBA	1556.0 (1175.8 - 1884.3)	723.9 (458.8 - 992.6)	103.0
SAO FRANCISCO	47.5 (8.1 - 82.9)	-26.1 (-46.1 - -2.8)	18.4
S. Dry			
COOPER CREEK	1091.5 (704.5 - 1499.3)	651.3 (387.9 - 936.7)	456.6
ORANGE	2013.3 (1491.0 - 2691.9)	1445.9 (1020.9 - 1981.7)	359.7
S. Mid Latitude			
FITZROY	11.3 (-47.8 - 110.3)	-5.0 (-42.4 - 61.2)	46.3
DARLING	3413.2 (1955.0 - 5220.0)	2314.1 (1174.2 - 3178.7)	1787.6

When the average monthly runoff over the year is compared for each catchment, clear trends can be seen, many of which are grouped by hydrobelts. For all Boreal catchments GLENS overestimates spring meltwater (freshet). In some cases, despite showing an increased amplitude, GLENS matches the observed signal and timing (e.g. Figures 2.4 and 2.5) quite well, these catchments are all in Northern Eurasia. Boreal catchments in North America however, are rather poorly represented by the GLENS modelling, frequently overestimating freshet, and MacPDM is shown to much more closely resemble observed flow in many cases. There are exceptions, for example Churchill and Winnipeg, where neither model captures the signal well. In general for Boreal catchments, MacPDM mostly underestimates runoff, although projected values are closer to the observed, with GLENS largely overestimating, particularly the freshwater spring melt.

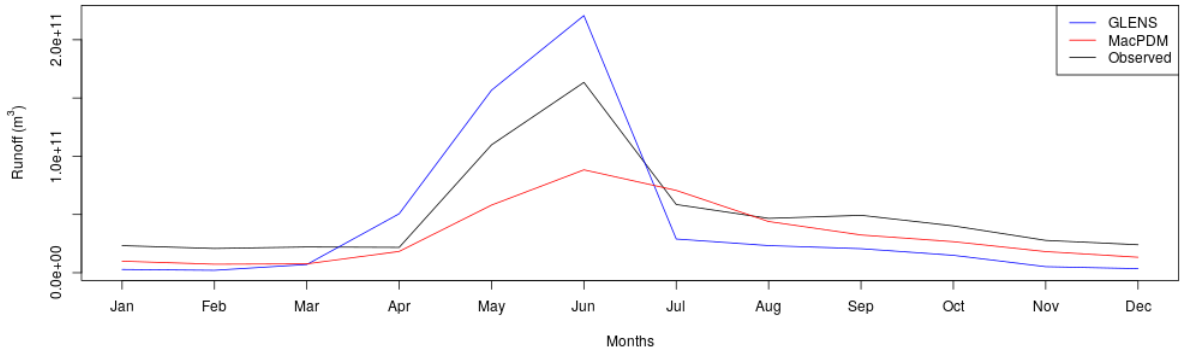


Figure 2.4: Difference in monthly average total catchment discharge/runoff between GRDC observed data and GLENS and MacPDM modelled outputs for Yenisey river.

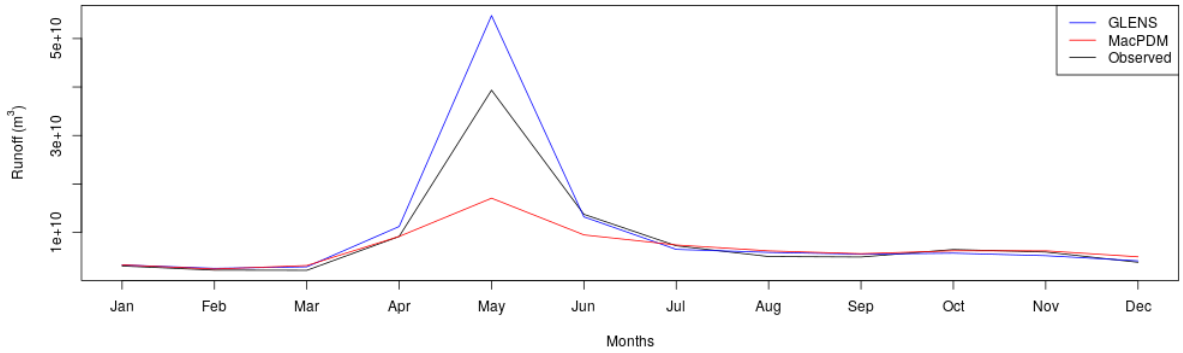


Figure 2.5: Difference in monthly average total catchment discharge/runoff between GRDC observed data and GLENS and MacPDM modelled outputs for Severnaya Dvina river.

Northern Mid Latitude catchments see a different combination of trends in response. Here there is a mixed picture, where in some catchments, generally European catchments (e.g. Figures 2.6 and 2.7), GLENS runoff is better at replicating the observed streamflow, with MacPDM greatly underestimating monthly values. Russian rivers, in common with their Boreal counterparts, generally see overestimation of freshet by GLENS, with MacPDM

more closely reflecting the observed values. For the Mid Latitude catchments found in North America to the west (Figures 2.8 and 2.9) MacPDM is a better fit, with GLENS again overestimating spring (and winter for Columbia) runoff. GLENS modelling better reproduces the magnitudes of runoff for the Mississippi catchment (Figure 2.10), which MacPDM, despite having the general seasonal trend correct, vastly underestimates. The eastern North American catchment (St. Lawrence) sees neither of the modelled simulations fit well, both projecting a greater amplitude in runoff, high in late winter/spring and low through summer and autumn, which is not seen in the observed streamflow - being consistent throughout the timeseries.

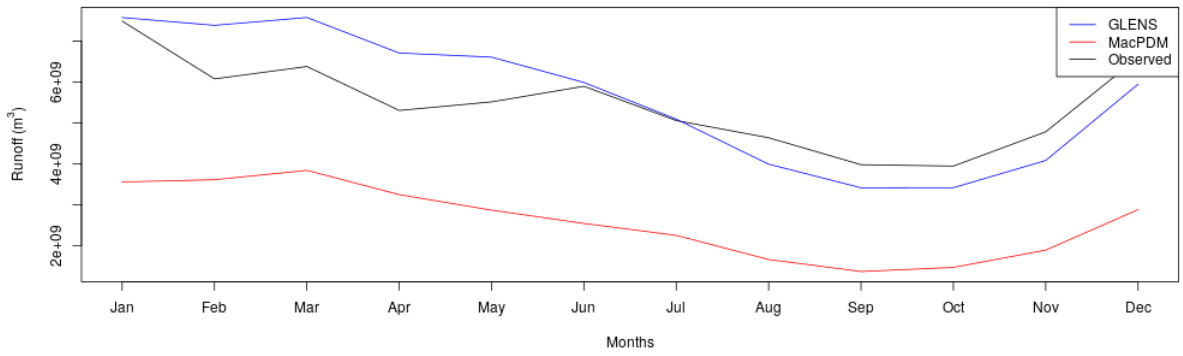


Figure 2.6: Difference in monthly average total catchment discharge/runoff between GRDC observed data and GLENS and MacPDM modelled outputs for Rhine river.

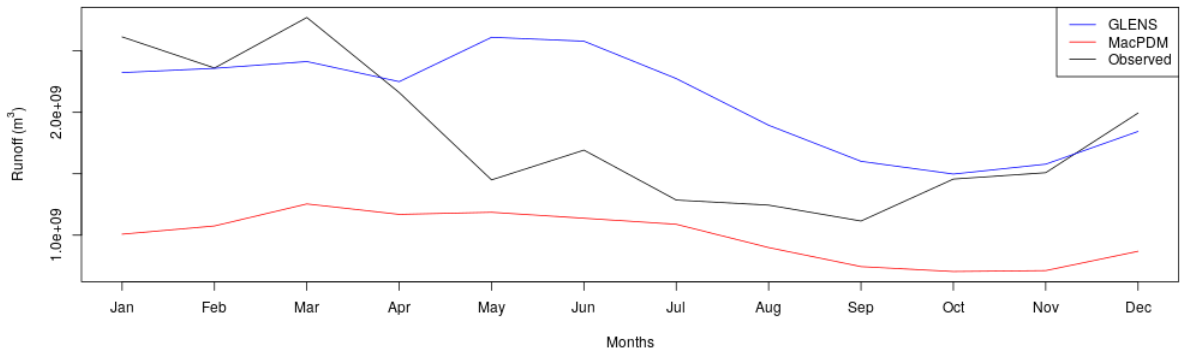


Figure 2.7: Difference in monthly average total catchment discharge/runoff between GRDC observed data and GLENS and MacPDM modelled outputs for Elbe river.

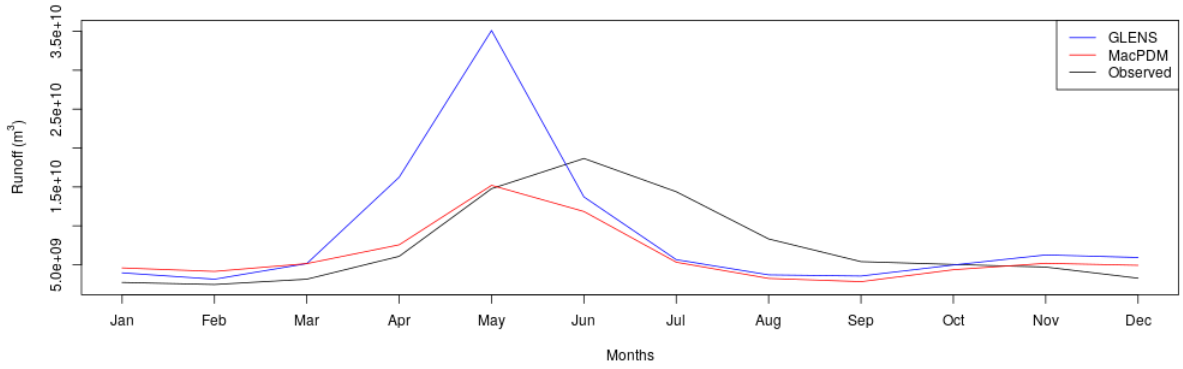


Figure 2.8: Difference in monthly average total catchment discharge/runoff between GRDC observed data and GLENS and MacPDM modelled outputs for Fraser river.

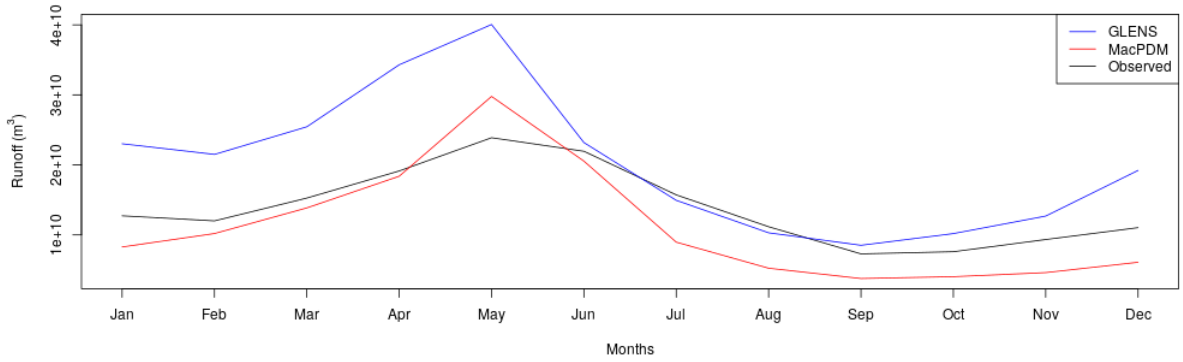


Figure 2.9: Difference in monthly average total catchment discharge/runoff between GRDC observed data and GLENS and MacPDM modelled outputs for Columbia river.

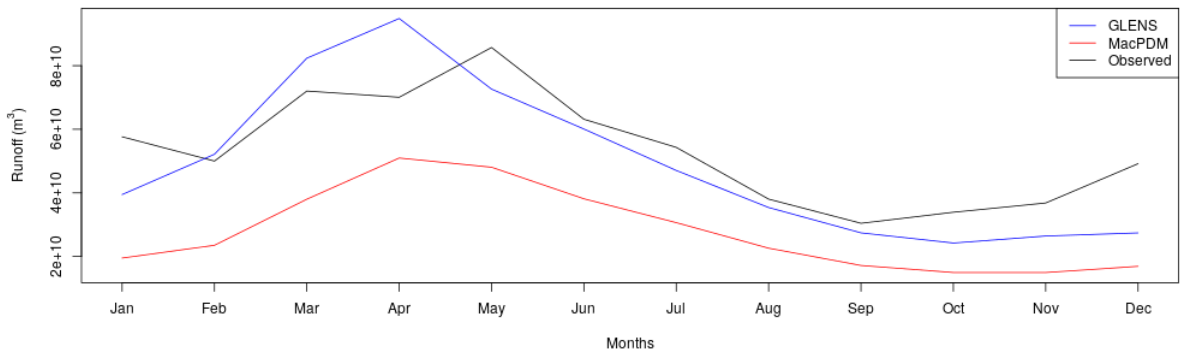


Figure 2.10: Difference in monthly average total catchment discharge/runoff between GRDC observed data and GLENS and MacPDM modelled outputs for Mississippi river.

The model response in the two Northern Dry catchments (Colorado and Rio Santiago 2.11) shows very poor agreement with the observed streamflow, greatly overestimating the volumes of water. Both models show similar trends, with GLENS runoff projecting greater runoff magnitudes than MacPDM, and in some instances MacPDM runoff (for autumn and winter in Colorado and January - May in Rio Santiago) is not so disparate from the observed.

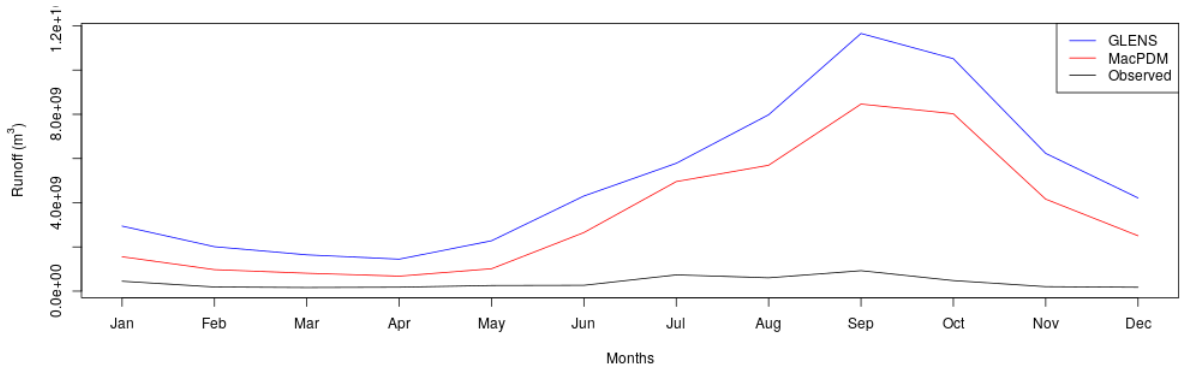


Figure 2.11: Difference in monthly average total catchment discharge/runoff between GRDC observed data and GLENS and MacPDM modelled outputs for Rio Santiago river.

The two catchments compared to observed GRDC streamflow in the Northern Sub Tropical hydrobelt have slightly contrasting messages, although modelled responses are similar for both and GLENS always estimates higher monthly runoff than MacPDM. The Irrawaddy catchment (Figure 2.12) sees a more muted signal in the modelled than observed values, underestimating from July to October and overestimating particularly from March to June. Figure 2.13 depicts how GLENS and MacPDM greatly overestimate the peak flow for the Chao Phraya river, and, despite agreeing on the timing (September), predicts this a month too early.

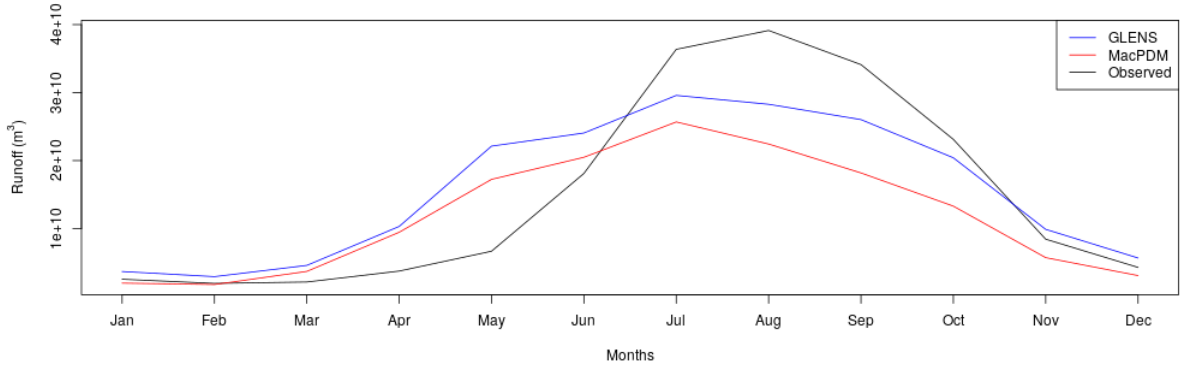


Figure 2.12: Difference in monthly average total catchment discharge/runoff between GRDC observed data and GLENS and MacPDM modelled outputs for Irrawaddy river.

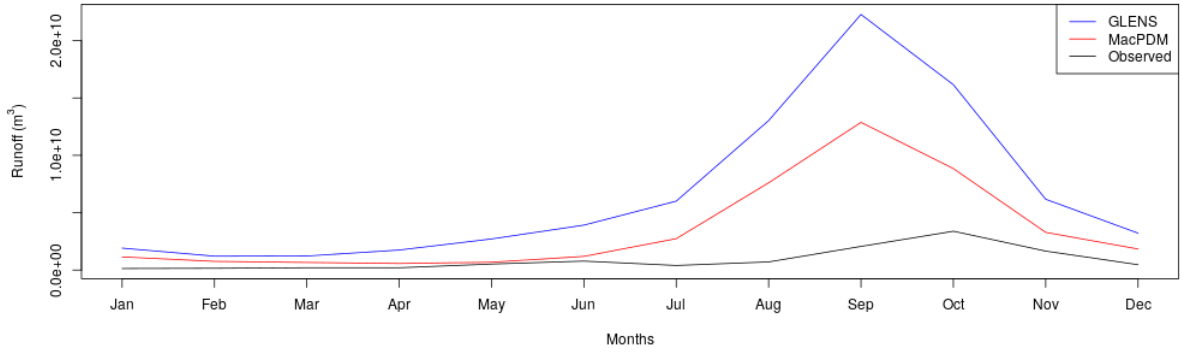


Figure 2.13: Difference in monthly average total catchment discharge/runoff between GRDC observed data and GLENS and MacPDM modelled outputs for Chao Phraya river.

For Equatorial catchments, there is again a mixed picture of responses and model fit. The two South American catchments see much better model fit by GLENS than MacPDM (which greatly underestimates flows), this is particularly true for the Xingu catchment (Figure 2.14) more so than Amazonas. Figure 2.15 for the Zaire river, however, shows that despite MacPDM once again underestimating flows (with GLENS overestimating), the modelling response fits more closely with the observed streamflow than for GLENS projections.

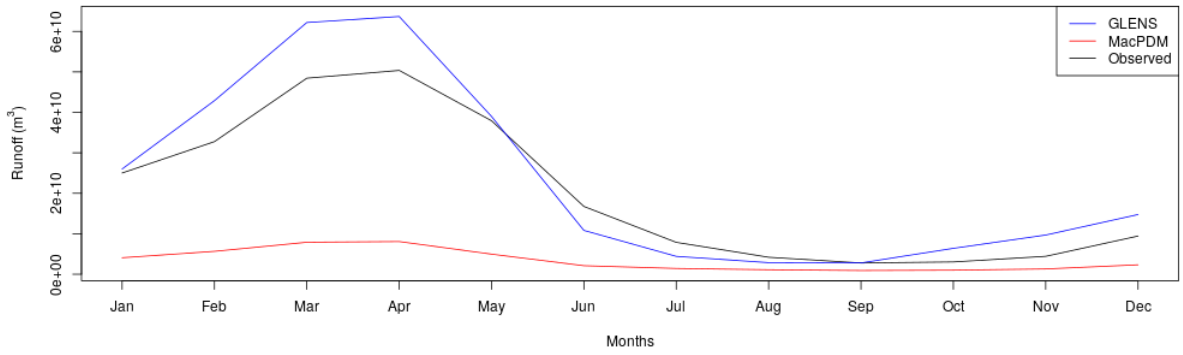


Figure 2.14: Difference in monthly average total catchment discharge/runoff between GRDC observed data and GLENS and MacPDM modelled outputs for Xingu river.

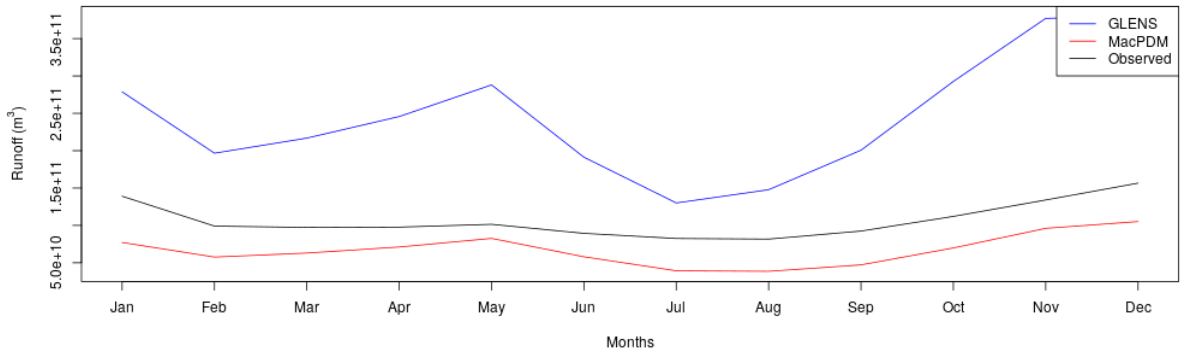


Figure 2.15: Difference in monthly average total catchment discharge/runoff between GRDC observed data and GLENS and MacPDM modelled outputs for Zaire river.

Catchments in the Southern Sub Tropical hydrobelt present a conflicted message. For the Burdekin river (as with the Northern Sub Tropical catchment of Irrawaddy) the modelled response is dampened in comparison to the observed, and for both cases underpredicts the peak flow in February and overpredicts flows from March to October. Also, similarly to the Chao Phraya, flows for the Rio Parnaiba are vastly overestimated, with a peak flow projected by both models in March-April, which is not apparent in the observed streamflow. The response in the Sao Francisco catchment (Figure 2.16) is seen to be slightly more unique, with MacPDM far better replicating observed flow from January to May, and GLENS more closely matching observed values from September to December.

However, MacPDM is seen to project total annual runoff values which are more alike to that of the observed, due to GLENS greatly overestimating runoff between January and April.

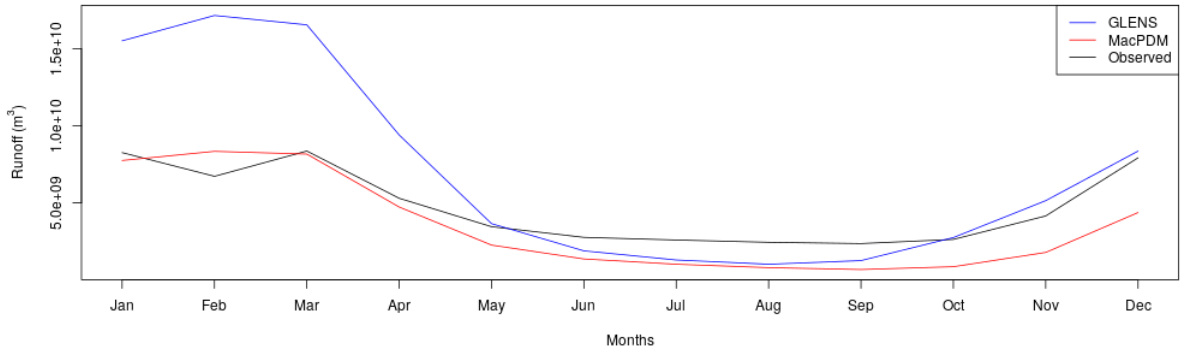


Figure 2.16: Difference in monthly average total catchment discharge/runoff between GRDC observed data and GLENS and MacPDM modelled outputs for Sao Francisco river.

As for the Northern Dry catchments, the Southern Dry catchments of Cooper Creek and Orange, show similar responses between the models (GLENS consistently estimates higher values than MacPDM) and vastly overestimate streamflow, showing a signal in the timeseries of higher summer flows that is simply not present in the observed.

The response in the Southern Mid Latitude Darling catchment (Figure 2.17) is very similar to that seen in the Southern Dry catchments. However, Figure 2.18 for the other catchment reported for this hydrobelt, the Fitzroy, depicts better agreement with observed streamflow, despite once more showing a more supressed amplitude for the modelled runoff when compared to observed, in which summer streamflow is indeed high, as predicted (incorrectly) by the models for the other Southern Dry and Mid Latitude catchments.

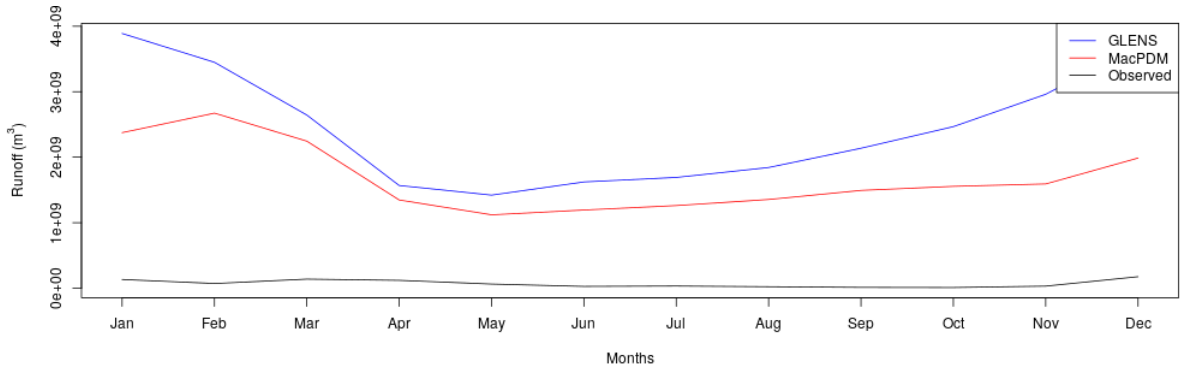


Figure 2.17: Difference in monthly average total catchment discharge/runoff between GRDC observed data and GLENS and MacPDM modelled outputs for Darling river.

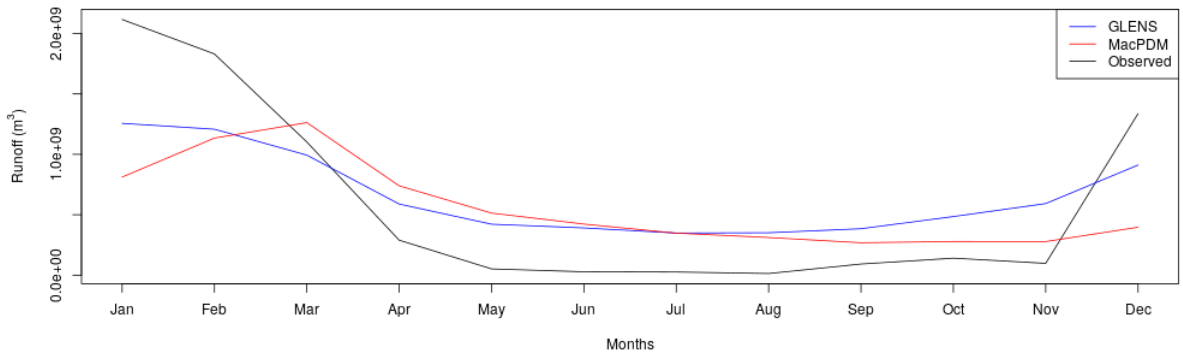


Figure 2.18: Difference in monthly average total catchment discharge/runoff between GRDC observed data and GLENS and MacPDM modelled outputs for Fitzroy river.

The full set of graphs can be found in Appendix B.

2.3.2 Projected differences under SG and RCP8.5

2.3.2.1 38 catchments used in validation

Tables 2.4 and 2.5, as well as all part c) of the graphs in Appendix B, show projected differences between mean modelled runoff in 2050-70 under scenarios of RCP8.5 or SG in comparison to the baseline (2015-30).

Some general themes can be determined from the response. On the whole, the SG scenario manages to maintain the overall magnitudes, timings and trends of the baseline response for both GLENS and MacPDM. Some notable exceptions to this however are the Darling River in Australia and the catchments of central Europe. The runoff projected under RCP8.5 remains much more similar to the baseline for the Darling catchment (Figure B.38), with SG greatly increasing projected runoff for all months under both models. In Europe the picture is less clear, with RCP8.5 runoff from MacPDM generally matching baseline flows more closely than SG for the Danube, Rhine and Elbe (Figure B.17, B.16 and B.15), but conversely matching better for SG under the GLENS model outputs.

Model projections from MacPDM and GLENS follow very similar patterns in their overall annual trend as well as in individual responses, e.g. months of peak flow and whether SG or RCP8.5 is higher in a specific month. GLENS almost always predicts higher monthly runoff values than MacPDM, with a few exceptions, mostly in the Boreal catchments.

In general catchments in Boreal locations e.g. Figure B.5 (as well as the Northern Mid Latitude Russian catchments of Don, Volga and Neva) see little change to their monthly flows under SG, when compared to baseline values, but do see changes under RCP8.5. This is on the whole a shift to an earlier month of peak flow and a dampening of this

spring flow.

European catchments (Rhine, Elbe, Danube) see almost exclusively higher monthly runoff under SG than RCP8.5, with the difference being more pronounced in the GLENS modelling. Mid Latitude North American catchments also, in general, see this trend of higher runoff under SG, however this is often the reverse for winter and early spring months. As with some Boreal catchments, the peak spring runoff tends to be dampened under RCP8.5 when compared to SG and the baseline.

Northern Sub Tropical catchments (Irrawaddy and Chao Phraya, Figures B.27 and B.28) see projected lower runoff for almost all months under SG when compared to RCP8.5, with the signal following the same general trend for both scenarios.

This lower runoff under SG can also be seen for the Equatorial catchment Zaire (Figure B.29). But is notably the reverse for Amazonas and Xingu catchments (Figures B.30 and B.31), with SG runoff either being very similar or slightly higher under SG when compared to RCP8.5 projections.

Southern Sub Tropical catchments (Figures B.32, B.33 and B.34) have a less clear message, with on the whole runoff values being similar between the two scenarios. Some months with SG runoff being greater than RCP8.5 (Burdekin - December to March, Sao Francisco - September to January) and some months seeing greater runoff under RCP8.5 than SG (Rio Parnaiba and Sao Francisco - February to March).

Cooper Creek and Orange catchments (Figures B.35 andB.36), in the Southern Dry hydrobelt, consistently see higher projected runoff under solar geoengineering than the Climate Change scenario RCP8.5.

Higher runoff under SG than RCP8.5 is also generally seen in the Southern Mid Latitude catchments, especially true for the Darling river (Figure B.38) and also true for the Fitzroy river (B.37) for all months outside March and April; when peak flows under RCP8.5 take runoff above that projected under the SG scenario.

Analysis of Table 2.4 reveals that peak monthly runoff does indeed get shifted a month earlier (negative values) in general for Boreal catchments under RCP8.5, with this signal being more pronounced for the GLENS than MacPDM modelling, with the two different models differing in exactly which catchments see this shift in peak runoff. Monthly minimum runoff is also seen to change in only a few number of Boreal catchments under RCP8.5, but in two (Assinibone and Red) this shift to earlier minimum flow is quite large.

The Northern Mid Latitude catchments see the largest changes in peak and minimum monthly runoff timings (except for the extreme negative shift (-4) in monthly peak runoff for the Colorado catchment). Most notably a shift of +4 months in peak RCP8.5 runoff is projected for the Danube under GLENS, -4 months in peak runoff for Columbia under GLENS RCP8.5, +6 months in minimum monthly runoff under GLENS RCP8.5 and -4 and -5 minimum monthly runoff under GLENS and MacPDM RCP8.5. There are no shifts in monthly peak or minimum runoff seen for either of the Northern Sub Tropical catchments (Irrawaddy and Chao Phraya) and only limited changes for Equatorial and Southern Sub Tropical catchments, markedly a positive monthly shift in peak runoff for GLENS RCP8.5 scenario in 2 of the Equatorial catchments and a positive monthly shift in minimum runoff for GLENS RCP8.5 scenario in all of the Southern Sub Tropical catchments. In the Southern Dry catchments there is a clear negative shift to earlier monthly peak runoff (-1 for Cooper Creek and -2 for Orange, but also -1 for Southern Mid Latitude Darling catchment) under GLENS RCP8.5, with a positive shift in monthly minimum runoff seen under the same scenario for the Southern Dry catchments.

Overall, shifts projected by GLENS are slightly more extreme than those projected by MacPDM, and there is not always agreement between the two models about the location (i.e. which catchments) and direction of change.

Almost all catchments for both MacPDM and GLENS see no change in monthly peak or minimum runoff under the solar geoengineering scenario. Only two catchments (Neva: -2.5 shift in monthly minimum under GLENS and Cooper Creek: -2 shift in monthly minimum under MacPDM) see changes in timing of more than one month and only 8 of the 38 catchments see any change in either monthly minimum, maximum or both.

Table 2.4: Differences in time shift (in plus or minus months) of Monthly Peak and Minimum runoff between model (MacPDM and GLENS) and scenario (RCP8.5 and SG) for 38 global catchments, from mid century (2050-70) to baseline (2015-2030).

River	Monthly Peak				Monthly Minimum			
	GLENS		MacPDM		GLENS		MacPDM	
	RCP8.5	SG	RCP8.5	SG	RCP8.5	SG	RCP8.5	SG
Boreal								
KOLYMA	-1	0	0	0	0	0	0	0
LENA	-1	-1	0	0	1	1	0	0
AMUR	-1	0	0	0	0	0	0	0
YENISEY	-1	0	0	0	0	0	0	0
OLENEK	0	0	-1	0	1	0	0	0
S. DVINA	0	0	-1	0	0	0	0	0
MACKENZIE	-1	0	-1	0	0	0	0	0
SASKATCHEWAN	0	0	0	0	-2	1	0	0
ASSINIBOINE	-1	0	1	0	-1	0	-1	0
RED	-1	0	0	0	-3	0	-1	0
WINNIPEG	0	0	0	0	0	0	0	0
CHURCHILL	0	0	0	0	0	0	0	0
ALBANY	-1	0	-1	0	0	0	0	0
N. Mid Latitude								
YANGTZE	0	0	-1	0	0	0	0	0
ELBE	0	0	2	0	-1	0	0	0
RHINE	0	0	0	-1	0	0	0	0
DANUBE	4	0	-1	1	-1	0.5	1	0
NEVA	0	0	-1	-1	6	-2.5	0	-0.5
VOLGA	0	0	-1	0	-4	0	-5	0
DON	-1	0	0	0	1	0	-1	0
COLUMBIA	-4	0	-2	0	0	0	0	0
MISSISSIPPI	0	0	-1	0	0	0	0	1
ST. LAWRENCE	0	0	0	0	0	0	0	0
FRASER	-1	0	-1	0	0	0	0	0
N. Dry								
COLORADO	-4	0	-1	0	0	0	-1	0
RIO SANTIAGO	1	0	1	0	0	0	0	0
N. Sub Tropical								
IRRAWADDY	0	0	0	0	0	0	0	0
CHAO PHRAYA	0	0	0	0	0	0	0	0
Equatorial								
ZAIRE	1	0	0	0	0	0	0	0
AMAZONAS	1	0	0	0	0	0	0	0
XINGU	0	0	0	0	0	-1	1	0
S. Sub Tropical								
BURDEKIN	0	0	0	0	1	0	0	0
RIO PARNAIBA	0	0	-1	0	1	0	1	0
SAO FRANCISCO	0	0	0	0	1	0	0	0
S. Dry								
COOPER CREEK	-1	0	0	0	1	0	1	-2
ORANGE	-2	0	0	0	1	0	0	0
S. Mid Latitude								
FITZROY	1	0	0	0	-1	-0.5	0	0
DARLING	-1	0	0	0	0	0	0	0

The patterns in Table 2.5 are less immediately obvious, but again general trends can be deciphered.

Possibly rather remarkably, given that the magnitudes of annual runoff are quite different between the projections from the GLENS and MacPDM, percentage changes in 2050-70 annual runoff from the baseline are pretty similar in both models for the scenario of RCP8.5 and for SG. Overall, when percentage changes in annual runoff differ greatly between scenarios, larger changes are seen under RCP8.5 than SG for GLENS and MacPDM. However, this is not always the case with larger (and indeed some of the largest) annual percentage changes seen under solar geoengineering for Olenek, Saskatchewan, Assiniboine, Burdekin, Sao Francisco, Cooper Creek and the Southern Mid Latitude catchments (Fitzroy and Darling) and with GLENS projecting greater increases in annual runoff than MacPDM.

The direction of change is not particularly consistent within hydrobelts, or for RCP8.5 vs SG. Sometimes the RCP8.5 scenario projects a decrease in annual runoff whilst SG projects an increase, sometimes this is the reverse and sometimes both scenarios project the direction of change to be the same.

Bigger percentage differences can often, but not always, be seen for amplitude (difference between minimum and maximum monthly runoff) than for the change in annual mean runoff, with some catchments seeing more than 100% change in amplitude; for example Assiniboine, Red, Albany, Mississippi, St. Lawrence, Rio Santiago, Amazonas, Xingu, Rio Parnaiba and Sao Francisco. However, apart from Rio Parnaiba, these very high amplitude changes are exclusively seen to result from MacPDM, with the projected percentage change in amplitude being generally much more moderate under GLENS.

Similarly to percentage changes in annual runoff, trends in the direction of change are not all that clear.

Table 2.5: Percentage differences in Annual Change and Seasonal Amplitude of runoff between model (MacPDM and GLENS) and scenario (RCP8.5 and SG) for 38 global catchments, from mid century (2050-70) to baseline (2015-2030).

River	Annual Change				Amplitude			
	GLENS		MacPDM		GLENS		MacPDM	
	RCP8.5	SG	RCP8.5	SG	RCP8.5	SG	RCP8.5	SG
Boreal								
KOLYMA	28.9	-2.6	29.4	-5.6	-24	-16.3	2.4	-5.7
LENA	14.2	1.5	17.7	-0.5	-47.6	-43.1	-55.7	-58.9
AMUR	34	-8.4	37.5	-8.7	-46.1	-42.3	-45.3	-52.6
YENISEY	2.1	-1.6	5.6	-2.9	-27.1	-28.6	-31.9	-35.7
OLENEK	3.6	9.9	3.9	12.8	-44.4	-43	-61.8	-57.6
S. DVINA	1.4	-1.3	5.7	-1.6	-28.5	-18.4	-31	-37.9
MACKENZIE	17.6	4.8	18	0.6	-25	-4.2	-10.7	-11.1
SASKATCHEWAN	14.5	19	3.9	21.8	25.2	21.1	63.4	31.1
ASSINIBOINE	-11.8	12.8	-20	36.6	16.2	16.7	159.6	151.8
RED	-18.3	5.6	-26.7	18.8	36	19	156.8	159.7
WINNIPEG	2.4	3.8	-2.5	1.4	33.2	16.5	215	199.5
CHURCHILL	6	5.4	1.2	4.6	46	20.7	61.1	40.9
ALBANY	-0.4	-4.6	-8.4	-3.8	19.8	26.7	173.6	151
N. Mid Latitude								
YANGTZE	9.2	8.4	12.5	8.6	-31.5	-18.9	-35.8	-34.1
ELBE	-16.1	2.2	-17.4	7.4	26.3	22.3	-14.4	-16.6
RHINE	-13.5	2.9	-16.7	5.7	-10.4	-15.8	72.3	95.3
DANUBE	-11.3	4.7	-16.8	8.7	-17	-18.6	-8.6	-15
NEVA	2.4	0.5	2.6	-0.4	-16.5	-22.6	-3.8	-18
VOLGA	0.7	-2	-3.7	-3.8	-34	-33.7	-24.8	-18.8
DON	-11.5	-8.2	-15.9	4.9	-21.7	-20.6	-32.7	-31.2
COLUMBIA	10.5	1	5.3	2	17.9	19.4	21.4	24.1
MISSISSIPPI	-12	3.8	-18.4	15	68.2	60.8	148.4	75.3
ST. LAWRENCE	-5.2	-7.2	-9.6	-4.4	23.2	28.2	239.4	201.6
FRASER	17.8	1.1	15.1	-1.6	-32	-21.4	-9.9	-23.2
N. Dry								
COLORADO	-21.2	8.4	-24.5	16.8	12.8	23	91	61.3
RIO SANTIAGO	0.6	-5.5	-0.5	-4.3	29.1	31.2	227.2	211.9
N. Sub Tropical								
IRRAWADDY	6.4	2.7	7.6	4.6	-48.3	-44.7	-57.7	-61.4
CHAO PHRAYA	14.4	-3.7	25.5	-2.1	-17.5	-23.2	-69.4	-68
Equatorial								
ZAIRE	5.8	-3.4	19	-4.4	-9	-15.3	-12	-19.2
AMAZONAS	-5.9	1.6	2	6.4	47.5	30.4	167.8	150.2
XINGU	-21.5	-9.3	-22	-6.7	87.6	89.5	114.3	122.8
S. Sub Tropical								
BURDEKIN	5.7	22.4	11.6	28.6	15.5	44.4	5.5	3.9
RIO PARNAIBA	-17.4	-10.3	-23.2	-15	127.2	85.9	128.8	110.5
SAO FRANCISCO	4.3	13.7	9.9	18.7	34	28.7	123.5	122.9
S. Dry								
COOPER CREEK	20.1	48.7	10.6	38	-26.5	-22.5	-50	-52.6
ORANGE	-17.2	-8.8	-16.4	-1.4	3.1	-12.8	-11.3	-26.5
S. Mid Latitude								
FITZROY	16.7	54.3	15	44.8	0.9	18.2	-18.2	-9.5
DARLING	47.7	86.3	15.5	61.2	-38.5	-19.5	-4.8	-13.4

2.3.2.2 Global analysis using hydroregions

The graphs in Figures 2.19 - 2.22 presents the spread of gridcell level runoff under 3 scenarios (baseline - 2015-30, SG - 2050-70, RCP8.5 - 2050-70) and 2 models (GLENS, MacPDM), dividing into 8 hydrobelts which themselves are subdivided to give 26 hydroregions. The distribution of the gridcell values for each of these hydroregions is depicted in each of the 26 graphs, with the 25th, 50th (median) and 75th percentiles marked with horizontal lines on the violin plots. In many cases, the largest disparities in spread of gridcell runoff for each hydroregion are between the two models. There are clear differences in the 25th, 50th and 75th percentiles which are more immediately obvious that any variation within the model under the 3 scenarios. Values for GLENS are also seen to frequently be higher than MacPDM, in agreement with the analysis outline above. In many cases the 25th percentile of GLENS is larger than the 50th percentile of MacPDM, however this is not always the case, particularly for a number of Boreal catchments, including Boreal North America and Boreal Asia (West Siberia), as well as Northern Mid Latitude Asia. When examined carefully, the graphs also show that the scenario for SG more closely represents the baseline both in overall shape and in position of the percentiles, although this is not always true. Differences in RCP8.5 from the baseline tend to indicate higher 25th, 50th and 75th percentile values, notable exceptions to this are hydrobelts all found in the Americas and are Northern Dry North America and Northern Sub Tropical North America, Equatorial South America and Southern Sub Tropical South America.

Figures 2.23 - 2.26 depict percentage changes in annual gridcell runoff from future RCP8.5 and SG scenarios (2050-70) to the baseline (2015-30) for hydroregions. In general, changes seem to be greater under MacPDM than GLENS. For both model cases Boreal Northern Hemisphere catchments see increases to runoff under RCP8.5, but slight decreases or little change under SG. For MacPDM Northern Hemisphere Dry catchments generally see decreases in runoff under both RCP8.5 and SG, with the exception of Northern American which sees increased runoff under SG. The reverse is true for GLENS where all scenarios except Central Asia under SG and North America under RCP8.5 see increases in runoff, in some places large increases, e.g. Africa and the Middle East. Catchments in the Mid Latitude Northern Hemisphere show two trends, in Asia there is increased runoff under RCP8.5 and decreases under SG, with the reverse true in Europe and North America, although the increases under SG are only slight, or negligible under GLENS. The Northern Sub Tropical catchments of Africa and Asia, both see quite large increases in runoff under RCP8.5, with decreases under GLENS, the reverse is true for North America, although the changes are more moderate here. Equatorial catchments all respond differently, but the

changes under SG are smaller, under RCP8.5 runoff is projected to increase over Africa and Asia, but decrease over South America. The Southern Dry catchments either see little or small (greater under GLENS) increased change (Australia and South America) or larger reductions in runoff (Africa), with the response similar under both scenarios. In the Southern Mid Latitude catchments all scenarios project increases in runoff, except for Africa under RCP8.5, and SG is projected to greatly increase runoff over Australia, and to a lesser extent South America. The Southern Hemisphere Sub Tropical catchments see less deviation from the baseline, with small increases in runoff except for Africa under SG and South America under RCP8.5.

Table 2.6 aims to summarise the main trends in percentage change of annual mean runoff across the hydroregions. Hydroregions are grouped by whether the scenario of solar geoengineering increases or decreases mean annual runoff in comparison to the scenario of climate change, or whether there is no significant difference between the scenarios. Hydroregions are also grouped by whether both future scenarios see a positive percentage change in future mean annual runoff from the baseline, both see a negative future percentage change or whether the scenarios see a contrasting response, with one future scenario increasing mean annual runoff from baseline conditions and the other decreasing it (determined by whichever scenario is shown to be greater or lesser than the other in terms of percentage change).

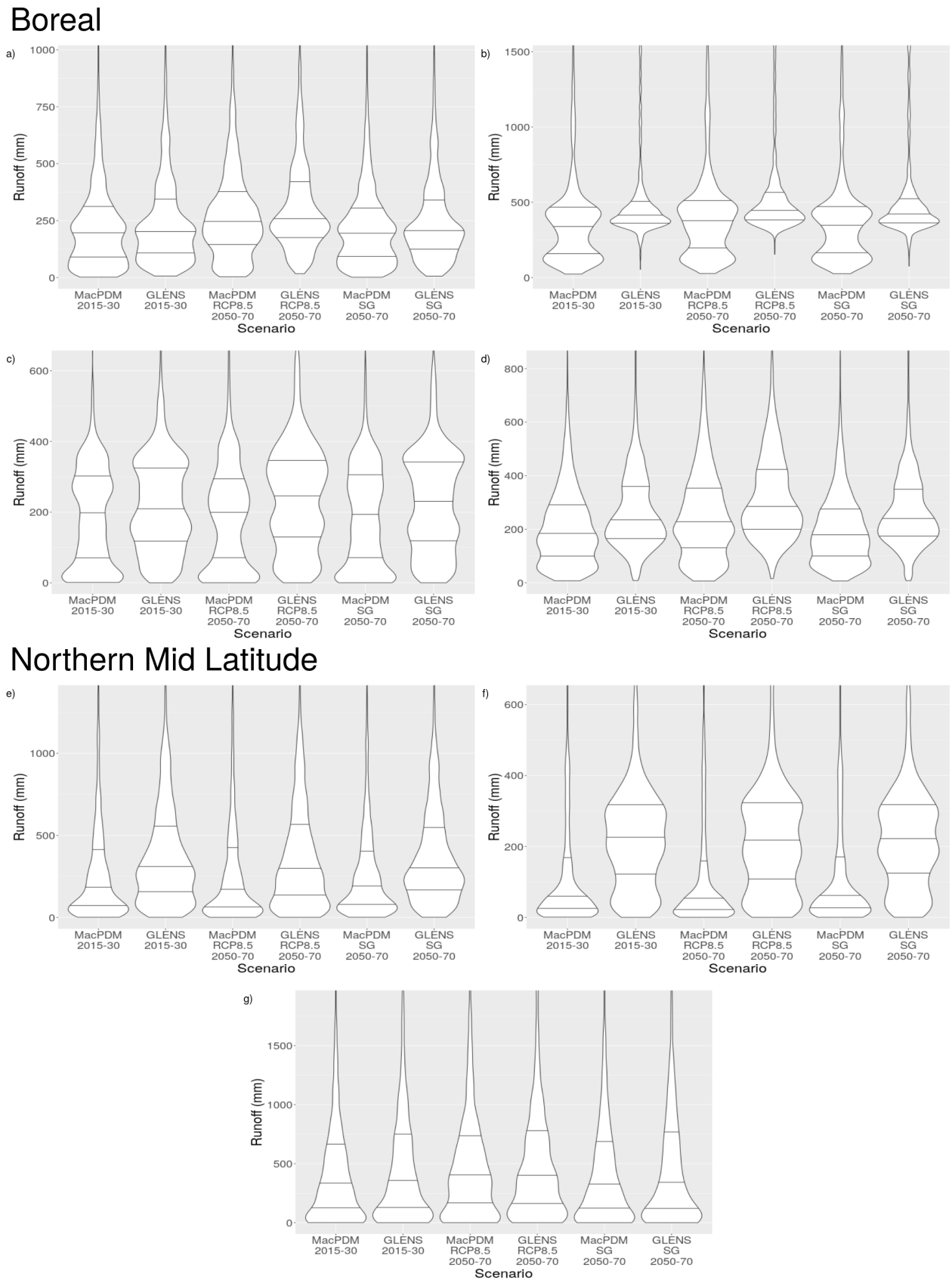


Figure 2.19: Violin plots to display differences in model (MacPDM vs. GLENS) and scenario (RCP8.5 vs. SG) projections from control period for a number of different hydroregions - a) Boreal North America, b) Boreal Europe, c) Boreal Asia (West Siberia), d) Boreal Asia (East Siberia), e) Northern Mid Latitude North America, f) Northern Mid Latitude Europe, g) Northern Mid Latitude Asia.

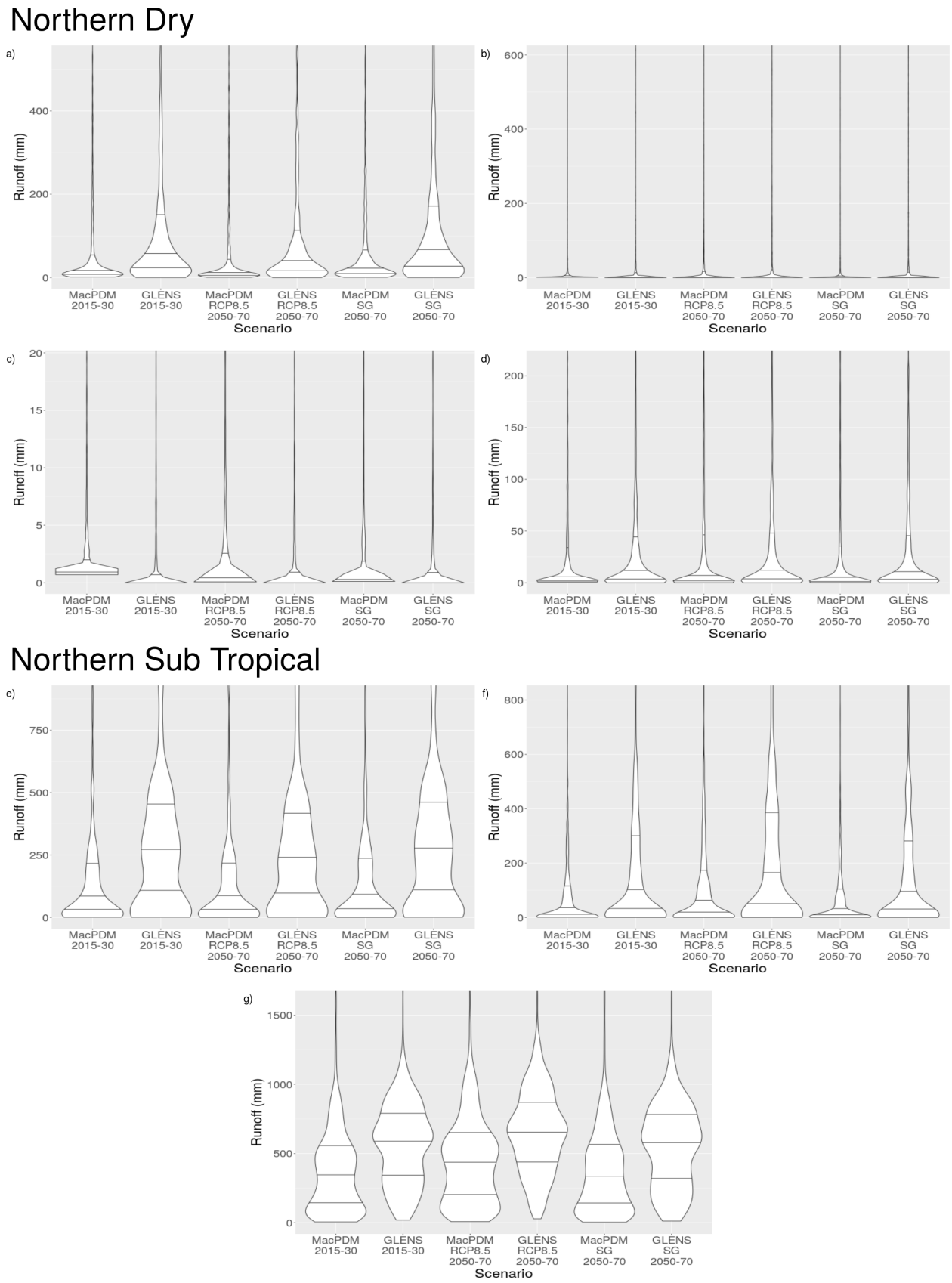


Figure 2.20: Violin plots to display differences in model (MacPDM vs. GLENS) and scenario (RCP8.5 vs. SG) projections from control period for a number of different hydroregions - a) Northern Dry North America, b) Northern Dry Africa, c) Northern Dry Asia (Middle East), d) Northern Dry Asia (Central Asia), e) Northern Sub Tropical North America, f) Northern Sub Tropical Africa, g) Northern Sub Tropical Asia.

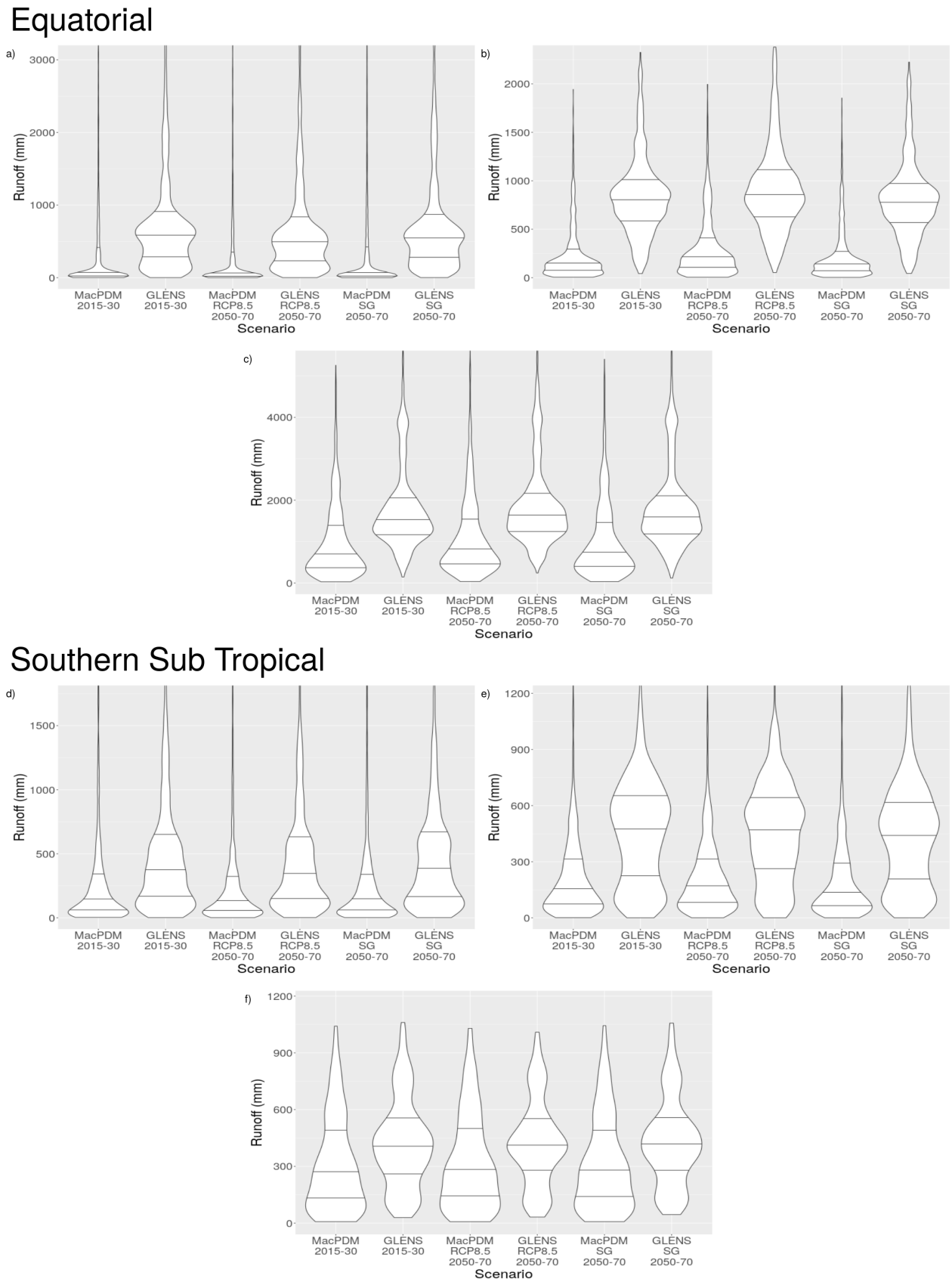


Figure 2.21: Violin plots to display differences in model (MacPDM vs. GLENS) and scenario (RCP8.5 vs. SG) projections from control period for a number of different hydroregions - a) Equatorial South America, b) Equatorial Africa, c) Equatorial Asia, d) Southern Sub Tropical South America, e) Southern Sub Tropical Africa, f) Southern Sub Tropical Australia and Oceania.

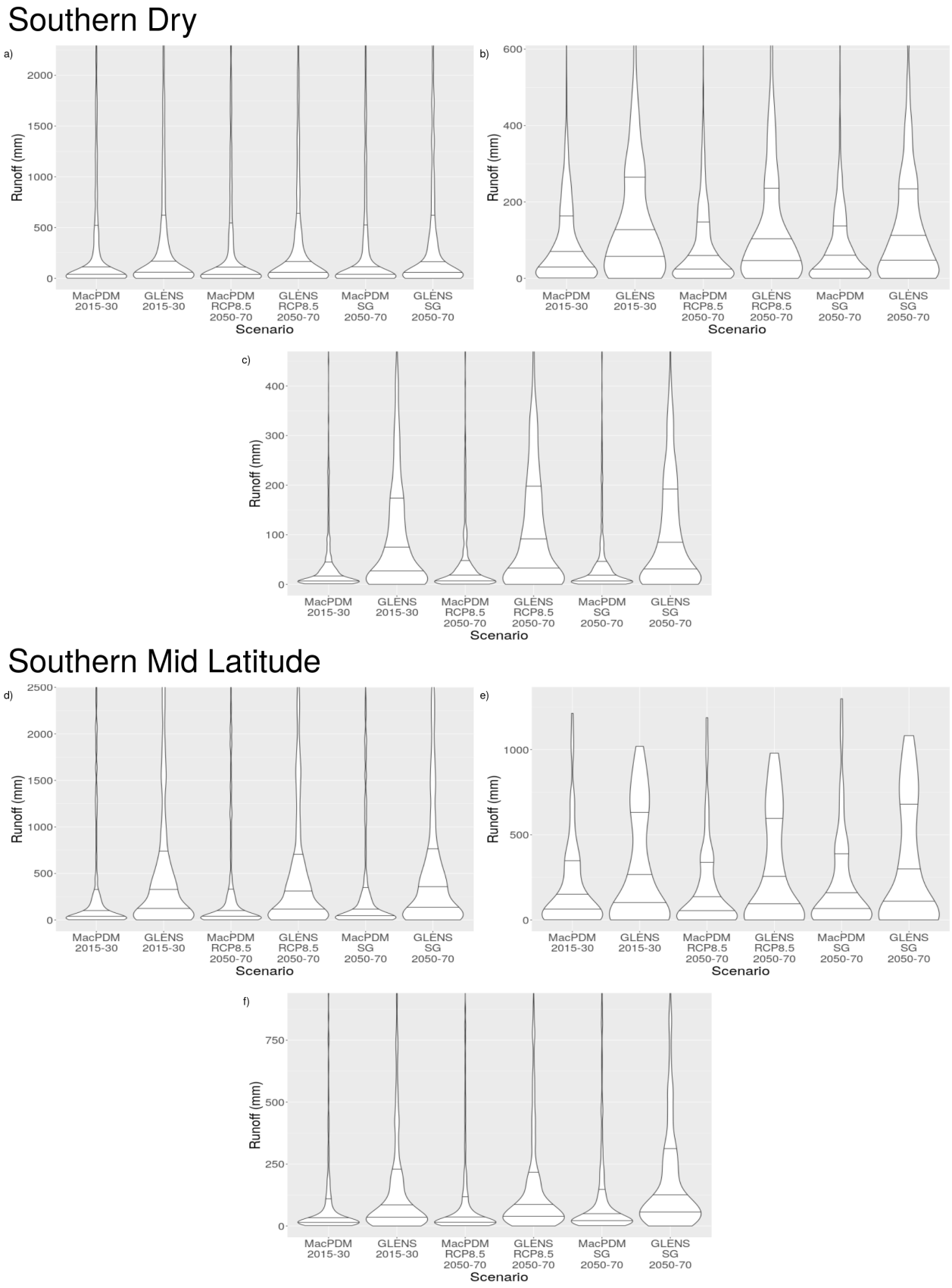


Figure 2.22: Violin plots to display differences in model (MacPDM vs. GLENS) and scenario (RCP8.5 vs. SG) projections from control period for a number of different hydroregions - a) Southern Dry South America, b) Southern Dry Africa, c) Southern Dry Australia and Oceania, d) Southern Mid Latitude South America, e) Southern Mid Latitude Africa, f) Southern Mid Latitude Australia and Oceania.

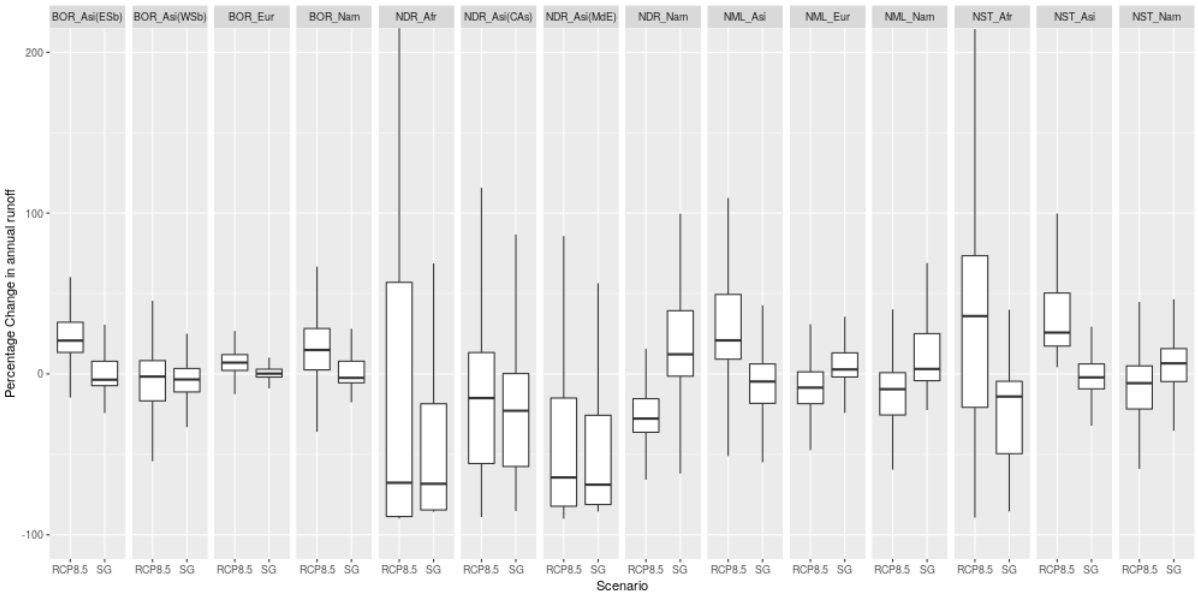


Figure 2.23: Percentage changes in future mean annual runoff (2050-70) by gridcell for RCP8.5 and SG under MacPDM modelling for Northern Hemisphere hydroregions.

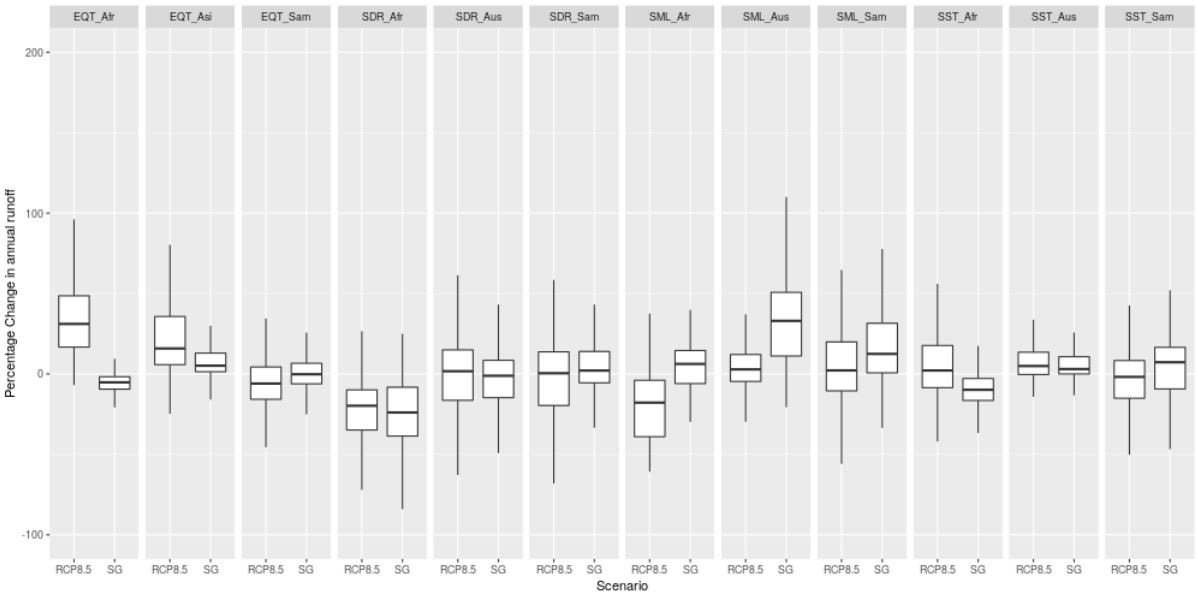


Figure 2.24: Percentage changes in future mean annual runoff (2050-70) by gridcell for RCP8.5 and SG under MacPDM modelling for Equatorial and Southern Hemisphere hydroregions.

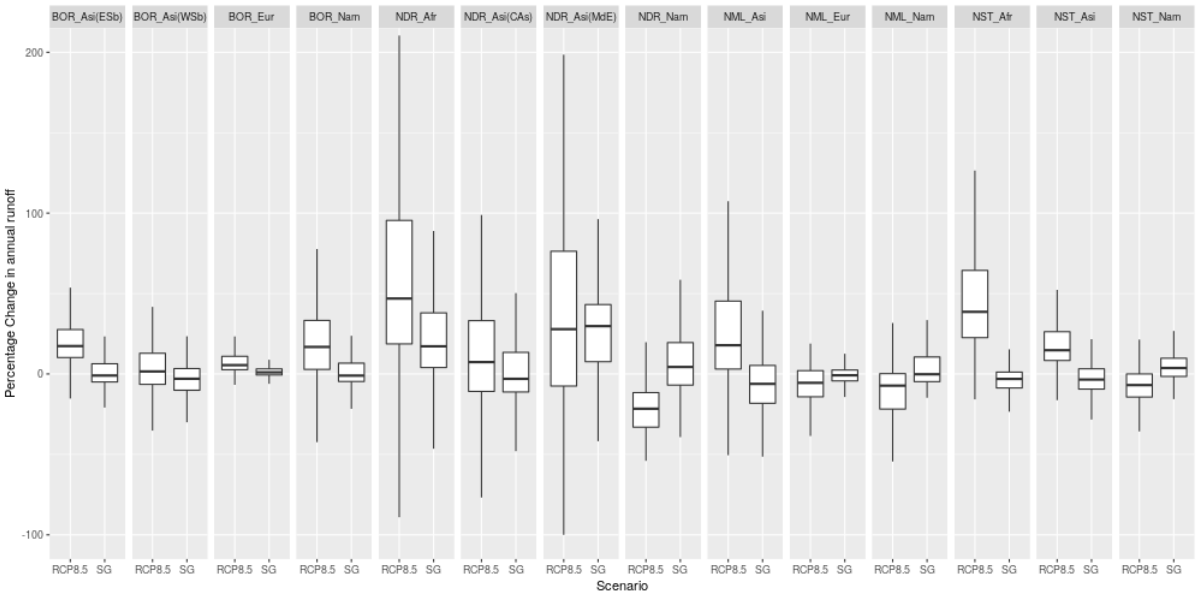


Figure 2.25: Percentage changes in future mean annual runoff (2050-70) by gridcell for RCP8.5 and SG under GLENS modelling for Northern Hemisphere hydroregions.

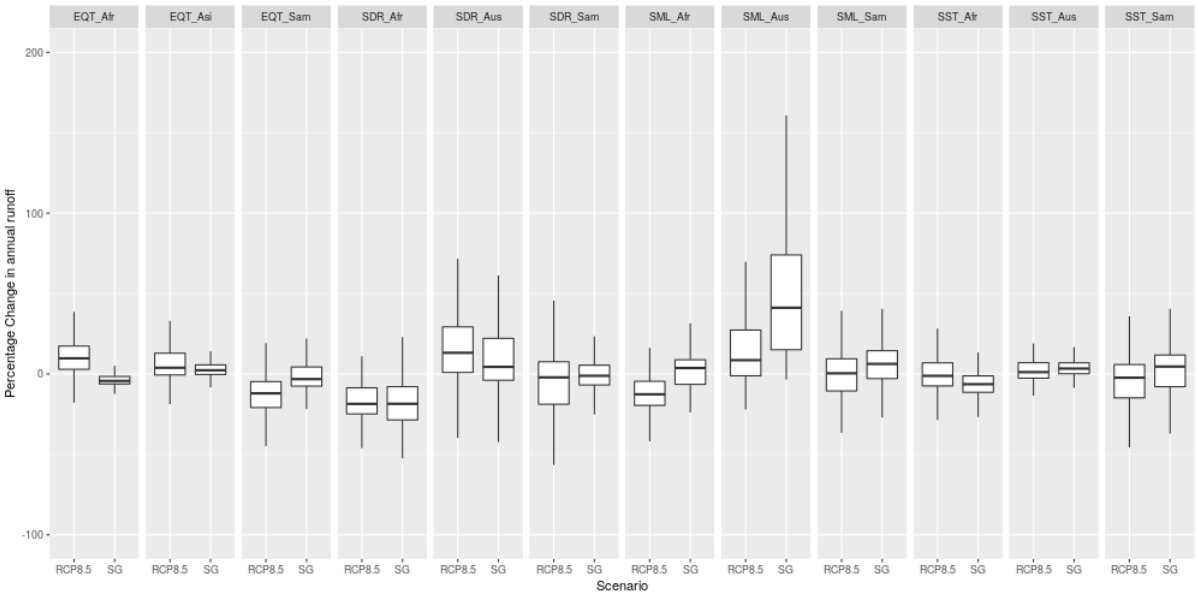


Figure 2.26: Percentage changes in future mean annual runoff (2050-70) by gridcell for RCP8.5 and SG under GLENS modelling for Equatorial and Southern Hemisphere hydroregions.

Table 2.6: General trends across the hydroregions for percentage change from the baseline in future (2050-70) mean annual runoff under RCP8.5 and SG.

	Positive % change	Negative % change	Divergent % change
SG < RCP8.5	Boreal Asia (E. Siberia) N. Sub Tropical Africa N. Sub Tropical Asia		N. Mid Latitude Asia Equatorial Asia
SG > RCP8.5	S. Mid Latitude Australia		N. Dry N. America
SG ≈ RCP8.5		S. Dry Africa	

2.4 Discussion

It is seen that, in general, GLENS overestimates and MacPDM underestimates annual runoff. GLENS modelled runoff is also frequently of greater monthly amplitude than MacPDM, which sometimes can result in improved or conversely poor fit to the observed streamflow, often dependent on catchment location and characteristics. For example, MacPDM tends to project more similar runoff magnitudes and trends in Boreal, particularly Russian, catchments (largely due to the overestimation of freshet in GLENS). On the other hand, GLENS is much closer in its projections to observed streamflow in European and some North and South American catchments (e.g. Mississippi, Xingu). In other cases, neither model replicates the observed monthly values well, mainly by overestimating streamflow. A few catchments, e.g. Columbia, demonstrate an interesting response in which one model correctly captures magnitudes and trends for a portion of the timeseries but performs poorly for the remaining months, (MacPDM in late winter/ early spring) whilst the other model (GLENS in summer) better replicates the signal for another section of the timeseries but also misestimates flows in the other portion of time. In the case of the Columbia river this seemingly is not some sophisticated difference in model response, but affirmation of GLENS' tendency to overestimate and MacPDM's tendency to underestimate, with both having a greater amplitude in signal than the observed. Therefore, it is more "luck" than correct representation of the hydrological system that leads to the closer agreement of modelled and observed flow in each section of the timeseries. This highlights the need to carefully interpret model agreement with real-world measurements and also the impact it may have on the choice of the "best" model.

Although this is a study examining differences between online vs. offline models and it has been found here that the online model overestimates and the offline model underestimates annual runoff, this is a very specific online and offline case and wider conclusions cannot be drawn from this - i.e. extrapolation to other models. Other studies have found, for example that LSMs tend to predict lower runoff than GHMs, the reverse trend to what has been found here (Haddeland et al., 2011).

The inclusion of interactive vegetation within CLM4.5, and not within MacPDM, is likely to have a large impact on the model response. Vegetation is hugely interconnected with the hydrological cycle, influencing evapotranspiration and runoff (Beaulieu et al., 2016, Dunn and Mackay, 1995). It is also thought to be very responsive to climate changes in precipitation, temperature and CO_2. This is important, as differences between climate change and solar geoengineering may be attenuated or perpetuated by the response of vegetation,

and therefore a models ability to replicate this will likely have a marked impact on model results. Climate change and solar geoengineering themselves will likely also influence the growth of vegetation through alterations to temperature and hydrological variables (including amplitude) and the physiological response of plants, for example changes in water use efficiency and stomatal conductance (Dagon and Schrag, 2016). The novel conditions of elevated CO_2 (as is the case for climate change), but lower surface temperatures, possess questions for how vegetation may respond to SG. There is however, little understanding at present about exactly how vegetation will respond to changing CO_2 levels, and to any extent much less understanding than we have for how vegetation responds to temperature changes (Swann, 2018). Increasing CO_2 levels will simultaneously increase water use efficiency (as stomata can take in more CO_2 in one go and therefore need to open less, thus losing less water to transpiration) and increase plant growth (which would lead to more water use and greater leaf surface areas - in turn increasing transpiration). The balance between these conflicting responses, with particular uncertainty surrounding the influence of CO_2 on increasing plant growth, will govern how vegetation responds as a whole to changes in CO_2 levels, of relevance to both climate change and solar geoengineering scenarios, but arguably of more importance under SG because the temperature affects on vegetation clearly seen under climate change would not be present (Swann, 2018). Dagon and Schrag (2019) found that through a coupled carbon and hydrological cycle, greater understanding could be gleaned about the impact of solar geoengineering on vegetation, which whilst present in CLM4.5 is absent from MacPDM. Dagon and Schrag (2019) also found in their modelling of SG through solar dimming (reduction of incoming solar radiation to mimic the reflective effects of stratospheric aerosols) with inclusion of vegetation ability to change stomatal conductance and LAI values, that plants were possibly driving the general reduction in the hydrological cycle under SG, interpreted by the reduction in transpiration. Whilst this is undoubtably important, it is hard to quantify exactly how influential the presence of vegetation is on model results, in particular when the percentage changes in annual runoff under SG (2050-70) from the baseline (2015-30) are rather similar between GLENS and MacPDM and not significantly greater under GLENS as may be suggested by the impact of reduction in transpiration by vegetation (Dagon and Schrag (2019) and GLENS used very similar models, CLM4 and CLM4.5 respectively).

Another likely source of differences in the response between GLENS/CLM4.5 and MacPDM is the method employed to calculate evapotranspiration. Even within a single hydrological model (MacPDM), the equations for potential evapotranspiration can have a large impact (Gosling and Arnell, 2011). The modelling by MacPDM in this comparison with GLENS

used the Penman-Monteith equation to calculate PET. Gosling and Arnell (2011) found greater variability globally when the Penman-Monteith method was used in validation of the model with observed flows for 50 catchments. In contrast to the Priestley-Taylor method, Penman-Monteith was shown to produce less runoff in drier catchments and more runoff in wetter catchments. Although not directly interpretable in this way, this does suggest a potential reason for the greater amplitude of change in future runoff under MacPDM than GLENS - if the method of evapotranspiration calculation is more responsive to wet and dry conditions.

Figure 2.3 depicts differences in mean annual total runoff between modelled and observed values. In addition to the GLENS and MacPDM models and observed GRDC streamflow, the GRUN 0.5° gridded observed dataset was included to allow interpretation of how the gridded nature of the modelled data may be confounding results. It can be seen that in general the GRUN data agrees more closely with the GRDC observed flow than either of the models. However, there are still reasonable disparities for some catchments, which does indicate that the gridded nature of the data, or at least the differences between comparing gridded runoff totals and observed streamflow, is having some influence on the results.

On the whole, however, even though the magnitudes projected can be quite different, the general trends in catchment runoff are rather similar for GLENS and MacPDM; particularly in the direction of change in response to either climate change or solar geoengineering forcing. This suggests that despite differences in absolute magnitudes and amplitudes between the two models, to some extent they are responding in the same way to the same input forcing data. This agreement in response is reassuring in so much as that even if there is uncertainty in the absolute values and magnitude of change, the direction of change is more reliable.

A marked exception to this model agreement however, is the clear inaccuracies from GLENS modelling, arising from the overestimation of peak spring flows in cold catchments. Catchments in which MacPDM often quite closely matches the observed streamflow for. This overestimation of freshet by GLENS can be seen in Russian and North American catchments and suggests one reason for the general overestimation of annual runoff by GLENS. Possibly differences in MacPDM's more simple per degree day treatment of snow melt and GLENS' more complete treatment of the energy balance is leading to these large discrepancies. However, the response is confusing as CLM4.5 was felt to represent snowmelt well, at least much better than glacier melt. Often, the overestimation of spring melt

(and other instances of overestimation) by GLENS is balanced out by underestimation for other times in the year, resulting in the overestimation at the annual scale being less pronounced than would be from looking at the spring months alone.

However, in other instances, GLENS much more correctly replicates observed streamflow than MacPDM. For example, the observed seasonal trend for the river Xingu is well matched by CLM4.5, however is severely underestimated by MacPDM. Guimberteau et al. (2014) find that the inclusion of multiple soil layers (as is true for CLM4.5 but not MacPDM) improves the evapotranspiration and runoff projections during the dry season for the Xingu catchment in the ORCHIDEE model. This is interesting, and highlights the importance of model structure, particularly when streamflows are low, but is unlikely to be able to explain the different model responses we see from GLENS and MacPDM.

A clear theme in the results is the poor representation of dry catchments by either the GLENS or MacPDM model. This is something that has often been acknowledged in hydrological models. Gosling and Arnell (2011) found, for previous model testing of MacPDM (in common with other GHMs, e.g. WBMPlus (Fekete et al., 1999) and VIC (Nijssen et al., 2001)), that in very dry catchments all model simulations overestimated annual runoff. The same response is seen in the GLENS land surface model (CLM4.5), indicating that the positive bias in dry catchments is more common and widespread to models than just GHMs, possibly indicating fundamental misrepresentation of some hydrological processes.

There is, however, another explanation. Neither MacPDM nor GLENS take account of human interventions in the system, which, when considered, have been shown to improve model simulations (Veldkamp et al., 2018). The response of greatly overestimating streamflow is not exclusively applicable to truly dry catchments. The Chao Phraya which flows through 30% of Thailand, which receives moderate rainfall - between 1,100 and 1,600 mm annually, is not especially dry. However, the basin has seen huge human influences over the course of the 20th and 21st century. Increases in population have led to the construction of multiple storage dams along its stretches and many irrigation canals have been built to service huge areas of irrigated agricultural land. The degree of water consumption means the system of the Chao Phraya is "closing", with most of the water flow being abstracted for some means and resulting in minimal flows out of the catchment during the dry season (Molle, 2002). As the observed GRDC streamflow is from the most recent time period, these effects will be clearly seen in the recorded river levels, accounting for the disparities between observed and modelled values (which do not take account of these modifications).

The abstraction from other rivers in dry (or seasonally dry) regions which are densely populated likely goes some way to helping explain the vast underestimation of river flow by models which do not include this information.

Similarly, it is likely that instances of large differences in the amplitude of modelled and observed values, for example the St. Lawrence river in North America, can also be explained to some extent by the modification of flows. The observed streamflow for the St. Lawrence is rather constant throughout the year, particularly when contrasted with the modelled projections. Other rivers which display a similar pattern include the Churchill and Winnipeg, both also in North America. The St. Lawrence river is fed by outflow from Lake Ontario which, since the construction of the Moses-Saunders dam (1958), has been controlled. Further regulation of river flow also occurs due to the creation of a series of channels and locks (St. Lawerence Seaway), which make the river navigable to large ships (Hudon et al., 2010, Boyer et al., 2010). This modification of flow was not included in the GLENS or MacPDM modelling.

When MacPDM and GLENS are compared using their projections in change to mean annual runoff from the baseline (2015-30) to years 2050-70, for both the RCP8.5 and SG scenarios, remarkably the percentage changes predicted are pretty similar. This can either be interpreted as both models correctly interpreting climate signals, or that these input signals are so strong that they manifest themselves clearly in the modelled output or it can be seen as a possible example of model equifinality, where multiple modelling methods reach the same correct conclusion, regardless of the "correctness" of the approach.

Differences between the modelled projections for RCP8.5 and SG are not altogether that clear when examining catchments, nor that consistent within hydrobelts. In general, the magnitudes of change in monthly peak and minimum runoff and in annual total runoff from the baseline are lower under solar geoengineering than the climate change scenario. However, this is not the case when considering changes to amplitude of monthly runoff across the year, which are usually just as great under SG as RCP8.5. One noticeable difference in the response between RCP8.5 and SG is the earlier shift to peak runoff from snowmelt in cold catchments. This earlier timing of freshet is something that is already being observed under current climatic warming (Hodgkins and Dudley, 2006). The fewer changes in month of peak and minimum runoff under SG than RCP8.5 implies that solar geoengineering can generally preserve at least these aspects of the climate signal, and the fact that this is true for both GLENS and MacPDM gives greater confidence in the response.

It was noted that amplitudes projected under MacPDM were on occasion quite extreme (sometimes more than 100% increase) and almost always saw greater percentage changes than under GLENS. This suggests that MacPDM is more sensitive and responsive in monthly changes in inputs than GLENS is. As well as possibly arising from the method of evapotranspiration used (mentioned above), further potential explanations may lie in the more simple structure of MacPDM which maybe cannot hold a memory for previous events in a way a more complex model (for example one including more soil layers) can, as well as the absences of dynamic vegetation in MacPDM can account for this. The results must be a factor of model structure, given the two models respond in different ways to the same forcing, however it would be hard to go much beyond this speculation without thorough hypothesis testing with control over model structure limiting the number of simultaneous changes in the model.

Cheng et al. (2019) find, in their analysis of multiple hydrological variables, mean global total runoff to be reasonably maintained at baseline present day levels under GLENS, whilst runoff is seen to increase from now until 2100 under RCP8.5. Soil moisture in the top 3.8m is also shown to remain at roughly present day levels, with this seen to decrease by 2100 under RCP8.5. There are, however, considerable differences when examined by region, with notable responses being a reduction in 3.8m soil moisture over India, Northern China and Northern Africa, whilst the reverse is seen, with increases under RCP8.5. The converse signal (increase in soil moisture under SG and reduction under RCP8.5) can be seen for Western Europe, Central and Southern US and Australia, with the Amazon seeing decreases in soil moisture and Western Russian seeing increases in soil moisture under both scenarios, although in both cases to a lesser extent under SG. They acknowledge how these regional changes arise due to the GLENS modelling aiming not only to maintain a different variable (temperature and not anything hydrological) but to do this at the annual scale (Cheng et al., 2019).

Figures 2.23 - 2.26 show that SG deviates less from the baseline than RCP8.5 in the majority of instances. Northern Dry catchments see the largest change and are the only location where MacPDM and GLENS greatly disagree in their sign of change, with huge decreases to runoff under both RCP8.5 and SG for MacPDM, and less extreme but mostly increases in runoff for GLENS. The reduction in soil moisture seen in Cheng et al. (2019) over Northern Africa under SG is in agreement with the findings from MacPDM here, although Cheng et al. (2019) project increases under RCP8.5 whilst MacPDM projects decreases for RCP8.5. As explained above, GLENS sees the reverse trend to MacPDM, projecting increases in runoff. Soil moisture and runoff should not be conflated however

as they respond differently to climate forcings. Increases in runoff in Boreal catchments is again corroborated by increases in soil moisture for Western Russian, but there is less change to runoff than to soil moisture. Reduction in runoff over Central Asia under SG is more pronounced under MacPDM than GLENS, but is in agreement with soil moisture changes (Cheng et al., 2019). Increases to soil moisture in Western Europe, Central and Southern US and Australia under SG are all seen for runoff from MacPDM and GLENS modelling, with this increase particularly pronounced over Australia. Decreases in soil moisture over the Amazon under SG are not really replicated for runoff, with Equatorial South America seeing little or only small changes, the decreases in runoff are larger under RCP8.5. Overall, these results show that the sign of change in response of future runoff to either solar geoengineering or climate change is highly dependent on the specific region being discussed. This highlights the need for more regional research but also the challenges that will be faced in trying to reach global agreement on the best course of action when some areas are projected to gain from solar geoengineering whilst in other areas it may worsen climate impacts in comparison to climate change.

It is well known that inter- (between model) and intra- (within model) model uncertainty exists within model types (e.g. GCMs) and this is often examined in studies through use of multiple models and ensemble runs of the same model, but Haddeland et al. (2011) also highlight that variability in projections from different models types is also a large area of uncertainty and impact studies of climate change should consider use of model types other than solely GCMs if we wish to capture more of the uncertainty in the modelled world. This is particularly important in emerging fields such as the study of SG because the relative youth of the field means much fewer models and applications are available and there is a tendency to only interpret GCM outputs.

Despite some clear trends that have emerged in this research, the interpretation of differences between runoff projections from the GLENS and MacPDM modelling is often unclear and, as outlined earlier in this chapter, it would be largely impossible to pinpoint exact reasons for these differences which arise from differing model structure; as far too many components vary between the models (Clark et al., 2011). GLENS, even with the more detailed and possibly comprehensive treatment of hydrology in CLM4.5, is not shown to out perform MacPDM in all instances, in fact sometimes more poorly replicating observed values. This should be remembered if ever the assumption is made that a more complex model equals a better model. In actuality, all models are merely the product of current scientific understanding, often guided by the perceptions and even biases of the modeller. They should be used to guide our comprehension of how systems may change

in the future, for we have nothing else to go on, but it should always be remembered that their outputs are possible projections, not prophecies.

Finally, as undoubtably is going to be stated many times throughout this research, the findings of this chapter are entirely reflective of the specific model scenarios that have been used. Whilst the GLENS modelling, in its attempt to meet multiple climate objectives at the same time and using multiple non-equatorial locations, is some of the most sophisticated solar geoengineering modelling we have at present, great efforts should be made to examine as many realistic scenarios of SG as possible; in the hopes that we may find any potential flaws and issues ahead of deployment (if it were to occur). Recent research (Visioni et al., 2020), has indeed uncovered flaws in the climate responses to stratospheric aerosols required for more even cooling of the planet. A large limitation of injecting stratospheric aerosols at the equator is the unequal cooling that results; undercooling the poles and overcooling the equator. GLENS addressed this through multiple extra-equatorial injection locations. However, a fundamental requirement for this approach to be effective is the stratospheric polewards transport of the sulphate aerosols. Visioni et al. (2020) find that stratospheric heating induced by these aerosols can, in fact, block them from reaching, and subsequently cooling the surface of, the poles. This should again encourage caution in overstretching any findings of this research beyond the specific model setup and inherent modelled and imperfect nature of the results. We do have natural analogues to solar geoengineering (volcanic eruptions) which provide indication of short term effectiveness, however the usefulness is limited when it comes to understanding other possible aerosols (e.g. calcite) or longer term effects. Kravitz and MacMartin (2020) highlight how there are still a number of uncertainties (and these are just the known unknowns) within stratospheric aerosol geoengineering, which must be addressed in order to improve confidence in the technology. For example, stratospheric processes involving aerosol growth and sub-grid scale particle mixing, as well as is in the climatic response and subsequently potential impacts.

Despite the fact that at times MacPDM is shown to produce better agreement with observed river flow, overall the model tends to underestimate rather than overestimate runoff. GLENS, on the other hand, more frequently overestimates runoff and, even though there appears to be a bias to overestimate or falsely project high spring melt which is not seen in the GRDC observed streamflow, this is seen as the favourable direction of bias. This research examines minimums and extreme low runoff. The tendency of GLENS to not overstate these values and in fact often underestimate them, therefore, is seen to allow more conservative projections of drought runoff and water scarcity (the subject of the

following two chapters). When there is so much uncertainty surrounding not only the possible scenario of solar geoengineering used for any future deployment, but also in the modelling itself, it seems unwise to falsely inflate potential impacts, especially if these findings are extrapolated to solar geoengineering research as a whole and not preserved within the context of the current scenario. In addition to this, the GLENS modelling involves very extreme cases of climate change (RCP8.5) and solar geoengineering (offsetting all temperature rise). This is necessary when studying climate responses, as a sufficient signal-to-noise ratio is required in order to interpret the overall climate response on top of normal climatic variability. However, as others have said, this is less justifiable in impact studies, where there is greater danger of the findings being misconstrued. For this reason, the focus has been on middle of the century projections (2050-70), when the effects are less extreme.

2.5 Conclusion

This chapter has examined differences in model projections that arise when an "offline" and "online" model is used to simulate hydrological processes, forced by the same climate changes. Two scenarios of future change, climate change and solar geoengineering, were used to explore how each of the models may impact the scenario results differently. General conclusions are that neither model clearly outperformed the other in replicating observed streamflow, and that in general the "online" model, GLENS, tended to overestimate streamflow, whilst the "offline" model, MacPDM, more frequently underestimated values. The greatest degree of disparity in all of the modelling was seen to be between the two models used, and overall both models tended to project the same direction of change for the future scenarios of RCP8.5 and SG. This work supports the well understood issue of model uncertainty and the need not only to model different scenarios of solar geoengineering but also to use different models to do this. It was challenging and often times impossible to discern the specific model attributes which were driving the differences. However, it is likely that the different natures of the models, with the climate model being focused more on an energetic perspective and the hydrological model more so on a water balance approach, will influence the results through the different methods of calculation used in each of the approaches. The large differences between model outputs found in this research suggests that future controlled experiments looking at how small perturbations in model structure can impact solar geoengineering projections would be of great use.

Chapter 3

Drought Runoff under Solar Geoengineering

3.1 Introduction

Drought, like flooding, is a phenomenon of the extremes. Unlike flooding however it develops slowly over time (Van Loon, 2015), often making it harder to monitor and predict the onset of an event. It can be loosely defined as a deficit of water when compared to normal conditions and can have many drivers and exacerbators, be that natural, for example meteorological or hydrological, or human induced, e.g. through population stress or overconsumption. Often, it is a combination of these factors and the exact drought signal is unique to each location; another characteristic which can make study of drought challenging, particularly at the global scale. Climate change is projected to increase both the longevity and severity of droughts in different regions of the globe over the coming century. The IPCC's special report on extreme events (Field et al., 2012) expressed medium confidence in the increased intensity and duration of droughts in some regions, most notably West Africa and southern Europe, whilst acknowledging that in others (e.g. northwestern Australia and central North America) the reverse has occurred with droughts becoming less extreme. Medium confidence is also had in the intensification of droughts during the 21^{st} century from some localities and seasons, specifically southern, central Europe and the Mediterranean, southern Africa, central North America, Mexico, Central America and northeast Brazil. However, the dependence of drought signals on individual model projections and the method of calculation used, mean that low confidence in future drought change exists in other parts of the world.

It is often posited that some solar geoengineering approaches will weaken the hydrological cycle (Tilmes et al., 2013), reducing precipitation, and it would seem to follow from this that droughts would therefore worsen under SG, at least in some locations. However, as we have previously discussed and explored, the situation is far more intricate. It is likely that different regions will see quite different effects of a changing climate under either climate change or solar geoengineering and most importantly the projected outcome of any solar geoengineering experiment is entirely dependent on the specific scenario used. Whilst it is true that current approaches to SG with stratospheric aerosol geoengineering cannot fully correct for temperature and precipitation at the same time (Irvine and Keith, 2020), as well as the present focus of experiments being to adjust for future temperature change (therefore lowering precipitation), this does not have to be the case; a reduction in precipitation is not intrinsic to SG. The GLENS experiments see smaller changes in precipitation in comparison to more traditional equatorial injection approaches thanks to the multiple and adjustable injection locations.

Impacts from extremes of climate are often when humans and all life on earth feel the effects of change most keenly. For this reason, it is of great interest to understand how extremely low runoff, here termed drought runoff, will be affected under the GLENS scenario of stratospheric aerosol geoengineering. As with the previous chapter which compared runoff directly outputted by GLENS with that generated by the hydrological model MacPDM (forced with the corresponding climate inputs), the time period 2050-70 will be used to examine how drought runoff differs under future projections of climate change (RCP8.5) and SG. This is so that the effects of SG are not overstated; given that this research is using a scenario with an extreme level of temperature offsetting through SG.

3.1.1 Types of drought and drought propagation

Drought can be grouped into four main categories: meteorological drought; hydrological drought; agricultural drought and socioeconomic drought (NCEI, 2021, Mishra and Singh, 2010). Other classifications and names have been used (for example soil moisture, groundwater), but the main distinguishing factors between the groupings are in what part of the earth system or which sectors/actors are the effects of the deficit in water seen. Meteorological drought refers to an insufficient amount of precipitation for a given place and time when compared to average conditions. Agricultural drought, also termed soil moisture drought, occurs when soil moisture levels are reduced, often resulting in crop decline or failure. Along with a deficit of precipitation, evapotranspiration can often play a part in agricultural drought. Hydrological drought occurs when surface runoff, subsurface runoff and streamflow fall below levels required to maintain normal conditions or activities (e.g. navigation) and can follow on from meteorological and soil moisture drought. Finally, socioeconomic drought is the point when drought development leads to an inability to meet the supply of water required for socioeconomic activities.

It is important here to make a distinction between drought and water scarcity (Van Loon and Van Lanen, 2013). Whilst the two are intertwined, drought is very much driven by natural forces; whereas water scarcity arises from the unsustainable use of a water resource, be that because there are too many people for the water supply in that area or because there is too much water being abstracted for residential, industrial and agricultural use. Drought and water scarcity can both occur at the same time, amplifying the overall impact on the environment and society. However, whilst water scarcity can in some cases be avoided through more careful management, drought is an unavoidable natural hazard, the effects of which, like all natural hazards, can be made worse by human actions (Van Loon and Van Lanen, 2013).

The absence of water seen during a drought can manifest itself in many forms. It is often instigated through a lack of precipitation, which may then translate, if the paucity is long or extreme enough, into reduced soil moisture, streamflow and groundwater. If this occurs in conjunction with increased water abstraction for growing crops, supplying water to industry/manufacturing or for drinking water, then these pressures can further exacerbate conditions and this decline in the available water can lead to more extensive and severe drought. Although an oversimplification of the process, drought can be seen to propagate through the system from precipitation through to runoff, soil moisture and streamflow with the signal eventually being seen in the groundwater levels (Van Loon, 2015). Exact means and routes of propagation are unique to each locality, its geology, soils and catchment characteristics, resulting in different timings and responsiveness in the drought signal of each of these main components of the hydrological system for which drought can be measured. The rate of change and transition into drought conditions can roughly be seen to slow with the propagation through the system, for example meteorological drought can develop over a relatively short period of time, whereas groundwater drought is determined more by occurrence of longer term multi-annual cycles than seasonal change. For example, in the UK most groundwater droughts have been found to coincide with the North Atlantic Oscillation's negative phase of the 7 year cycle, with weaker storms and reduced precipitation (Rust et al., 2019). However, the full picture of drought cannot fully be determine solely from precipitation trends. Local characteristics and responses as well as other aspect of climate, particularly temperature and evapotranspiration, must also be considered to understand hydrological drought (Van Huijgevoort et al., 2013). For this reason, many choose to examine hydrological drought as this encompasses more extensive drought occurrence, likely having greater impact on the environment and society.

Hydrological drought can be further subdivided into different types based on the characteristics, timings and driving forces (Van Loon, 2015). The prevalence of these different hydrological drought types varies across regions depending on what initiates and perpetuates the drought conditions. These forces can generally be considered to be precipitation or temperature led. The most obvious is classical rainfall deficit drought which is solely controlled by lack of precipitation and which can occur anywhere at anytime. Further hydrological drought types which are instigated by a lack of precipitation are rain-to-snow-season drought and wet-to-dry-season drought both of which see a dearth of rainfall in the rain and wet seasons, respectively, which then continues into the subsequent season. Temperature is the main driver and controller of cold snow season drought in which lower than normal snow season temperatures can result in 3 subtypes, A - in which the snow

season starts too early, B - when the persistent cold conditions delay the snow melt and C - when there is no recharge to the system. Conversely, if the snow season is warmer than usual, warm snow season drought can occur, either through subtype A - which sees snow melt beginning too early or B - which occurs alongside a lack of rainfall and results in an absence recharge to the system. Further cold climate droughts include snowmelt drought in spring (where snowmelt is below average conditions either due to high temperatures meaning insufficient snow accumulated over the winter or that there was not enough snow falling in winter) and glaciermelt drought during summer (in which cooler summer temperatures prevent glaciers from melting). A final category of hydrological drought is termed composite drought, and refers to the collection of a succession of drought occurrences over time. It is clear from examining the drivers of each of these types of drought that the likelihood of each will change with future climate change through the general increase in temperatures and more variable precipitation. Alongside the drivers of precipitation and temperature, evapotranspiration, although unable to generate droughts alone, has been found to exacerbate hydrological drought (Teuling et al., 2013, Joo et al., 2017).

3.1.2 Drought indices

Different methods for the study of drought are appropriate in different contexts, if you are a water authority trying to predict if a drought event will occur that year or if water levels in the river will fall below navigable conditions, different approaches are required than for study of longer term future projections of global drought prevalence under different climate change pathways. The cause and development of droughts can vary greatly depending on the specific catchment conditions and characteristics, the location in the world and the particular seasonality of the area in question. Drought is also very complex in terms of its dimensions, it can be defined in terms of duration, magnitude, intensity, severity, geographical extent and frequency/return period (Zargar et al., 2011). Given this, along with the "creeping" nature of drought development, it makes devising a single and complete metric to study the phenomenon fully at the global scale an improbable aspiration. For this reason, an abundance of complementary metrics have been developed for the analysis of drought. There now exists more than 100 indices used to define and quantify drought (Zargar et al., 2011), although many follow similar methods or are adaptations of prior indices, and so only the most widely used will be discussed here.

One of the most widely used indices is the Standardized Precipitation Index (SPI) (McKee et al., 1993, Edwards and McKee, 1997). Long term cumulative precipitation records (e.g. monthly summed) are fit to a probability distribution chosen by the user (often the gamma

distribution), which is then standardised through a transform to the normal distribution. Values of the SPI relate to the number of standard deviations a given cumulative precipitation amount lies from the mean conditions and can therefore indicate conditions which are drier than would be expected on average (Lloyd-Hughes and Saunders, 2002). As the SPI is normally distributed, values between -1 and 1 are considered near normal and given 95% of values fall within 2 standard deviations, SPI values below -2 are considered extremely dry (Hayes, 2000). The precipitation inputs can be accumulated for different periods of time (taking the monthly mean of that period - e.g. DJF), meaning the SPI can be computed for different lengths of time, typically 3 (SPI-3), 6 (SPI-6) or 12 (SPI-12) months (Keyantash, 2018). Computation is applied individually for each month or period, allowing for differences in seasons to be considered (Lloyd-Hughes and Saunders, 2002). The SPIs strengths lie in its easy interpretation and straight forward method using more readily available variables (unlike the Palmer Drought Severity Index (PDSI) which requires water balance calculations), along with its standardized nature meaning comparisons can be drawn between different locations. However, being a standardized metric it has been criticised for its inability to compute magnitudes and severity of droughts, something that is important when trying to live with and manage a water resource rather than studying purely for academic purposes. Another factor related to this is that given it is based on a probability distribution, extreme droughts have the same probability of occurring for all regions of the world when examined over the whole time period, therefore meaning global analysis of areas more prone to drought cannot be identified over these extended periods (Lloyd-Hughes and Saunders, 2002). It also lacks a complete treatment of the nature of drought, focusing solely on precipitation, and is sensitivity to the time period chosen for the analysis. Further standardized metrics have been developed based on this approach, encapsulating different parts of the water system, for example the Standardized Precipitation Evapotranspiration Index (SPEI) (Vicente-Serrano et al., 2010) and the Standardized Runoff Index (SRI) (Shukla and Wood, 2008). These indices address one large criticism of the SPI, the lack of consideration of temperature change, which is included through ET. This is particularly important when using the indices for projection of future drought under climate change and associated temperature rise. The common nature of these methods also means that they can be used to study drought propagation.

Another metric which has been extensively used over the last 50 years is the PDSI (Wells et al., 2004), which uses a water balance to assign values to the condition from extremely wet (>4) to extremely dry (<-4). It has received criticism for its inability to be used to study large spatial areas with very different climatologies as the results, being sensitive

to specific location and derived from a method which behaves differently under various climate conditions, are not comparable. In addition, Alley (1984) explains the limitations of the method due to a number of assumptions which are made, regarding aspects such as potential evapotranspiration (PET), soil moisture capacity, the generation and timing of surface runoff and the absence of snowmelt, use of 9 averaged climatic groupings and the method of transitioning between wet and dry conditions. Nonetheless, Palmer was the first to try and quantify drought severity, also defining a beginning and end to the event, and the metric has been shown to perform reasonably well at identifying and characterising drought on longer timescales (Dai, 2019). Wells et al. (2004) worked to improve the shortcomings of the PDSI by creating a self-calibrating PDSI, which was shown to produce improvements in the metric's ability to assess and compare results across different regions.

Other well established popular methods are Percent of Normal, Deciles, Effective Drought Index, Crop Moisture Index, Surface Water Supply Index and Normalized Difference Vegetation Index (Zargar et al., 2011, Mishra and Singh, 2010). They focus on different aspects of the drought space, from meteorological to soil moisture to hydrological.

All drought indices have received criticism for one reason or another, however providing consideration of the limitations of each is acknowledged and the information that they can actually convey is understood, they can provide very useful indications and warnings of drought occurrence and conditions.

3.1.3 Threshold methods and low flow analysis

Methods to determine when water levels (be that in runoff, reservoirs, streamflow or groundwater, to name a few) fall below a set threshold are also used to indicate drought or at least the potential for drought-like conditions. Percentiles of the exceedance probability are often used, usually falling between Q95 and Q70 (Van Loon, 2015), which denotes the level exceeded 95% to 70% of the time. Thresholds can be fixed in time or vary (e.g month to month, season to season). When examined for a given water resource, a deficit volume of water based on the amount of water falling short of the threshold can also be computed, with recovery time also estimated base on the amount of time it will take to achieve sufficient surplus levels to counteract this deficit (Fleig et al., 2006). McCabe et al. (2017) used Q80 as the threshold to study drought occurrence using 3 month moving average runoff. When runoff fell below Q80 the area was considered to be in drought, with the period of drought ending when runoff levels exceeded Q80. Analysis of duration and frequency of drought was then undertaken.

In a study of low streamflow across Europe, Marx et al. (2018) used a threshold of Q90 at the daily timescale to assess the projected impact of various levels of climate change (warming of 1.5, 2 and 3 °C). They find that under increasing levels of warming (e.g. from 1.5 to 3 °C), the change in low flow values from the baseline period (1971-2000) are heightened and there is more robustness in the results. Low flows are shown to decrease under climate change for the Mediterranean, which is attributed to reductions in precipitation, whilst they are seen to increase in the Alpine and Northern areas of Europe (covering Norway, Sweden, Finland, Estonia, Latvia, Lithuania, and parts of Poland, Belarus and Russia), a result explained by alterations in snow accumulation. The global analysis of Van Huijgevoort et al. (2014) also found monthly discharge low flows (Q80) to increase in cold regions along with changes in the timing of the snowmelt peak. In addition to this, low flow values were shown to decrease with climate change in some of the driest regions (for example in southern Australia, the Zambezi and Chubut rivers), but little agreement existed in the direction of change of low flows in humid regions. Van Huijgevoort et al. (2014) warns how low flow is not always directly related to drought characteristics of duration and deficit, drought conditions could worsen even if low flow values did not change (this was true for some cold regions) and drought was projected to increase (around 65%) in more basins than low flow was projected to decrease (51%) (i.e. signalling drier conditions). They also acknowledge the influence of specific model projections on the results, for instances there was not a consistent trend in low flows for the Amazon region.

Van Huijgevoort et al. (2013) examine drought runoff using a combined drought identification method which consists of a threshold level method (Q80) and inclusion of consecutive dry period method, to better identify droughts in ephemeral systems. They find that drought events identified by different models can vary quite considerably and instead focus on the multimodel ensemble median and variability. The greatest differences between models were seen in dry regions, with reasonably large differences seen in cold regions, but greater agreement was found in regions of high runoff. Despite the variation between models, the ensemble median was able to identify major drought occurrence.

3.1.4 Current studies of drought under solar geoengineering

At present, given the relatively few numbers of modelling outputs for solar geoengineering scenarios, there are understandably correspondingly few studies of drought under solar geoengineering. Odoulami et al. (2020), also using the GLENS dataset, found solar geoengineering could roughly maintain the risk of extreme droughts in Cape Town, South Africa to present-day levels, unlike under climate change for which the risk is increased. They

also found precipitation levels remain much less altered from present-day under SG than under RCP8.5, which corroborates with the finds in Chapter 2 which sees smaller changes to annual runoff under solar geoengineering, but decreases under RCP8.5 for the mid latitude africa hydrobelt which covers much of the study area. The 2015-2017 drought in the Western Cape Province, which was brought about by a 3 year deficit in winter rainfall, was widely reported and referred to as "Day Zero" drought, as the population of Cape Town anxiously anticipated the day when the water supply would be entirely depleted. Thankfully, through careful management that day was avoided, but it has been projected that the probability of a drought of this magnitude will greatly increase in the future under climate change, from 0.7% at present to 80% in 2100 under the most extreme scenarios (Pascale et al., 2020). Around 80% of the precipitation that falls over the Western Cape Province arrives during the southern hemisphere winter as part of cold fronts, therefore Odoulami et al. (2020) also examined changes in these patterns, finding stratospheric aerosol geoengineering could alleviate some of the future changes under RCP8.5 which are projected to increase risk of severe drought. As this particular drought event was driven by exceptionally low precipitation, the method employed by Odoulami et al. (2020) took a probabilistic approach to examine extreme precipitation event attribution. Defining the event as the 3 year magnitude of precipitation between 2015 and 2017, they found that the return period of a present-day 1 in 100 year event became a 1 in 6 year and 1 in 75 year event under RCP8.5 and SG respectively.

Whilst promising for this region, it is unlikely that these benefits will be seen in all areas, particularly in parts of northern and equatorial Africa and sub tropical and mid latitude Asia, which see increases in annual runoff under the GLENS scenario of RCP8.5 but not SG (see Chapter 2), although clearly this is not a linear relationship and assumptions about drought changes cannot be made purely from annual runoff. Indeed, Da-Allada et al. (2020) did find under the GLENS modelling, using 2050-2069 as the future reference period, changes in the West African summer monsoon for some regions. They observed declines in monsoonal precipitation in the southern Sahel and Western Africa under solar geoengineering, which are areas that see increase in precipitation under RCP8.5. They attribute this precipitation decline to northward shift of monsoon rains with a changing monsoon circulation that arises from the decreased thermal gradients induced under the scenario of solar geoengineering. Whilst this does not explain whether droughts would become worse under these conditions (and to any extent most likely much less than scenarios of equatorial stratospheric aerosol injection which lead to even more uneven temperature changes), the West African summer monsoon does dominate as the main source of precip-

itation in the region and changes to it would clearly impact on society and the environment there. Earlier analysis (Haywood et al., 2013), using a different scenario of solar geoengineering, warns that the method of deployment is of great importance. If aerosols were to be injected solely in the Northern Hemisphere this would increase Sahelian drought, and it is shown that Northern Hemisphere volcanic eruptions have preceded real occurrences of Sahelian drought. Whilst the work cites how injection solely in the Southern Hemisphere would likely lead to much wetter conditions in the Sahel, this specific modelling case projects significant drying over parts of Brazil, highlighting the complex nature of the problem and the challenges with devising a globally beneficially method of solar geoengineering.

Another study using the GLENS dataset examines changes in terrestrial drying trends across the Americas (Xu et al., 2020). They make use of an aridity index (P/PET) as well as analysis of other climate variables instrumental in the assessment of dry conditions (temperature, precipitation, soil water, P-ET and PET) to explore relative changes in conditions at the end of the century under scenarios of climate change, solar geoengineering and carbon capture and storage. The P/PET indicator was chosen above use of another more complex aridity indicator as the focus of the analysis was to examine large scale changes in two very different scenarios (RCP8.5 and SG), a logic which is also followed in this chapter; however, the justification here is around ensuring the outputs are more interpretable and comparable. It should be remembered that aridity and drought are not the same thing, with aridity describing the general climatic conditions and drought distinguishing those occasions when there is less water than under normal conditions for the time period of study. When examining the whole land area of the Americas, P/PET is maintained and even increased from present-day under the GLENS solar geoengineering scenario, signifying wetter terrestrial conditions, even with a slight decreases in precipitation, in direct contrast to conditions under RCP8.5 which sees continued decline in P/PET. This highlights what is widely understood, that looking at precipitation trends alone will not give the full picture of drying conditions, as reducing evaporation by a larger amount than the precipitation could actually cause a wetting of conditions to occur. The response however is more nuanced when considering results for 4 main regions of the Americas: western US, eastern US, southern Brazil and northern Brazil. In all regions carbon capture and solar geoengineering can similarly offset the drying projected under climate change, except for over the Amazon (northern Brazil), where only carbon capture is effective in inhibiting the drying relative to present-day. Here, stratospheric sulphate injection can only offset some of the drying, resulting in future conditions still being quite a

bit drier than present-day. This is explained as resulting from a shift in precipitation from the deep to sub tropics causing local decline in precipitation which is not accompanied by as large a reduction in PET (argued to be due to more cloud coverage over the tropics or because of vegetation differences), therefore resulting overall in drier conditions than at present. When the results of carbon capture and solar geoengineering are normalised by the amount of global temperature rise they offset, solar geoengineering is found to be less effective than carbon capture, although as expected the response is initially faster under solar geoengineering.

Curry et al. (2014) look at how various extremes change under the GeoMIP scenarios of solar geoengineering (G1 - solar dimming/insolation reduction) and climate change ($4xCO_2$), including change in number of consecutive dry days. Under the G1 scenario very few areas of land see a statistically significant difference, the exception to this are large parts of Europe (but not the Mediterranean) and western Russia (both which see modest increases in consecutive dry days of up to 3 days), southern Canada also sees some modest increases of up to 5 additional days of consecutive dry conditions compared to the baseline. The biggest changes in consecutive dry days arises over central Amazon and Tanzania with an increase in up to 17 additional days. Although less frequent, some decreases in consecutive dry days are seen, namely over southern Saudi Arabia and Egypt where decreases of as many as 23 days can be seen. The changes under the scenario of climate change are much more extreme, showing large increases in consecutive dry days (up to 30) for southern Africa, northwestern Africa, the Mediterranean, southern US, Mexico and Central America and eastern Brazil, with some significant increased change seen in coastal eastern, southern and western Australia. Decreases in number of consecutive dry days (by as many as 20 days) occur over large parts of eastern Russia and China for the scenario of climate change in comparison to the baseline.

3.1.5 Chapter Outline

It is very challenging to comprehensively assess the full impacts and occurrence of drought under future changing climate across the whole globe. As has been discussed previously in this chapter, there are many differing drivers for drought and drought propagation in different catchments (fast or slow response) and under various climates (e.g. monsoonal, arid, boreal). On the basis that a single drought metric which can encapsulate all of the important biotic and abiotic relevant characteristics of drought is unattainable, the use of a single drought metric has been avoided in this analysis. Instead a threshold level approach has been taken, examining changes in Q95 and Q80 runoff. By examining

changes in extreme low flows across the earth under a scenario of climate change (RCP8.5) and solar geoengineering (SG) and contrasting the response from each to a baseline period (2010-30), an overall picture of how each scenario may impact drought in the future can be gained. However, other drought metrics will likely project different results to those from analysing changes in the low flow, as low flow is not always indicative of drought conditions when calculated by other means (Van Huijgevoort et al., 2014).

3.2 Method

3.2.1 Extreme value analysis of monthly minimum runoff

To study how occurrences and magnitudes of extremely low runoff will change in the future under climate change and solar geoengineering, Extreme Value Analysis was conducted using the Generalised Extreme Value distribution. L-moments (Hosking, 1990) were used as the method of calculation, which can produce better results when using small sample sizes. Hosking (1990) found lower root-mean-square error when estimating the GEV distribution using L-moments in comparison to maximum likelihood estimation for sample sizes under 100. L-moments "are expectations of certain linear combinations of order statistics" (Hosking, 1990) and the first 4 L-moments can be used to estimate the mean, scale (analogous to the standard deviation), skewness and kurtosis of a distribution.

For each of the 38 catchments studied in Chapter 2, a timeseries of minimum monthly runoff each year was constructed for both the climate change and solar geoengineering scenarios and each of the ensemble members (3 full timeseries for RCP8.5 and 20 for SG). Monthly area weighted average runoff in mm was calculated across the gridcells for each catchment, from which the monthly minimum each year was deduced.

A 1 in 20 year return period, i.e. the magnitude of minimum monthly runoff which has a 5% probability in any given year, was chosen to represent extreme low minimum monthly runoff, being sufficiently infrequent to represent rare events but not so long that it could not be encapsulated in the length of the time series used.

In order for as many years as possible to be included in the analysis, so that the calculations were as robust as could be, a method was devised to run the Extreme Value Analysis (EVA) over the whole time period. This was permissible due to the timeseries first being detrended to remove the non-stationarity in the data, as stationarity is required for the EVA method. Figure 3.1 depicts how this was achieved. A spline was used to find the long term trend in the timeseries, this was subtracted from the data,

with the mean of the spline then added back in to put the timeseries back in the correct order of magnitude. The extRemes package in R was then used to calculate the 1 in 20 return period with 5 and 95% confidence intervals (fit_GEV = fevd(data, type="GEV", method="Lmoments"), ci(fit_GEV, return.period=20)). The only current method in the extRemes for estimating confidence intervals with the L-moment approach is to apply a parametric bootstrap (Gilleland and Katz, 2016). The stochastic nature of the output meant 100 iterations were run for each catchment and the mean of these values was taken forward. To assess minimums in EVA the negatives of the timeseries were taken to allow for maximum likelihood to be calculated. To return the outputs to the original scale, the negatives of the resultant return periods were calculated.

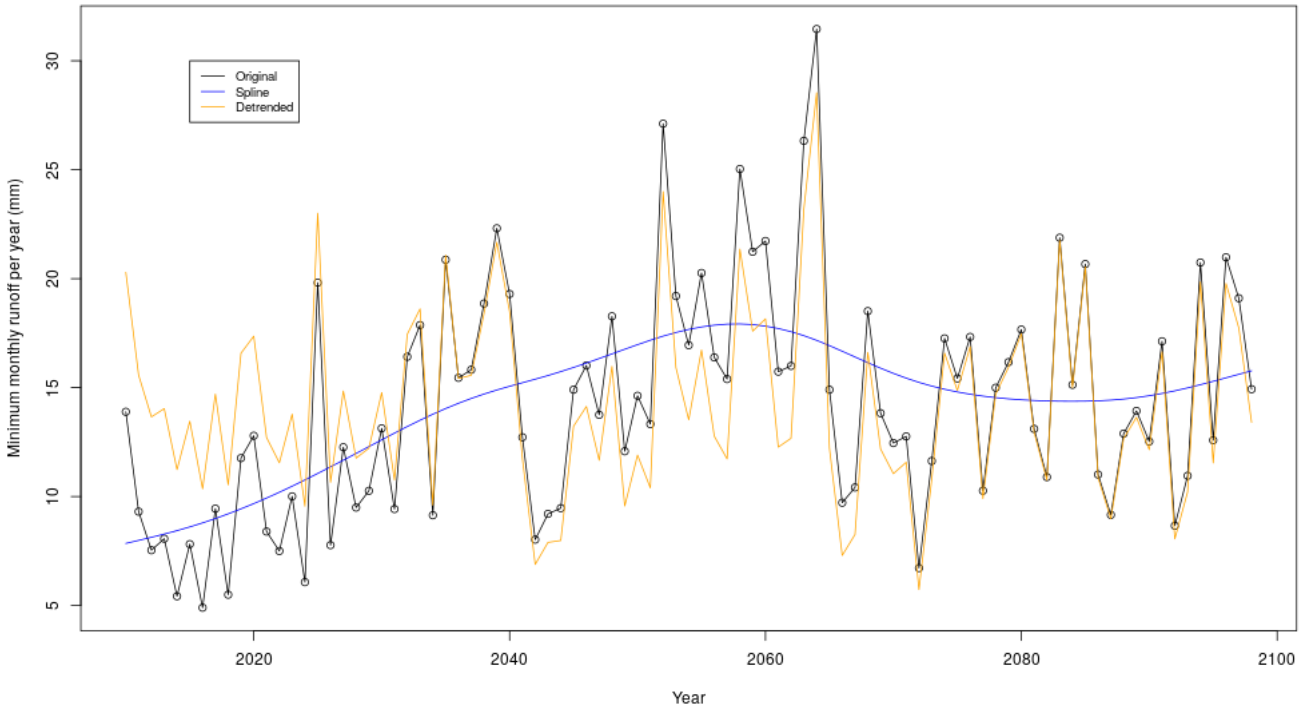


Figure 3.1: Example of detrended timeseries of monthly minimum each year.

To find the 1 in 20 year minimum monthly runoff value for the time periods of interest (2010-30 and 2050-70), the general signal of change across the years (which had been removed through the detrending) needed to be added back in, the mean of the spline was subtracted from the return level and the spline values were added back in. This was carried out by repeating the 5% probability minimum monthly runoff in a year (i.e. 1 in 20 return period), with the reverse of the detrending added back in to the data by subtracting the mean of the spline and adding the spline timeseries. For each 20 year time period the mean of these values was calculated.

Other research has looked at ensuring that the use of calendar years did not split the minimum low flow duration (for example from mid December to mid January), however this was not necessary or possible in this evaluation as the finest resolution of the data was by calendar month and therefore this information would not have been able to be deciphered. Whilst the low flow duration cannot be divided in this method due to the resolution, there is a chance that if a given season has exceptionally low flow, and say both December and January were very low, each month would constitute the lowest flow in their calendar year. However, other studies (Marx et al., 2018) found little difference in results when the years were defined by calendar or hydrological year.

3.2.2 Low flow statistics

The monthly low flow statistics (Q95 and Q80) were calculated per gridcell for each of the 21 year time periods - Baseline 2010-30 (20 ensemble runs), RCP8.5 2050-70 (3 ensemble runs), SG 2050-70 (20 ensemble runs). For soil moisture, percentiles of 20-11% have been considered moderate drought and 10-6% considered severe drought, with values between 5 and 3% seen to represent extreme drought and between 2 and 0% to represent exceptional drought (Andreadis et al., 2005). Therefore, the selection of Q80 and Q95, which cover moderate to extreme drought, seem to be reasonable thresholds for low flow to allow wider understanding of future changes in drought. In this work Q95 represents, for a given time period (here 21 years), the magnitude of monthly runoff which occurs at least 95% of the time across the whole time period. The percentage difference between the future scenario and the baseline ((FS - BL)/BL x 100) as well as the absolute difference (FS-BL) were calculated to compare how the scenario of climate change and solar geoengineering differ from the baseline. Other studies (Marx et al., 2018) have used daily values to compute a low flow value for each year, then taking the average across those years to give the low flow threshold for that time period. However, only monthly data was available for this study, and given there would be much less interannual variation in 12 values rather than 365, the whole time period was used to compute the low flow statistics.

Temporal aspects of drought should also be considered and whilst drought severity and length are not linearly related (Van Loon et al., 2014, Van Loon and Laaha, 2015), duration of time below the threshold does indicate worse drought conditions. Further analysis of low flow considered the number of consecutive months that fell below the Q95 and Q80 values for each gridcell. Results were summarised by hydroregion to allow interpretation of which areas may be more greatly affected. The values of maximum number of consecutive months below the threshold for each gridcell was calculated using the threshold that corresponded

with each scenario (baseline 2010-30, RCP8.5 2050-70, SG 2050-70) as well as using the baseline threshold to categorise low flow in the future scenarios.

3.2.2.1 Seasonality in low flow

The seasonality of the occurrences of low flow (below the Q95 and Q80 threshold) was attempted to be quantified using the following method:

1) For each gridcell, the number of months which fell below the low flow threshold was summed for each unique month (Jan - Dec) across the study years. For each scenario, the 12 values for each ensemble member (i.e. 20 ensemble members for SG) were further added together to give a total number of months for each unique month which fell below the threshold. For example, there may have been 68 Januarys for the Solar Geoengineering scenario in years 2050-70 which fell below the Q95 threshold for that gridcell.

2) These 12 values (1 per month) were then adjusted to be the proportion of all the months that they represent. For example, if 68 Januarys fell below the Q95 threshold and there were a total of 200 months for the whole dataset which fell below the threshold then the proportion of Januarys would be 68/200 = 0.34.

3) The standard deviation (s.d.) of these 12 proportional values was then taken to give a value of variation (here to be termed seasonality) in low flow across the year for each gridcell for the specific time period (2010-30 for the baseline and 2050-70 for RCP8.5 and SG).

4) As the proportions of months below the threshold have been taken, the maximum s.d. value (0.2886751) occurs when all of the months which fall below the threshold occur in 1 of the 12 months, i.e. vals = (1,0,0,0,0,0,0,0,0,0,0,0). The minimum s.d. is zero and occurs when all of the proportions for each month equal 1/12. For this reason, the values can be normalized into the range of 0-1 by dividing through by the maximum (0.2886751), where 0 represents no seasonality in the gridcell data - i.e. all of the months have the same proportion of low flow values, and where 1 represents extreme seasonality - i.e. 1 of the 12 months has all of the low flow occurrences in it.

5) Then to assess how the seasonality changes in the future, the normalized s.d. gridcell value for the baseline (2010-30) was subtracted from each future scenario (RCP8.5 and SG in 2050-70). These results could take a value in the range of -1 to 1, being -1 if the future had no seasonality (normalized s.d. = 0) and the baseline had extreme seasonality (normalized s.d. = 1) and being 1 if the future had extreme seasonality and the present

had no seasonality. In reality few values would exist in these extremes, with the changes being more subtle.

6) Gridcell differences in seasonality were then displayed based on hydroregion groups.

These future values of change in seasonality from the baseline can be interpreted as positive values represent an increase in the seasonality - i.e. low flows are more concentrated in specific months, and negative values show a decrease in seasonality - i.e. low flow values are more spread out across different months.

A potential draw back of this method is that it cannot distinguish, for example, between low flow only being in January and Febuary, v.s. only in January and July, when in the real world this would have a large influence on the continuation and impact of the low flow on the overall risk of drought. However, earlier analysis in the development of this method did examine the raw values of months below the threshold and it was seen that only rarely for any hydroregion were two distinct peaks in the month with most low flow values seen. On the whole either there was little seasonality where low flow had similar proportions for each of the 12 months or there was a single smooth peak. Only the Equatorial Africa and Northern Dry Middle Eastern hydroregions exhibited two clear peaks, with two slight peaks within an overall prolonged peak seen for Equatorial Asia, Southern Dry Australia and Southern Mid Latitude Australia.

3.3 Results

Figure D.1 depicts the standard deviation of daily precipitation within each year for the RCP8.5 and SG scenarios. It can be seen that the standard deviation by the end of the century is higher for the RCP8.5 scenario ensemble members than for SG, which would suggest that more extreme precipitation events occur under RCP8.5. In contrast the standard deviation under SG remains rather consistent from present-day to the end of the century, suggesting less change in the distribution of daily precipitation for each year and in the extremal values of precipitation. Whilst this does not conclusively tell us anything about larger reductions in low flows under climate change, it does suggest that future projections of RCP8.5 would be more likely to see larger decreases in precipitation (and thus low flows) than SG, which sees more consistent patterns to the end of the century. Solar geoengineering studies have indeed found this; Curry et al. (2014) in their examination of the GeoMIP models, find the duration of dry periods to be greatly increased under the climate change scenario for areas of the sub tropics, something that is not shown for the solar geoengineering scenario.

3.3.1 Extreme Minimum Monthly Flow

Figure 3.2 shows changes in the 20 year minimum monthly runoff return level under the baseline (2010-30) and two future (2050-70) scenarios of climate change (RCP8.5) and solar geoengineering (SG). A number of the 38 catchments haven't been included in the graph. Red, Winnipeg, Assiniboine, Churchill, Kolyma, Olenek, all had values at or extremely close to zero and the St. Lawrence river saw no difference between the scenarios. The Elbe exhibited the same trend as Rhine and Danube, as did Don when compared to Volga, and Lena when compared to Yenisey. There are a few main themes in the change to the 20 year return period; catchments where little significant change occurs, catchments where the direction of change in future low flow is the same under RCP8.5 or SG, catchment where the magnitude of change is similar under both scenarios and catchments where climate change increases or decreases the 20 year return period whilst SG sees smaller changes from the baseline.

In Boreal catchments, as well as a number of Northern Mid Latitude catchments (e.g. Fraser, Volga), a significant increase in the 20 year monthly minimum return level is seen under RCP8.5 for 2050-70 when compared to the baseline (2010-30). In some of these catchments (Yenisey, Volga, Amur, MacKenzie) the return level projected under the scenario of solar geoengineering is significantly lower than that under RCP8.5 and is much closer to the baseline value. Whilst in others (Severnaya Dvina, Saskatchewan, Albany, Neva) there is little difference between the projected increase in return level under the future scenario of climate change or solar geoengineering. The European catchments display a significant decrease in the 20 year minimum monthly runoff under RCP8.5 in comparison to the baseline, with smaller changes (not significantly different) under SG. Changes in many other catchments are not significantly different. Exceptions to this include the Amazonas and Xingu, both of which also see a significant decrease in minimum monthly 20 year return level under RCP8.5, with much smaller change under SG. Significant decreases in the minimum monthly runoff are also seen under RCP8.5 for the Rio Parnaiba and Orange catchments, with smaller change for the Rio Parnaiba under SG and little/no difference between the RCP8.5 and SG scenarios for the Orange catchment. However, as we know the model performs poorly in replicating observed streamflow for these catchments, interpretation of these results should be treated with caution. Similarly, although the minimum monthly runoff 20 year return level is significantly increased under RCP8.5, and to a greater degree under SG, for the Darling catchment, the model also does not show good fit to the monthly streamflow here.

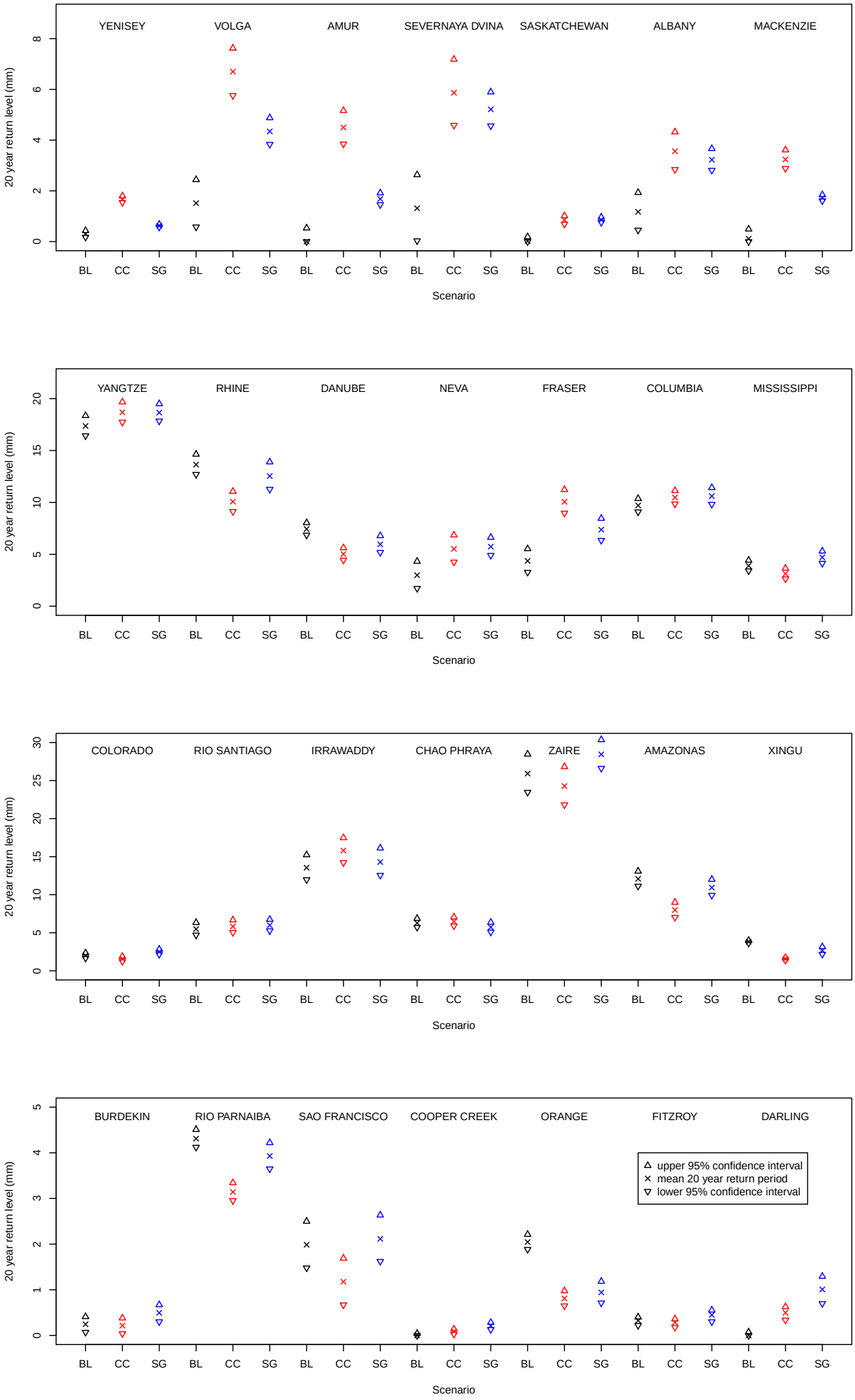


Figure 3.2: Results from the extreme value analysis showing the 20 year return level of monthly minimum runoff in each catchment, with comparison between baseline (BL) 2010-30 in black, RCP8.5 (CC) 2050-70 in red and Solar Geoengineering (SG) 2050-70 in blue.

3.3.2 Analysis of gridcell level low flow

It can be immediately seen from examining Figures 3.3 and 3.4 that a greater extent and magnitude of percentage change in Q95 monthly low flow can be seen under the future scenario of climate change when compared to the scenario of solar geoengineering. The absolute change (in mm) in Q95 from the baseline can be seen in Figures 3.5 and 3.6.

Figures C.1 - C.4 show the percentage and absolute changes in Q80, which exhibit a rather similar global pattern in directions of change to that of Q95. A notable difference is in the region of Indonesia, the Philippines and New Guinea where there are larger increases in percentage and absolute change of Q80 in southern New Guinea and central Indonesia which are not seen for Q95 and a general decrease in absolute change dominates in this region for Q95. This suggests that whilst the extreme low flow (Q95) is lower under RCP8.5, Q80 is higher than present-day, so there are fewer occurrences of the magnitude of low flow seen in the present (even if the most extreme values are even more extreme in the future). Present-day low flows are more consistent in value between Q95 and Q80, but in the future there is a steeper gradient in the exceedance curve at the low flow end. This would imply an increase in the general condition of low flows and whilst there is potential for more extreme dry conditions, these would likely be more short lived under future projections of RCP8.5.

Larger and more extensive percentage changes in Q95 low flow from the 2010-30 baseline values are seen for the future (2050-70) scenario of climate change as opposed to the less extreme changes seen under the scenario of solar geoengineering. Large areas of the Northern Hemisphere high latitudes see big percentage increases in low flow under RCP8.5, however there are a patches in central northern Russia and south west of the Hudson Bay in Canada which conversely see large percentage decreases in Q95 low flow. Parts of south eastern Russia and north eastern China see an increase in Q95 low flow, whilst many parts of eastern China, coastal Southeast Asia, the Philippines, Indonesia and northern Australia see a percentage decrease in Q95 under RCP8.5. Central Europe and parts of southern Africa and the Congo also see similar decreases in Q95 low flow, whilst Turkey, central to northern United States, parts of Mexico and northern Central America see larger (up to 90%) percentage decreases in Q95 low flow. One of the most significant areas of change, however, is South America, over which the majority of change is negative, with the largest percentage decreases in Q95 low flow seen over Brazil, central Chile and southern Argentina. In contrast, large percentage increases in Q95 low flow are projected for RCP8.5 over southern India and to a lesser extent eastern India into Bangladesh, along

the Himalayas and southern and south eastern China. Percentage increases in low flow are also seen under RCP8.5 south of the Sahel and in East Africa.

Many of the large percentage changes in Q95 low flow seen under RCP8.5 are not present under the scenario of solar geoengineering. Percentage increases are seen in many of the same parts of Boreal climates, but are less extreme and extensive. The large percentage decreases in Q95 seen over the Americas are not replicated under SG, with either the negative change being much smaller, or in fact reversed for central to northern USA and southern Brazil, with increases in Q95 low flow seen here. Similarly the decreases in low flow seen over Turkey and the southern areas of central Europe are also reversed to show increases in Q95 low flow. Other notable areas of difference are Australia, which sees large increases in low flow and Indonesia and New Guinea which see weak increases in Q95. While many areas appear to have improved conditions under SG than RCP8.5, either through reversal of a decrease to an increase in low flow Q95 values or through a smaller percentage change (assuming an increase or no change in low flow is positive, which of course many not always be the case), there are exceptions. Areas of eastern India through to Bangladesh and northern parts of Southeast Asia see decreases in Q95 under SG, where generally this is not seen under RCP8.5. There are reversals of direction of change seen over eastern China and south eastern Russia. The southern section of this area generally sees some quite large decreases in Q95 runoff under RCP8.5, with weak increases under SG and the northern section which in general has large increases under RCP8.5, sees decreases in Q95 runoff for the solar geoengineering scenario.

Percentage change between present and future scenarios cannot show the whole picture as percentage changes may be large even if the absolute changes (in mm) in monthly Q95 runoff are not. In general, some of the largest absolute increases in Q95 seen under RCP8.5 can be found over Boreal catchments, where some of the largest percentage increases are also located. Other areas which see large absolute increases in Q95 monthly runoff include eastern Tibet (north of Myanmar) and coastal eastern Russia. Large percentage decreases in absolute Q95 runoff are seen across much of Indonesia, the Philippines and New Guinea, as well as in relatively small patches in southern Chile and the border between Ecuador and Colombia. It should be noted that many of the regions of greatest change are rather mountainous.

Under solar geoengineering the absolute changes (mm) in Q95 monthly runoff tend to be rather small for much of the globe and indeed almost always smaller than under RCP8.5. In general, the areas of largest change are the same as under RCP8.5, e.g. decreases in

northern high latitudes and increases around the Philippines and southern Chile. The most notable difference is the increase in absolute Q95 runoff for Indonesia and much of New Guinea for the scenario of solar geoengineering, areas which see large decreases under RCP8.5.

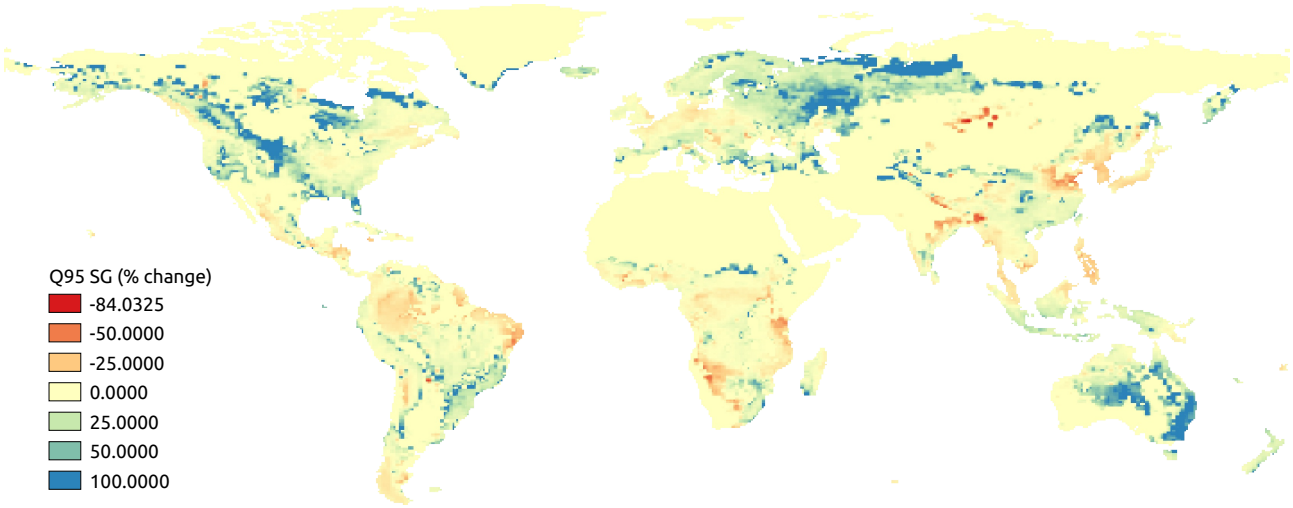


Figure 3.3: Percentage difference in Q95 between SG 2050-70 and Baseline 2010-30 - (SG-BL)/BL x 100.

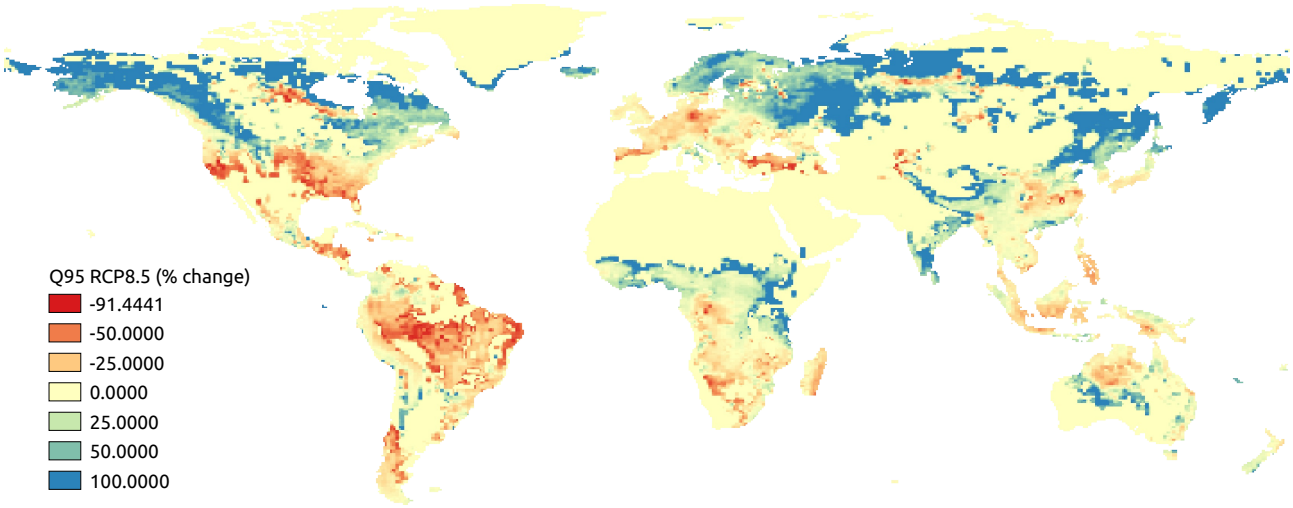


Figure 3.4: Percentage difference in Q95 between RCP8.5 2050-70 and Baseline 2010-30 - (RCP8.5-BL)/BL x 100.

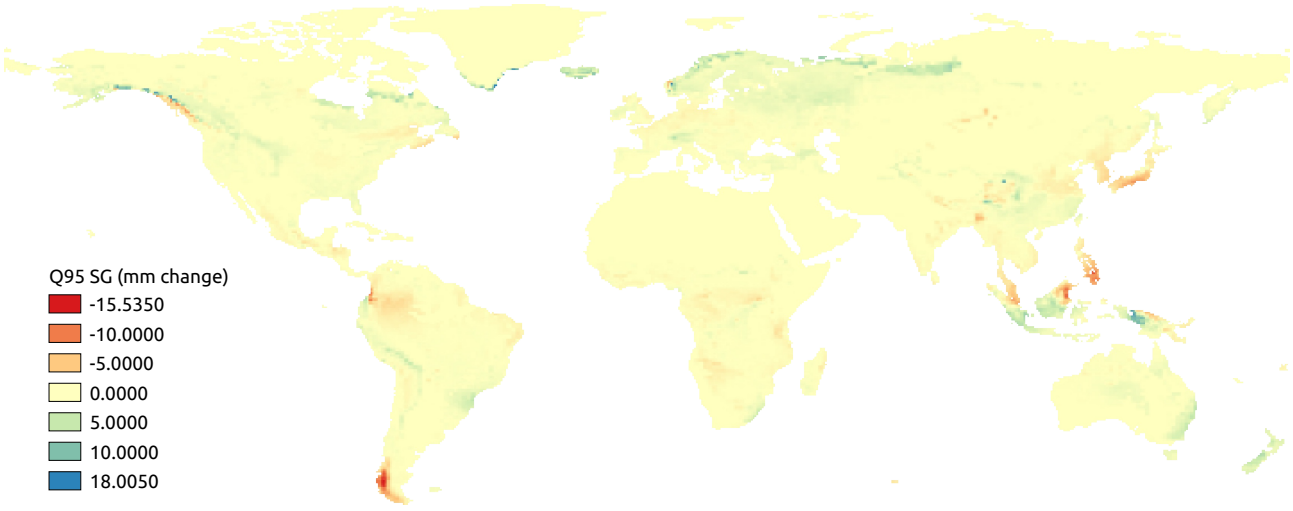


Figure 3.5: Absolute (mm) difference in Q95 between SG 2050-70 and Baseline (2010-30) - SG-BL.

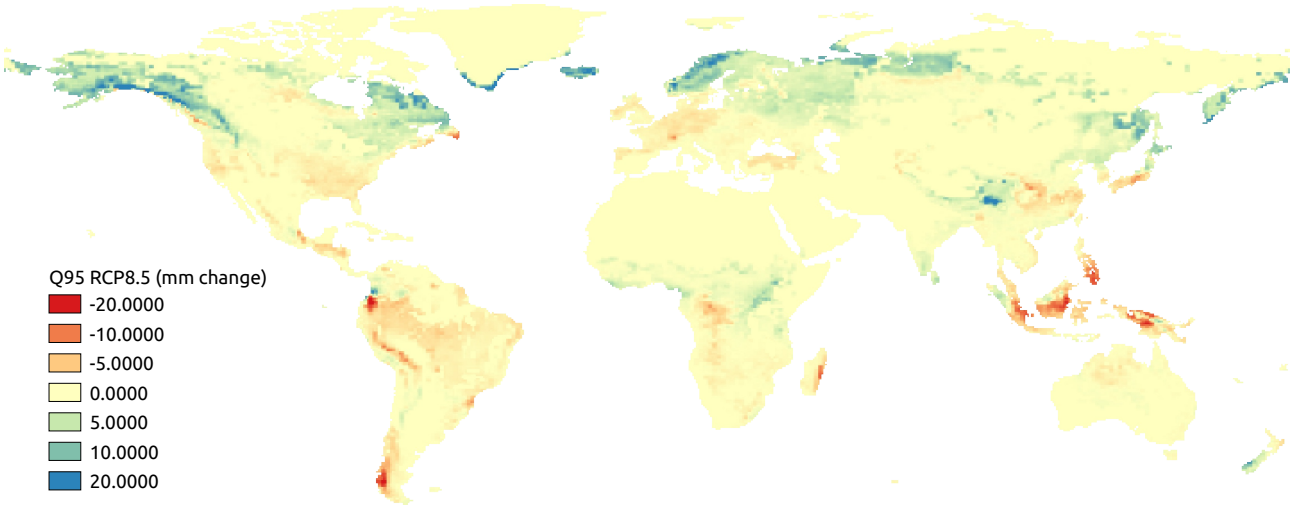


Figure 3.6: Absolute (mm) difference in Q95 between RCP8.5 2050-70 and Baseline (2010-30) - RCP8.5-BL.

Table 3.1 examines the timeseries of months which fall below the Q95 and Q80 monthly low flow threshold which corresponds to each of the scenarios (baseline 2010-30, RCP8.5 2050-70 and SG 2050-70), finding the maximum number of consecutive months in each of the 21 year periods for which runoff is below the threshold. This was calculated per gridcell and the median value and interquartile range across the gridcells in each hydroregion is taken. Calculated in the same way, Table 3.2 shows the corresponding values when the baseline 2010-30 Q95 or Q80 threshold is used to calculate the number of consecutive months below the threshold, rather than the threshold relating to each of the future scenarios. Only hydroregions which show any change have been included in the tables for ease of reading. For the majority of hydroregions little change is seen in the maximum number

of consecutive months below the threshold, when the Q95 or Q80 threshold calculated for the corresponding time period has been used. On the whole the maximum number of consecutive months roughly doubles under Q80 when compared to values for Q95. No change greater than 1 month is seen when the threshold corresponding to the future scenario is used for the calculation, however, larger changes are shown when the baseline threshold of Q95 or Q80 is used for the future scenarios.

For the maximum number of consecutive months below the Q95 or Q80 low flow threshold which corresponds with each scenario, areas which see no change under SG and an increase under RCP8.5 include Boreal North America with Q95 threshold, Boreal Europe with Q80, Boreal Asia (Eastern Siberia) with Q95 and Q80, Northern Dry Asia (Middle East and Central Asia) with Q80, Southern Sub Tropical Australia with Q95. Under the same conditions, Northern Dry North America and Equatorial South America with Q95 show an increase in maximum number of consecutive months below the threshold under both RCP8.5 and SG. The only hydroregions which sees a decrease in maximum number of consecutive low flow months under RCP8.5 is Northern Mid Latitude Europe with Q95 (also decrease under SG). Areas that only see a change in the maximum number of consecutive low flow months under the scenario of solar geoengineering show a decrease in Boreal North America with Q80 and an increase in Equatorial Asia with Q95. Southern Dry Australia sees the most change, with an increase in the maximum number of consecutive dry months under RCP8.5 and decrease under SG for the Q80 threshold.

When changes in the maximum number of months below the low flow threshold are calculated using the baseline (2010-30) threshold, in general larger differences can be seen. With the baseline threshold now used, Boreal catchments generally show a decrease in maximum number of consecutive months below the threshold under RCP8.5, with small (if any changes) under the scenario of solar geoengineering. Non Boreal hydroregions which saw an increase in maximum number of consecutive low flow months under RCP8.5 and no/little change under SG when the threshold for each corresponding scenario was used tend to see this same trend when the baseline threshold is used, but the increase in maximum consecutive months is sometimes greater (2 months rather than 1). This is true for Northern Dry North America (but now also Q80 as well as Q95), Equatorial South America (Q80 and Q95), Northern Dry Asia (Middle East) (Q80 and Q95) and Southern Sub Tropical Australia (Q95). Additional hydroregions which now see increases in the maximum number of consecutive low flow months under RCP8.5 include Northern Mid Latitude North America (Q95), Northern Sub Tropical North America (Q95 and Q80), Equatorial S. America (Q95 and Q80), Southern Sub Tropical South Amer-

ica (Q95), Southern Dry South America (Q95 and Q80), Northern Dry Africa (Q95 and Q80), Northern Sub Tropical Africa (Q95), Southern Dry Africa (Q95 and Q80), Southern Mid Latitude Africa (Q80), Equatorial Asia (Q95) and Southern Dry Australia (Q95). Of these Equatorial South America, Southern Dry South America, Northern Dry Africa, Northern Sub Tropical Africa, Southern Dry Africa, Northern Dry Asia (Middle East) and Equatorial Asia also see an increase in the maximum number of consecutive months below the baseline threshold under the scenario of solar geoengineering. The only hydroregions which sees an increase in the maximum number of consecutive low flow months for SG but not RCP8.5 is Northern Mid Latitude Asia under Q95. More frequently the maximum number of consecutive months below the low flow threshold is decreased under the scenario of solar geoengineering. Excluding the Boreal areas, this is true for Southern Mid Latitude South America (Q80), Northern Mid Latitude Europe (Q95), Southern Mid Latitude Africa (Q95), Southern Sub Tropical Australia (Q80), Southern Dry Australia (Q95 and Q80) and Southern Mid Latitude Australia (Q95 and Q80).

Very few significant changes can be seen in the seasonality of low flow (Figures 3.7 and 3.8). Only for Equatorial Asia using the Q95 threshold, Southern Mid Latitude Africa (Q95) and Southern Mid Latitude Australia (Q95), all of which show an increase in seasonality under RCP8.5 and little to no change under SG, as well as Boreal Europe using the Q80 threshold, which sees a decrease in seasonality under RCP8.5 but again little to no change under SG, could the signals shown be considered different enough for this to be significant.

Table 3.1: Median (across the gridcells in each hydroregion) of the maximum length of consecutive months at or below Q95 and Q80, with the respective interquartile ranges in brackets.

Hydroregion	Q95			Q80		
	Baseline (2010-30)	RCP8.5 (2050-70)	SG (2050-70)	Baseline (2010-30)	RCP8.5 (2050-70)	SG (2050-70)
Boreal N. America	2 (2-3)	3 (2-3)	2 (2-3)	5 (4-5)	5 (4-5)	4 (4-5)
N. Dry N. America	2 (2-3)	3 (2-4)	3 (2-3)	5 (4-6)	5 (4-6)	5 (4-6)
Equatorial S. America	2 (2-3)	3 (2-3)	3 (2-3)	4 (4-5)	4 (4-5)	4 (4-5)
Boreal Europe	3 (2-4)	3 (2-4)	3 (2-4)	5 (5-6)	6 (5-7)	5 (5-6)
N. Mid Latitude Europe	3 (2-3)	2 (2-3)	2 (2-3)	5 (4-6)	5 (4-6)	5 (4-6)
Boreal Asia (E. Siberia)	2 (2-2)	3 (2-4)	2 (2-2)	4 (4-5)	5 (4-6)	4 (4-5)
N. Dry Asia (Middle East)	2 (1-3)	2 (1-3)	2 (1-3)	4 (4-6)	5 (4-6)	4 (4-5)
N. Dry Asia (C. Asia)	2 (2-5)	2 (2-5)	2 (2-5)	4 (4-6)	5 (4-7)	4 (4-7)
Equatorial Asia	3 (3-4)	3 (3-4)	4 (3-4)	7 (6-8)	7 (6-8)	7 (6-8)
S. Sub Tropical Australia	3 (2-5)	4 (3-5)	3 (3-4)	6 (5-7)	6 (5-7)	6 (5-7)
S. Dry Australia	3 (2-4)	3 (2-5)	3 (2-4)	6 (5-7)	7 (5-8)	5 (4-7)

Table 3.2: Median (across the gridcells in each hydroregion) of the maximum length of consecutive months at or below Q95 and Q80, with the respective interquartile ranges in brackets. Using baseline 2010-30 thresholds.

Hydroregion	Q95			Q80		
	Baseline (2010-30)	RCP8.5 (2050-70)	SG (2050-70)	Baseline (2010-30)	RCP8.5 (2050-70)	SG (2050-70)
Boreal N. America	2 (2-3)	2 (1-3)	2 (2-3)	5 (4-5)	3 (2-4)	4 (3-5)
N. Mid Latitude N. America	2 (2-3)	3 (2-4)	2 (2-3)	5 (4-6)	5 (4-7)	5 (4-6)
N. Dry N. America	2 (2-3)	4 (3-5)	2 (2-3)	5 (4-6)	6 (5-8)	5 (4-6)
N. Sub Tropical N. America	3 (2-4)	4 (3-5)	3 (2-4)	6 (5-7)	7 (5-9)	6 (5-7)
Equatorial S. America	2 (2-3)	3 (3-4)	3 (2-3)	4 (4-5)	5 (4-5)	4 (4-5)
S. Sub Tropical S. America	3 (2-4)	4 (3-5)	3 (2-4)	5 (4-6)	5 (5-7)	5 (4-6)
S. Dry S. America	2 (2-3)	3 (2-5)	3 (2-4)	5 (4-6)	6 (5-8)	5 (4-7)
S. Mid Latitude S. America	3 (2-4)	3 (3-5)	3 (2-4)	6 (4-7)	6 (5-7)	5 (4-7)
Boreal Europe	3 (2-4)	2 (1-3)	2 (2-3)	5 (5-6)	4 (3-5)	5 (4-5)
N. Mid Latitude Europe	3 (2-3)	3 (2-4)	2 (2-3)	5 (4-6)	5 (4-7)	5 (4-6)
N. Dry Africa	2 (1-3)	3 (2-5)	3 (2-5)	4 (4-5)	5 (4-6)	4 (4-6)
N. Sub Tropical Africa	2 (1-4)	3 (2-5)	4 (2-5)	5 (4-6)	5 (4-6)	5 (4-6)
S. Dry Africa	4 (3-5)	5 (4-6)	5 (3-6)	6 (5-7)	7 (6-7)	6 (5-7)
S. Mid Latitude Africa	3 (2-4)	3 (2-4)	2 (2-3)	5 (4-6)	6 (5-7)	5 (4-6)
Boreal Asia (W. Siberia)	3 (2-4)	3 (2-4)	3 (2-4)	5 (4-6)	4 (3-5)	5 (4-5)
Boreal Asia (E. Siberia)	2 (2-2)	1 (1-2)	2 (1-2)	4 (4-5)	2 (2-3)	4 (3-4)
N. Mid Latitude Asia	3 (2-4)	3 (2-4)	4 (3-5)	6 (5-7)	5 (4-7)	6 (5-7)
N. Dry Asia (Middle East)	2 (1-3)	4 (2-6)	4 (2-5)	4 (4-6)	5 (4-6)	5 (4-6)
Equatorial Asia	3 (3-4)	4 (3-4)	4 (3-4)	7 (6-8)	7 (6-8)	7 (6-8)
S. Sub Tropical Australia	3 (2-5)	4 (3-6)	3 (2-4)	6 (5-7)	6 (5-7)	5 (5-6)
S. Dry Australia	3 (2-4)	4 (2-6)	2 (2-4)	6 (5-7)	6 (4-8)	5 (4-7)
S. Mid Latitude Australia	2 (2-3)	2 (2-3)	1 (1-2)	5 (5-6)	5 (4-6)	4 (3-5)

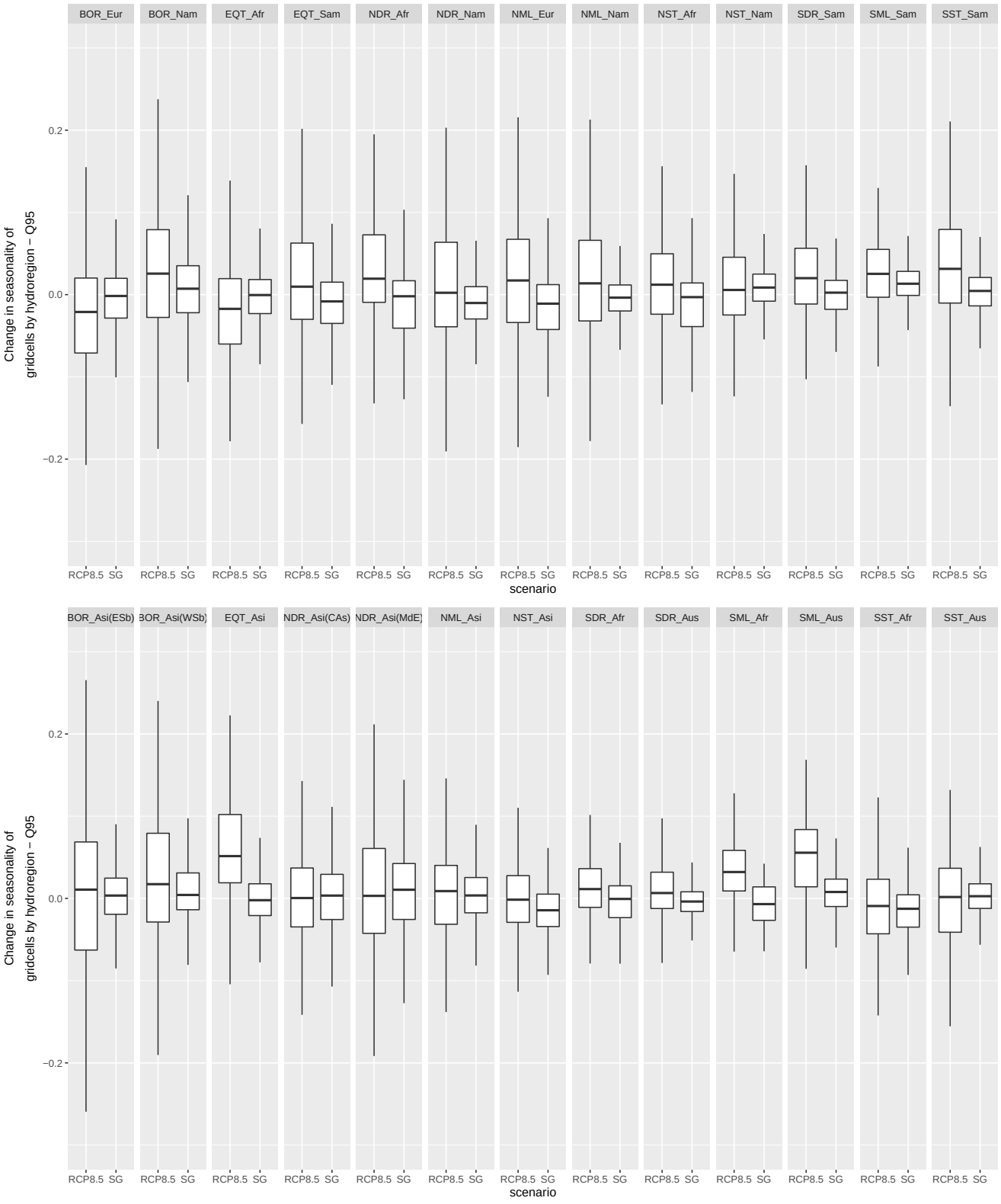


Figure 3.7: The change in seasonality of months below the Q95 low flow runoff threshold (see methods) from baseline (2010-30) to future scenario (2050-70) per gridcell, grouped by hydroregion.

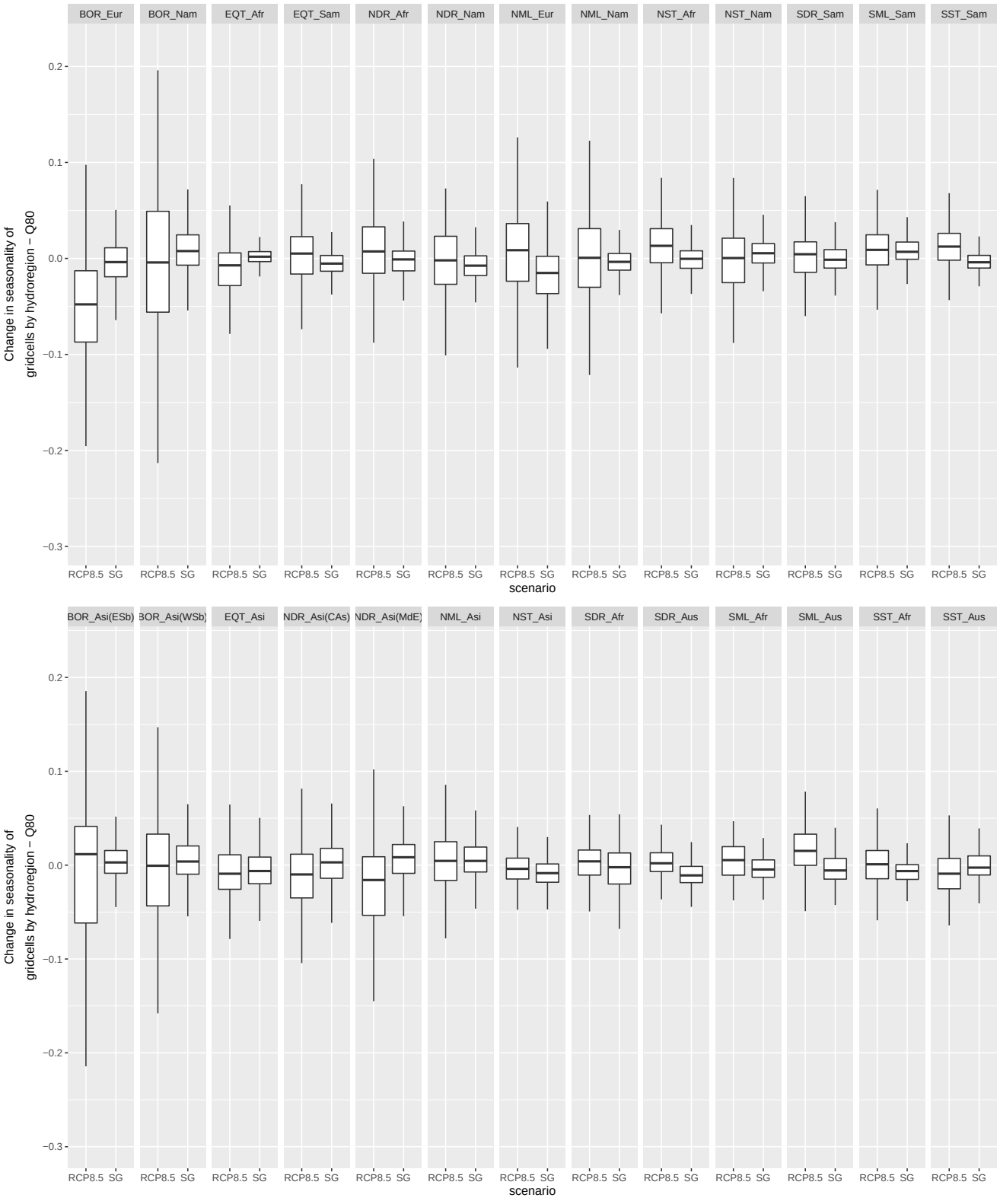


Figure 3.8: The change in seasonality of months below the Q80 low flow runoff threshold (see methods) from baseline (2010-30) to future scenario (2050-70) per gridcell, grouped by hydroregion.

3.4 Discussion

Large increases in both the 20 year minimum monthly runoff return level and the Q95 and Q80 low flow were shown across Boreal catchments and some Northern Mid Latitude

areas under the scenario of climate change, with the return level under the scenario of solar geoengineering often, but not always, seeing smaller changes from baseline values. This would indicate that in these catchments solar geoengineering helps to maintain present-day conditions. This may not necessarily be a good thing, for example here an increase in the minimum runoff is seen under RCP8.5, which would imply lower likelihood for drought severity seen in the present climate. However, it is not as simple as interpreting an increase in low flow as a positive thing. In lots of places that see an increase (e.g. boreal climates) this is linked to increased snow melt with warmer temperatures. The environments and ecosystems of these regions have adapted to climates over long time periods, so any rapid or extreme changes will have an impact and large changes, be that an increase or decrease, could be very damaging for ecosystems. Increases in Q95 low flow are still seen under solar geoengineering, which implies SG cannot offset all of the change seen under RCP8.5. It may be particularly important to note that this is occurring mostly in higher latitudes, as many scenarios of solar geoengineering (although less so under the multiple injection locations used for the GLENS analysis) see undercooling of the poles due to the reduced transport of aerosols from the Equator.

Other areas where it seems more straightforward to interpret the value of solar geoengineering in changes in the 20 year minimum monthly runoff return level include European catchments and those of Amazonas and Xingu in Brazil which all see significant decreases in the return level from the baseline value under RCP8.5, with smaller changes seen for solar geoengineering. These are both areas which are recognised by the IPCC with medium confidence as seeing an intensification of drought over the coming century (Field et al., 2012).

When examining changes in the Q95 and Q80 thresholds of low flow from the baseline (2010-30) to the future (2050-70) scenario, again it can be seen that much larger changes occur under RCP8.5 than SG. Areas of potential benefits of solar geoengineering, in which SG moderates the impact of RCP8.5 in greatly decreasing low flow from the present-day, can be seen over much of the Americas, in Turkey, southern Central Europe, parts of Australia and East Asia. Indonesia and much of New Guinea could also see benefits from solar geoengineering, with increases in the absolute (mm) values of low flow Q95 runoff, whereas there are large decreases under RCP8.5. Areas of potential negative consequences of solar geoengineering, most commonly with greater decreases to low flow than under climate change, include parts of eastern India and Bangladesh as well as northern areas of Southeast Asia. This is possibly linked to changes in monsoon conditions often reported for solar geoengineering studies, however beyond larger changes in seasonal patterns of

climate this is not likely as the monsoon is associated with some of the wettest conditions and the low flows are likely to all occur in the dry season. Over different parts of eastern China and south eastern Russia solar geoengineering appears to either increase low flow when RCP8.5 decreases it, or the converse. This is interesting, given the near proximity of the areas which see directly contrasting responses to solar geoengineering and climate change. However, there is still large uncertainty in the wider conclusions that can be drawn from this work, as the findings here are specific to the climate model and scenario of solar geoengineering that has been used. Whilst agreement in the regional climate change signal with existing research gives confidence in the results, it is harder to say more definitively whether the large differences in regional drought under the differing climates (be that SG or RCP8.5) are consistent without a greater number of climate models running this specific scenario of SG.

In an attempt to understand the nature of drought changes in greater depth, the maximum number of consecutive months below the low flow threshold were computed using both the threshold corresponding to each future scenario (RCP8.5 or SG) and the baseline threshold. As might be expected, larger changes in the maximum number of consecutive low flow months were seen when the baseline threshold was used, given that the projections of future climate are often more extreme than the present-day, thus meaning future values fall below the present-day thresholds more frequently. Areas which see increases in maximum number of consecutive dry months under RCP8.5 (with the RCP8.5 low flow threshold) include many of the Boreal catchments, as well as dry catchments (Northern Dry (North America, Middle East, Central Asia), Southern Dry Australia) and those known to see drying under climate change (e.g. Equatorial South America, Southern Sub Tropical Australia). The increase in maximum number of consecutive dry months across Boreal areas (implying worse drought conditions) seems in contrast to the increase in low flow threshold seen for these areas (implying improved drought conditions). However, it does seem logical that if the threshold value is a higher level of runoff, and less extreme, then it is more likely you will see consecutive occurrences of this value. Areas in which solar geoengineering presents an opportunity to improve drought conditions in comparison to future climate change include Southern Dry and Sub Tropical Australia, many of the Boreal hydroregions and Northern Dry Asia (Middle East and Central Asia).

In contrast to when the threshold of low flow for the corresponding time period is used, when the baseline threshold of low flow is used to find the maximum number of consecutive months below the threshold, the number of months decreases over Boreal catchments under RCP8.5 but remain rather similar under SG. This is unsurprising as it has been shown

that climate change will increase the low flow values across Boreal areas, with smaller changes seen under the scenario of solar geonengineering. When the baseline threshold is used more extensive areas see an increase in the maximum number of consecutive months below the threshold, including many parts of North and South America, Northern and Southern Africa, Equatorial Asia and the Middle East and Southern Sub Tropical and Dry Australia. Some of these areas see little difference in the maximum number of consecutive dry months between RCP8.5 and SG when the baseline threshold is used, however many see fewer consecutive dry months under solar geoengineering, including Northern Mid Latitude Europe and Southern Mid Latitude South America and Africa as well as Sub Tropical, Dry and Mid Latitude Australia. Only in Northern Mid Latitude Asia is SG projected to increase the length of maximum consecutive dry months when RCP8.5 does not.

It would have been interesting to see if changes existed in future "seasonality" of low flow occurrences. If seasonality were to increase in the future then low flows would be more concentrated in specific months, which could mean shorter more intense droughts. Conversely, if seasonality were to decrease in the future with a wider spread of low flow across different months, this may indicate more infrequent but potentially longer lived occurrences of drought. However, little change was detected, perhaps because the method was not sensitive enough to pick up what would be quite subtle changes in the low flow annual signal. Areas which do see change mostly see an increase in seasonality, as is the case for Equatorial Asia, Southern Mid Latitude Africa and Southern Mid Latitude Australia under RCP8.5 (little change is seen under SG). Boreal Europe sees a decrease in seasonality under RCP8.5, which seems to fit with the current findings of increased low flow threshold values and maximum number of consecutive months of low flow in the future, which implies the influence of snow melt with warmer temperatures and an assumption could be made that this would also mean a less distinct period of low runoff during cold conditions. Again, negligible change is seen under the scenario of solar geoengineering suggesting an ability to preserve present-day climatology characteristics.

When compared to existing studies of dry and drought conditions using the GLENS modelling ensemble, the findings support the general conclusions that solar geoengineering could reduce the large negative impacts climate change will have on drought across the Americas (Xu et al., 2020) and South Africa (Odoulami et al., 2020). Analysis of changes in number of consecutive dry days under different climate change and solar geoengineering scenarios (Curry et al., 2014) also finds much larger changes under the climate change scenario than for the experiment of solar dimming. These areas are many of the same seen

here to experience worse drought conditions under RCP8.5, including southern Africa, parts of USA, Mexico and Central America as well as eastern Brazil and parts of coastal Australia. As has also been found here, Boreal catchments see a decline in drought conditions from present under climate change. Under the scenario of solar geoengineering Curry et al. (2014) find it could be beneficial in reducing the number of consecutive dry days over parts of the Middle East, whilst having a more notable negative impact over central Amazon and Tanzania. However, these areas also see increases in consecutive dry days under climate change.

Despite these findings, which largely agree with existing model projections on the main regions of the world which will experience increased drought over the 21st century, it would be unwise to attempt to draw any specific location based conclusions about the possible impacts of solar geoengineering from this work. Instead it provides a very useful indicator of regions which are likely to see an increased risk of drought under RCP8.5 possibly ameliorated by solar geoengineering, or in fact worsened, perhaps when climate changes provide opportunities for drought conditions to improve under RCP8.5 projections. These regions of interest which have been identified warrant further future investigation to understand if these changes are also seen under different scenarios of solar geoengineering run across a wider suite of models.

An aspect of drought which has not been explicitly examined here is the spatial extent of drought and whether or not this changes over time and under each of the scenarios. However, some level of analysis of this can be done by examining Figures 3.3 to 3.6. Andreadis et al. (2005) explore past droughts across continental USA using severity-area-duration curves which include both the spatial and temporal extent of the drought in determining its severity and also found that runoff drought can recover quicker than soil moisture drought from short spells of precipitation, whilst also concluding that the absence of short lived bursts of precipitation can understandably prevent recovery. This is important to note in terms of how precipitation distributions may change under future climate scenarios. As has been mentioned, the higher standard deviation in daily precipitation each year under the scenario of climate change (Figure D.1) likely means more variation and extremes of precipitation, which possibly would produce these shorter burst of precipitation sufficient to drive drought recovery. Therefore, despite greater decreases in low flow threshold values under RCP8.5 than SG, it is possible that there is also more opportunity for drought recovery under the more varied precipitation of the climate change scenario. This is speculative, as it is not something that has been examined in enough detail to conclude from this research. It does however, exemplify the need for detailed consideration of

differences in projected future climatology distributions between climate change and solar geoengineering scenarios, beyond the study of averages and individual percentiles, if we are to fully comprehend the impact of interventions such as stratospheric aerosol injection. Saft et al. (2015) find changes to the rainfall-runoff relationship (with reduced runoff for a specific rainfall value) under prolonged periods of drought in Australia, with this becoming more pronounced in larger catchments under drier climates, shallower slopes and reduced forest extent. This further supports the need for detailed understanding of how changes in climate and runoff are interconnected and the implications for drought.

Large scale climate cycles, such as the El Niño Southern Oscillation (ENSO) are known to be linked to droughts across the world. Climate models have been able to replicated the occurrence of some ENSO driven droughts (Corzo Perez et al., 2011); although climate models on the whole do not model ENSO particularly well (Bellenger et al., 2014). ENSO driven droughts have been shown for example over Africa, Indonesia and South America, however the method of drought calculation alters the detection and classification of drought. The study of this was beyond the scope of this research, but given that the full impacts of increasing stratospheric aerosol for solar geoengineering are not known (for example how the stratospheric warming that comes from the aerosols presence in the stratosphere may block transport to high latitudes (Visioni et al., 2020)), it is of great importance that more climate model simulations and scenarios are carried out if we are to really understand how droughts may change under possible scenarios of solar geoengineering.

Van Huijgevoort et al. (2013) also stress the importance of individual models on the projection of drought events, finding that different models can find rather different characterisations of drought. This also confirms the need for a greater number of climate model simulations of solar geoengineering before more conclusive understanding of drought change can be reached. This should ward against general conclusions about how drought will be impacted by solar geoengineering, not least because only a single scenario of solar geoengineering has been examined. Different approaches to stratospheric aerosol injection would likely yield quite different regional results.

3.5 Conclusion

Projections of climate change which follow the RCP8.5 emissions route show unequal burdens of change and negative consequences across the globe. However, in some places these changes may present opportunities. In offsetting much of the global change seen

under RCP8.5, the GLENS scenario of solar geoengineering often offers benefits for future drought conditions across much of the world. However, the influence of SG on runoff varies by region and there will also be challenges and negative outcomes; which in some areas may be due to reversing potentially beneficial changes under RCP8.5. Areas which suffer most extreme changes in drought conditions under unmitigated climate change, in terms of reductions in the 20 year minimum monthly return level, include European and Brazilian catchments. These areas also see large decreases in the Q95 and Q80 low flow values, with this also projected over other parts of the Americas, in Turkey, parts of Australia and East Asia. In many of these regions solar geoengineering presents a positive future picture, ameliorating much of this negative change and preserving the return level and low flows closer to the present-day. In addition to this, some areas may see increases in values for the low flow threshold from the present-day under SG, whilst the same locations see large decreases under RCP8.5, for example Indonesia and New Guinea. Positive influences of solar geoengineering, in terms of reduced numbers of consecutive dry months (i.e. those below the Q95 or Q80 threshold), when compared to changes to drought conditions under RCP8.5 are seen in Southern Dry and Sub Tropical Australia, the Middle East and Central Asia, locations concurrent with the other findings of reduction in future consecutive dry days under solar geoengineering (Curry et al., 2014).

Other areas may see benefits under climate change, and regions which see increases in both 20 year minimum monthly return levels and Q95 and Q80 low flow thresholds include many Boreal catchments and some Northern Mid Latitude catchments. These potentially beneficial changes, at least in terms of drought reduction, are often countered by the affects of solar geoengineering; implying worse future conditions under the scenario of SG. Other areas which may see more direct negative consequences under solar geoengineering, through not just reversing positive changes under RCP8.5 but making negative changes under climate change worse, include parts of eastern India, Bangladesh and northern areas of Southeast Asia.

This research provides a preliminary analysis of how low flows may change under SG, through examination of the GLENS stratospheric aerosol geoengineering modelling experiments. However, the uncertainty in runoff projections between different models makes it difficult to generalised these findings beyond the specific scenario of SG used; most especially if trying to draw regional conclusions rather than just building an overall global picture of change. In order to corroborate, or indeed challenge, the findings of projected changes in drought seen here, it is necessary that more measures of drought are assessed using a wider selection of models and future solar geoengineering scenarios.

Chapter 4

Water Scarcity under Solar Geoengineering

4.1 Introduction

Climate change and population rise are both predicted to increase the prevalence of water scarcity around the globe as we move further into the 21st century (Schewe et al., 2014, Vörösmarty et al., 2000). Globally, the estimated number of people thought to be living in areas exposed to water scarcity varies depending on scale and method used, but it is thought that there are somewhere in the region of 1.6 to 2.4 billion people affected (Gosling and Arnell, 2016). Schewe et al. (2014) project that warming of 2°C from early 21st century levels, will cause a 21% increase in global exposure to severe (or chronic) water scarcity. There is, however, considerable variation across the different regions of the globe. Many of the areas projected to see increases in water scarcity due to climate change lie in regions where a greater extent of aridity is seen, these include southern and central North America, the Mediterranean and parts of Europe, the Middle East, northern and southern Africa and Australia (Arnell, 2004, Gosling and Arnell, 2016, Feng and Fu, 2013). Some projections show a decrease in water stress for South and East Asia (e.g. (Arnell, 2004)), whilst other project an increase (Gosling and Arnell, 2016).

Water scarcity is just one of the many effects predicted to befall global populations and ecosystems in the coming century as a result of climate change. This mounting plethora of effects, alongside increasing implausibility of keeping global warming within safe limits, has led to a growing interest in methods of geoengineering. Projections of solar geoengineering under asymmetric hemispheric forcing conditions through injection in the Northern Hemisphere predict a reduction in Sahelian precipitation (Haywood et al., 2013), whilst scenarios using equatorial injection project a weakening of the monsoon (Tilmes et al., 2013). Less extreme changes are projected under the GLENS scenario with multiple injection locations, but nonetheless the results of Chapters 2 and 3 indicate that conditions under SG will not be the same as present-day. When examining water scarcity however, there is an additional dimension to the change over time, this is in how the population (and their demands on the system - not always linearly related) will change in the future. Whether some areas will see concurrent or conflicting changes in projections of natural water supply and population change complicates the picture of how solar geoengineering may impact different regions in the future.

4.1.1 Global Water Scarcity

Global water scarcity arises from three main factors: changes in the amount (and/or quality) of water available to an individual, community or nation; changes in the numbers of people accessing that resource in a given area and changes in the way a population

uses the water resources within a specific catchment. The term water scarcity can have multiple definitions, but here it will be defined as being when there is a scarcity of water for human use. Two further terms are water stress and water shortage. Water stress can arise when there is insufficient access to or mobilisation of the available water resource (be that due to over abstraction, poor transportation/infrastructure, lack of affordability, or some other reason). It is commonly seen to be a ratio of use-to-availability, with high water stress occurring when this is greater than 40 percent. Water shortage is considered to be related to a physical shortage of water due to over population and high population densities in a given area, meaning there is not enough water to sufficiently supply all people living in the catchment (or to grow adequate quantities of crops for the given number of people) (Rockström et al., 2009).Water scarcity can be measured in many ways, but all will indicate the amount of water available to each member of a society in a specified geographical space; be that country, town, village or hydrological catchment.

Projections for future emissions pathways (e.g. RCPs outlined in Chapter 1), as well as estimates for future population numbers are required to predict water scarcity over the following decades. Moving forward, Schewe et al. (2014) examine how the availability of water (in terms of river discharge) will be affected under climate change RCP8.5 and a 2°C warmer world; the global pattern can be seen in Figure 4.1. Population projections (Samir and Lutz, 2017), depicted in Figure 4.2, have been estimated using the Shared Socioeconomic Pathways (SSPs) first outlined by O'Neill et al. (2014).

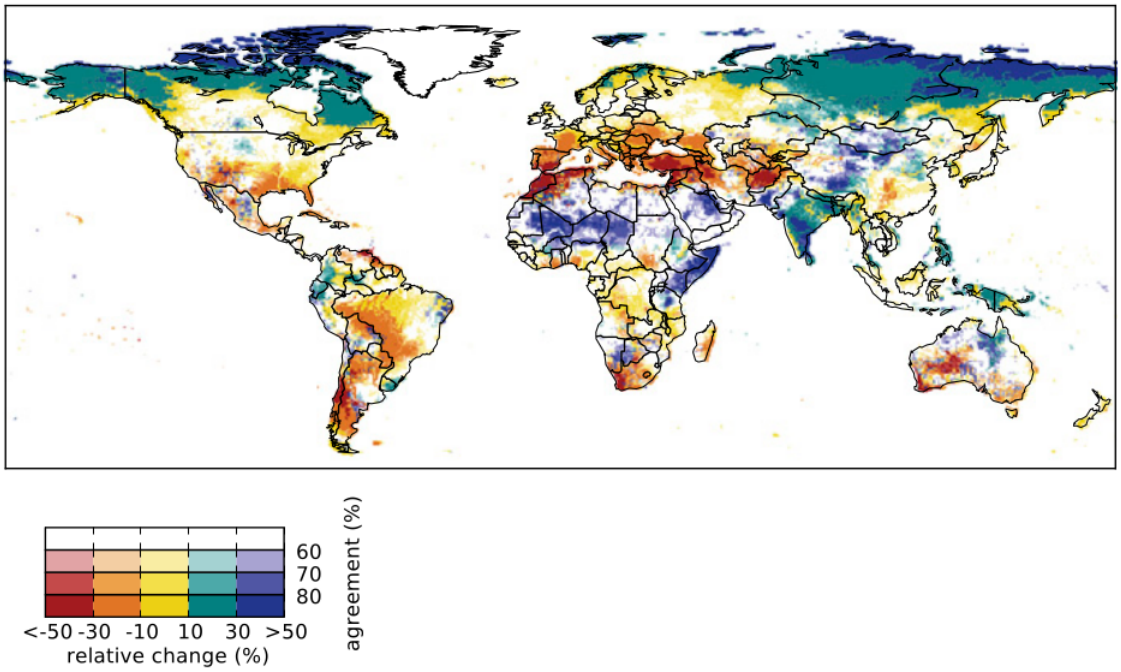


Figure 4.1: Relative change in annual river discharge at 2°C compared with present-day, under RCP8.5. Colour hues show the multimodel mean change, and saturation shows the agreement on the sign of change across all GHM GCM combinations. From Schewe et al. (2014).

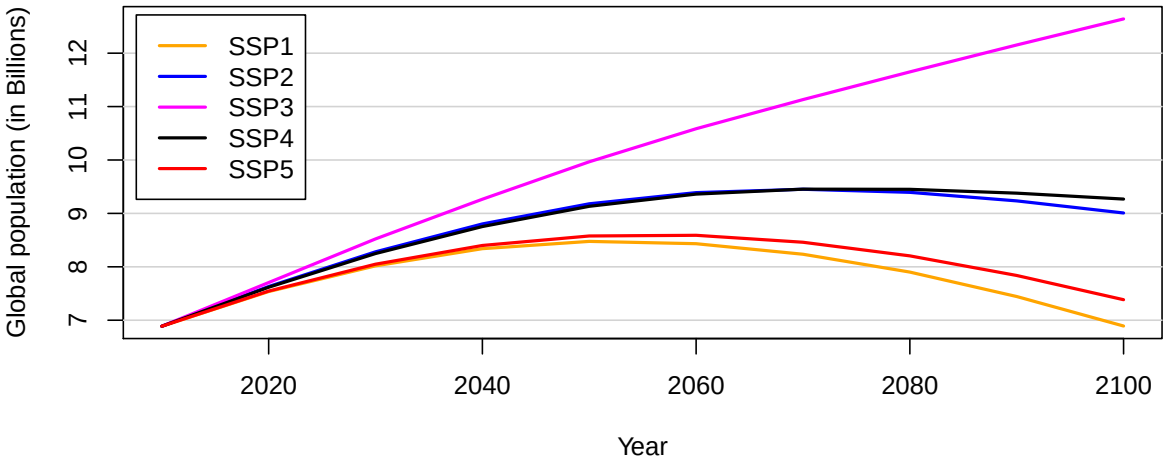


Figure 4.2: Future global population projections under the five SSPs. The population pathways SSP2, 3 and 5 are found to be compatible with a future where solar geoengineering may be implemented and so are used in this research.

Multiple methods exist for the calculation of water scarcity within a region; ranging in complexity and in the number of assumptions and generalisations which they include. One simple, and widely used (Liu et al., 2017, Gosling and Arnell, 2016, Schewe et al., 2014, Kummu et al., 2010), metric is The Falkenmark Water Stress Indicator (also termed the Water Crowding Index - WCI) (Falkenmark and Rockström, 2004). The WCI is a measure of physical water availability for each person within a catchment, measured in m^3/capita/year of water, and despite its relative simplicity it can provide a useful estimation of water scarcity conditions across the world. A value of 1000m^3/capita/year or lower is classed as "severe water scarcity" (Falkenmark and Molden, 2008, Falkenmark et al., 2007). These values do not represent in a crude sense the amount of water each person needs for domestic purposes (which if considered to be 50 litres per day would result in a threshold of less than 20m^3/capita/year), but instead characterises the amount of water needed to grow adequate amounts of food for each person (Rijsberman, 2006).

Another measure often used is called the Water Stress Index (WSI), this measure examines the ratio between available water resources and withdrawals from these sources (e.g. aquifers, lakes, rivers), with a ratio greater than 0.4 indicating a population's exposure to water scarcity. It has been estimated that between 1.6 and 2.4 billion people were living in catchments exposed to water scarcity in 2000 and Gosling and Arnell (2016) explore how global WCI and WSI values are projected to change under climate change by 2050; this can be seen in Figure 4.3. The number of people in water scarcity is projected to rise to 3.1 billion by 2050 (using WCI) (Gosling and Arnell, 2016).

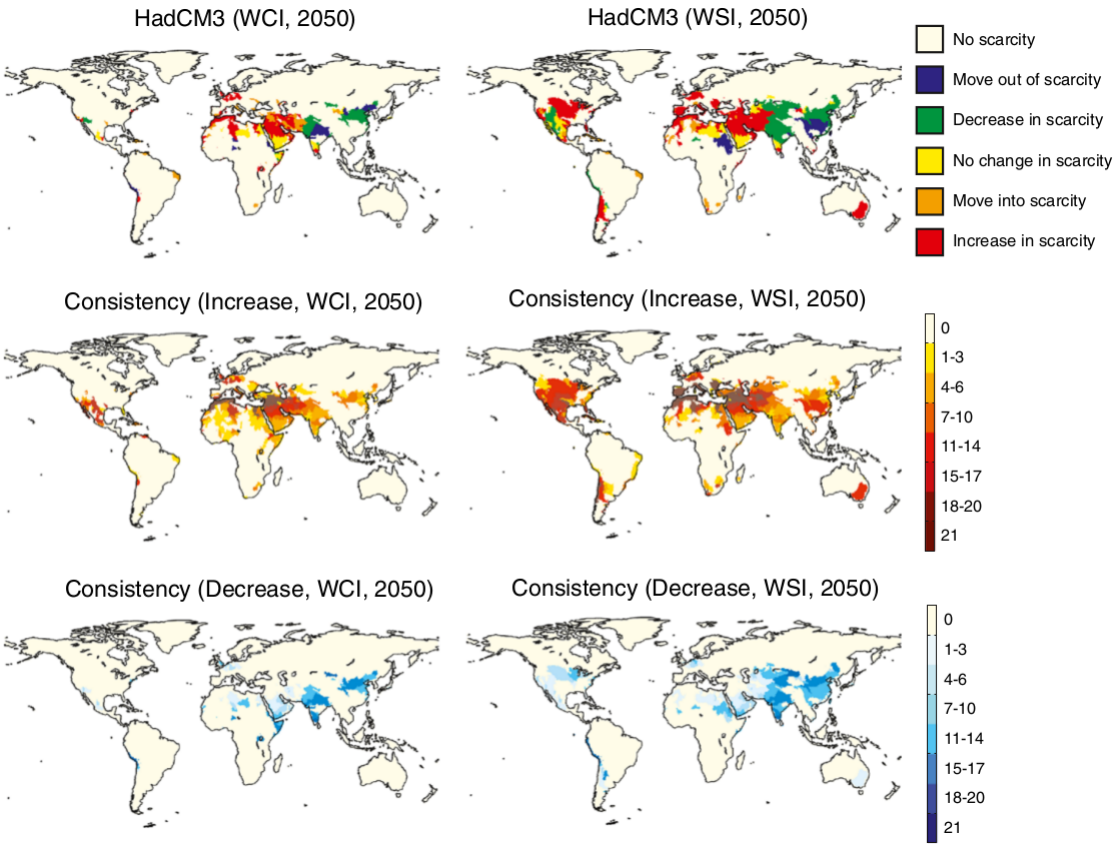


Figure 4.3: The effect of climate change only on exposure to water scarcity in 2050 under the SRES A1B scenario, using the WCI (1,000 m^3/capita/year; left panels) and the WSI (0.4; right panels). Top panels display the change in scarcity classes with the HadCM3 GCM only. The other panels show consistency across 21 simulations (with all CMIP3 models), in terms of the number of simulations out of 21 that show an increase in exposure (indicative of where there is an increase in scarcity or a watershed moves into water scarcity; middle panels), or decreases (a decrease in scarcity or move out of scarcity; bottom panels). From Gosling and Arnell (2016).

4.1.2 Chapter Outline

Changes in water availability and population numbers in the future will greatly impact societies, countries and civilisations as a whole. These impacts will not only be determined by how many people are trying to share the available water resources but also by the type of climate that we live with in the future. The climate model projections of solar geoengineering currently available show that a future solar geoengineered world will not look the same as the present-day and that there are trade-offs between maintaining precipitation and temperature trends. Solar geoengineering may also have far reaching impacts on our societies and ecosystems which we have yet to anticipate. It is vital that if geoengineering techniques such as SG are to be implemented, we know ahead of time our best estimations for how they may impact upon our world. Hydrological changes would have many impacts, but one of particular pertinence to governments and society, especially when considered in conjunction with projected population change, is that of water scarcity. Impacts on water, being a basic requirement for life, is something we must understand in the future

and therefore how SG is predicted to impact the amount of water available is of great importance. This chapter will estimate how water scarcity may change under scenarios of climate change (RCP8.5) and solar geoengineering (SG), using the GLENS modelling projections. Analysis of numbers of people exposed to water scarcity will be given. In addition to projections under RCP8.5 and SG, projections under only changes in population (climate remains at 2010-30 levels) will also be computed.

4.2 Materials and Methods

4.2.1 Climate model and scenarios

The GLENS dataset (described in detail in the preceding chapters) will be used to examine how water scarcity changes under a scenario of climate change (RCP8.5) and stratospheric aerosol geoengineering. For each scenario (climate change - RCP8.5, solar geoengineering - SG) a number of ensemble members were projected, 20 RCP8.5 members were run from 2010-30 with 3 extended to the end of the century and 20 SG ensemble members were generated from 2020-2100. Important implications for the results are the relative extreme nature of both scenarios (as RCP8.5 tracks the highest levels of projected emissions and temperature change, with the SG experiment designed to offset all warming above present-day levels) and the multiple locations in the injection of sulphur dioxide.

4.2.2 Population scenarios

Whilst RCPs (van Vuuren et al., 2011) are used to characterise possible future pathways for radiative forcing from greenhouse gas concentrations and the climatic changes that may arise from these, the Shared Socioeconomic Pathways (SSPs) outline a number of options for the development pathways of socioeconomic variables. The most recently devised climate change pathways have now been developed to incorporate both the RCP and SSP, however these were not being used at the time that the GLENS project was conducted. A number of these SSPs (Table 4.1) will be used in this research and they are designed to be used in combination with the RCPs to generate the possible range of future climate change scenarios and impacts for the globe, based on both emissions and socioeconomics, as well as explore mitigation and adaptation techniques (O'Neill et al., 2014). Not all of the combinations between the 5 SSPs and 4 RCPs are compatible. For example, SSP1 (where the global population follows a sustainable development route) is not compatible with RCP8.5 (the highest projected emissions scenario where anthropogenic greenhouse gas emissions continue to rise unabated). Each of the SSPs is faced with societal challenges from climate change, be that adaptation, mitigation, or both. Of the scenarios, SSP1 and

SSP4 both see low mitigation challenges due to rapid (or reasonably rapid) development of technologies to provide low carbon energy (O'Neill et al., 2014). Given that implementation of solar geoengineering is only likely in a future world where greenhouse gas emissions remain high and there has not been sufficient development of this low carbon infrastructure, it seems that only SSP2, SSP3 and SSP5 are sensible future scenarios to consider. Figure 4.2 depicts the global population trends until 2100 under these 3 SSPs. The SSP scenarios were chosen to depict future population projections because they are constructed in a way that fits with the climate projections (RCP8.5 and SG injections based on initiation from RCP8.5) to be used in this research and because they offer a wide range in the future landscape of global populations.

Table 4.1: The SSP scenarios (O'Neill et al., 2014).

	Short description	Details of the SSP
SSP2	Middle of the Road	Recent trends continue but decreased use of resources and energy.
SSP3	Fragmentation	Extreme poverty and population growth mean it is difficult to either mitigate or adapt.
SSP5	Conventional Development	Good economic growth makes it easy to adapt, but difficult to mitigate the effects of climate change as there is still mainly fossil fuel energy provision.

4.2.3 The WCI

In order to estimate the WCI, values for both the total volume of water available within a given catchment and the number of people living in that area are required. An estimate is then made for the water available to each individual in the catchment by dividing the total volume of water by the number of people in the catchment, to give the m^3/capita/year.

Drawbacks of this method include that there is an assumption of uniform distribution of the people in the catchment as well as a uniform distribution and availability of the total volume of water in the catchment. This is especially problematic in highly urbanised settings where the WCI can underestimate water scarcity, due to localised areas of high population density within a large catchment in which the total runoff available cannot necessarily reach the people who need it. Conversely, overestimation of water scarcity may occur in areas where populations have access to runoff from neighbouring, less populated, catchments. It is clear that the ease of access to this natural resource varies (sometimes widely) both spatially and temporally, depending not only on settlement locations and physical distribution but also on management practices within each area (Liu et al., 2017, Rijsberman, 2006). Kummu et al. (2010) also highlight how if the threshold for water

scarcity in a catchment is reached, then all of the people living in that catchment are seen to be living in water scarcity. However, in reality it is unlikely that all of these people are actually experiencing water scarcity due to this uneven distribution of water. Water consumption can differ rather significantly between regions, cultures and climates which adds another layer of complexity (Rijsberman, 2006). This being said, much of the water within a catchment is not used for personal consumption and the WCI also does not consider how the use of industrial and agricultural practices differ across regions. Despite these limitations, the WCI is still considered to be a useful measure of global and regional water scarcity; but analysis and interpretation of results from research undertaken using this metric must bear these factors in mind.

Uncertainty in WCI calculations can arise from either of the two input variables; runoff projections vary depending on the Global Climate Model (GCM) and/or Global Hydrology Model (GHM) used and there are a number of different possible paths for future population change to take. In this chapter multiple models have not been used to make projection, however 3 scenarios of future population are used, along with runoff from 20 ensemble members outputted directly from the GLENS modelling (allowing for intramodel but not intermodel variation to be examined). The measure is highly reliant on the population numbers for the catchment and, whilst under historical settings this is reasonably reliable, for future calculations this results in a large degree of uncertainty. In an attempt to encapsulate some of the population dependent variation, and help understand the influence of population on water scarcity values, regional and global WCI estimations are made for 3 future population projections. Additional uncertainty is also dependent on the metric for water scarcity that is used (Alcamo et al., 2007), however only the WCI will be considered here.

The scale at which water scarcity is analysed is also critical. Here water scarcity is calculated at the catchment level, with these values then aggregated to give regional and global figures. However, calculation at the country (Schewe et al., 2014, Arnell, 2004) and grid cell (Arnell et al., 2011, Oki et al., 2001) level can also be used. Whilst investigation at the grid cell scale can lead to over estimation of the number of people living in water scarcity due to water transfer between grid cells, analysis at the much larger country scale can result in an under estimation in the number of people exposed. This is due to the possibility for small pockets of water scarcity to exist within the larger country which are masked when the total country population and water resources are used to make calculations (Schewe et al., 2014). In this research the catchment scale has been used, as it seems logical to make calculations for a physically based water scarcity measure derived

from physical boundaries, although it must be acknowledged that this ignores any inter-catchment transfer within a country. The numbers of people exposed to water scarcity is, however, assessed at the country level (through the use of Sub-regions - the UN geoscheme groupings of multiple countries around the globe (United Nations, 2019)) because it is important to consider which populations may collectively be most exposed to this resource challenge from a social and political point of view. People are mobile, catchments are not, therefore in order to calculate how water scarcity changes through time it is important to consider how a country's population may fluctuate. Figure 4.4 shows the distribution and location of the Sub-regions across the globe. These Sub-regions have been used here as opposed to the Hydroregions which were used for Chapters 2 and 3, because whilst largely similar in their global divisions, the Sub-regions are devised to represent groups of populations; an important aspect of water scarcity.

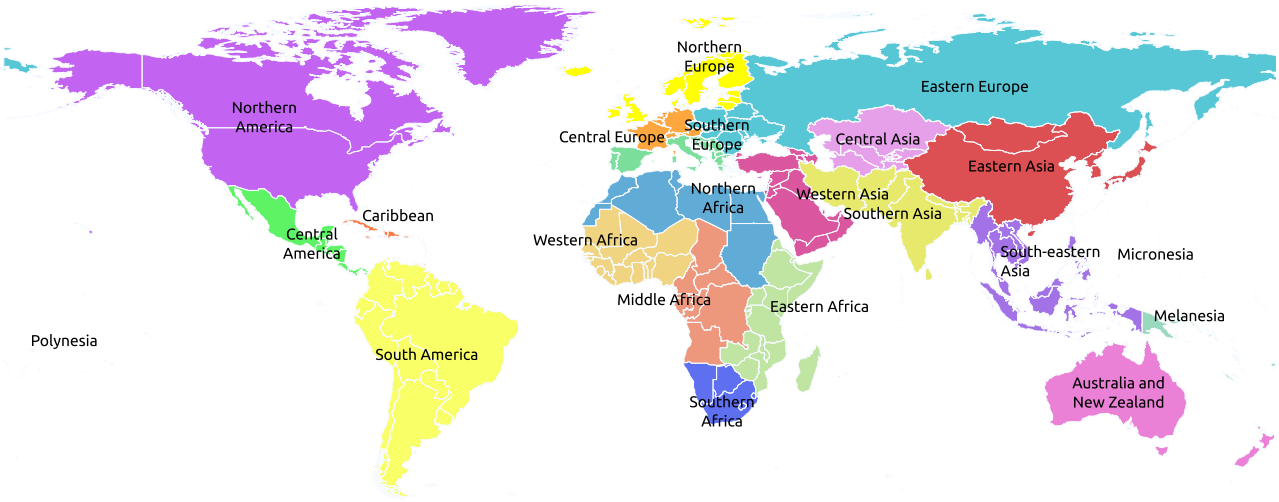


Figure 4.4: The Sub-regions of the globe as defined by the UN geoscheme (United Nations, 2019).

The river catchment boundaries across the globe were characterised using the drainage direction map (DDM30, (Döll and Lehner, 2002)) to give 11,558 global catchments. Of these catchments, those in Antarctica and Greenland were removed from the Sub-regions in the United Nations Geoscheme (United Nations, 2019); which is used here to classify Sub-regions of the globe and allow finer resolution analysis than global summaries. The catchments covering Greenland were removed due to the challenges faced in reliably calculating runoff in this area, leaving the remaining 10,741 catchments which were to be used in Global and Sub-region WCI calculations.

Figure 4.5 provides an overview of the data pre-processing required for the WCI calcula-

tion. To obtain the total volume of water in each of the 10,741 global river catchments used in this study, global total runoff (surface and sub-surface) for each of the 20 RCP8.5 and 20 SG ensemble GLENS simulations was obtained at a 1.25 × ∼0.98 degree spatial resolution and monthly temporal resolution in units of mm s^{-1}. This global data was then spatially disaggregated to a 0.5×0.5 degree resolution using a mass conserving downscaling technique (remapcon in Climate Data Operators (CDO) (Schulzweida, 2019)) in order to match the spatial resolution of the population data to be used (SSPs) to calculate WCI. The remapcon operator in the CDO software uses First-order Conservative Remapping (Jones, 1999). To find the total annual volume of runoff in each of these grid cells, the depth of runoff was first converted to monthly totals and then multiplied by the area of the grid cell to give the monthly volumes of runoff. These were then aggregated to the yearly scale and this annual runoff within each 0.5×0.5 degree area unit was spatially aggregated to the 10,741 global river catchments, in order for WCI within each of these catchments to be calculated.

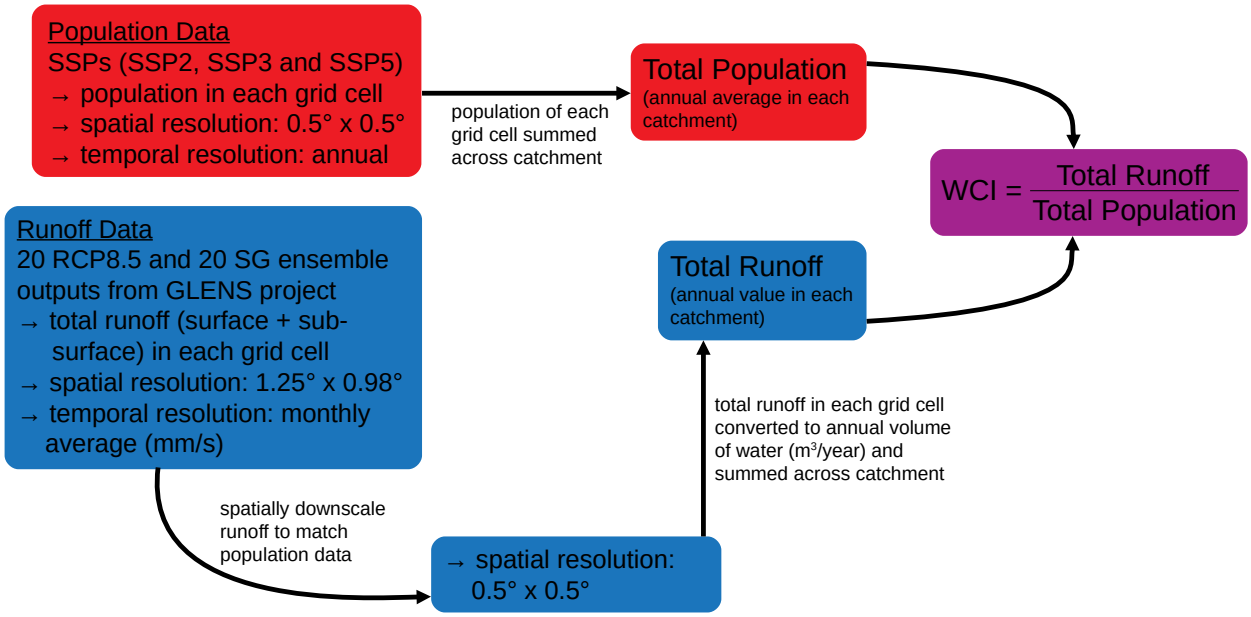


Figure 4.5: Schematic to show the data pre-processing required before calculation of water scarcity.

To complete the WCI calculation, an estimation of the total population within each catchment was required. Annual population projections from the SSPs 2, 3 and 5 were also collated at the 0.5×0.5 degree spatial resolution (O'Neill et al., 2014) and the population of each grid cell within the 10,741 catchments was aggregated. For each catchment, for each year, the annual volume of runoff in the catchment was then divided by this total

population in the catchment to give a WCI value in m^3/capita/year. If the WCI value for a catchment was <1000 m^3/capita/year of water, the threshold for severe (or chronic) water shortage (Falkenmark et al., 2007, Falkenmark and Molden, 2008, Kummu et al., 2010), then this catchment was defined as being in water scarcity and the number of people within that catchment was recorded.

Global figures are important for understanding the overall influence of solar geoengineering on water scarcity, but regional (and finer) scale changes are what influence the lives of each person on the planet. For this reason water scarcity was computed at two spatial scales: Global and Sub-region. Catchment scale values of water scarcity were aggregated to the Global and Sub-region levels and the total number of people in water scarcity within each of these two larger spatial units obtained. Not all of the catchments perfectly lay within one Sub-region and so where the catchments crossed multiple Sub-regions the fraction of the catchment which lay within each was used to assign to the Sub-region that fraction of the total number of people in water scarcity from the catchment.

4.2.4 Statistical Analysis

For each of the three SSP scenarios used and each of the Sub-region and Global spatial scales, the statistical difference between the SG and RCP8.5 ensemble runs was assessed at each year from 2020 to 2089. Due to the nature of the water scarcity metric, multimodal behaviour is exhibited as regions move in/out of water scarcity. For this reason a t-test is not an appropriate statistical method to apply, as it assumes the data is normally distributed. Instead a permutation test has been use to examine whether the difference in the median between the SG and RCP8.5 group at each year is statistically significant. The null hypothesis is that that there is no difference between the feedback and control group. A one-sided permutation test was used to detect when the SG value was statistically significantly higher than the RCP8.5 value. By permuting the data (mixing up the data group labelling so they may now be randomly assigned to the other group) and finding the difference in the median between the newly labelled SG and RCP8.5 group, then repeating this a number of times (200 permutations for each year were used here), it can be seen whether the difference in median between the original SG and RCP8.5 group is statistically significantly different to that for any of the permutations. For each year the differences in median values for each of the 200 permutations was ranked, then using the rank of the original data a p-value was estimated for that year:

$$\mathrm{p} = 1 - \frac{rank(x_0) - 1}{n} \tag{4.2.1}$$

where x_0 is the difference between the median of the original SG and RCP8.5 group and n is the number of permutations carried out. A high rank indicates that the difference between the median of the original SG and RCP8.5 group is in the upper tail of the distribution of differences in median and thus that it is statistically significantly different than the difference in median when the groups are randomly assigned members.

Given that the sample sizes for the permutation test differed, being 20 for solar geoengineering and 3 for climate change, it is interesting to investigate the power of the test. In general, as the sample size increases so does the power of the test. To investigate this, a sample size of 10 and 3 was used for the solar geoengineering group, with the sample (10 or 3) being randomly chosen from the 20 ensemble runs 30 times to give a representation of different sample sets. When examining differences between scenarios for the global totals, no real trend could be detected. However, there were notable patterns that could be seen at the Sub-region level. It was found that decreasing the sample size for the solar geoengineering group from 20 to 10 and 10 to 3 most often results in a later year being found as the first year of statistically significant difference between the climate change and solar geoengineering groups. In addition to this, the sample size of 3 could only find any significant difference between the two groups in around a third of the 30 random draws of 3 (from the 20 ensemble members). This indicates that as the sample size of the solar geoengineering group decreases not only does it take longer for a significant difference to be detected, but that when the sample size is very small (3) the differences between the groups often can't be detected. This can be explained by the fact that with both groups having such a small sample size (3) it is much harder to detect a difference between the original groupings and the randomly assigned groups when it comes to ranking them, because that original grouping is likely to turn up a few times as a randomly assigned group as well. Whereas for the larger sample sizes of 10 and 20 this is not so much a problem, as it is much less likely the original group would turn up as one of the randomly assigned groups, if at all. Table E.1 outlines the year the two groups are first significantly different for the solar geoengineering group sample sizes of 20, 10 and 3.

Something that should be acknowledged, in the context of conducting hypothesis tests for each Sub-region, is the problem of multiple-hypothesis testing. When a single hypothesis test is conducted (say at the 5% significance level) there is a probability (e.g. 5%) that the null hypothesis is incorrectly rejected and the result is a Type I error (false positive). However, as the number of hypothesis tests being carried out increases, the probability of committing a Type I error across the group of tests also increases - far beyond 5%. To address this, a number of techniques have been developed to correct for this amplification

of Type I error in multiple-hypothesis testing, broadly split into controlling for family-wise error rate (e.g. Bonferroni inequality) or controlling for the false discovery rate. However, these themselves can come with additional problems, for example use of the family-wise error rate adjustment, in controlling the overall error rate (probability of at least one Type I error), results in a reduced power of the test. Whilst it is necessary to appreciate the importance of issues with multiple-hypothesis testing, the number of hypothesis tests used here is relatively small and so despite still having an effect, that effect will be lower (although not necessarily insignificant) than if a larger number of tests were used.

4.2.5 Comparison with only population changing in the future

To allow for deeper understanding of what is driving water scarcity projections in the future an additional "Population" scenario was computed. The average annual runoff volume in each catchment was taken between 2010 and 2030 and this annual value was repeated for each year. The 3 population scenarios were then used with these runoff timeseries to determine the level of water scarcity if the climate remained the same but population trends still changed into the future. This, when compared to the scenarios of RCP8.5 and SG, allows for an understanding of how much of the future projection of water scarcity comes from population change and how much arises from climatic change.

4.3 Results

The global pattern of water scarcity ($<1000 m^3$/capita/year) projected under the RCP8.5 and SG scenarios using SSP2, SSP3 and SSP5 is shown in Figure 4.6. The graph gives the 5%, 50% (i.e. median) and 95% values from quantile regression with lowess smoothing applied. The shaded area shows the space covered by these quantiles for each scenario.

The total number of people exposed to water scarcity globally is seen to increase above 2010-2020 levels ($\sim$2-3 billion) in all RCP8.5 and SG scenarios (dropping back below 3 billion under the RCP8.5-SSP5 and SG-SSP5 scenarios for some of the ensemble members after around 2060 and 2080 respectively). Unsuprisingly, the highest water scarcity is seen under SSP3 where rapid population growth and poor energy technology developments lead to a world where the challenges for mitigation and adaptation are high. Global water scarcity is first shown to be statistically significantly (at p=0.05) higher in the SG scenario of a solar geoengineered future world than under the RCP8.5 scenario of climate change, from the year 2038 for SSP2, 2034 for SSP3 and 2043 for SSP5.

For each Sub-region, the numbers of people in water scarcity under each of the six climate-

population scenarios was computed in the same way as for Figure 4.6 and the statistical difference between the RCP8.5 and SG scenarios was determined. The Sub-regions in which the projections of water scarcity showed statistically significant differences have been included in Figure 4.7.

Of these Sub-regions, Southern Asia (Figure 4.7(a)) is seen to have by far the highest number of people exposed to severe water scarcity (as many as 3.5 billion by the end of the century). The SG scenario projects the levels of water scarcity above those for the RCP8.5, with this becoming statistically significant for all population scenarios on or before 2040. Figure 4.7(b) shows Western Africa to have the second highest water scarcity numbers, with as many as 1.3 billion people being affected. The solar geoengineering scenario is also shown to worsen the effects of water scarcity for this Sub-region.

Of the remaining Sub-regions with a clear strong signal Eastern Africa (Figure 4.7(c)) and Eastern Asia (Figure 4.7(d)) also show there to be increased numbers of people in water scarcity in a world under solar geoengineering as opposed to climate change alone. The Sub-region of Western Asia (Figure 4.7(e)) does show a strong statistically significant relationship in the other direction, however, with the SG scenario actually decreasing the number of people in water scarcity by 2055 for all SSPs. The two Sub-regions of South America (Figure 4.7(f)) and Central America (Figure 4.7(g)) both also show that solar geoengineering may help to reduce the number of people exposed to water scarcity due to extreme climate change.

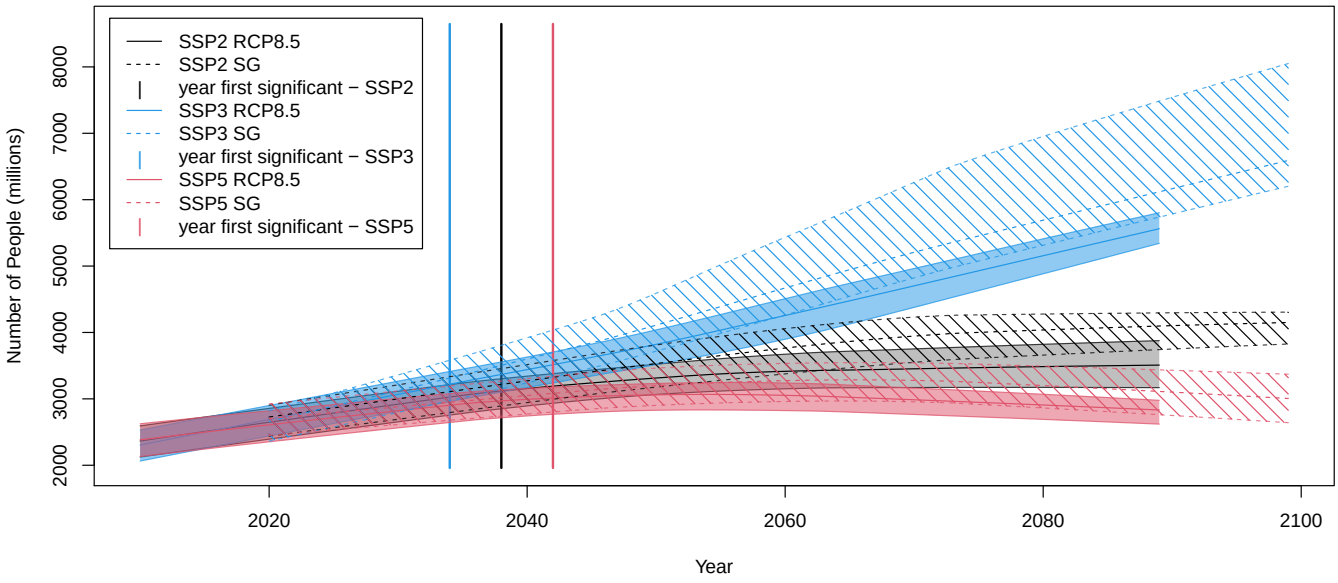
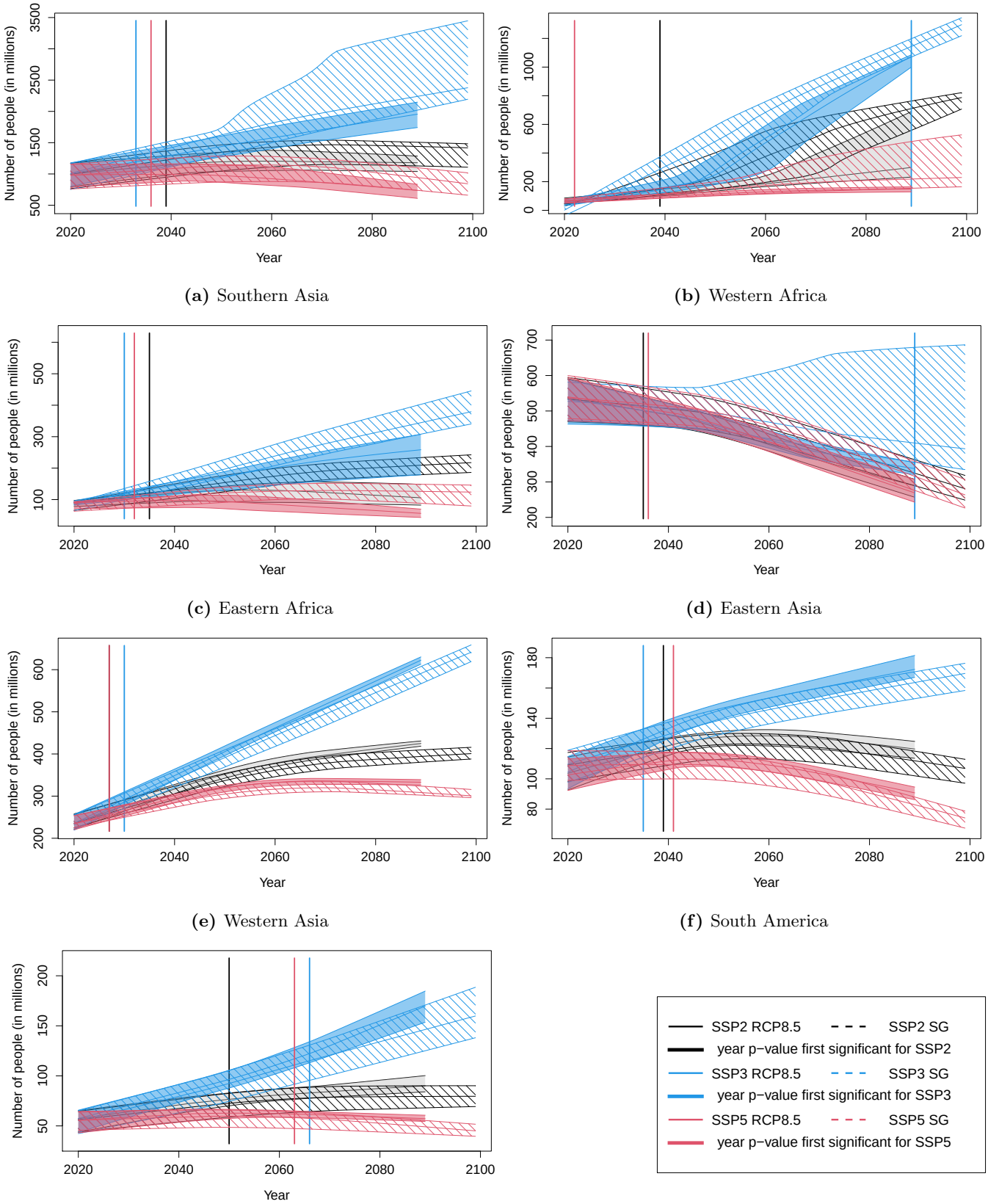


Figure 4.6: The number of people in water scarcity across the globe using the RCP8.5 and SG 20 ensemble members. The shaded area contains the 5th and 95th percentiles. The year the permutation test shows a pointwise statistically significant difference ($p<=0.05$) for the first time between the RCP8.5 and SG scenarios can be seen as a vertical line on the graph.



(a) Southern Asia

(b) Western Africa

(c) Eastern Africa

(d) Eastern Asia

(e) Western Asia

(f) South America

(g) Central America

Figure 4.7: The number of people in water scarcity in each Sub-region using the RCP8.5 and SG 20 ensemble members . The shaded area contains the 5th and 95th percentiles. The year the permutation test shows a pointwise statistically significant difference (p<=0.05) for the first time between the RCP8.5 and SG scenarios can be seen as a vertical line on the graph.

Figure 4.8 provides an overview of how water scarcity in each Sub-region may be affected by solar geoengineering. The cartogram maps display (for each population pathway) the percentage difference between RCP8.5 and SG in the future number of people in water scarcity for each Sub-region. The results could seem counter-intuitive and so to clarify, areas which show positive change on the graph (blue) are areas which would benefit from solar geoengineering, through fewer people being exposed to water scarcity under the scenario of SG than climate change. Negative changes (yellow to red), indicate the reverse, with solar geoengineering presenting a threat and projecting more people in water scarcity under SG than RCP8.5. The areas of each Sub-region are distorted to represent the number of people in the region, indicating the relative importance, when considered globally, of change in each Sub-region. Sub-regions in which the signal is similar across the 3 population scenarios would imply that any differences between future water scarcity projections of RCP8.5 and SG are driven more by climate. Whereas those areas exhibited more varied response between the 3 population pathways would indicate that future changes in population may have a large role in water scarcity in that region.

It can be seen across all of the Americas and under all population pathways that solar geoengineering would reduce the numbers of people in water scarcity in comparison to the climate change scenario. This is also true for Southern Africa, Southern Europe, Western Asia, Southeastern Asia and Australia and New Zealand. However, the significant difference is weaker in the latter 2 regions under SSP5. Conversely, an increase in the number of people experiencing water scarcity under SG in comparison to RCP8.5 is consistently seen across the 3 population pathways for Northern Europe, Northern, Eastern Western and Central Africa as well as Central, Southern and Eastern Asia; the magnitude and significance of the change does vary between SSPs. The greatest increase in water scarcity between SG and RCP8.5 is seen for Western, Central and Eastern Africa, where the change always has high statistical significance. High, but more variable, percentage difference between the future scenarios is also seen for Southern and Eastern Asia, where the change is greatest under SSP3. Areas with the least consistency in direction and magnitude of percentage change between RCP8.5 and SG include Eastern Europe and more specifically Western Europe - for which the greatest variability can be seen, with an increase in water scarcity under SG for SSP2 and 3 but a decrease in water scarcity under SSP5. Conversely, Eastern Europe sees a decrease in water scarcity for the solar geoengineering scenario when compared to projections for climate change under SSP2 and 3, with an increase (although weakly significant) under SSP5.

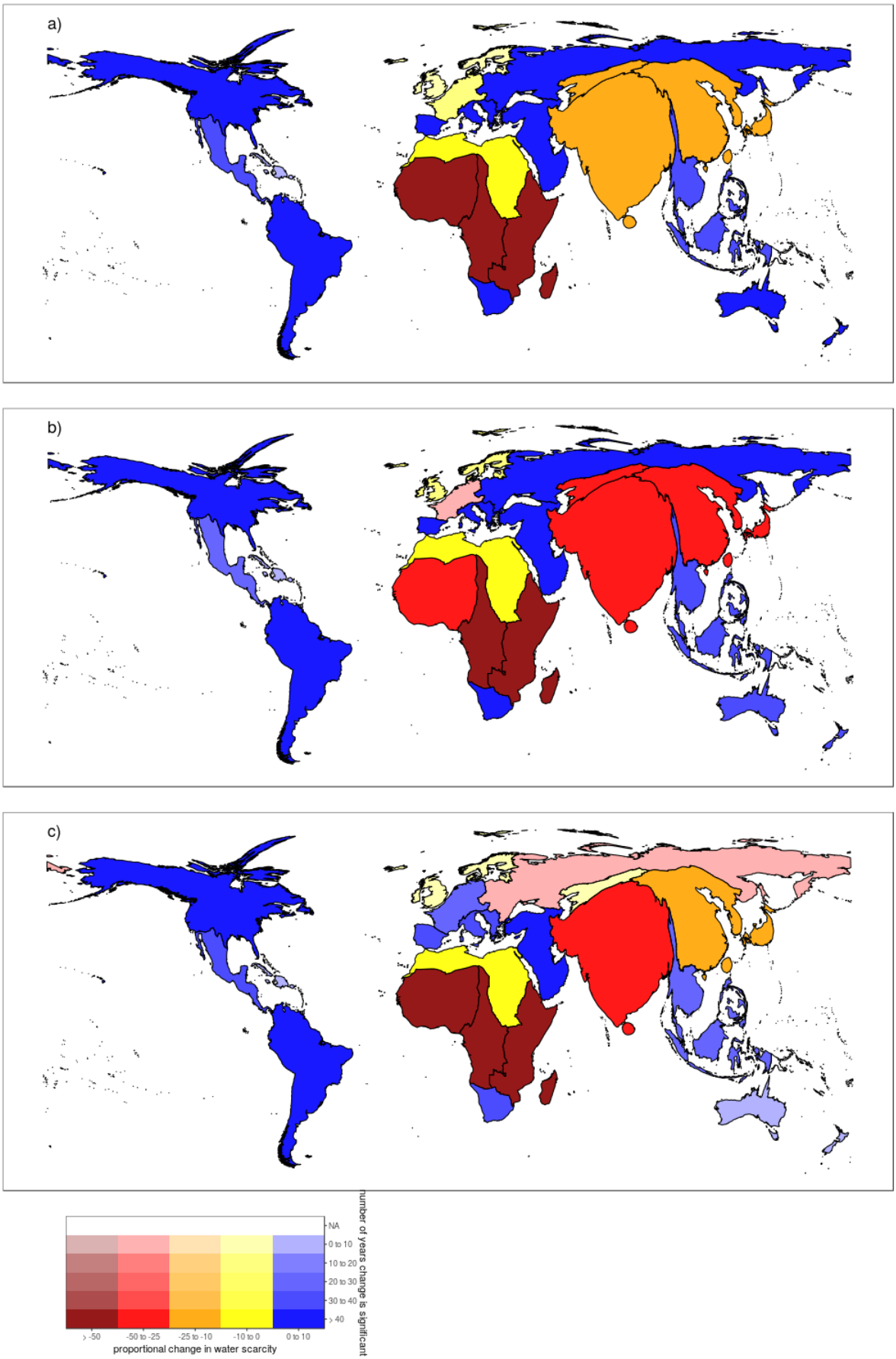


Figure 4.8: The 3 cartograms (under a) SSP2, b) SSP3 and c) SSP5 population projections) show the proportional future change in people exposed to water scarcity when the solar geoengineering scenario is compared to RCP8.5 ((RCP8.5 - SG) / RCP8.5 *100). The distorted areas of each Sub-region represents the number of people in water scarcity, the colour represents the magnitude of proportional change and the shading gives the degree of certainty in the signal of water scarcity through the total number of years across the ensembles for which the difference between the scenarios is statistically significant.

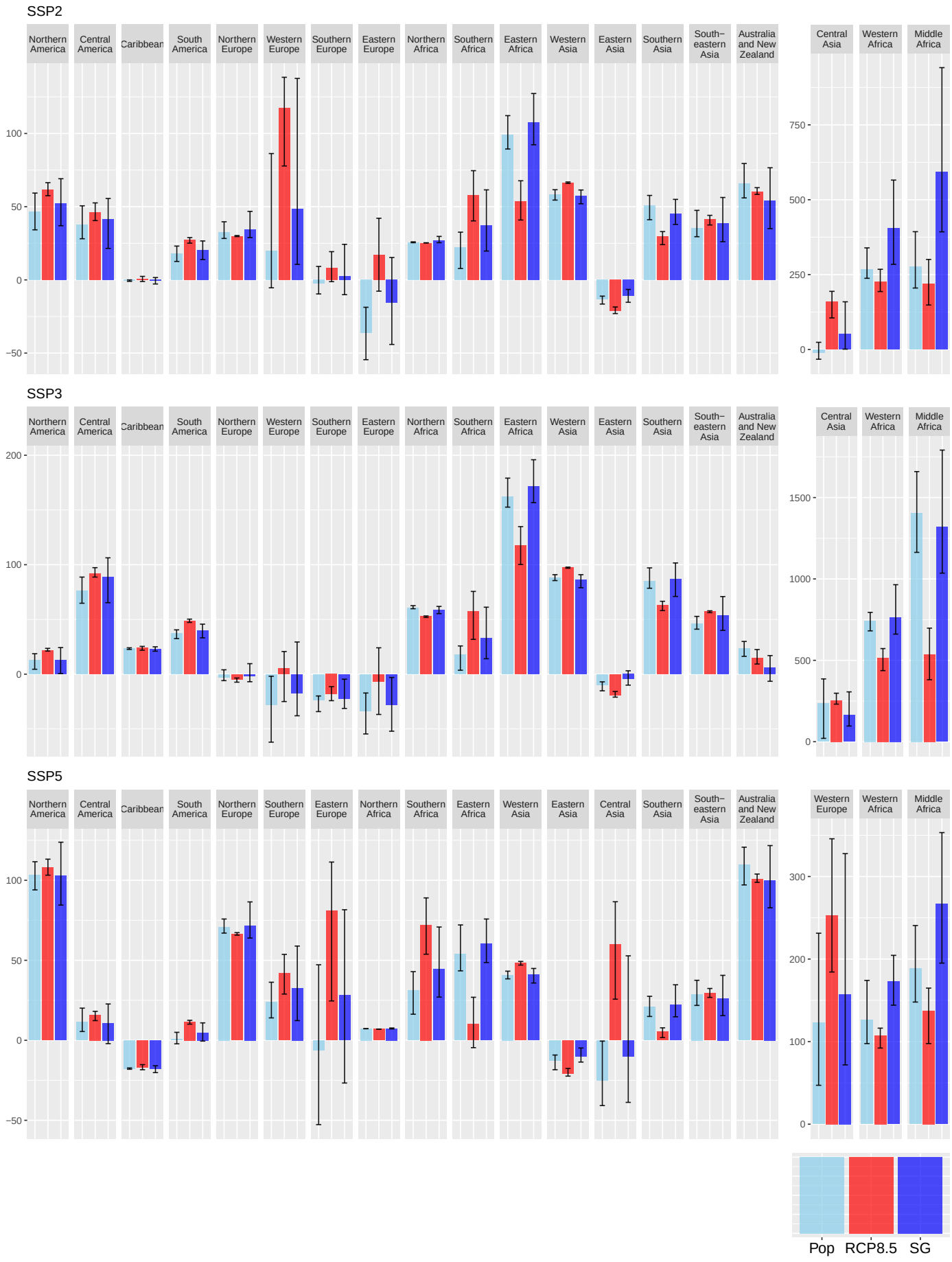


Figure 4.9: Percentage change in water scarcity from baseline (2010-30) under 3 population pathways (SSP2, 3 and 5) and 3 future (2050-70) scenarios (only change in population, RCP8.5 and SG). The bars show the ensemble mean, with the range being the maximum and minimum values across the ensemble.



Figure 4.10: Percentage change in water scarcity from baseline (2010-30) under 3 population pathways (SSP2, 3 and 5) and 3 future (2050-70) scenarios (only change in population, RCP8.5 and SG). The bars show the ensemble mean, with the range being the maximum and minimum values across the ensemble.

Figure 4.9 shows percentage change in water scarcity for each Sub-region in the future (2050-70) under three scenarios (only change in population, RCP8.5 and SG) in comparison to the baseline (2010-30). Note that this is different to Figure 4.8 which displayed percentage differences directly between the two future scenario (RCP8.5 and SG), with no reference to the baseline. Figure 4.10 contains the same information as Figure 4.9 but has been grouped by climate scenario to allow quick comparison of the affects of different population pathways on the projections. Figures F.1 - F.5 have been included in the Appendix with varying y-axes to allow more detailed consideration of percentage changes for each Sub-region and scenario. The additional scenario, here termed "Population", follows each of the future changes in population under the 3 SSPs, but keeps climate constant at the baseline period (2010-30), to allow understanding of how population changes alone would influence future levels of water scarcity. The graphs show the mean of the ensemble members with the error bars showing the maximum and minimum values across all of the ensemble members. The fact that only 3 ensemble members were available for the RCP8.5 projections could explain why sometimes these error bars have a smaller range, as the sample size was smaller. Melanesia, Polynesia and Micronesia have not been included because there is no difference in percentage change between the scenarios.

It can be seen that the percentage change in water scarcity from the baseline can vary considerably between SSP scenario and climate scenario. Frequently, changes under the Population (using 2010-30 baseline climate) and SG scenario are shown to be similar, with larger differences from the Population change shown when compared with RCP8.5. The change under SG is often in the same direction as for RCP8.5, but to a lesser degree.

On the whole the greatest projected percentage changes in population exposed to water scarcity occur under the SSP3 pathway, which is unsurprising given the largest future changes in population are seen for most areas under this pathway (one particular exception to this being Western, Southern and Eastern Europe).

Solar geoengineering is still shown to be beneficial to reducing future water scarcity for many areas and population pathways in the Americas (Figure F.1) in comparison to under RCP8.5. However, here it is shown that this is largely due to SG maintaining similar percentage increases in water scarcity from present as under the Population scenario, with RCP8.5 seeing larger increases.

Western Europe (Figure F.2(b)) is notable for just how dependent future projected water scarcity is on the population pathway used, and other parts of Europe also see large differences under the different SSPs. Other than in Northern Europe (Figure F.2(a)),

where RCP8.5 reduces future water scarcity projections, conditions are on the whole made worse in the future by climate change, with this affect generally being ameliorated by solar geoengineering, although not by as much as if the climate were the same as present-day.

The negative impact of solar geoengineering previously concluded for Western, Central and Eastern Africa (Figures F.3(b,c) and F.4(a)) is shown to arise from projections of climate change largely reducing increases in future water scarcity from the baseline in comparison to the Population and SG scenarios. In some areas under some pathways (e.g. Western and Central Africa under SSP2 and 5, Figure F.3(b,c)) solar geoengineering is actually shown to increase water scarcity in the future when compared to change under Population growth alone, the opposite to the effect climate change has. Southern Africa (Figure F.3(d)) sees much larger increases in future water scarcity under RCP8.5 than if the climate were not to change, which is not seen under SG. However, in Northern Africa (Figure F.3(a)) the reverse is true and although changes are relatively small between the scenarios, SG either exacerbates (SSP2) or maintains (SSP3) projections of future water scarcity in the absence of any further climate change, whilst projections under RCP8.5 could reduce the water scarcity exposure.

Of particular interest is the fact that conclusions drawn under the previous assessment, comparing future scenarios of RCP8.5 and SG directly, are complicated when change under population alone is considered. The projected change in Eastern Asia (Figure F.4(c)), which is shown to have large and significant increases in water scarcity under SG compared to RCP8.5, only arises because all the scenarios predict a decrease in water scarcity when compared to present, with SG reducing water scarcity to a lesser degree than RCP8.5 does (which was previously interpreted as solar geoengineering increasing risk of water scarcity in the future when compared to climate change). In fact, the scenario of solar geoengineering may slightly improve conditions beyond just population change alone, which is an important finding given the population in Eastern Asia is large. It is also interesting to note that rather unusually the direction and magnitude of percentage change is very similar for all three SSPs. The significant increase in water scarcity under SG, when compared to RCP8.5 projections, for Southern Asia (Figure F.5(a)) arises majoritively from the underlying population increase, with climate change under the RCP8.5 scenario counteracting the effects of increased population through increased runoff values.

Western, Central and South-eastern Asia (Figures F.4(b,d) and F.5(b)), however, seem to benefit from solar geoengineering when projections are compared to those for RCP8.5. The

most interesting trends occur across Central Asia (Figure F.4(d)), where the results differ quite considerably between future population pathways. Large increases in percentage change of water scarcity from the baseline are seen under RCP8.5 for SSP2 with little change under the Population scenario and much smaller increases under SG. Similarly, under SSP5 climate change is projected to increase future water scarcity (although to a lesser degree than under SSP2), whilst the Population and SG scenario see small to negative mean trends (although there is a huge range in the projections seen for SG). Under SSP3 on the other hand, there are much smaller differences between the three future scenarios, with Population also hugely increasing water scarcity levels here.

The change seen for Australia and New Zealand (Figure F.5(c)) suggests that all climate change (RCP8.5 and SG) could improve the conditions of water scarcity in the future when compared to change in population alone, although the percent changes are very dependent on the population pathway.

4.4 Discussion

It could be assumed that any method which can prevent large scale climate change and preserve climate conditions closer to the present-day would be a positive thing, and when considering the effects at a global scale this is undoubtably true. However, whilst solar geoengineering will likely maintain conditions closer to the present-day this does not mean that there will not be future regional impacts. There are likely trade-offs to be had between areas which may benefit from the climate being preserved at levels closer to the present-day, or in fact those areas which may see positive change (in terms of annual water scarcity) under climate change.

When totalled across the globe, the number of people living in catchments exposed to water scarcity is shown to be greater in a solar geoengineered world than one experiencing high levels of climate change and these findings are consistent across the 3 population pathways. Note that the WCI estimations for the number of people exposed to water scarcity globally calculated here, show agreement with the annual WCI projections of Gosling and Arnell (2016) of 2.6 billion people in water scarcity by 2020. The greatest proportion of the populations exposed to water scarcity live in East and South Asia, which is also found by Gosling and Arnell (2016) and is somewhat unsurprising given the large populations in these regions. The largest percentage increases in water scarce populations occur in Western and Middle Africa, and Hanasaki et al. (2013) also corroborate Africa as the region with the largest growth in future population experiencing water stress.

Rather different projections in future global numbers of people in water scarcity can be seen under each of the 3 population pathways. Despite the total projected population values being lower (due to differences in the method used), the results here show agreement with Hanasaki et al. (2013), with the largest global population in water scarcity projected under SSP3, followed by SSP2 and SSP5. Arnell and Lloyd-Hughes (2014) determine, when examining WCI projections from 19 models under the RCP8.5 SSP2 pathway, that the majority of the variation in the total global population projected to experience water scarcity arises from differences in the projected numbers of people in water scarcity across South and East Asia. This is due to the large proportion of total population exposed to water scarcity living in this area. Gosling and Arnell (2016) reach a similar conclusion and this highlights the importance of considering multiple model outputs when drawing conclusions, particularly for such highly populated regions.

The impact of the solar geoengineering scenario on levels of water scarcity becomes more complex when examined at the Sub-region scale. Catchments in populated areas, for example eastern to central North America, parts of Africa, northern to central China and the Mediterranean (Hanasaki et al., 2013) have been projected to see a rise in water resource stress conditions under climate change. On the other hand, Arnell (2004) project that South and East Asia are likely to see a decrease in water scarcity when examined at the annual scale, due to increases in total runoff in these regions. However, the projected seasonal distribution of this additional water is uneven, with the increase in precipitation largely being in the wet season, with little increase in runoff during the dry season (Arnell, 2004). This therefore means that any conclusions drawn from annual calculations may overstate the reduction in future water scarcity for these regions. Indeed, Mekonnen and Hoekstra (2016) found when calculating monthly water scarcity that these areas experienced water scarcity outside of the monsoon season. The results shown in this chapter, and calculated in the same way as Arnell (2004) using the WCI at an annual scale, also suggest a decrease in water scarcity across Eastern Asia under RCP8.5; whilst this decrease in exposure is importantly seen to be much smaller under the scenarios of population only change and solar geoengineering. Although Southern Asia is not reported to see a decrease in water scarcity from present under RCP8.5, the increase in exposure is much less than for solar geoengineering, which sees little difference than if climate were to remain the same as present-day and only population were to change. These are important conclusions and despite suggesting that in some areas climate change could be of benefit in alleviating water scarcity conditions at the annual scale, future research is warranted in investigating the seasonal water scarcity trends. Solar geoengineering on the other hand,

in maintaining the present-day climate more closely, could be interpreted as having more negative outcomes. It is clearly not as simple as this however, even in regions which may possibly see climate change reduce water scarcity exposure when temporal change is taken into consideration. Other concurrent negative climate impacts of climate change could be occurring, for example an increase in tropical storms or flooding, and the relative benefits or drawbacks of climate change vs. solar geoengineering must include consideration of all potential hazards.

When employing a method which takes account of daily differences in water supply and demand, allowing greater consideration of timing and whether water is available when it is needed, Hanasaki et al. (2013) find that few areas of the world see a reduction in water stress conditions. In contrast, when an annual accumulative runoff method is used, they find water scarcity to be alleviated for more areas under climate change (Hanasaki et al., 2013). By including seasonal excesses of water (i.e. often for areas which experience a wet and dry season, the increase in annual runoff comes from increased runoff in the wet season, which is not available during the dry season), the complexity of water availability throughout the year is better accounted for under climate change. Mekonnen and Hoekstra (2016) also demonstrate how calculations of water scarcity based on annual values can greatly underestimate the numbers of people exposed to water scarcity and this should be considered in any future research into water scarcity under solar geoengineering. Hoekstra et al. (2012) and Wada et al. (2011b) calculate water stress at the monthly timescale in order to include this temporal complexity in water supply. Future work which examined water scarcity at a finer temporal resolution could produce very interesting results if indeed it were shown that water scarcity was less impacted at say the monthly scale under the scenario of solar geoengineering as opposed to that of climate change, due to the more consistent levels of runoff throughout the year for SG.

Whilst some areas would see an increase in water scarcity in the future under solar geoengineering when compared to the projected effects under climate change, this could not be used to widely support a claim that solar geoengineering weakened the hydrological cycle as much of this comparative increase comes from maintaining present-day conditions in areas where climate change reduces water scarcity exposure. However, it must be understood that there are quite large differences in the variability of daily precipitation within each year under the RCP8.5 and SG simulations (Figure D.1). This is important to consider because whilst extreme daily precipitation will contribute to total annual runoff (and thus imply reduced water scarcity), this water may not be as accessible to the population as the same volume of precipitation falling over a greater number of days. There may

be an inability to capture all of the water in any extreme precipitation events and this increased irregularity in precipitation throughout the year may also hinder accessibility to the water resource. This effect, in addition to amplification of the seasonal variation mentioned above, could further contribute to an underestimation of water scarcity when calculated at the annual scale. The RCP8.5 precipitation seems to have more of these extreme precipitation days (shown through an increase in the standard deviation of daily precipitation each year over time, see Figure D.1), whilst the SG runs show smoother and more consistent daily precipitation. In reality, more of the water which falls in a solar geoengineered world may be more readily accessible to populations than under future climate change; given its more even distribution. These results suggest a more complicated picture than has been presented here, showing the numbers of people exposed to water scarcity rises under SG globally, in comparison to numbers under RCP8.5.

There is a spatial inequality in the projected impact SG will have on water scarcity across the globe and this raises important questions when considering technologies such as stratospheric aerosol injection which cannot be contained to localised areas and could be implemented by any country, with the impacts spreading beyond their borders. The issue of international cooperation is further confounded when examining water scarcity because many water resources are shared across international borders.

Despite the important differences that have been shown for future projections of water scarcity in a world where climate change is to some degree moderated, or not, by solar geoengineering, it is largely shown that overall population change will be the largest driver of future differences in water scarcity from the baseline. This is demonstrated both through the often large differences in projections of water scarcity under the 3 SSPs, but also through the calculation of a scenario of "Population" only change, where the climate remains at present-day conditions. The large percentage changes from the baseline in future water scarcity, which are projected even when only the population varies over time, indicate how significant population is to the reported numbers of people in water scarcity. This should be somewhat unsurprising given population is one of the two inputs to the metric, but it is interesting to see just how significant the changes in population could be and indeed that these are often more important in determining the future situation than any type of climate change. Vörösmarty et al. (2000) support these findings and show how population growth has a greater impact on water scarcity than climate change, with Wada et al. (2011a) citing anthropogenic drivers of water demand as having had a larger impact on past water stress than climate in a number of regions. Hanasaki et al. (2013) similarly conclude, when using the five SSPs for population scenarios, that the number of

people deemed to be in water stress is more of a response to the socio-economic scenario (i.e. water use dependent on population and development) than changes in climate.

Predictions for water scarcity are very dependent on the scenarios used to create them both in terms of the climatic and population trends and the results here should not be used to extrapolate findings about the influence of solar geoengineering on water scarcity beyond the specific GLENS scenario used. For this reason, further work must look at how water scarcity changes under a number of different solar geoengineering approaches and injection methods in comparison to the modelling of climate change. This is particularly pertinent given that it is known that the impact of solar geoengineering on the hydrological cycle is highly dependent on the method (Niemeier et al., 2013) and scenario. It would also be very interesting to see the results of solar geoengineering modelling experiments which aim to maintain present-day precipitation levels rather than temperature levels.

Uncertainty in estimations of water scarcity can result from: the climate model used to generate climate variables; the treatment of hydrological processes (which will alter runoff projections - particularly at a regional scale); the projections of future global populations and their water consumption habits and the measure employed to calculate a metric for water scarcity. Given this plethora of variables which can impact upon the numbers of people projected to be exposed to water scarcity, it is important to regard these findings as an initial assessment of water scarcity under solar geoengineering. Further work is required to address some of the uncertainties mentioned here, including the use of other water scarcity measures and calculation of runoff. However, these findings do indicate the importance of considering a wide range of impacts solar geoengineering could have, not only on climatic variables such as temperature, but how these effects can also cascade down to influence future populations.

The measure of water scarcity which has been implemented, although widely used, includes a number of assumptions made during its calculation. For example, it is assumed that the water available in the catchment can be evenly distributed to all those living in the region. This is clearly erroneous, given the difficulties of water supply in some rural areas, especially if they are far from streamflow in the catchment, as well as uneven precipitation across the basin due to topographic and climatic variability; these effects are felt more strongly in larger catchments. The WCI can be considered a "best case" scenario for water scarcity through assuming greater levels of water availability (given it does not take into account over-abstraction for human use) and spatial accessibility, through even distribution of water amongst the people in the catchment. In reality neither of these are

likely to be true and so the results here are on the more conservative side of future water scarcity projections. The choice of WCI threshold will also greatly influence the results, and whilst a threshold of 1000m^3/person/year is considered to signify severe water scarcity, use of a lower threshold (e.g. 500m^3/person/year which has been used to represent absolute water scarcity) would capture more extreme changes and differences between scenarios. Use of a threshold method can also be problematic and, despite the widespread use of the WCI, some are critical of the method and believe more research is needed to better validate the threshold choices with consumption rates around the world (Damkjaer and Taylor, 2017). An additional dimension of complexity not considered in the WCI arises from the interconnected global world we now live in, with the water we use as consumers not necessarily being derived from our home country. Virtual water use refers to the water associated with imported products and goods that was used in the country of origin to grow or manufacture the goods. Hoekstra and Mekonnen (2012) estimate the global annual water footprint to be 1385m^3/person/year, ranging from 2842m^3/person/year in the United States to 552m^3/person/year in the Democratic Republic of Congo.

The exclusion of spatial variability in water supply, when added to the previously mentioned effect of the annual method of calculation (assuming even temporal distribution), could further underestimate water scarcity. This suggests that the results from this chapter may be overly optimistic in terms of water scarcity alleviation from climate change in regions which see an increase in annual runoff. The WCI is also heavily influenced by the future population projections, which has been demonstrated in this analysis, and so caution must be taken in direct interpretation of future numbers of people in water scarcity. Rather it is safer to consider differences between scenarios in which the population changes in the same way under both. This research has also attempted to address some of these issues through the use of multiple population pathways, with all reasonable paths (i.e. SSP2, 3 and 5) under solar geoengineering being given equal consideration.

Despite its limitations, the WCI is a very useful metric for creating a general picture of global water scarcity and highlighting areas where high population density corresponds with lower annual runoff. However, it must be understood that the WCI does not account for global imbalances in the consumption of water or for abstraction rates. This "demand" side issue in the nature of water scarcity can be better encapsulated through calculations which include a use-to-availability ratio. Future research should look to compare water scarcity values and distributions using these complementary metrics, to explore uncertainties in projections of water scarcity under solar geoengineering and climate change with the use of various water scarcity measures. As population pathways also include assump-

tions about human actions, more divergent results may be found in the numbers of people exposed to water scarcity for each SSP pathway when a use-to-availability ratio is used in comparison to the WCI.

Whilst there are limitations to the WCI, it was chosen for this preliminary assessment of water scarcity under solar geoengineering for its ease of interpretation and ability to build up a general picture of trends across the world. This initial assessment suggests that, providing the method of stratospheric aerosol injection is designed to preserve more global climate variables than simply mean temperature, solar geoengineering can offer opportunities to alleviate increasing water scarcity seen under continued greenhouse gas emissions and climate change. However, in some areas solar geoengineering may present challenges, particularly when SG will maintain conditions closer to the baseline in cases where climate change is projected to reduce water scarcity below present-day estimates. Areas of particular interest to study water scarcity at finer temporal and spatial resolutions include those which see the largest differences in water scarcity projections under the two different scenarios. This is especially important for temporal resolution, in order to take account of uneven distribution of runoff increases across the year, which may have a larger impact on water scarcity projections under climate change.

4.5 Conclusions

Using the GLENS RCP8.5 and SG projections for global runoff, combined with population projections under the SSP scenarios, an initial assessment of water scarcity under solar geoengineering is undertaken, using the WCI metric of water scarcity. It is shown that the use of stratospheric aerosol particles injected at four global locations may increase global water scarcity in some areas during the next century above levels predicted under unmitigated climate change. However, this largely arises from solar geoengineering maintaining conditions closer to those of the present and raises interesting questions about how climate change, whilst largely projected to worsen future conditions, may be perceived to be beneficial in some places when water scarcity is calculated at the annual scale. This is clearly far too simplistic a conclusion, however, given many other climate factors will be altered, not likely for the best, and that the increases in runoff will not be evenly distributed throughout the year. However, it does highlight the challenges that may be faced in finding global agreement on a strategy for solar geoengineering given different regions are likely to see conflicting results, raising important ethical questions for the use of this technology. Of great interest is a principal finding that future changes in population are likely to have a larger impact on the degree of water scarcity than changes in climate

will, and that projections of future population are possibly more uncertain than those for climate. Future research is needed in order to evaluate how conclusions about location and severity of global water scarcity differ when different solar geoengineering scenarios, population projections, GCMs and water scarcity measures are used.

Chapter 5

Synthesis and Conclusion

5.1 Research Questions

This thesis set out to address a number of key issues in solar geoengineering research, including the problem of model uncertainty and the impacts on water resources; both in terms of the hazard (drought) and the risk (water scarcity). It was found that outcomes were heavily influenced by the model used, which needs to be remembered when attempting to draw wider conclusions from any modelling results. It was also demonstrated that, by and large, the scenario of solar geoengineering examined in this research could offset many negative consequences to water resources projected under extreme and unmitigated climate change. However, particularly when the dimension of human change is also included in the analysis (i.e. through the impact of population change on water scarcity), some regions which see the projected values of annual runoff increase under climate change may experience worsened conditions in a solar geoengineered future, with a comparative increase in levels of future water scarcity thanks to an absence of the increase in runoff under RCP8.5.

Even without consideration of different solar geoengineering scenarios, it has been shown in Chapter 2 that projected modelled outcomes can vary quite considerably when different models are used. This is unsurprising, as intra-model uncertainty is a well-known issue in climate change research. Inter-model variation also often presents large differences between model runs, something which has been seen and addressed in this research to an extent through the use of multiple scenario ensemble members. Studies often show that the mean (or median) of the ensemble across a number of different models performs better than any individual model (Sillmann et al., 2013). However, the multi-model mean will not always improve performance above that of a single model, for example if the model ensemble contains mostly models with a positive bias (Zaherpour et al., 2019). In addition to simply taking the mean across a number of model outputs, more sophisticated multi-model combination approaches involving machine learning to weight each model's contribution can also be implemented, although the complexity can impede physical interpretation of results (Zaherpour et al., 2019). Regardless of method, it is useful to consider results from different models when examining a specific climate scenario and the modelling intercomparison project set up for solar geoengineering, GeoMIP, works to achieve this goal. However, there are presently only a limited number of different models sophisticated enough to model stratospheric chemistry, which hampers the ability to properly assess projected outcomes of stratospheric aerosol geoengineering. When examining one specific solar geoengineering output (that of the GLENS project) and contrasting this to projections under the RCP8.5 realisation of climate change, Chapter 2 found that simulated

results generated through an "offline" or "online" method had large impacts on the runoff results. It was shown that whilst neither modelling output could be considered generally superior to the other, with both more poorly reflecting the observed values in different locations and in different months/seasons, the "online" model tended to overestimate runoff, with the "offline" model frequently underestimating runoff. It is also interesting to note, that taking an ensemble mean of the two sets of model projections would have better fit the observed data in a number of instances.

As the "online" runoff outputs are the projections used in Chapters 3 and 4 the often overestimation of runoff by the model is important to note, suggesting to some extent that as runoff projections are largely higher than observed values, conclusions about the severity and extent of drought and water scarcity are likely on the more conservative side. Differences between the model projections are particularly important in the hydroregions of Northern Dry Africa and the Middle East (areas prone to drought), where there are stark differences in the two sets of model projections, with the MacPDM outputs showing large negative percentage changes in mean annual runoff from the baseline under both RCP8.5 and SG, and the GLENS outputs showing clear positive percentage change in all cases. Whilst the results are most probably individualistic to the specific "offline" model (the GHM MacPDM.17) and "online" model (CESM1(WACCM)) used, it can be seen that the coupled model nature of the "online" model does generate considerably different results to that of the "offline" model. As climate models become more comprehensive and detailed it would be extremely interesting to examine more generally the difference between results generated "online" by GCMs and ESMs and those from which runoff production is generated "offline" with GHMs forced by climate outputs from the GCM/ESM. Where do the greatest variations in model outcomes arise from, is there more variation between "online" and "offline" models or within one of these groups? Is it possible that future climate models will become so good at characterising all parts of the earth system that global hydrological models will no longer be used? No doubt climate models are continually developing and a number now encompass enough of the processes on Earth to be termed Earth System Models. However, this is not true for all global models of the climate, with many simpler models not as sophisticated as CESM1(WACCM), the model used to generate the GLENS modelling results. CESM1(WACCM) models atmospheric chemistry and other processes which enable study of aerosol injections through solar geoengineering. However, other models lack these components and can only currently model solar dimming experiments (where the incoming solar radiation is directly reduced in the model to replicate the influence of stratospheric aerosols). As mentioned before in this

thesis, there is a duality between improving the representation of the real world in climate models and the complexity of these models making them increasingly at risk of becoming too hard to discern what is causing changes in the projected climate; in addition to the risk of misleading us into thinking they are more correctly reflecting the real world as a result of this increased complexity. Another issue is that different models often share components and this hampers a more rich understanding of possible model variation and outcomes. Nonetheless, the greater the variety of modelling that is undertaken, the more we can draw together common themes and results, which is critical for understanding of possible future impacts of solar geoengineering.

With this appreciation for model variability and runoff response from GLENS when compared to observed values, Chapter 3 considered the physical hazard posed by climatic changes to global water resources under a scenario of unmitigated climate change (RCP8.5) and solar geoengineering (SG). Large changes in the 20 year minimum monthly return levels as well as the value of Q95 and Q80 low flow runoff and number of consecutive months below this threshold were projected under the scenario of climate change, which were often, but not always, offset through use of solar geoengineering. Areas in which solar geoengineering particularly presented opportunities in ameliorating the projected negative impacts of climate change on a number of drought measures included southern Central Europe, areas of North and South America, the Middle East and Turkey, parts of Australia and East Asia. However, there were regions where solar geoengineering could be considered a threat in the future, worsening drought conditions when compared to those under RCP8.5 climate change, for example in many Boreal and some Northern Mid Latitude catchments, parts of eastern India, Bangladesh and northern areas of Southeast Asia. However, this increase in low flows under climate change may not always be a positive effect, for example in Boreal catchments. Whilst drought only identifies the hazard to human populations from changes in water resources, it also importantly represents the hazard to the environment and ecosystems which are valuable in their own right, not just for their wealth of life and beauty but also for the role they play in moderating the climate, and any change from "normal" conditions may be negative.

When the analysis steps beyond just consideration of hazard to examine risks to future populations the picture becomes more complex. Chapter 4 outlines the impact of climate change and solar geoengineering under the scenarios used in the GLENS project on future projections of water scarcity. Importantly, population projections are an additional dimension of change in this analysis and 3 future pathways have been used, representing different total global population values as well as regional changes. By considering

3 possible climate scenarios under these 3 population pathways, that of an unchanging climate, RCP8.5 and SG, it is possible to attribute some future changes in water scarcity as resulting from changes in population or climate. It is found that some of the largest changes in the future arise from the future projection of population change, with climate having a more limited influence. Large uncertainties exist in the future total values and composition of global populations (Keilman, 2020), with large differences often seen within regions under the various Shared Socioeconomic Pathways (SSPs) (O'Neill et al., 2014). Wide ranging projections of fertility, mortality and migration all contribute to this uncertainty (Azose et al., 2016). It is arguably harder to predict future patterns in human behaviour than those of the climate, meaning we may never be able to greatly reduce the uncertainty in future far off projections of water scarcity.

When the influence of climate scenario is examined, it can be seen that solar geoengineering may exacerbate water scarcity in Southern and Eastern Asia and Eastern Africa, although these results are mostly attributable to population changes which are counteracted by increased annual runoff under the climate change scenario. However, these findings may be largely influenced by the annual method of water scarcity calculation, as increases in annual runoff in a wet gets wetter, dry gets drier world of climate change will often be seen in seasons already receiving adequate water supply. Population change also seems to have some influence on the worsened outcomes for water scarcity in Middle and Western Africa under SG when compared to RCP8.5, but there appears to also be a reasonable influence from solar geoengineering itself here. Areas which clearly seem to benefit from solar geoengineering include Northern, Central and South America, as well as much of Europe and Australia and New Zealand (the only region which really sees more beneficial responses from solar geoengineering than a maintained present-day climate, i.e. the scenario where only population is changing into the future). Again, on the whole this is attributable to maintaining water scarcity closer to levels seen when only population changes.

Many of the key regions which could benefit and suffer from solar geoengineering show agreement for both the measures used to assess drought and water scarcity. Much of the Americas, Europe, Australia and the Middle East could see beneficial outcomes under the scenarios used in this analysis, whilst parts of Southern Asia, Southeast Asia and many regions of Africa (Western, Middle and Eastern) could see conditions exacerbated beyond the projected changes under unmitigated climate change. The divide between the projected winners and losers in this specific scenario of a future solar geoengineered world raises important geopolitical questions. If some regions are to benefit more from solar geoengineering, who gets to decide whether and what degree of solar geoengineering is

to be implemented? Is it even ever possible to reach global agreement on deployment or will history repeat itself with wealthier nations making changes to the climate and taking resources for themselves at the expense of more socioeconomically vulnerable countries? Future global power shifts may also have a role to play in this.

5.1.1 Road ahead for Solar Geoengineering?

As has been identified a number of times throughout this thesis, there is no magic wand to immediately halt and reverse the damage that has been done to our planet through anthropogenic emissions of greenhouse gases; which have developed in earnest since the industrial revolution. Even if we were to stop all emissions tomorrow, through the greenhouse gases already in the atmosphere we are committed to living with this present-day warmer world (than pre-industrial) over the coming centuries (Solomon et al., 2009, Matthews and Solomon, 2013, MacDougall et al., 2020) and with every year that passes without significant emissions reductions we are making the future situation worse. Preventing extreme warming and the worst effects of climate change, consequently preserving the wealth of biodiversity and the largely comfortably habitable conditions of the earth for humans, should surely represent a cause worth investigating all avenues of possible solutions for. There still exists considerable uncertainty in the science of solar geoengineering and this rightly raises concerns and caution about the technology. Fuelled by the uncertainty still surrounding possible outcomes of solar geoengineering, particularly due to impacts being dependent on method, and the global nature of these impacts which will not be equal in all locations, much research has also sprung up surrounding negative consequences of poorly executed solar geoengineering deployment. If countries were to go out on their own and start solar geoengineering, regional actions could have consequences further afield. For example, Jones et al. (2017) find that southern hemisphere only injection enhances tropical storms in comparison to global hemisphere injection and Haywood et al. (2013) detailed how northern hemisphere only injection could worsen Sahelian drought. Many also cite concern surrounding sudden cessation of solar geoengineering which could lead to rapid temperature rise and greatly threaten life on Earth. These concerns are all well-reasoned and serious consideration of them should be given, as such researchers in the solar geoengineering community have worked to address many of these issues. For example, Parker and Irvine (2018) discuss how termination shock is much more of an unlikely consequence of solar geoengineering than widely considered and Heyen et al. (2019) explore the free-driver problem (often discussed as a potential issue that if a single country or actor had a strong enough incentive to determine the set amount of global cooling, that they would implement solar geoengineering without global cooperation) and find that

counter-geoengineering could prevent this, although not without consequences.

Extensive thought has been given to the governance (Barrett, 2014, Jinnah et al., 2019, Reynolds and Horton, 2020, Reynolds, 2021) and ethics (Gardiner, 2011, Svoboda, 2012, Wieding et al., 2020) of solar geoengineering and there are strong feelings on both sides of the debate. The discussion surrounding these topics is beyond the scope of this work, which focuses to better understand the science that underpins these arguments. However, it must be recognised that the ethical and governance challenges of solar geoengineering are by no means smaller than the scientific ones. Alongside this, perpetuation of general assumptions about solar geoengineering as being truth are damaging (Reynolds et al., 2016) and are a reason for concerted efforts into improved modelling so we can better understand the risks and benefits solar geoengineering poses, as well as what climate outcomes it could and could not actually achieve.

Despite considerable effort and progress by those researching solar geoengineering, it has only been a serious topic since the 2000s (with Crutzen (2006)) and modelling has only really begun more formally in the last decade. This poses the question, if we are to need this technology as a complementary method to address climate change, can we learn enough fast enough? A reasonable amount of research has sprung up over the last decade, Figure 5.1 shows the numbers of publications which mention solar geoengineering or solar radiation management, and these are almost equally divided into those which consider the science of solar geoengineering and the ethics and governance challenges.

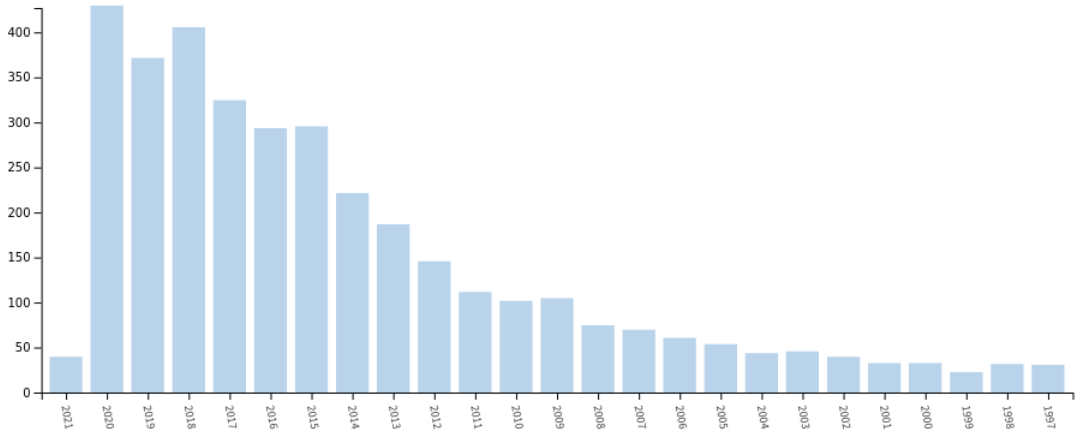


Figure 5.1: Year of "solar geoengineering" or "solar radiation management" publications from Web of Science search, February 2021.

Future developments may mean we can design a "perfect" solar geoengineering intervention for climate change which does not have some of the drawbacks of current methods, namely the unequal offsetting of precipitation and temperature changes. For example,

recent work by Seeley et al. (2020) has examined the possibility of designing spectrally specific methods of solar geoengineering. By targeting solar radiation management and the reflection of incoming shortwave radiation in just a specific set of wavebands, it may be possible to offset the warming forced by increased atmospheric CO_2 at both the tropopause and the surface. This dual offsetting would alleviate, in their simple horizontally homogeneous model, the reduction in precipitation that comes with fully offsetting the mean temperature rise from increased tropospheric CO_2 when employing spectrally uniform solar dimming experiments and other means of stratospheric aerosol geoengineering; simultaneously offsetting mean precipitation and temperature rise. They acknowledge that further work using fully coupled and spatially varying ESMs would be required to understand if regional precipitation could actually be returned to present-day conditions through this method, but it is nonetheless a promising step forward. It may be far too expensive to ever use this method and the technology to do it is also still not available, but this is not to say it will not be developed in the coming decades and some interesting methods which could facilitate spectrally specific solar geoengineering have already been conceptualised (Teller et al., 1996, Angel, 2006, Keith, 2010, Khlebtsov and Dykman, 2010, Berkovitch et al., 2010). Regardless, stratospheric aerosol geoengineering with sulphate aerosols will not be spectrally uniform (as in the solar dimming experiments such as GeoMIP's G1) and improved understanding of how regional precipitation changes are impacted could be gleaned through using the method Seeley et al. (2020) have devised.

Another potentially productive avenue, in terms of avoiding negative consequences of stratospheric heating and ozone depletion from stratospheric aerosol geoengineering with sulphate aerosols, could be to use a different material injected into the stratosphere. Calcium carbonate has been shown in the laboratory to have optical properties which could result in much less radiation being absorbed than for sulphate aerosols; thus causing much less stratospheric heating. Alongside this, calcium carbonate is thought to not activate the ozone-depleting halogen species in the way sulphate aerosols do; thus also not causing ozone destruction. However, being absent from the stratosphere at present, the true nature of calcium carbonate's interactions in the stratosphere are not known. The scientific experiment SCoPEX (if approved) aims to address some of the uncertainties surrounding this, as well as building our understanding of stratospheric chemistry and aerosol microphysics; vital for improving modelling assumptions and simulations (Keutsch Group, 2020).

No one should want to see a world in which solar geoengineering is deployed and there are clearly dangers and ethical issues which surround its use. Our primary focus should be on emissions reductions as extensively and as quickly as humanly possible. The challenges

in achieving this are considerable, but we are not yet seen to be committed to a world warmer than 1.5°C (Smith et al., 2019). However, the longer serious action is delayed the less attainable this goal becomes. Solar geoengineering should not be considered a get-out clause and in actual fact if our current understanding of transport mechanisms are incorrect, more favourable options of stratospheric aerosol injection may not be possible (Visioni et al., 2020).

5.2 Future work

As new modelling experiments of solar geoengineering are conducted, new analysis of the model results will be needed. This thesis has begun to examine the impacts of solar geoengineering beyond just consideration of climatic changes to include interaction with people. Given that there still exists uncertainty in the science of solar geoengineering and the impacts of climate change, conclusions about changes in drought and water scarcity will very likely change in the future as all projected impacts are scenario dependent. Future research should also strive to incorporate humans and ecosystems more completely into impact analysis of future solar geoengineering scenarios. Unlike future projections of climate change, for which we have a number of set pathways, the possibilities for future methods, deployment and spatial extents of different solar geoengineering scenarios are vast. Whilst there exists a plethora of possibilities between the prescribed climate change pathways, in general the impacts of climate change are just dependent on the projected future levels of greenhouse gases. In contrast, solar geoengineering could be implemented in a number of different ways (e.g. space mirrors, different stratospheric aerosols), each having a unique climate impact, and in addition could have much greater variation in localised impacts depending on, for example, the location of stratospheric aerosol injection. What could potentially be a large number of future solar geoengineering scenarios poses particular problems in achieving wide-spread analysis of the many societal impacts of changes in climate conditions. Nonetheless, without comprehensive understanding of both the hazards and risks, along with the benefits, of solar geoengineering future populations and environments would be left open to huge uncertainty and possible vulnerability if the technology were to ever be deployed. This makes it imperative that we have as great an understanding as possible about how different scenarios of solar geoengineering could impact phenomena such as drought and water scarcity. Future work in this area should focus on an increased use of different measures and metrics at various temporal resolutions, alongside more detailed regional analysis of impacts; something which is already being begun by the DECIMALS' projects (SRMGI, 2021).

Appendix A

Hydrobelts and hydroregions

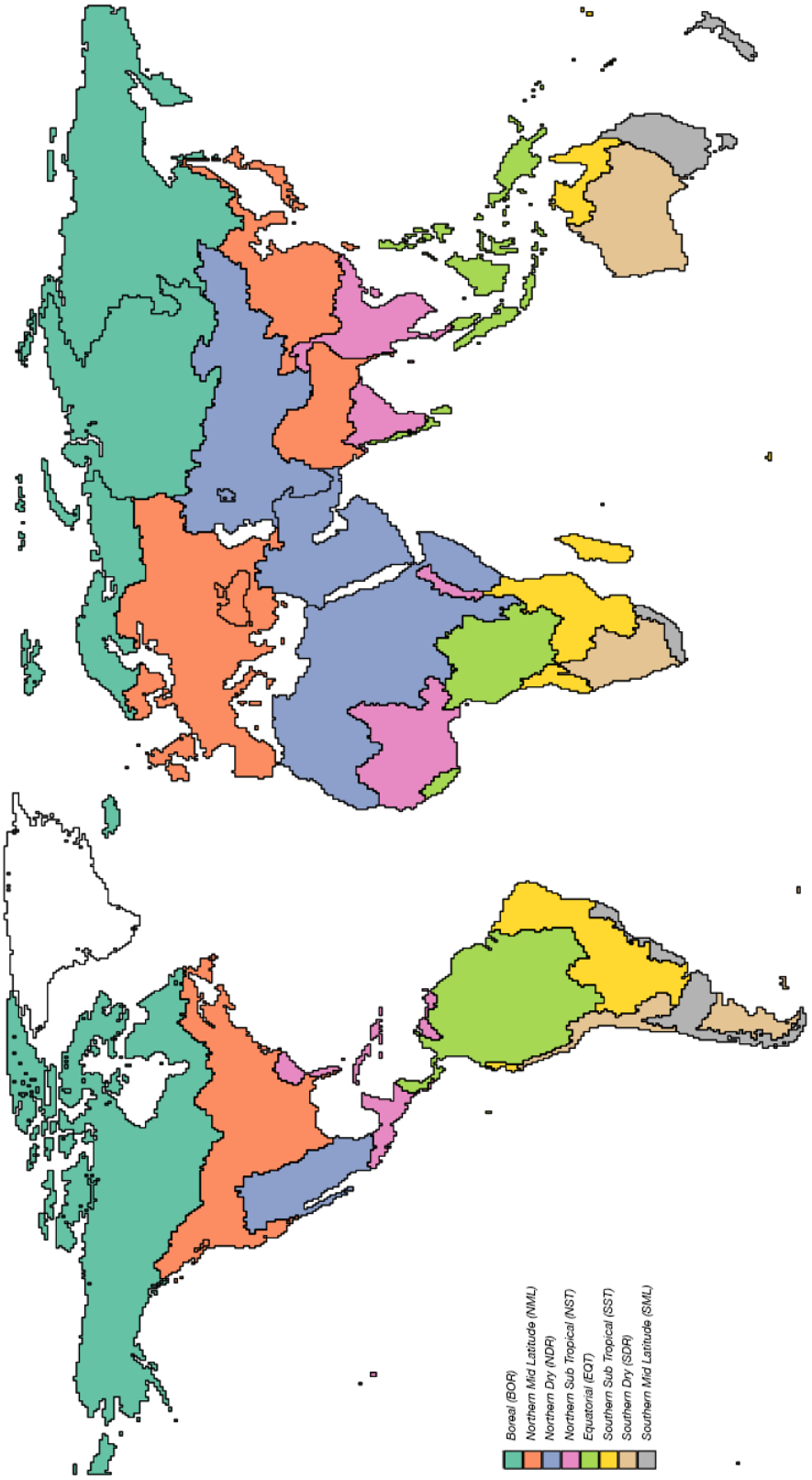


Figure A.1: Location of the 8 global hydrobelts (excluding Greenland) and 26 hydroregions as defined by Meybeck et al. (2013).

Appendix B

Catchment comparison graphs

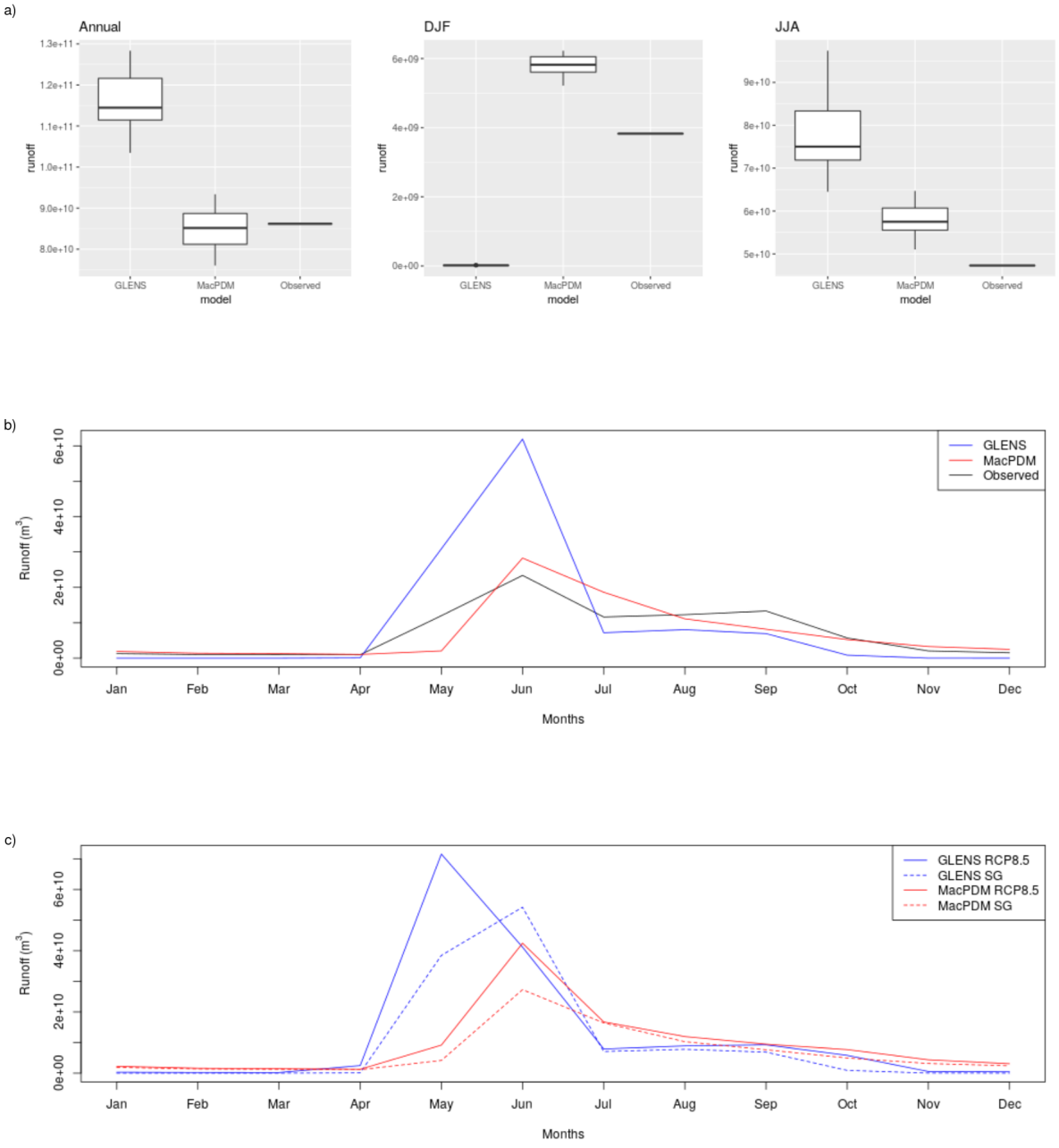


Figure B.1: Catchment comparison graphs for Kolyma catchment under Observed, GLENS and MacPDM results. Graphs show the ensemble mean modelled (2015-2025) and observed runoff distributions for a) annual, DJF and JJA and b) seasonal cycle and well as c) projected future (2050-70) runoff differences by model (MacPDM vs. GLENS) and scenario (RCP8.5 vs. SG).

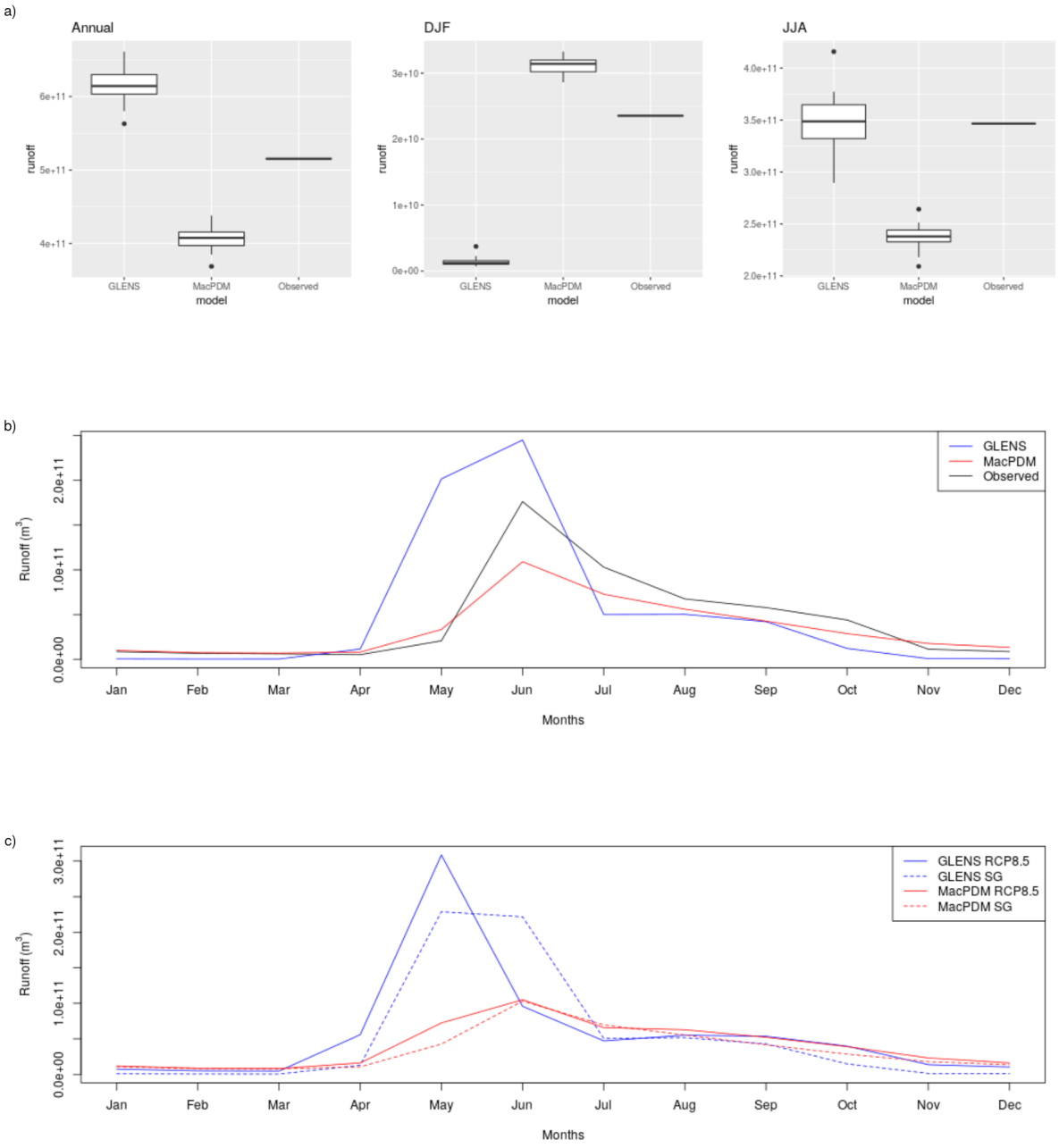


Figure B.2: Catchment comparison graphs for Lena catchment under Observed, GLENS and MacPDM results. Graphs show the ensemble mean modelled (2015-2025) and observed runoff distributions for a) annual, DJF and JJA and b) seasonal cycle and well as c) projected future (2050-70) runoff differences by model (MacPDM vs. GLENS) and scenario (RCP8.5 vs. SG).

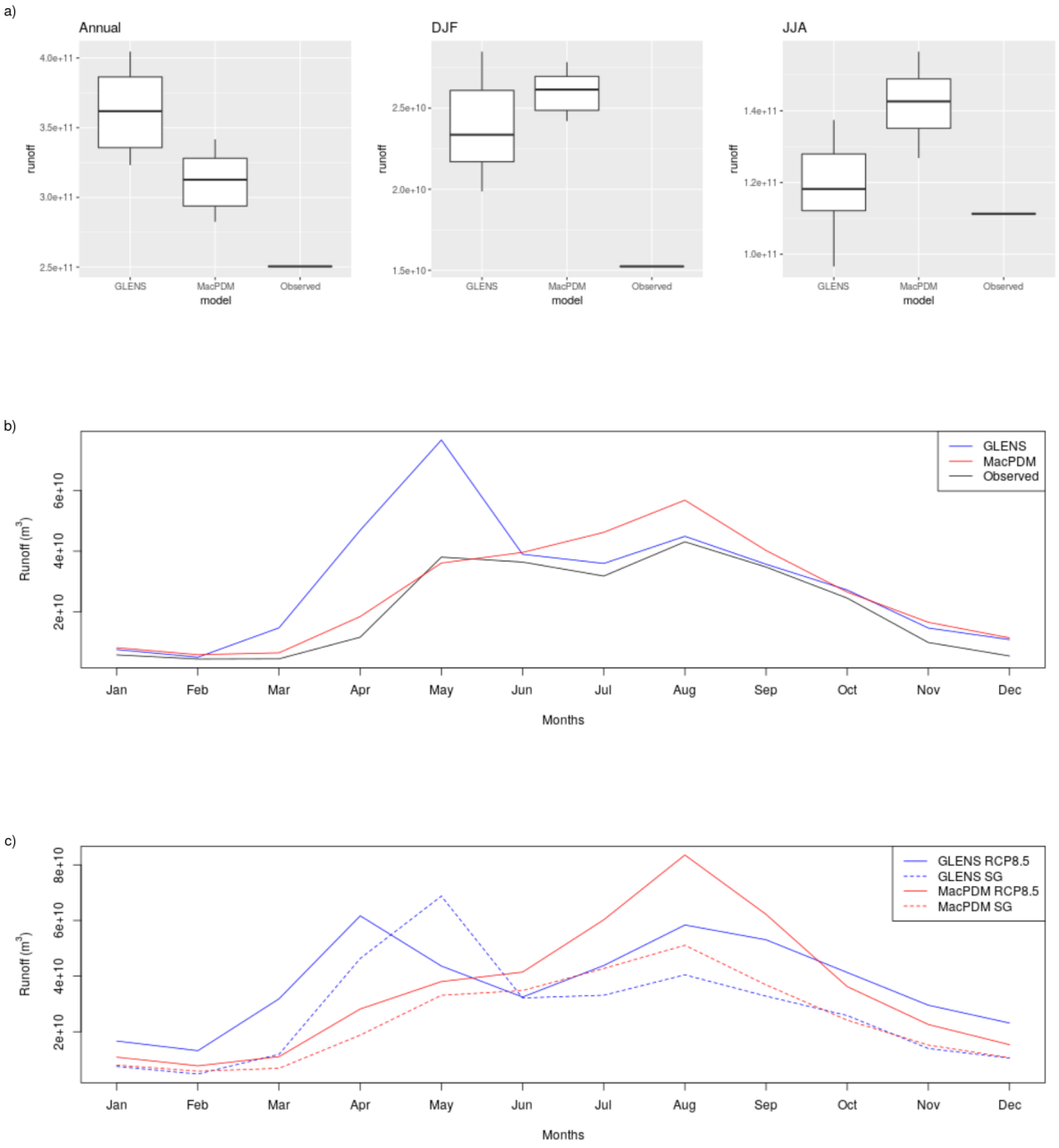


Figure B.3: Catchment comparison graphs for Amur catchment under Observed, GLENS and MacPDM results. Graphs show the ensemble mean modelled (2015-2025) and observed runoff distributions for a) annual, DJF and JJA and b) seasonal cycle and well as c) projected future (2050-70) runoff differences by model (MacPDM vs. GLENS) and scenario (RCP8.5 vs. SG).

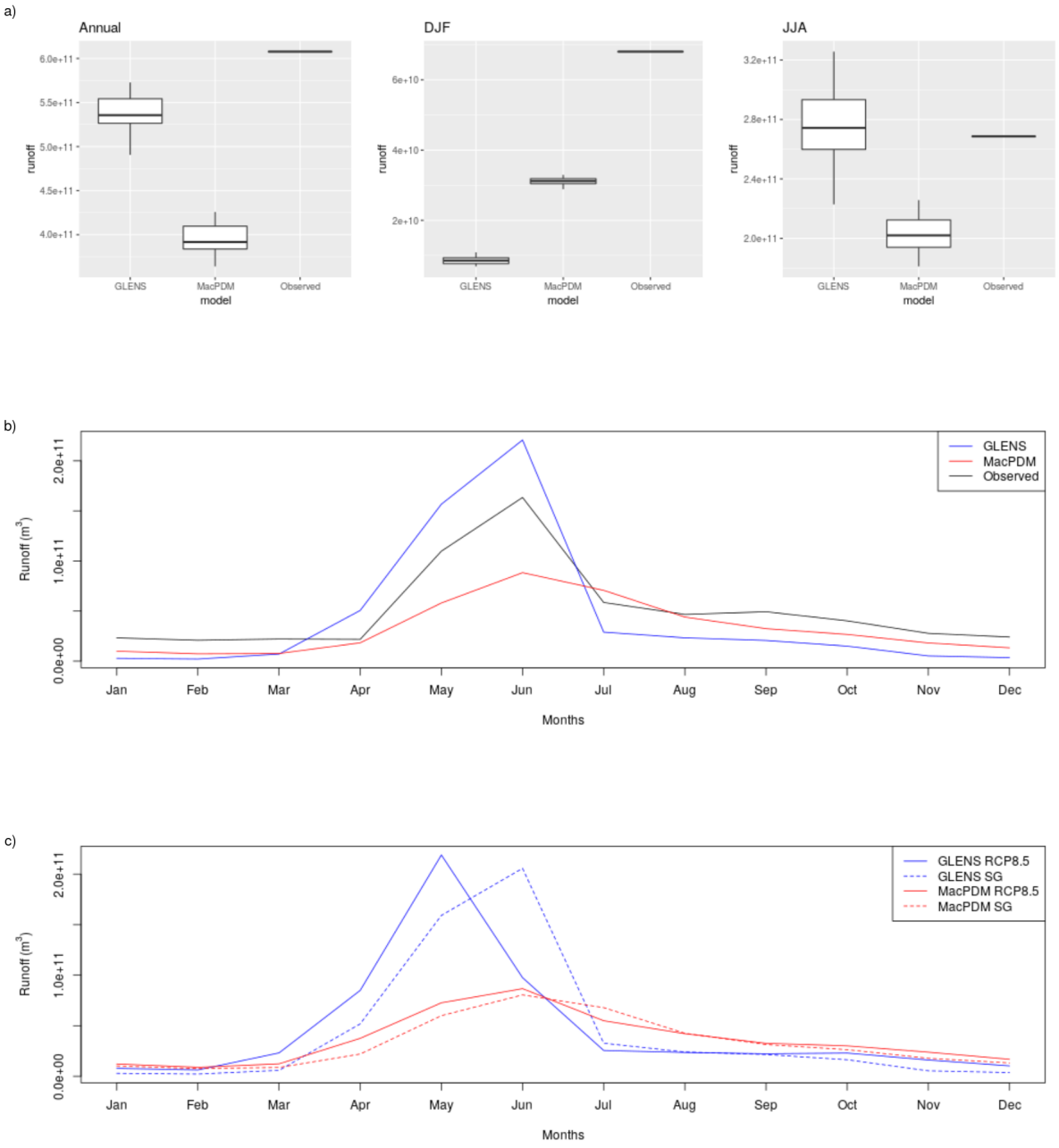


Figure B.4: Catchment comparison graphs for Yenisey catchment under Observed, GLENS and MacPDM results. Graphs show the ensemble mean modelled (2015-2025) and observed runoff distributions for a) annual, DJF and JJA and b) seasonal cycle and well as c) projected future (2050-70) runoff differences by model (MacPDM vs. GLENS) and scenario (RCP8.5 vs. SG).

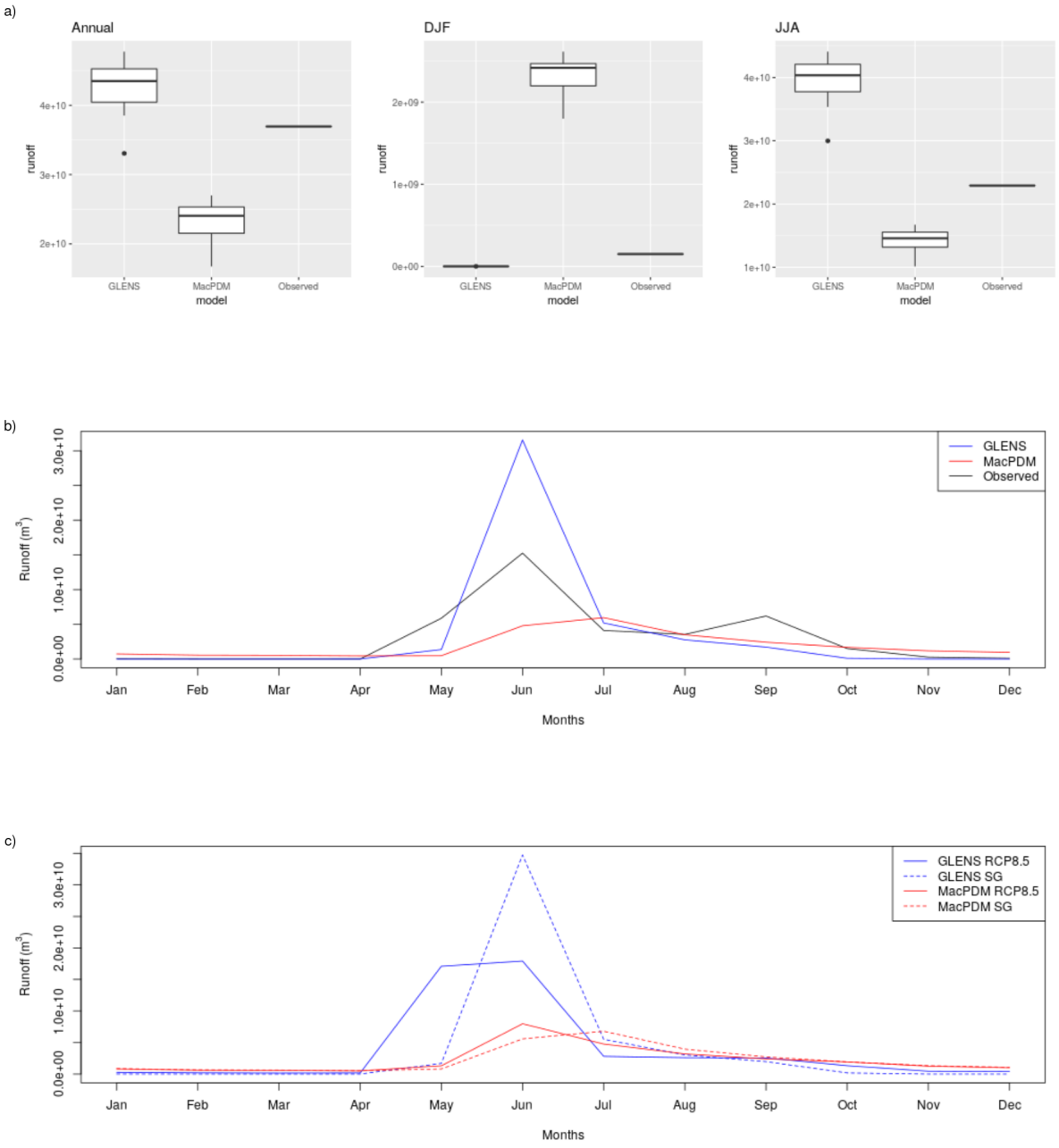


Figure B.5: Catchment comparison graphs for Olenek catchment under Observed, GLENS and MacPDM results. Graphs show the ensemble mean modelled (2015-2025) and observed runoff distributions for a) annual, DJF and JJA and b) seasonal cycle and well as c) projected future (2050-70) runoff differences by model (MacPDM vs. GLENS) and scenario (RCP8.5 vs. SG).

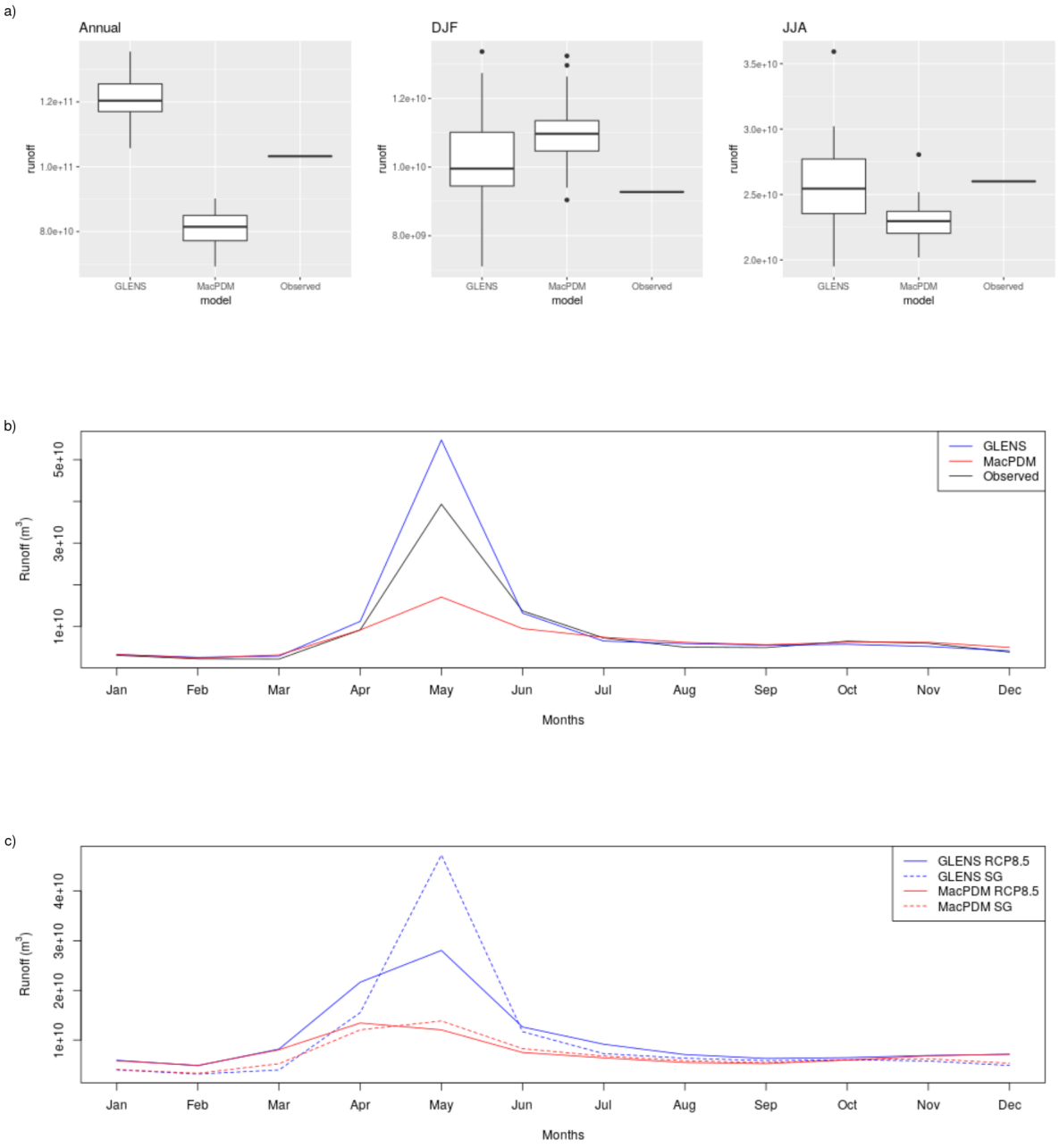


Figure B.6: Catchment comparison graphs for Severnaya Dvina catchment under Observed, GLENS and MacPDM results. Graphs show the ensemble mean modelled (2015-2025) and observed runoff distributions for a) annual, DJF and JJA and b) seasonal cycle and well as c) projected future (2050-70) runoff differences by model (MacPDM vs. GLENS) and scenario (RCP8.5 vs. SG).

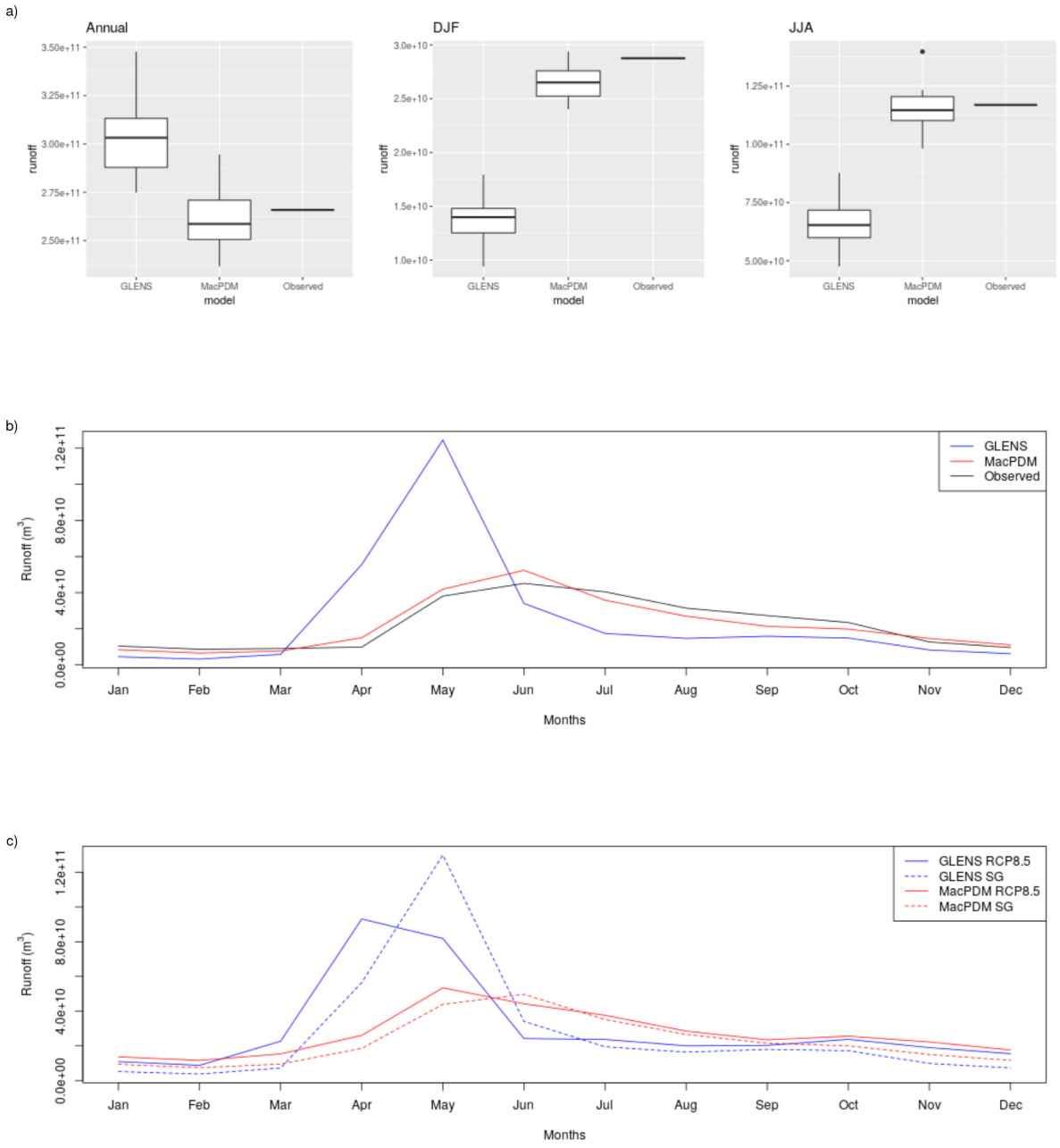


Figure B.7: Catchment comparison graphs for MacKenzie catchment under Observed, GLENS and MacPDM results. Graphs show the ensemble mean modelled (2015-2025) and observed runoff distributions for a) annual, DJF and JJA and b) seasonal cycle and well as c) projected future (2050-70) runoff differences by model (MacPDM vs. GLENS) and scenario (RCP8.5 vs. SG).

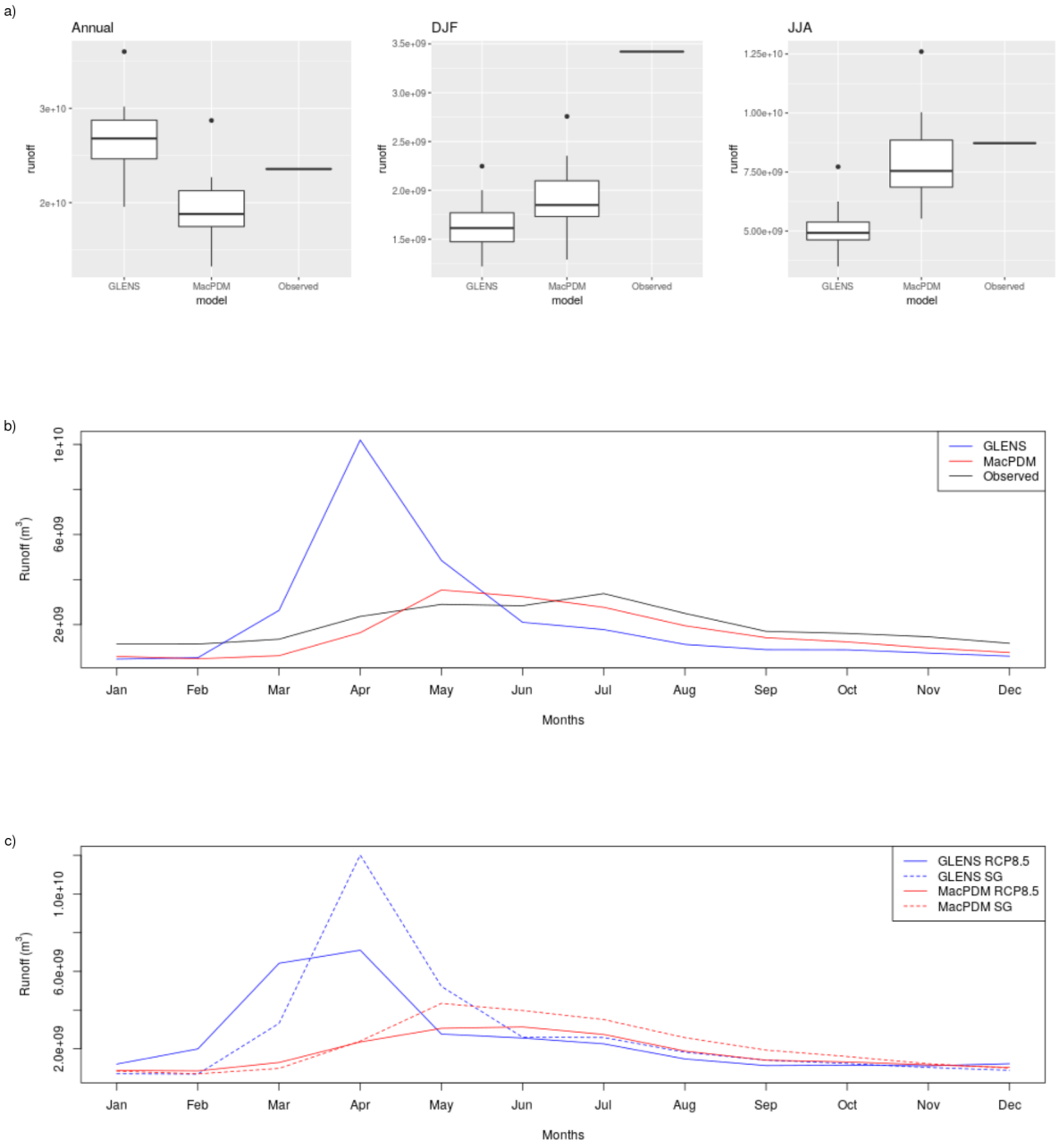


Figure B.8: Catchment comparison graphs for Saskatchewan catchment under Observed, GLENS and MacPDM results. Graphs show the ensemble mean modelled (2015-2025) and observed runoff distributions for a) annual, DJF and JJA and b) seasonal cycle and well as c) projected future (2050-70) runoff differences by model (MacPDM vs. GLENS) and scenario (RCP8.5 vs. SG).

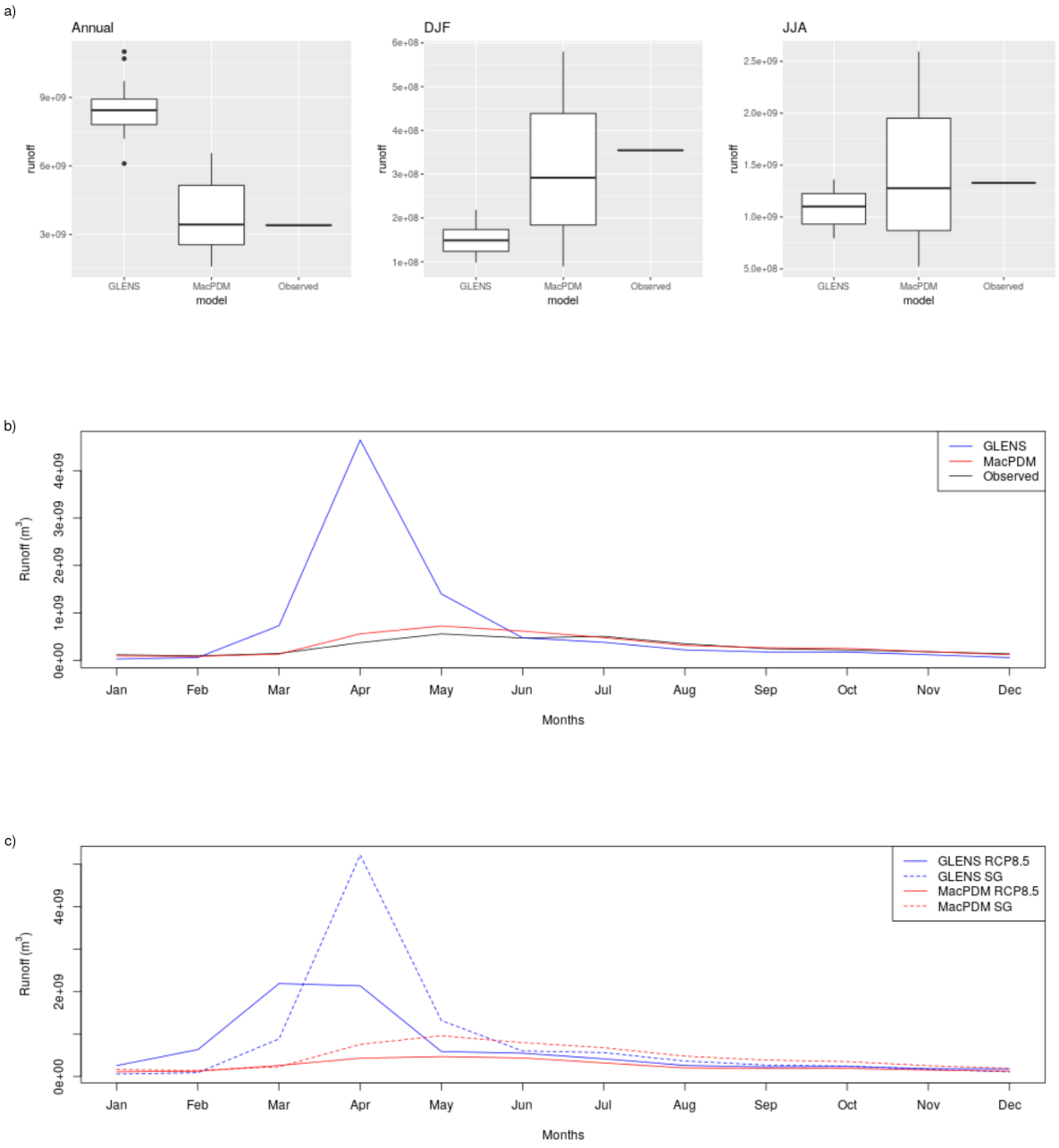


Figure B.9: Catchment comparison graphs for Assiniboine catchment under Observed, GLENS and MacPDM results. Graphs show the ensemble mean modelled (2015-2025) and observed runoff distributions for a) annual, DJF and JJA and b) seasonal cycle and well as c) projected future (2050-70) runoff differences by model (MacPDM vs. GLENS) and scenario (RCP8.5 vs. SG).

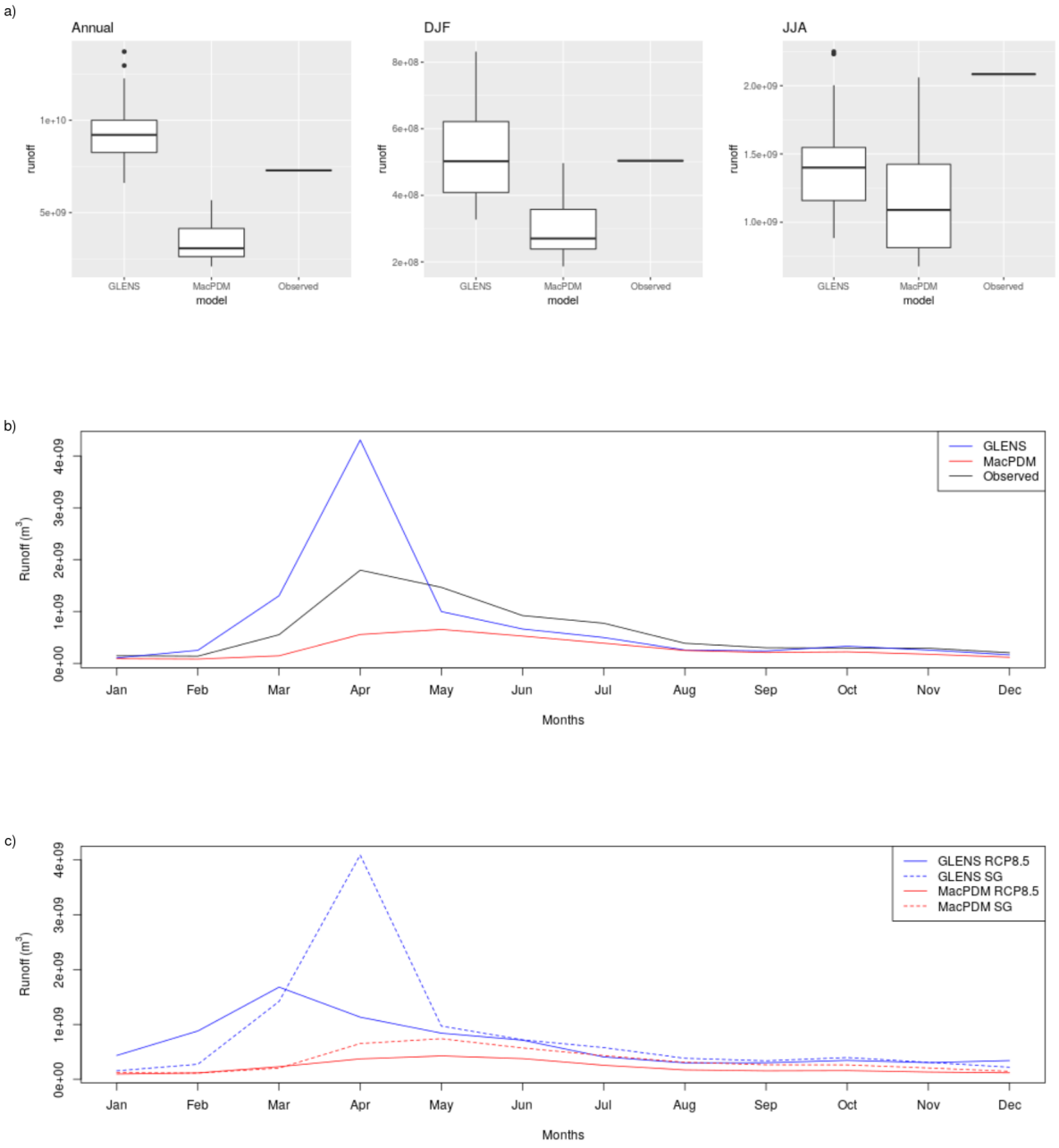


Figure B.10: Catchment comparison graphs for Red catchment under Observed, GLENS and MacPDM results. Graphs show the ensemble mean modelled (2015-2025) and observed runoff distributions for a) annual, DJF and JJA and b) seasonal cycle and well as c) projected future (2050-70) runoff differences by model (MacPDM vs. GLENS) and scenario (RCP8.5 vs. SG).

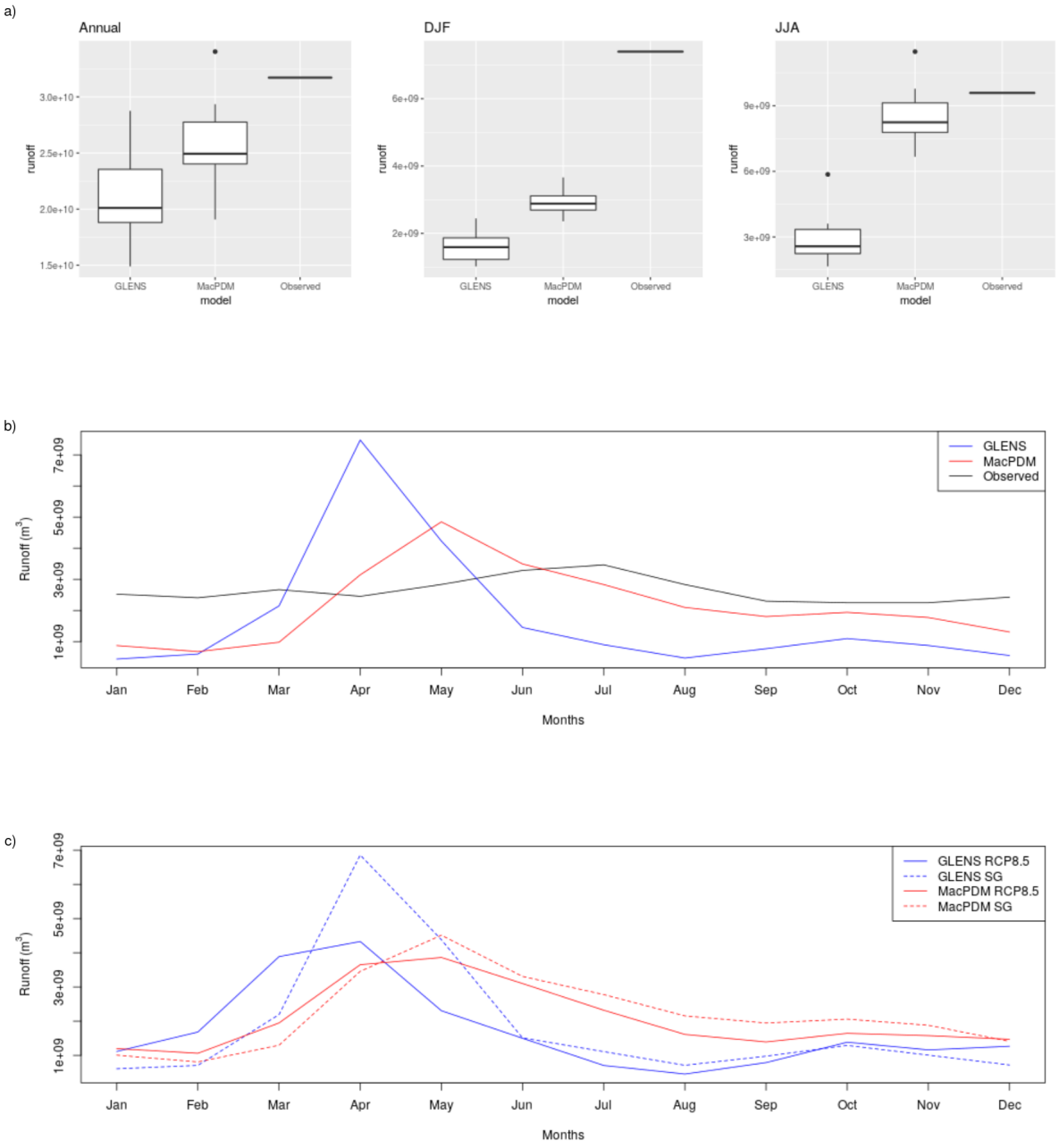


Figure B.11: Catchment comparison graphs for Winnipeg catchment under Observed, GLENS and MacPDM results. Graphs show the ensemble mean modelled (2015-2025) and observed runoff distributions for a) annual, DJF and JJA and b) seasonal cycle and well as c) projected future (2050-70) runoff differences by model (MacPDM vs. GLENS) and scenario (RCP8.5 vs. SG).

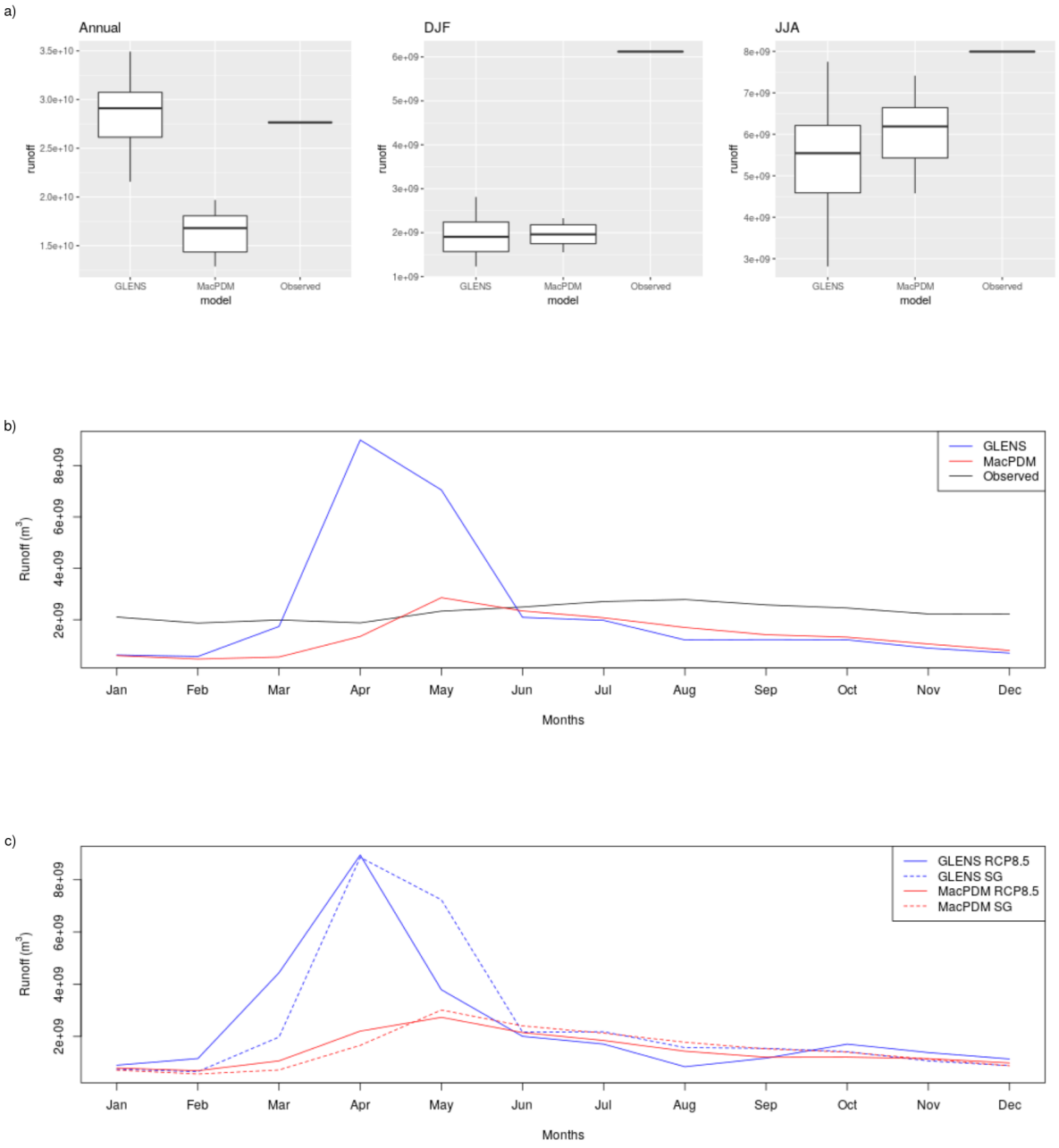


Figure B.12: Catchment comparison graphs for Churchill catchment under Observed, GLENS and MacPDM results. Graphs show the ensemble mean modelled (2015-2025) and observed runoff distributions for a) annual, DJF and JJA and b) seasonal cycle and well as c) projected future (2050-70) runoff differences by model (MacPDM vs. GLENS) and scenario (RCP8.5 vs. SG).

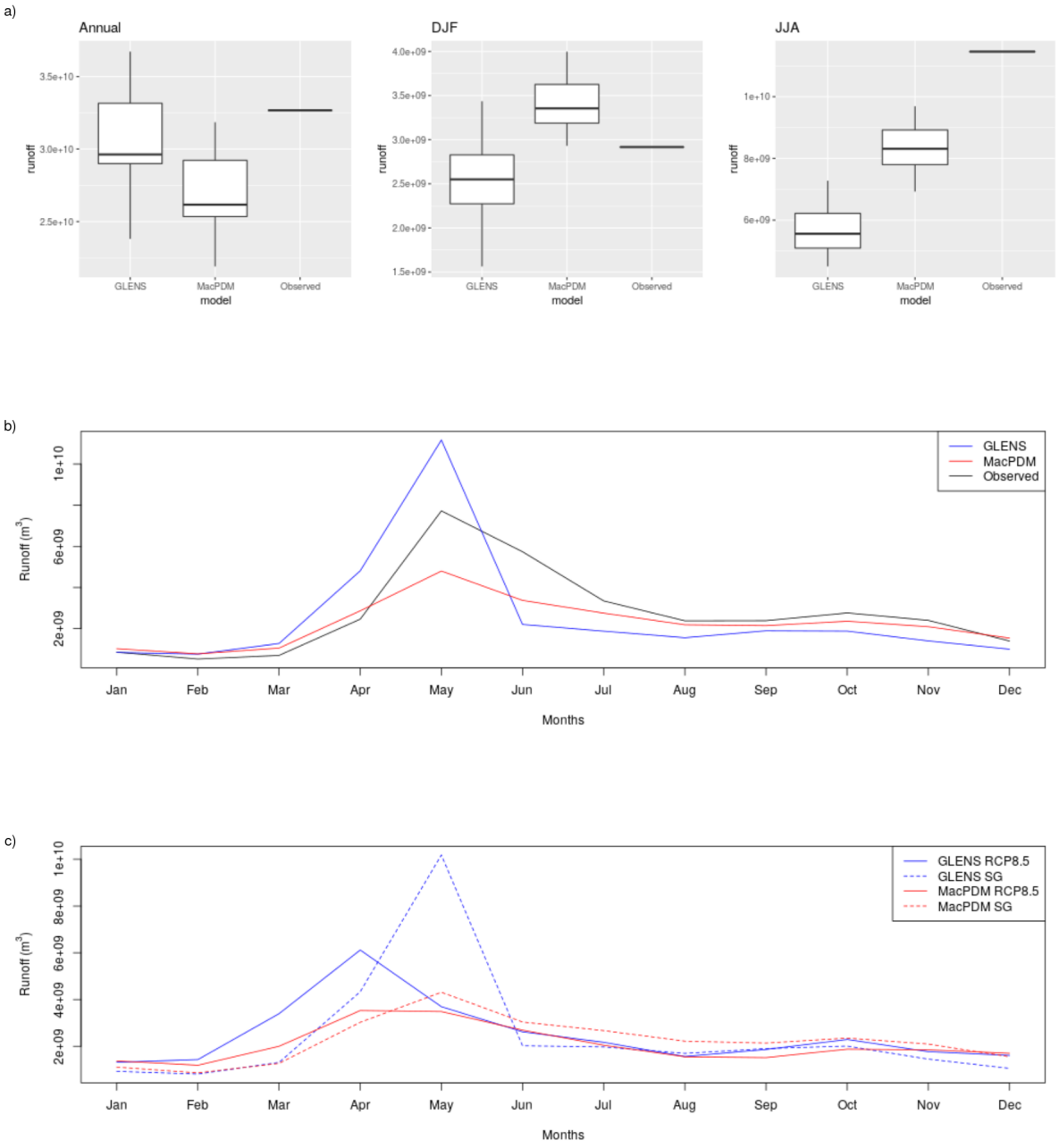


Figure B.13: Catchment comparison graphs for Albany catchment under Observed, GLENS and MacPDM results. Graphs show the ensemble mean modelled (2015-2025) and observed runoff distributions for a) annual, DJF and JJA and b) seasonal cycle and well as c) projected future (2050-70) runoff differences by model (MacPDM vs. GLENS) and scenario (RCP8.5 vs. SG).

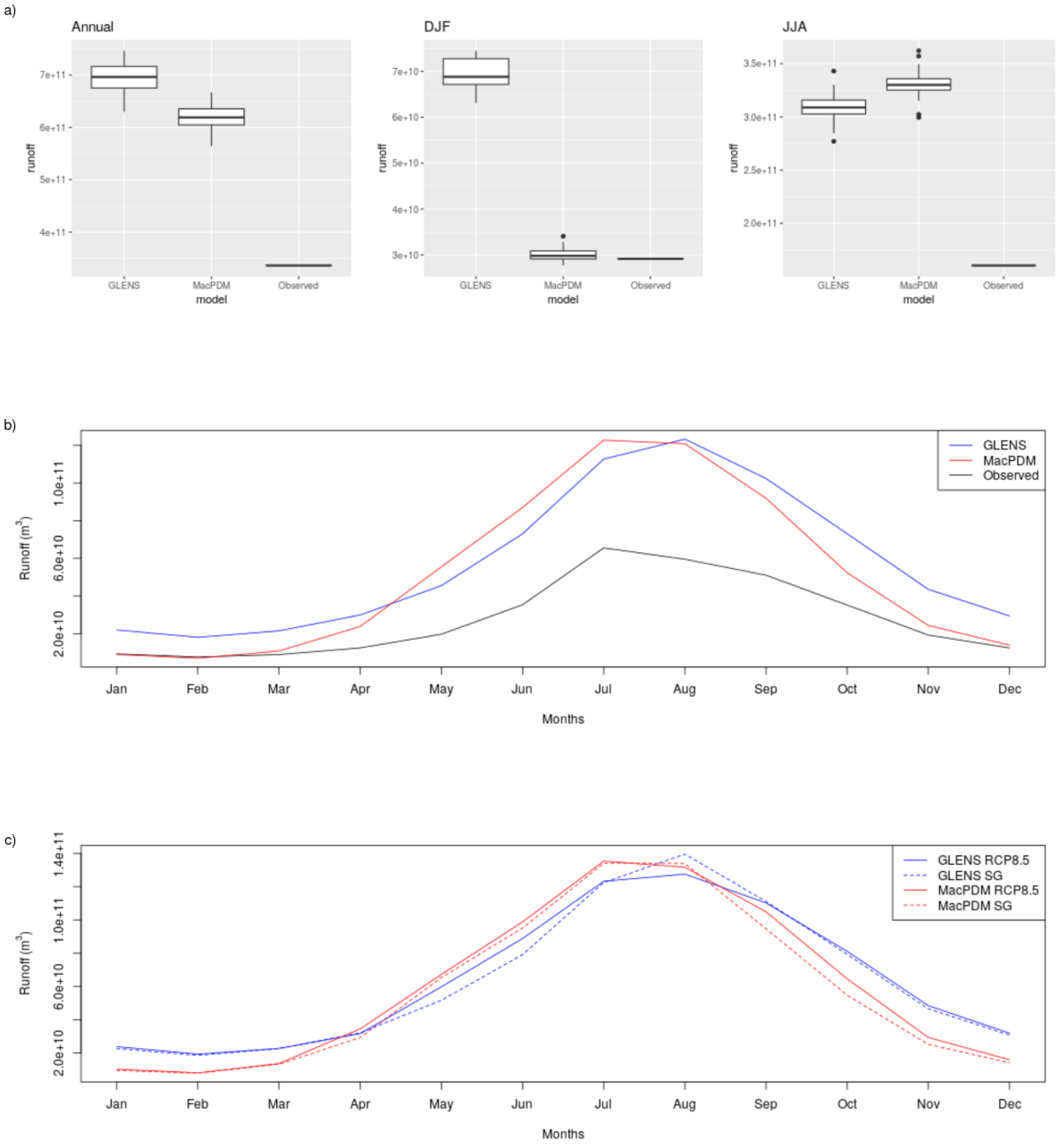


Figure B.14: Catchment comparison graphs for Yangtze catchment under Observed, GLENS and MacPDM results. Graphs show the ensemble mean modelled (2015-2025) and observed runoff distributions for a) annual, DJF and JJA and b) seasonal cycle and well as c) projected future (2050-70) runoff differences by model (MacPDM vs. GLENS) and scenario (RCP8.5 vs. SG).

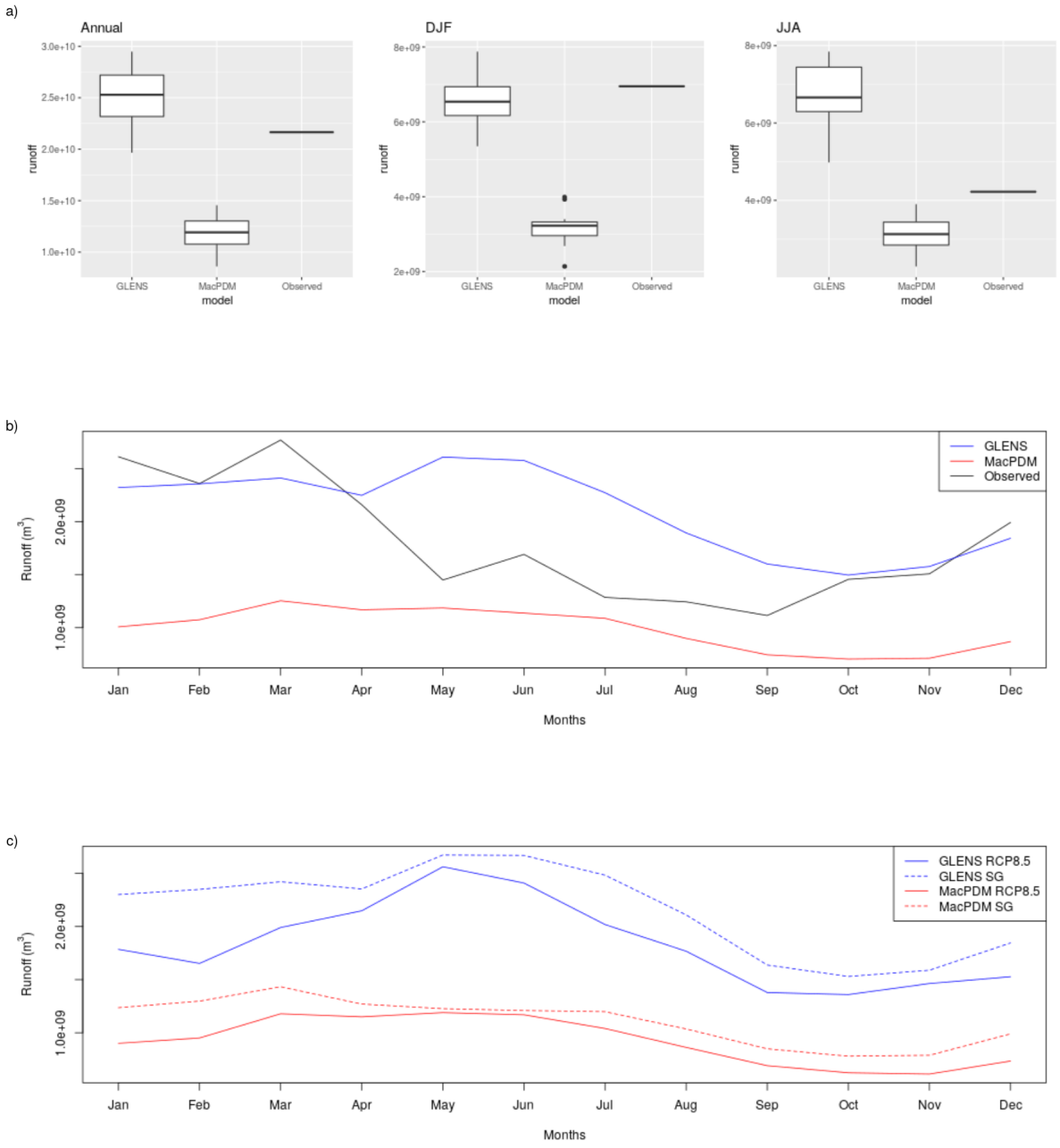


Figure B.15: Catchment comparison graphs for Elbe catchment under Observed, GLENS and MacPDM results. Graphs show the ensemble mean modelled (2015-2025) and observed runoff distributions for a) annual, DJF and JJA and b) seasonal cycle and well as c) projected future (2050-70) runoff differences by model (MacPDM vs. GLENS) and scenario (RCP8.5 vs. SG).

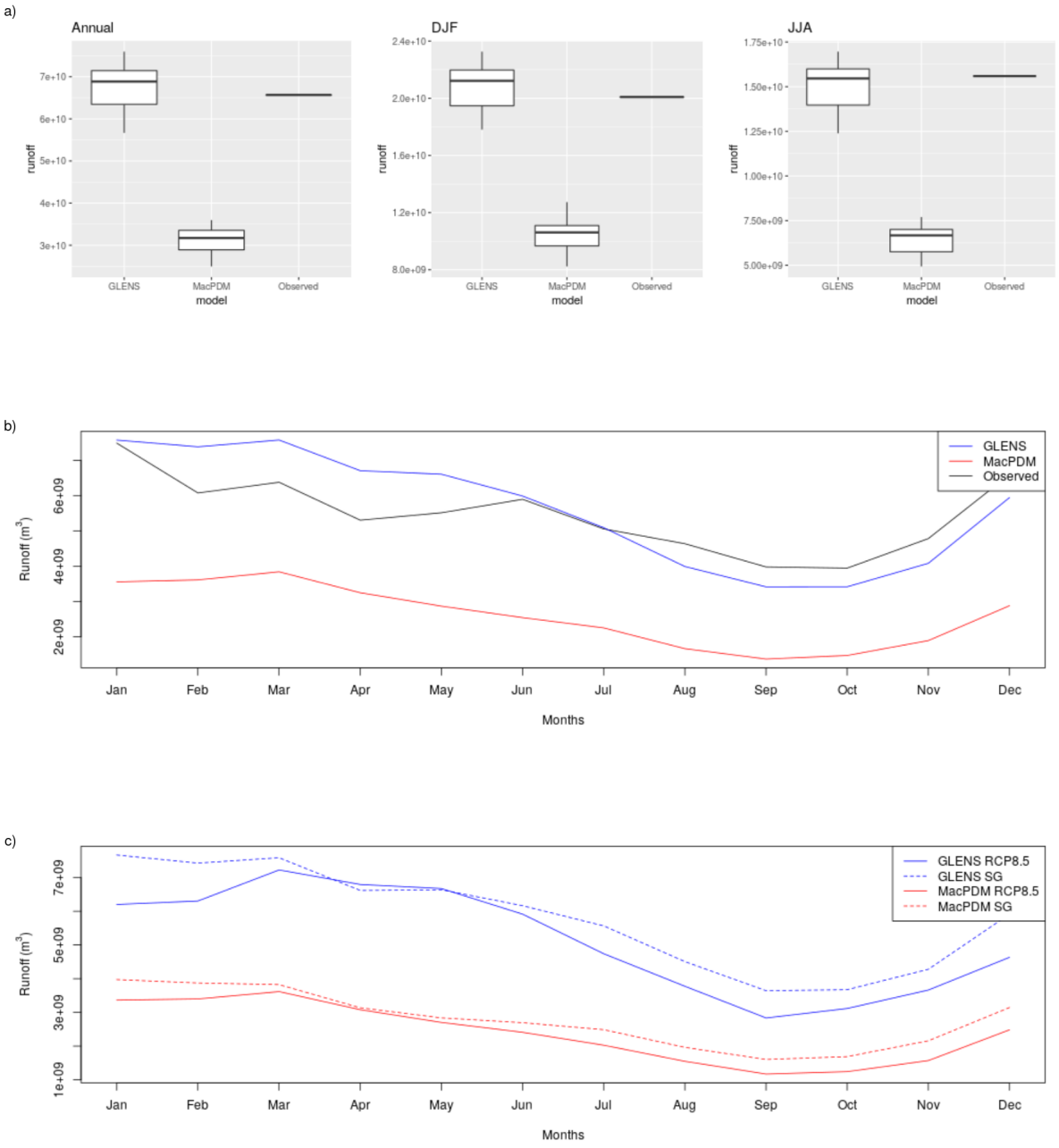


Figure B.16: Catchment comparison graphs for Rhine catchment under Observed, GLENS and MacPDM results. Graphs show the ensemble mean modelled (2015-2025) and observed runoff distributions for a) annual, DJF and JJA and b) seasonal cycle and well as c) projected future (2050-70) runoff differences by model (MacPDM vs. GLENS) and scenario (RCP8.5 vs. SG).

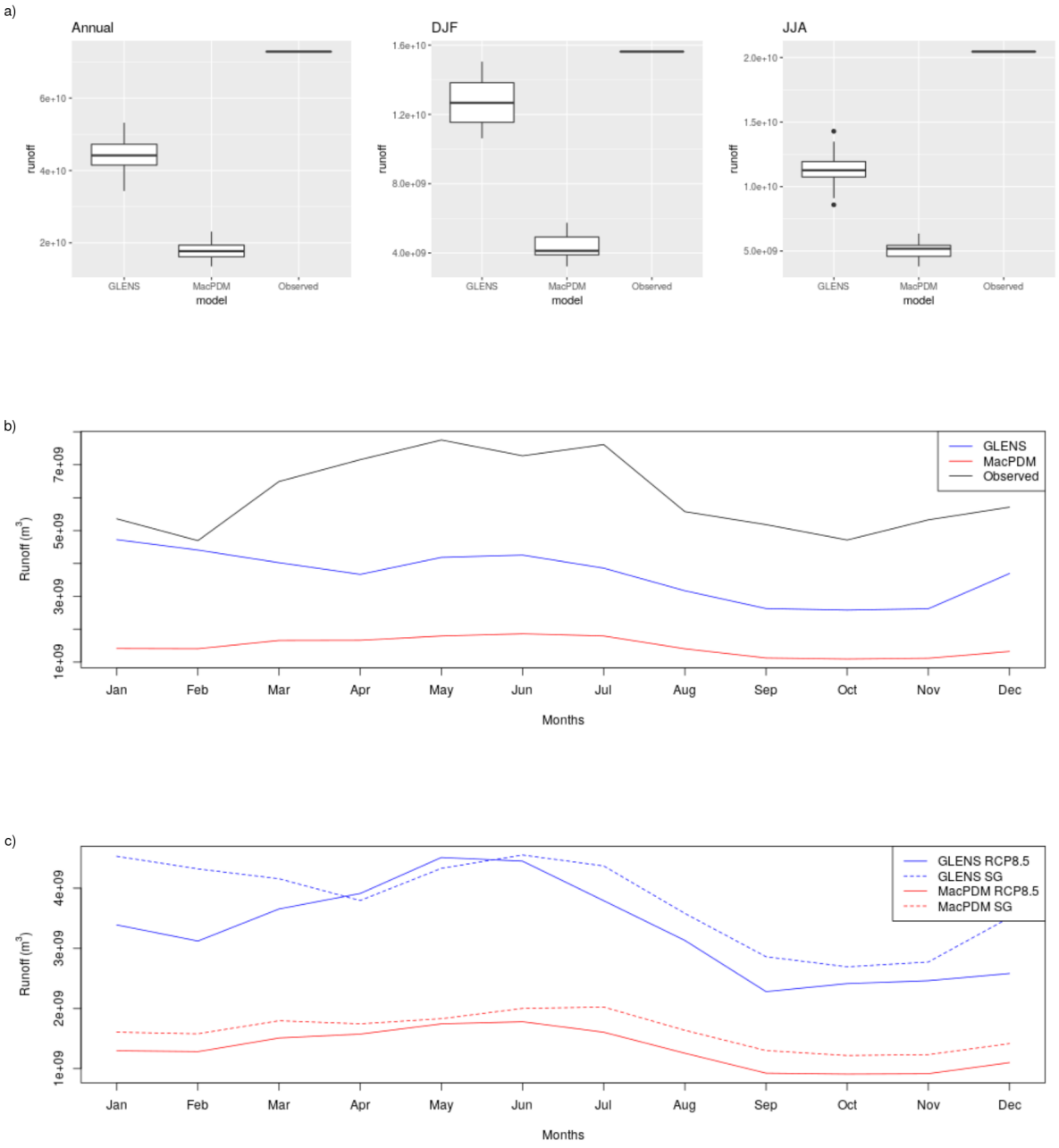


Figure B.17: Catchment comparison graphs for Danube catchment under Observed, GLENS and MacPDM results. Graphs show the ensemble mean modelled (2015-2025) and observed runoff distributions for a) annual, DJF and JJA and b) seasonal cycle and well as c) projected future (2050-70) runoff differences by model (MacPDM vs. GLENS) and scenario (RCP8.5 vs. SG).

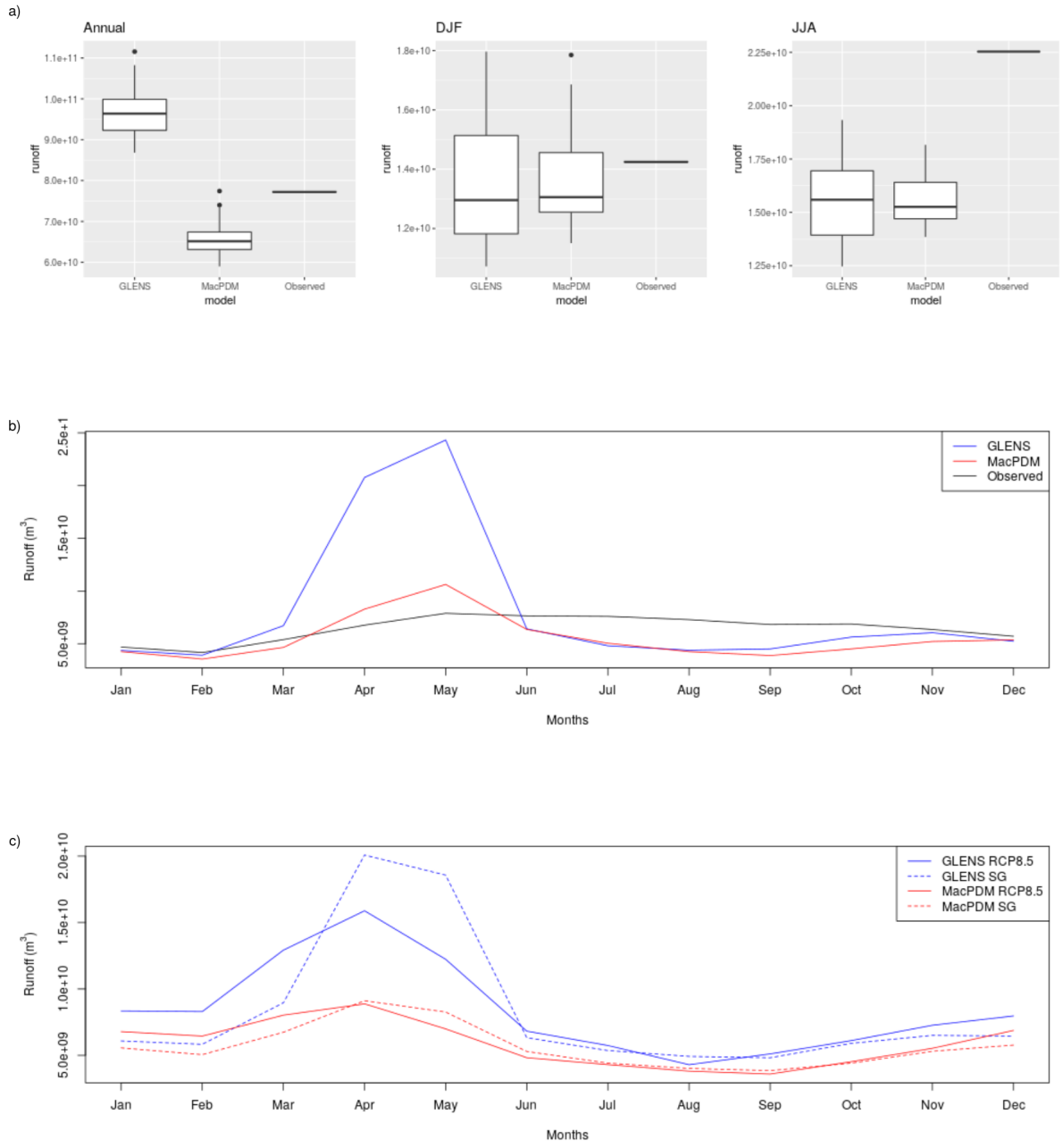


Figure B.18: Catchment comparison graphs for Neva catchment under Observed, GLENS and MacPDM results. Graphs show the ensemble mean modelled (2015-2025) and observed runoff distributions for a) annual, DJF and JJA and b) seasonal cycle and well as c) projected future (2050-70) runoff differences by model (MacPDM vs. GLENS) and scenario (RCP8.5 vs. SG).

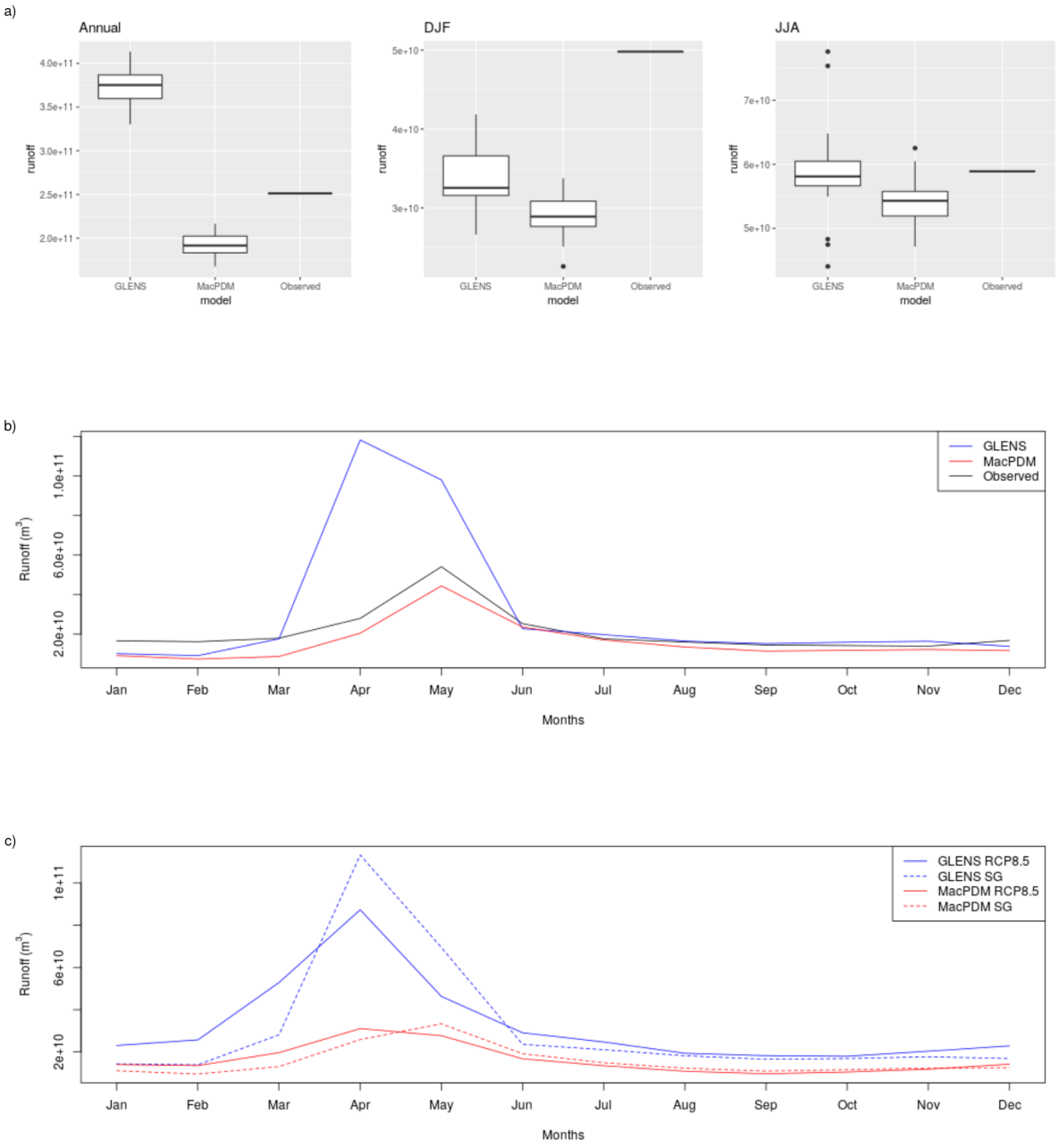


Figure B.19: Catchment comparison graphs for Volga catchment under Observed, GLENS and MacPDM results. Graphs show the ensemble mean modelled (2015-2025) and observed runoff distributions for a) annual, DJF and JJA and b) seasonal cycle and well as c) projected future (2050-70) runoff differences by model (MacPDM vs. GLENS) and scenario (RCP8.5 vs. SG).

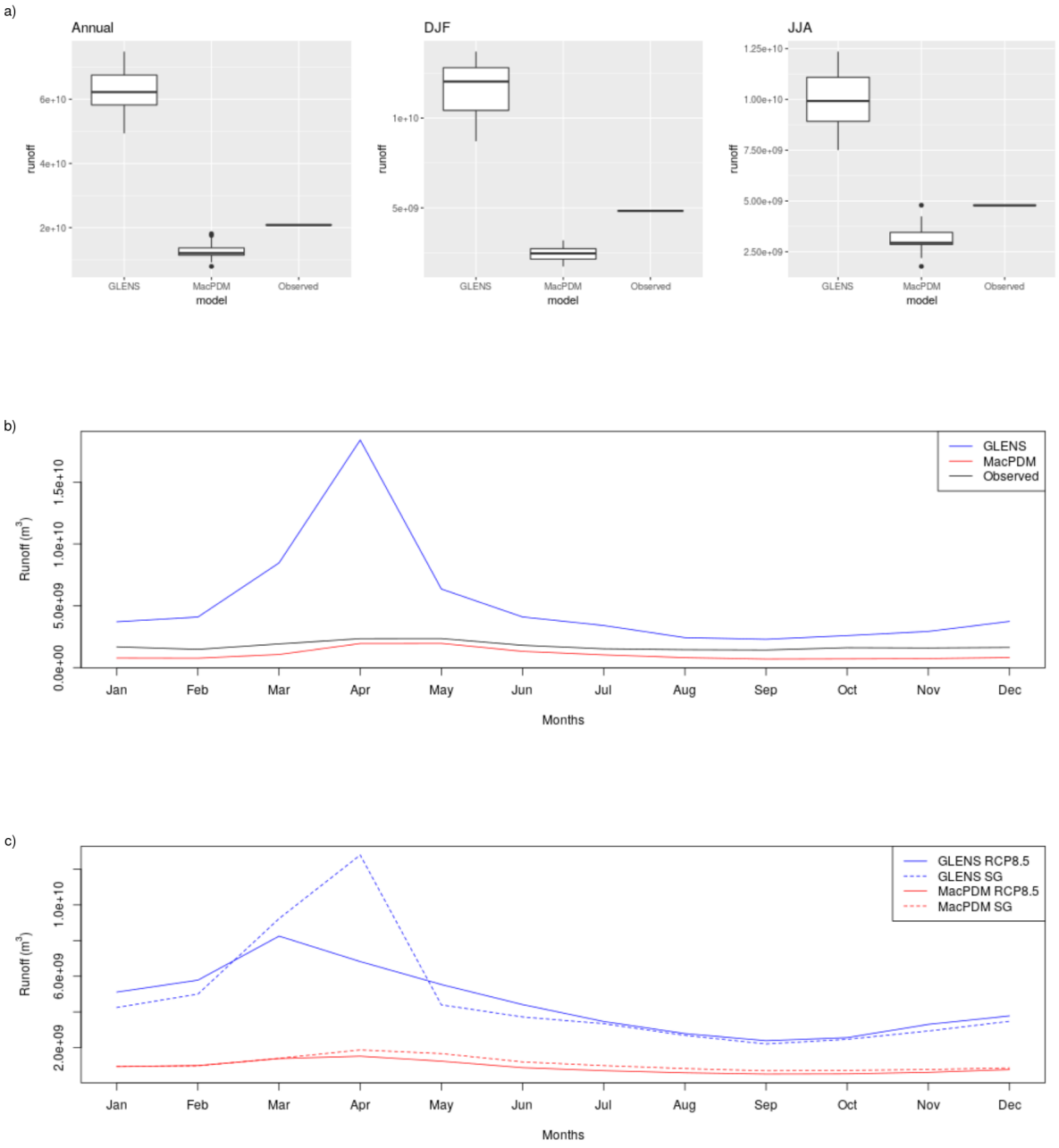


Figure B.20: Catchment comparison graphs for Don catchment under Observed, GLENS and MacPDM results. Graphs show the ensemble mean modelled (2015-2025) and observed runoff distributions for a) annual, DJF and JJA and b) seasonal cycle and well as c) projected future (2050-70) runoff differences by model (MacPDM vs. GLENS) and scenario (RCP8.5 vs. SG).

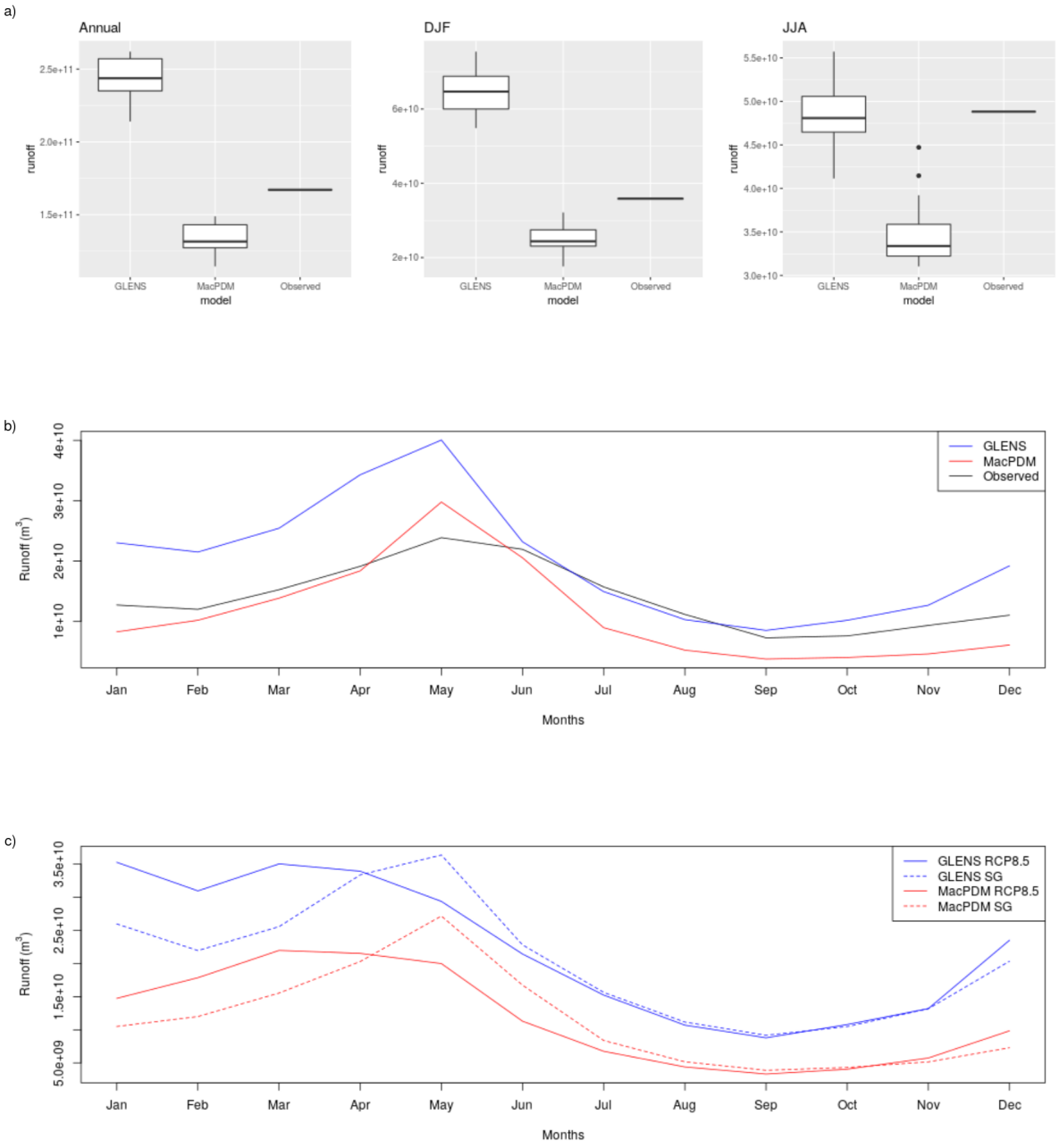


Figure B.21: Catchment comparison graphs for Columbia catchment under Observed, GLENS and MacPDM results. Graphs show the ensemble mean modelled (2015-2025) and observed runoff distributions for a) annual, DJF and JJA and b) seasonal cycle and well as c) projected future (2050-70) runoff differences by model (MacPDM vs. GLENS) and scenario (RCP8.5 vs. SG).

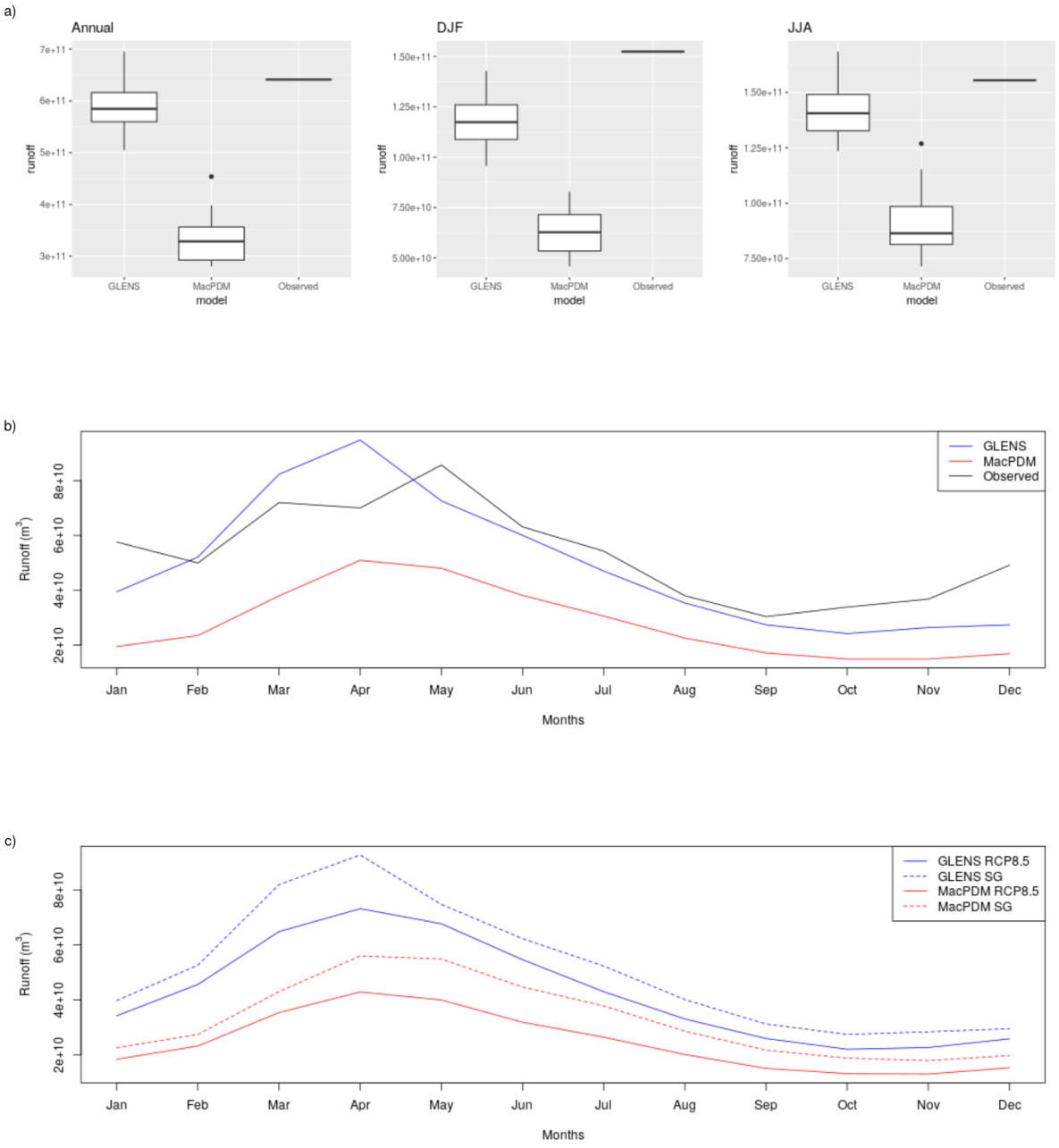


Figure B.22: Catchment comparison graphs for Mississippi catchment under Observed, GLENS and MacPDM results. Graphs show the ensemble mean modelled (2015-2025) and observed runoff distributions for a) annual, DJF and JJA and b) seasonal cycle and well as c) projected future (2050-70) runoff differences by model (MacPDM vs. GLENS) and scenario (RCP8.5 vs. SG).

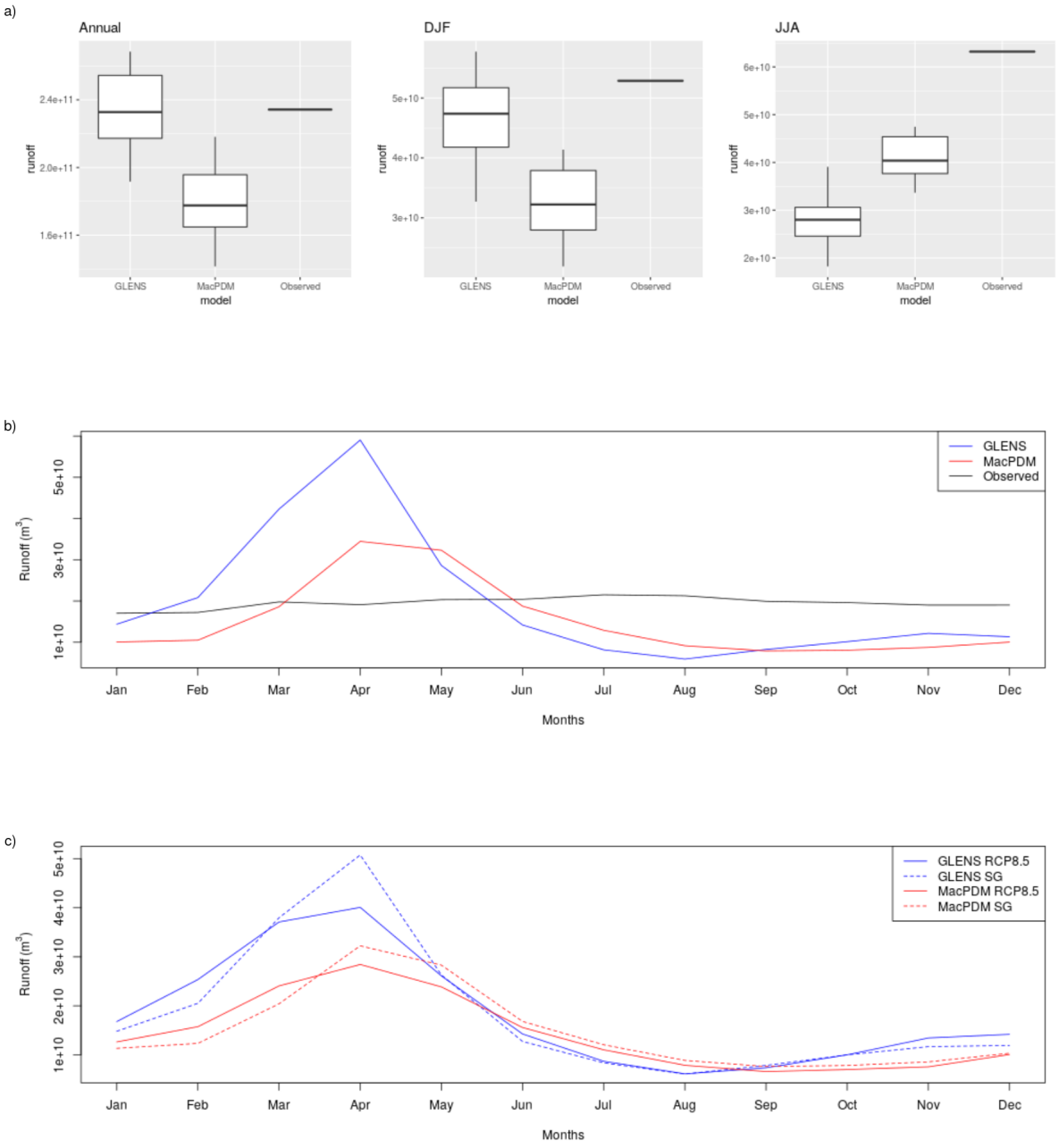


Figure B.23: Catchment comparison graphs for St. Lawrence catchment under Observed, GLENS and MacPDM results. Graphs show the ensemble mean modelled (2015-2025) and observed runoff distributions for a) annual, DJF and JJA and b) seasonal cycle and well as c) projected future (2050-70) runoff differences by model (MacPDM vs. GLENS) and scenario (RCP8.5 vs. SG).

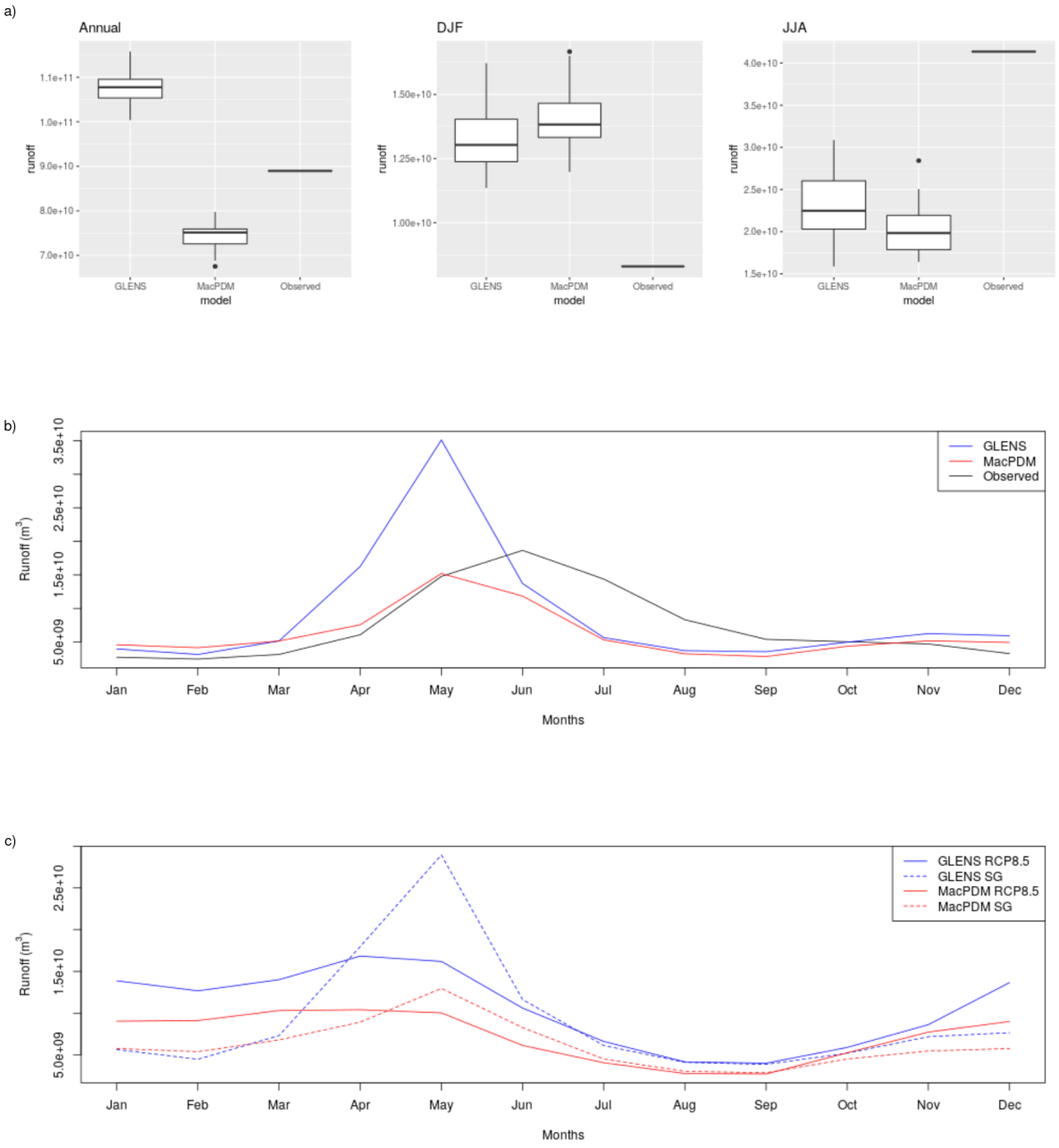


Figure B.24: Catchment comparison graphs for Fraser catchment under Observed, GLENS and MacPDM results. Graphs show the ensemble mean modelled (2015-2025) and observed runoff distributions for a) annual, DJF and JJA and b) seasonal cycle and well as c) projected future (2050-70) runoff differences by model (MacPDM vs. GLENS) and scenario (RCP8.5 vs. SG).

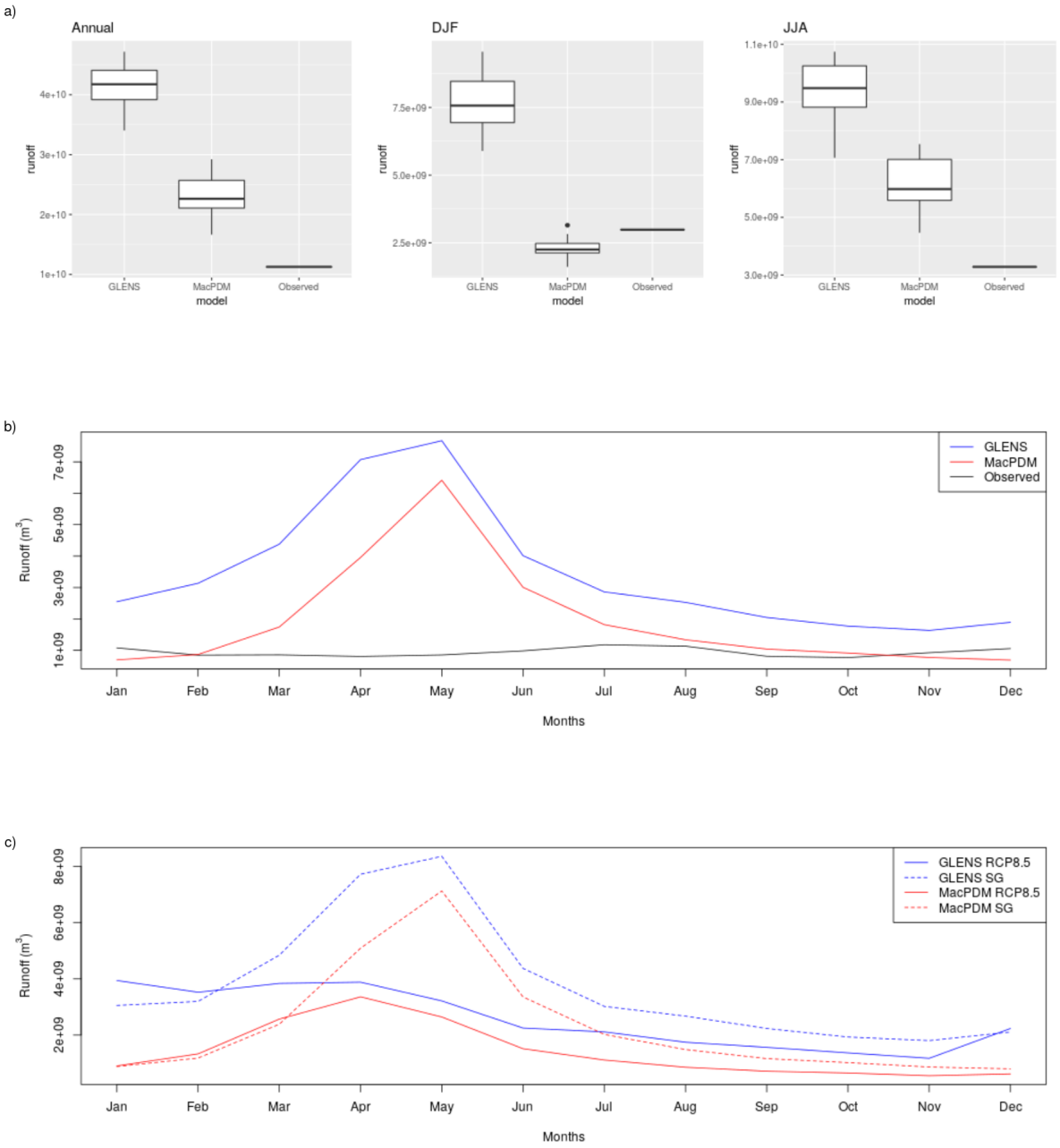


Figure B.25: Catchment comparison graphs for Colorado catchment under Observed, GLENS and MacPDM results. Graphs show the ensemble mean modelled (2015-2025) and observed runoff distributions for a) annual, DJF and JJA and b) seasonal cycle and well as c) projected future (2050-70) runoff differences by model (MacPDM vs. GLENS) and scenario (RCP8.5 vs. SG).

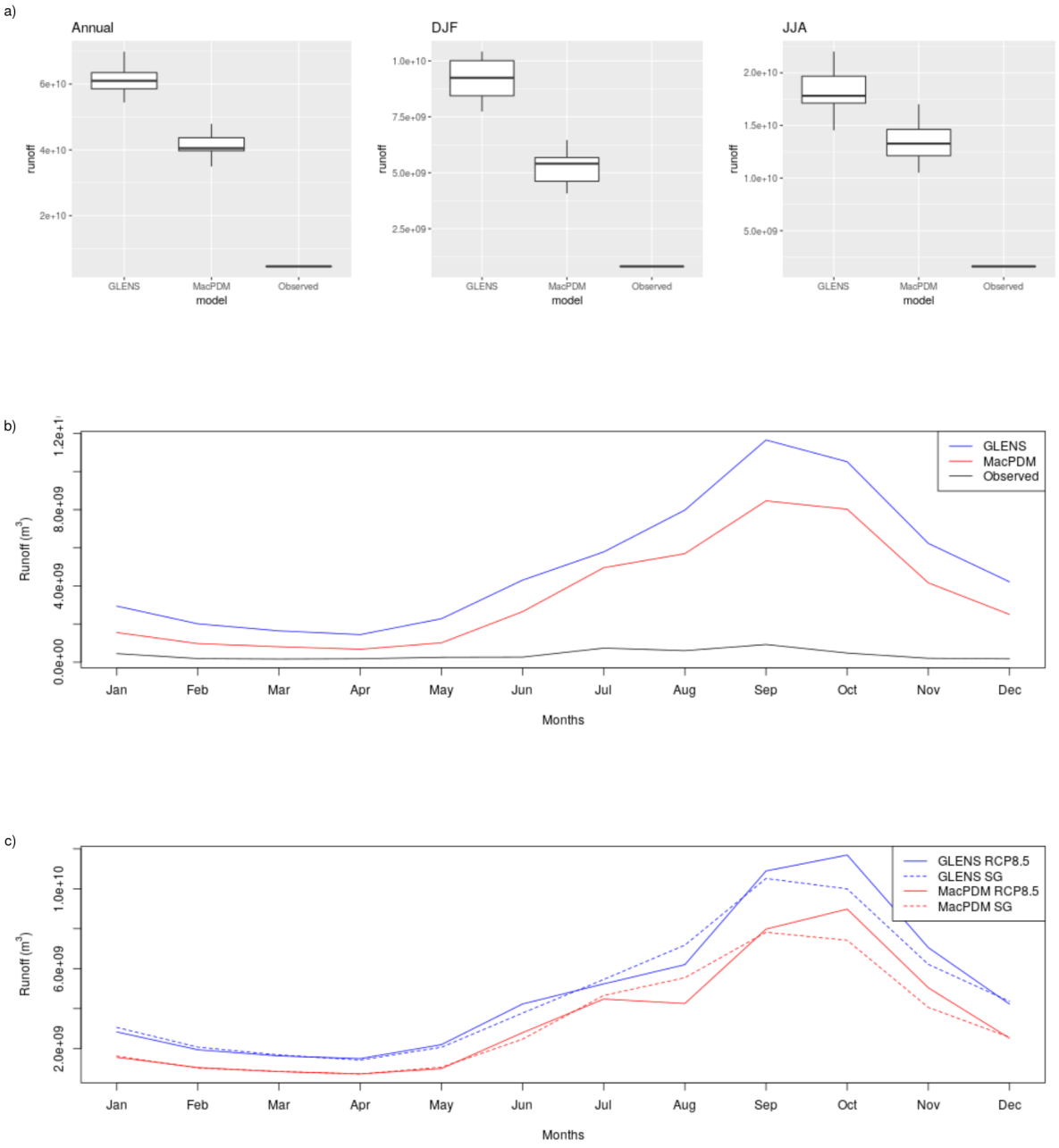


Figure B.26: Catchment comparison graphs for Rio Santiago catchment under Observed, GLENS and MacPDM results. Graphs show the ensemble mean modelled (2015-2025) and observed runoff distributions for a) annual, DJF and JJA and b) seasonal cycle and well as c) projected future (2050-70) runoff differences by model (MacPDM vs. GLENS) and scenario (RCP8.5 vs. SG).

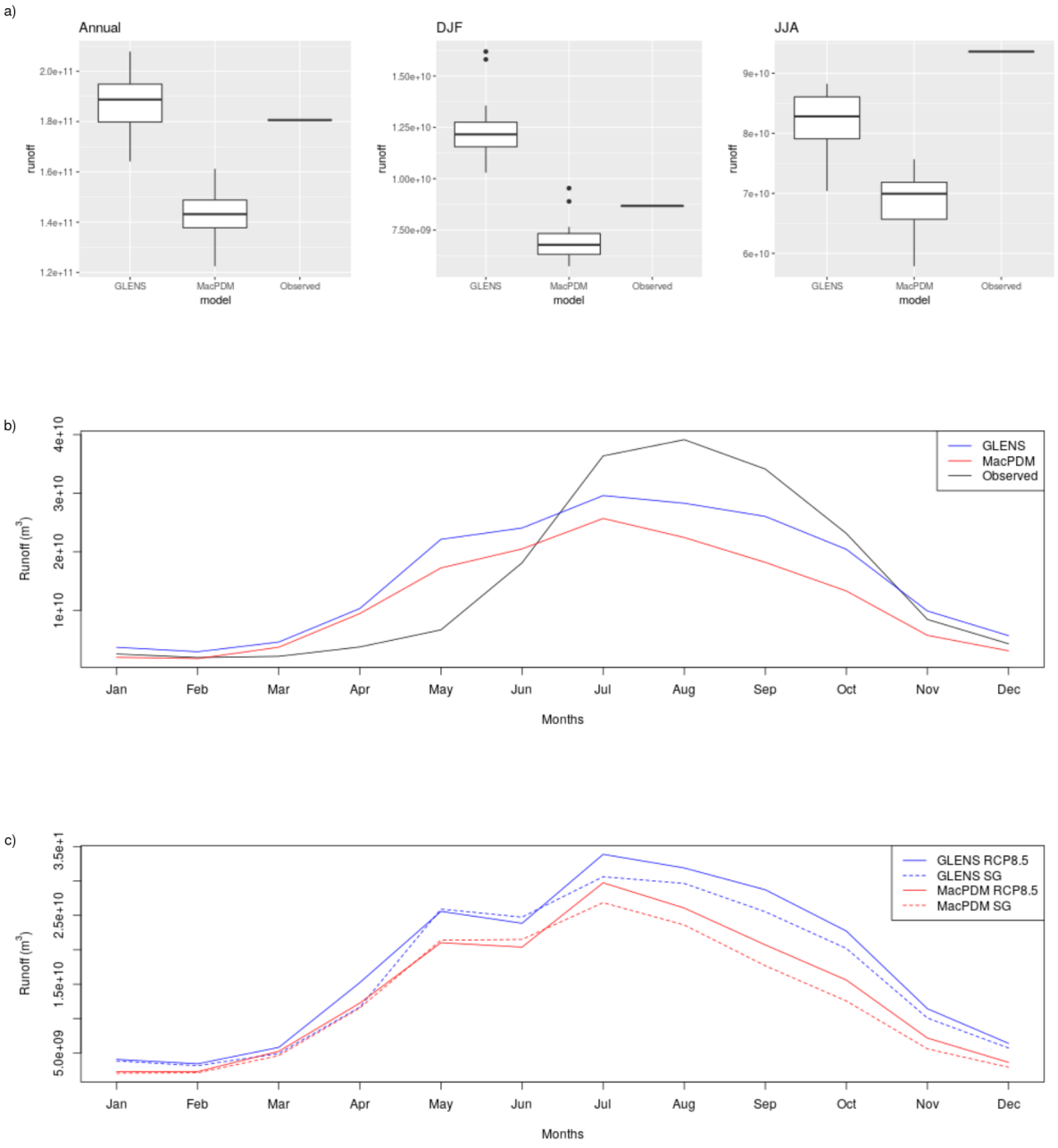


Figure B.27: Catchment comparison graphs for Irrawaddy catchment under Observed, GLENS and MacPDM results. Graphs show the ensemble mean modelled (2015-2025) and observed runoff distributions for a) annual, DJF and JJA and b) seasonal cycle and well as c) projected future (2050-70) runoff differences by model (MacPDM vs. GLENS) and scenario (RCP8.5 vs. SG).

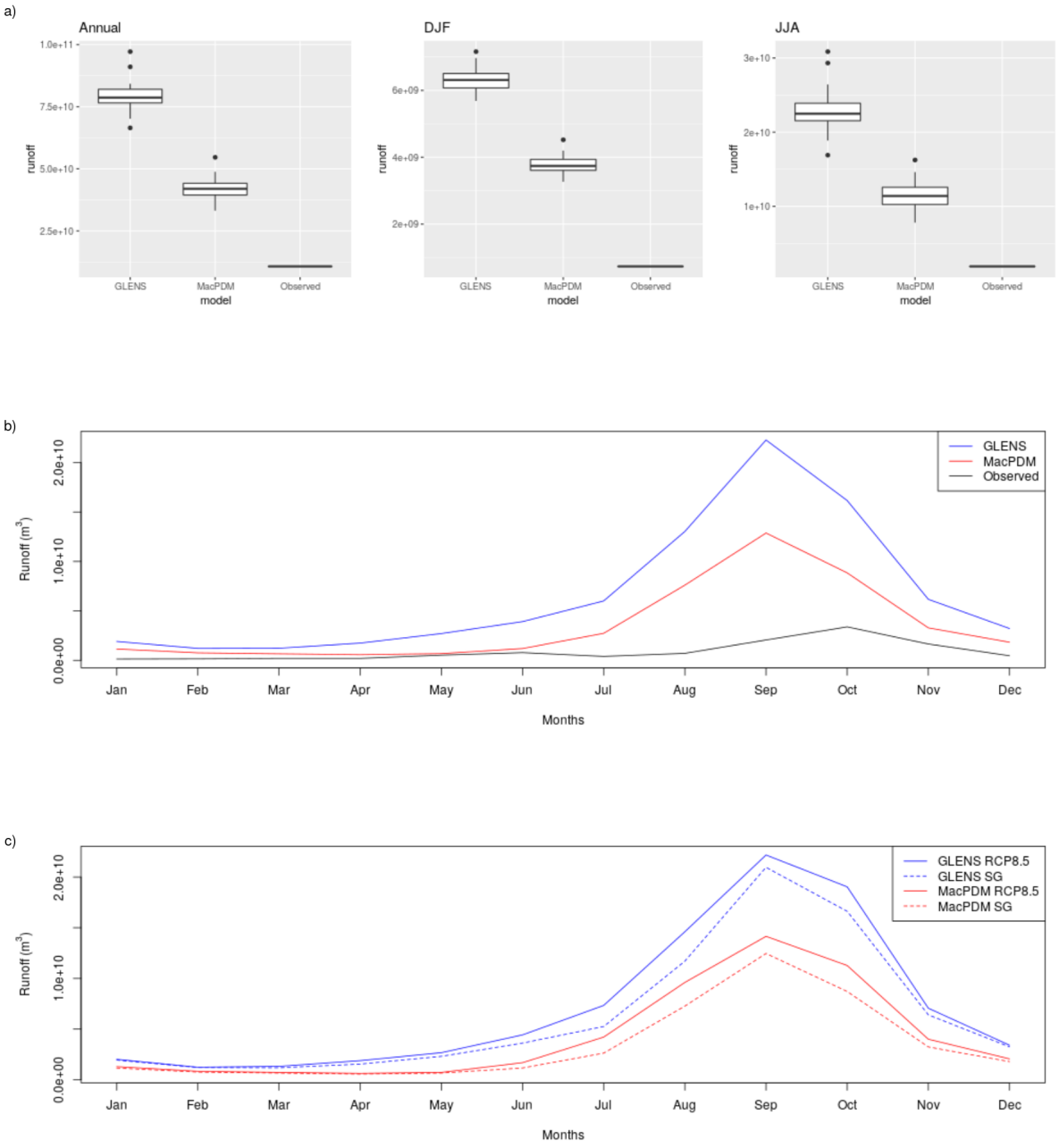


Figure B.28: Catchment comparison graphs for Chao Phraya catchment under Observed, GLENS and MacPDM results. Graphs show the ensemble mean modelled (2015-2025) and observed runoff distributions for a) annual, DJF and JJA and b) seasonal cycle and well as c) projected future (2050-70) runoff differences by model (MacPDM vs. GLENS) and scenario (RCP8.5 vs. SG).

Equatorial

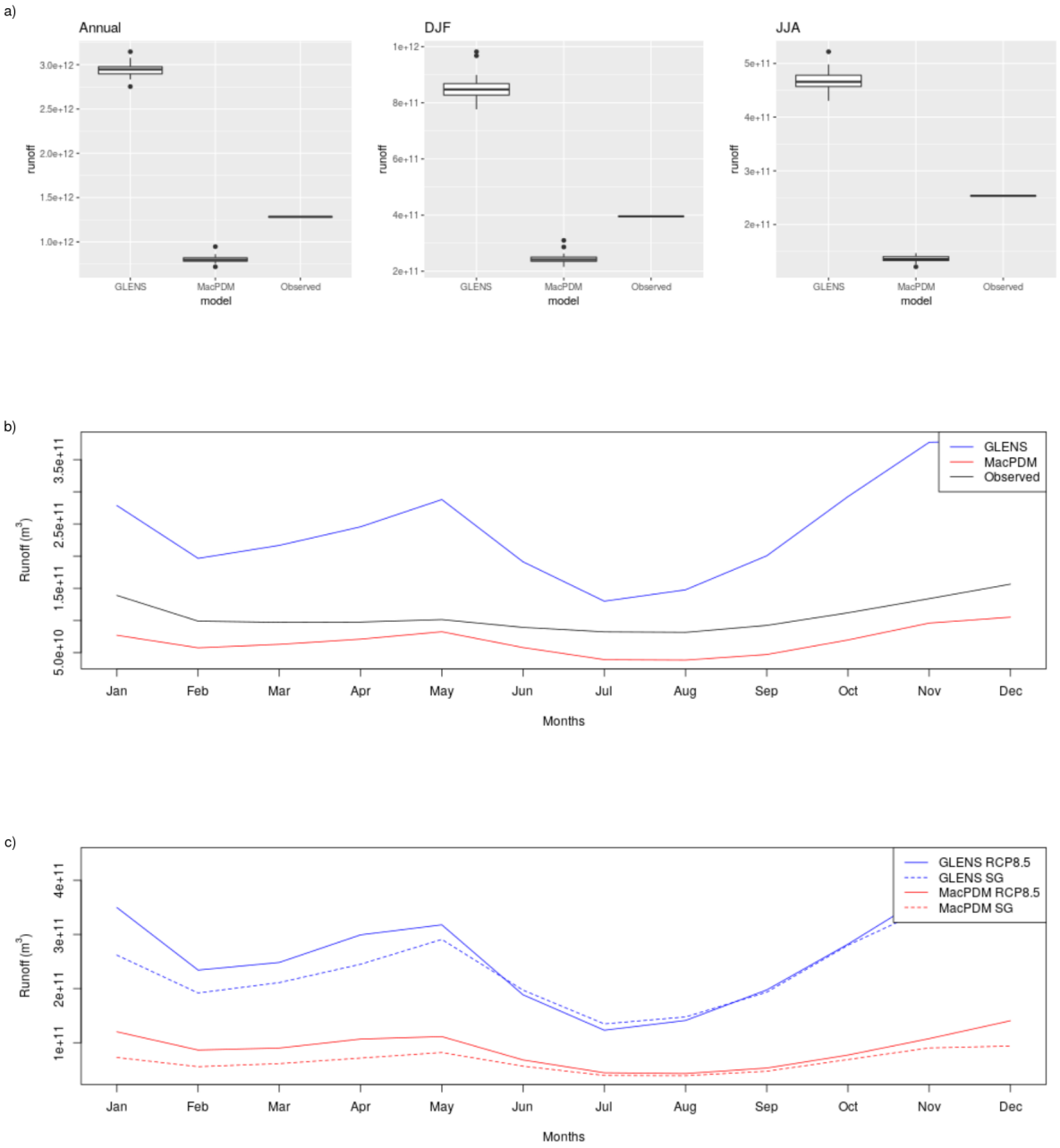


Figure B.29: Catchment comparison graphs for Zaire catchment under Observed, GLENS and MacPDM results. Graphs show the ensemble mean modelled (2015-2025) and observed runoff distributions for a) annual, DJF and JJA and b) seasonal cycle and well as c) projected future (2050-70) runoff differences by model (MacPDM vs. GLENS) and scenario (RCP8.5 vs. SG).

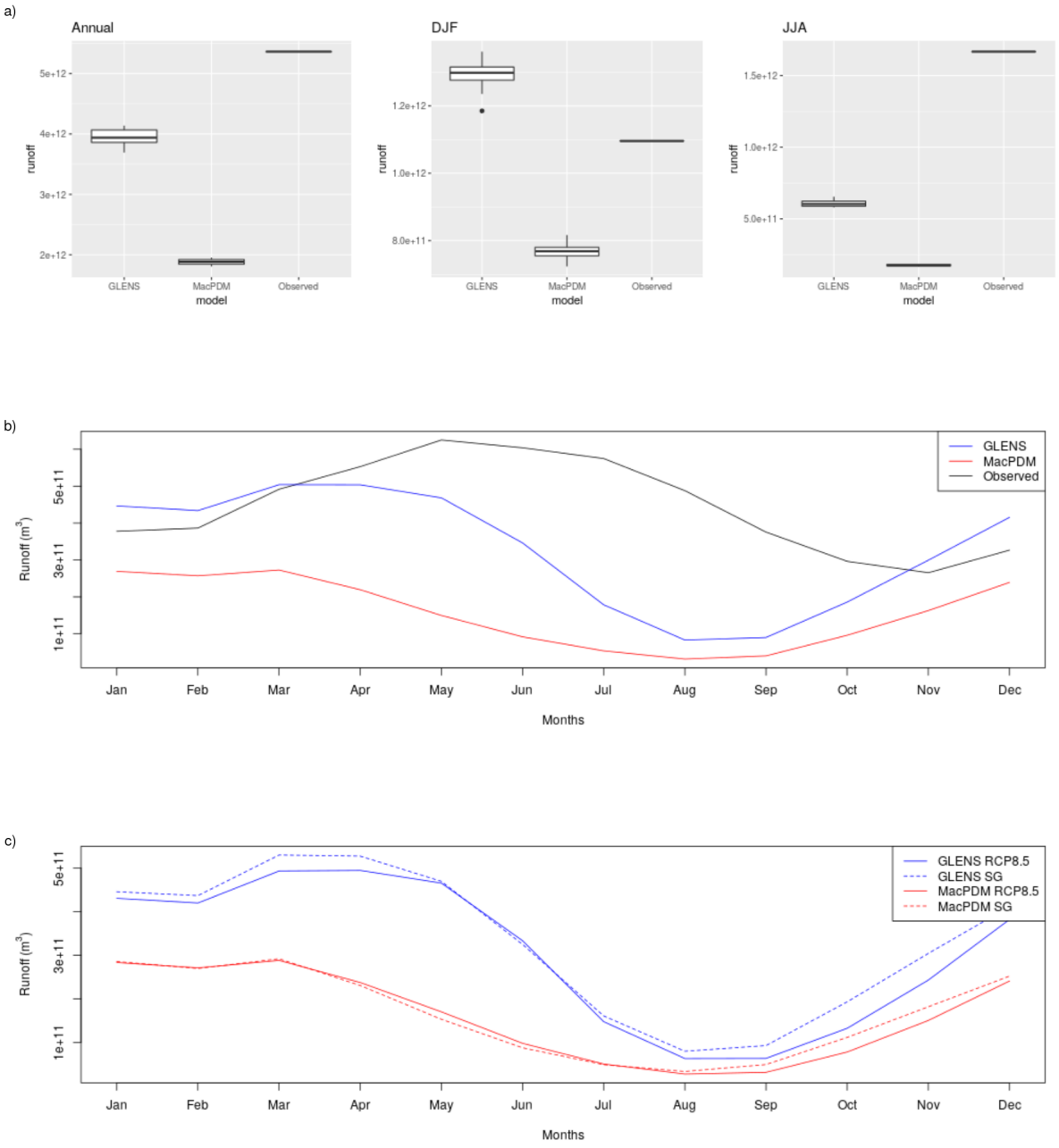


Figure B.30: Catchment comparison graphs for Amazonas catchment under Observed, GLENS and MacPDM results. Graphs show the ensemble mean modelled (2015-2025) and observed runoff distributions for a) annual, DJF and JJA and b) seasonal cycle and well as c) projected future (2050-70) runoff differences by model (MacPDM vs. GLENS) and scenario (RCP8.5 vs. SG).

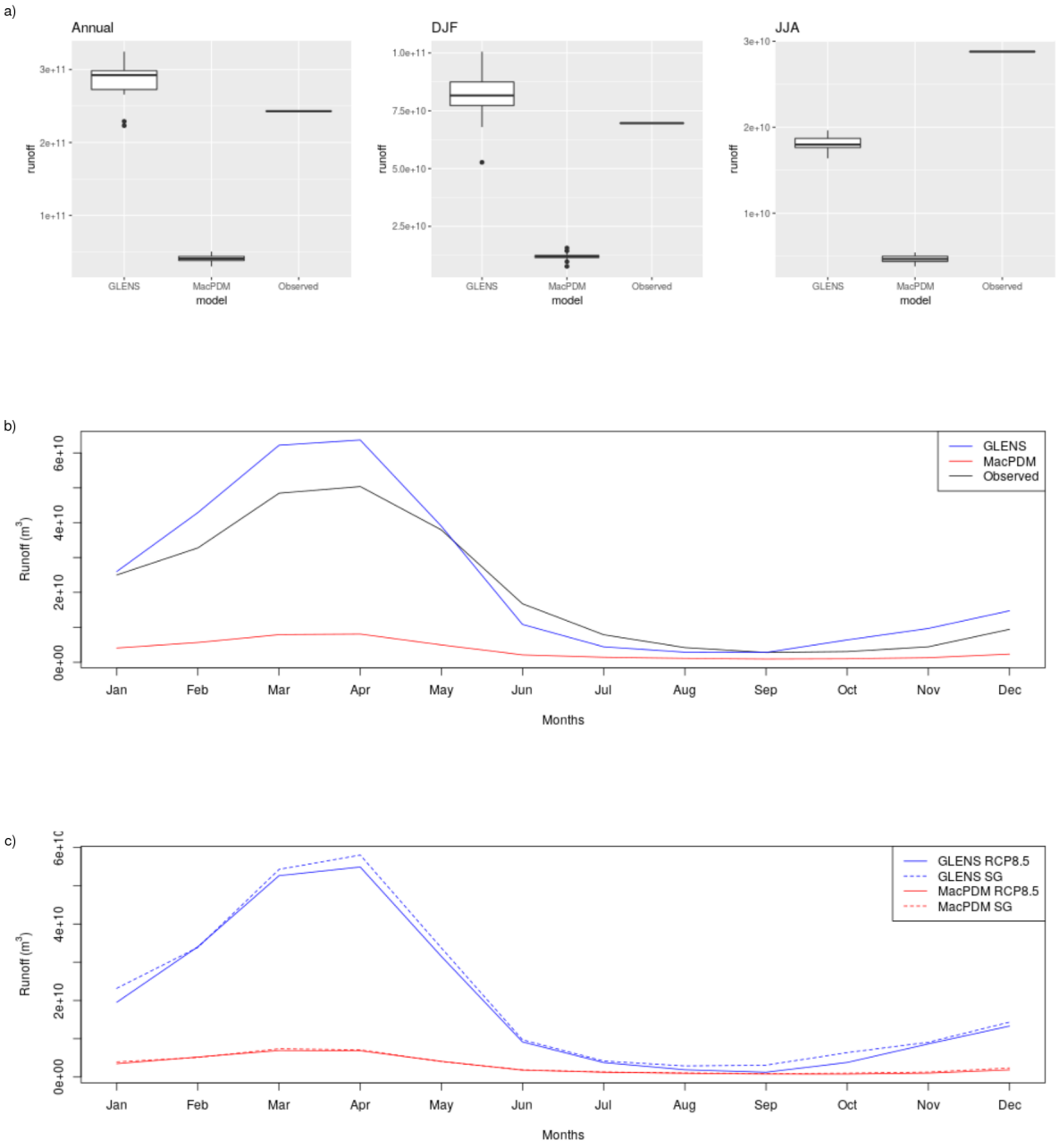


Figure B.31: Catchment comparison graphs for Xingu catchment under Observed, GLENS and MacPDM results. Graphs show the ensemble mean modelled (2015-2025) and observed runoff distributions for a) annual, DJF and JJA and b) seasonal cycle and well as c) projected future (2050-70) runoff differences by model (MacPDM vs. GLENS) and scenario (RCP8.5 vs. SG).

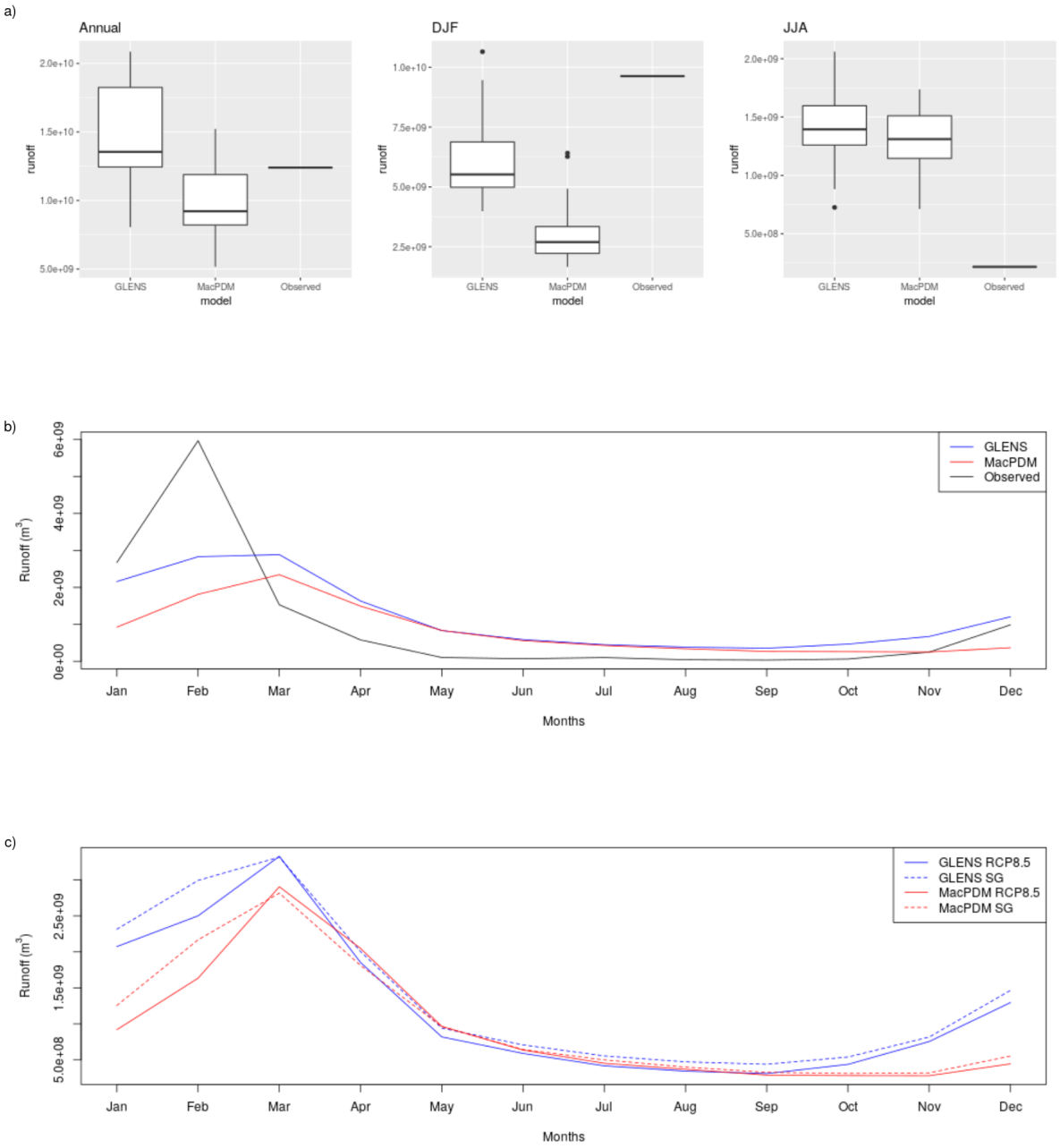


Figure B.32: Catchment comparison graphs for Burdekin catchment under Observed, GLENS and MacPDM results. Graphs show the ensemble mean modelled (2015-2025) and observed runoff distributions for a) annual, DJF and JJA and b) seasonal cycle and well as c) projected future (2050-70) runoff differences by model (MacPDM vs. GLENS) and scenario (RCP8.5 vs. SG).

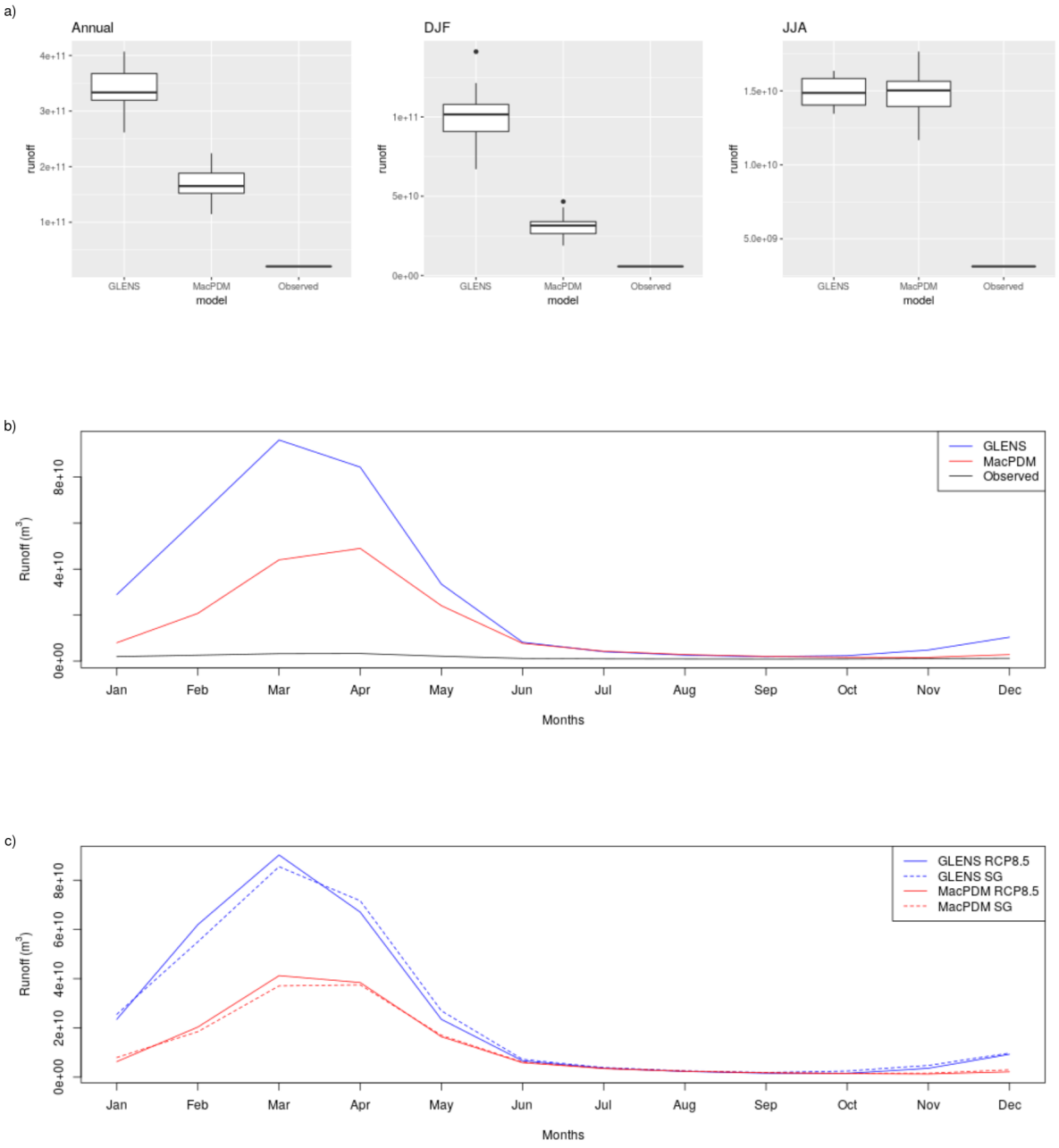


Figure B.33: Catchment comparison graphs for Rio Parnaiba catchment under Observed, GLENS and MacPDM results. Graphs show the ensemble mean modelled (2015-2025) and observed runoff distributions for a) annual, DJF and JJA and b) seasonal cycle and well as c) projected future (2050-70) runoff differences by model (MacPDM vs. GLENS) and scenario (RCP8.5 vs. SG).

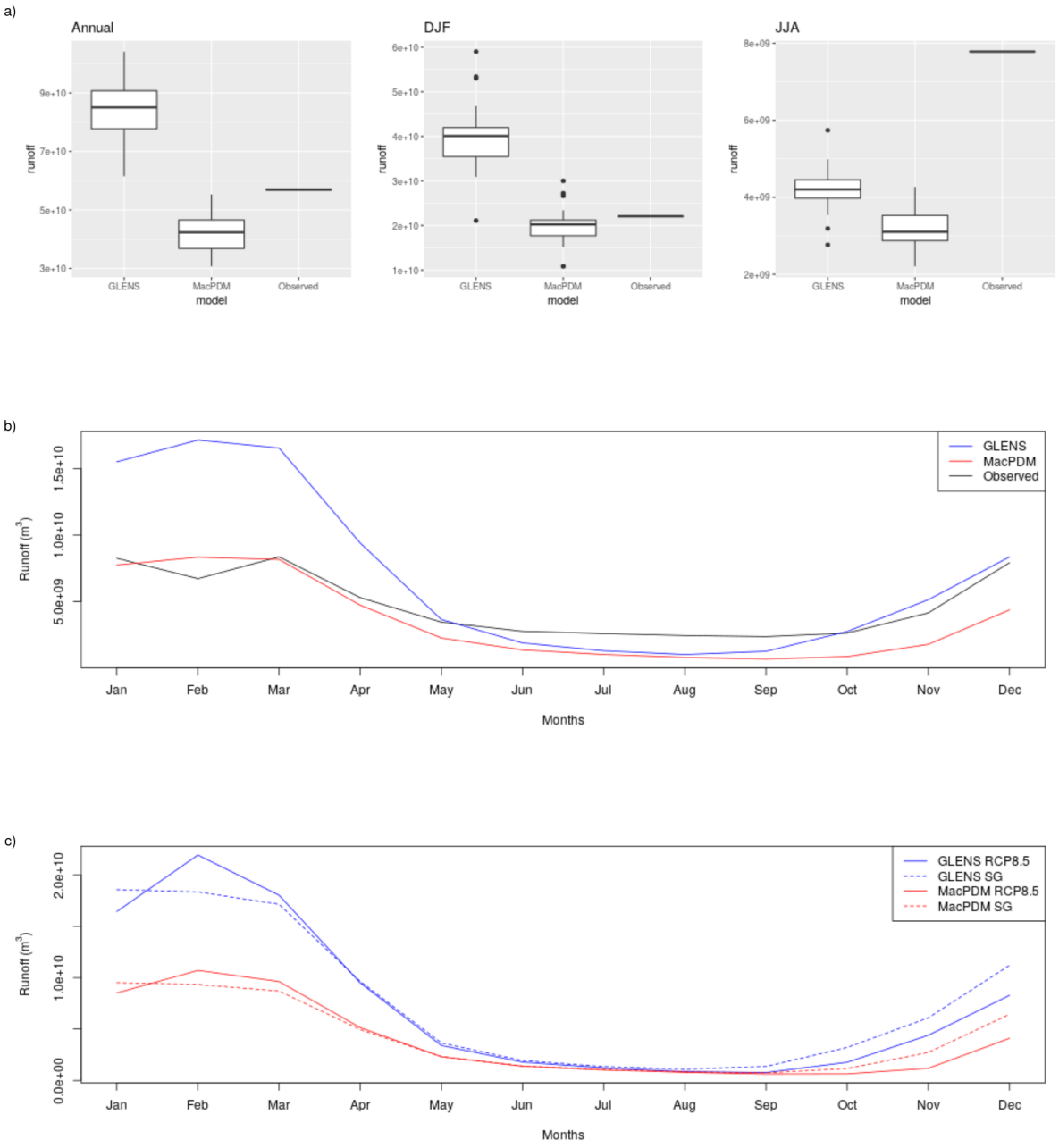


Figure B.34: Catchment comparison graphs for Sao Francisco catchment under Observed, GLENS and MacPDM results. Graphs show the ensemble mean modelled (2015-2025) and observed runoff distributions for a) annual, DJF and JJA and b) seasonal cycle and well as c) projected future (2050-70) runoff differences by model (MacPDM vs. GLENS) and scenario (RCP8.5 vs. SG).

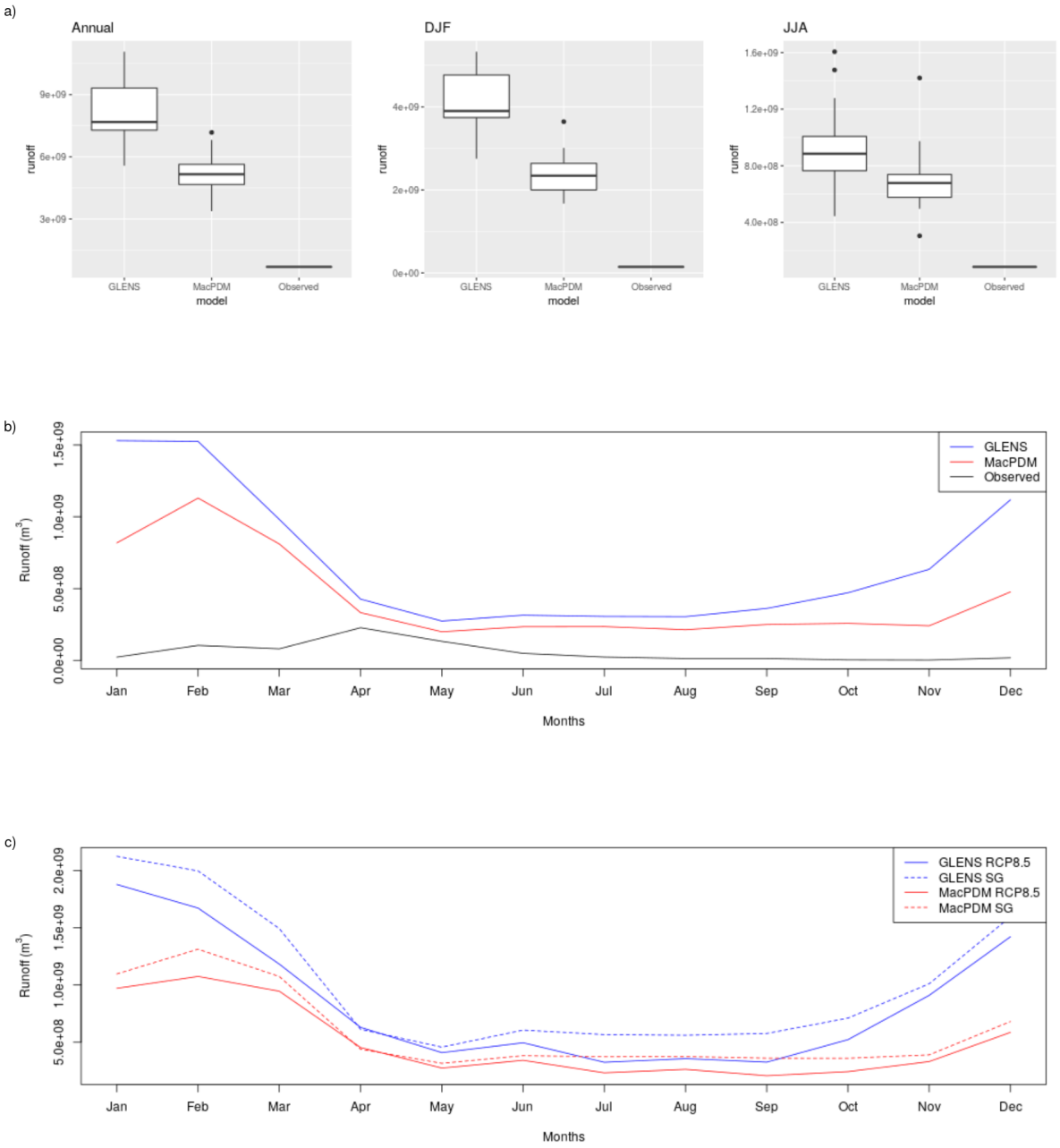


Figure B.35: Catchment comparison graphs for Cooper Creek catchment under Observed, GLENS and MacPDM results. Graphs show the ensemble mean modelled (2015-2025) and observed runoff distributions for a) annual, DJF and JJA and b) seasonal cycle and well as c) projected future (2050-70) runoff differences by model (MacPDM vs. GLENS) and scenario (RCP8.5 vs. SG).

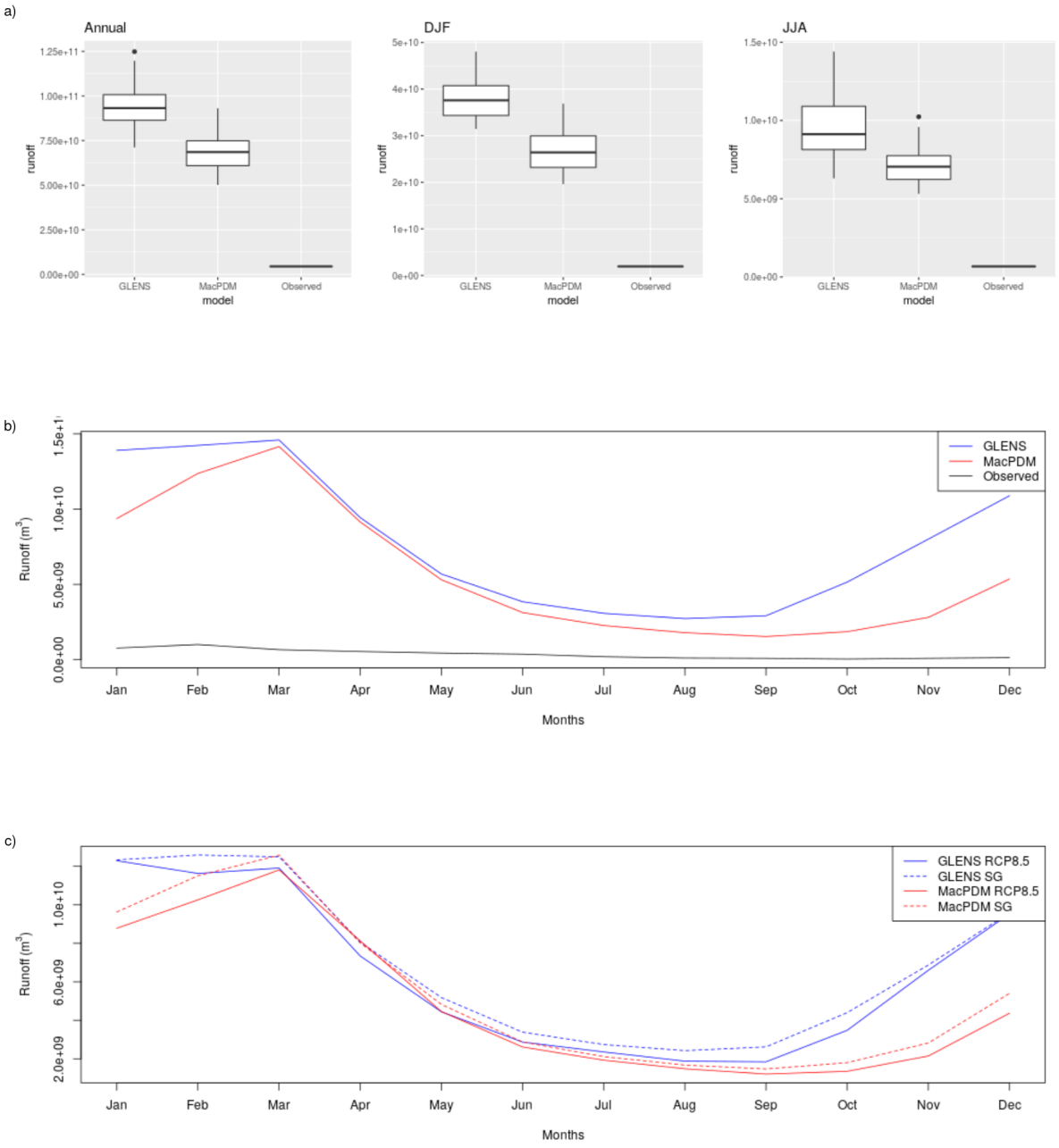


Figure B.36: Catchment comparison graphs for Orange catchment under Observed, GLENS and MacPDM results. Graphs show the ensemble mean modelled (2015-2025) and observed runoff distributions for a) annual, DJF and JJA and b) seasonal cycle and well as c) projected future (2050-70) runoff differences by model (MacPDM vs. GLENS) and scenario (RCP8.5 vs. SG).

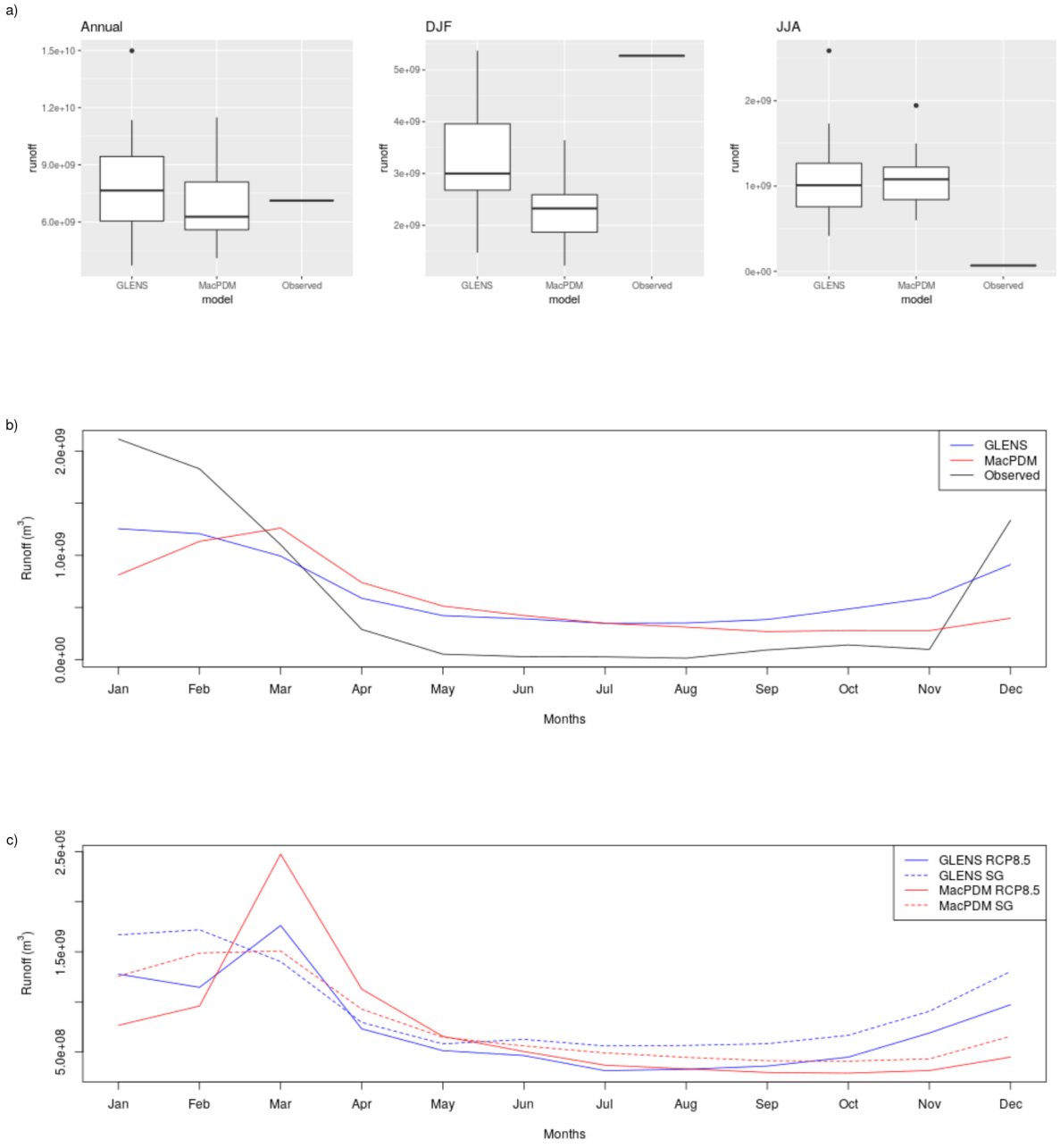


Figure B.37: Catchment comparison graphs for Fitzroy catchment under Observed, GLENS and MacPDM results. Graphs show the ensemble mean modelled (2015-2025) and observed runoff distributions for a) annual, DJF and JJA and b) seasonal cycle and well as c) projected future (2050-70) runoff differences by model (MacPDM vs. GLENS) and scenario (RCP8.5 vs. SG).

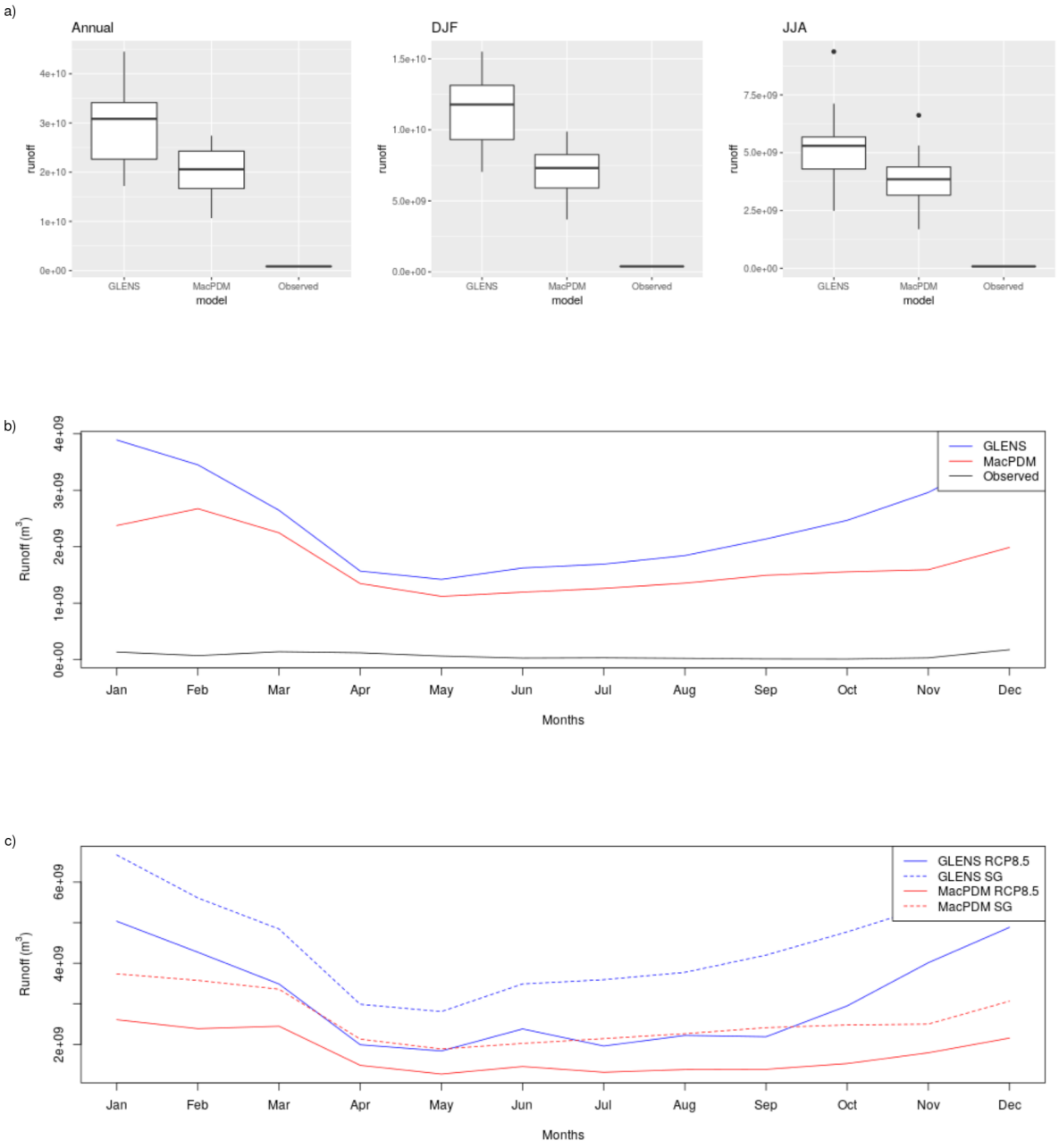


Figure B.38: Catchment comparison graphs for Darling catchment under Observed, GLENS and MacPDM results. Graphs show the ensemble mean modelled (2015-2025) and observed runoff distributions for a) annual, DJF and JJA and b) seasonal cycle and well as c) projected future (2050-70) runoff differences by model (MacPDM vs. GLENS) and scenario (RCP8.5 vs. SG).

Appendix C

Low flow quantile change maps - Q80

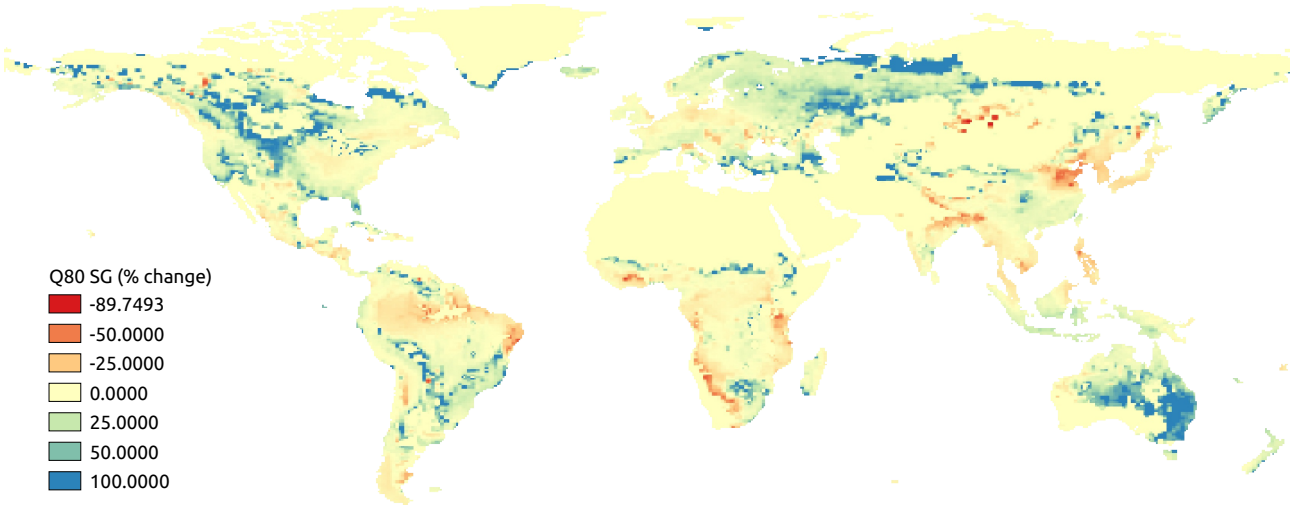


Figure C.1: Percentage difference in Q80 between SG 2050-70 and Baseline (2010-30) - (SG-BL)/BL x 100).

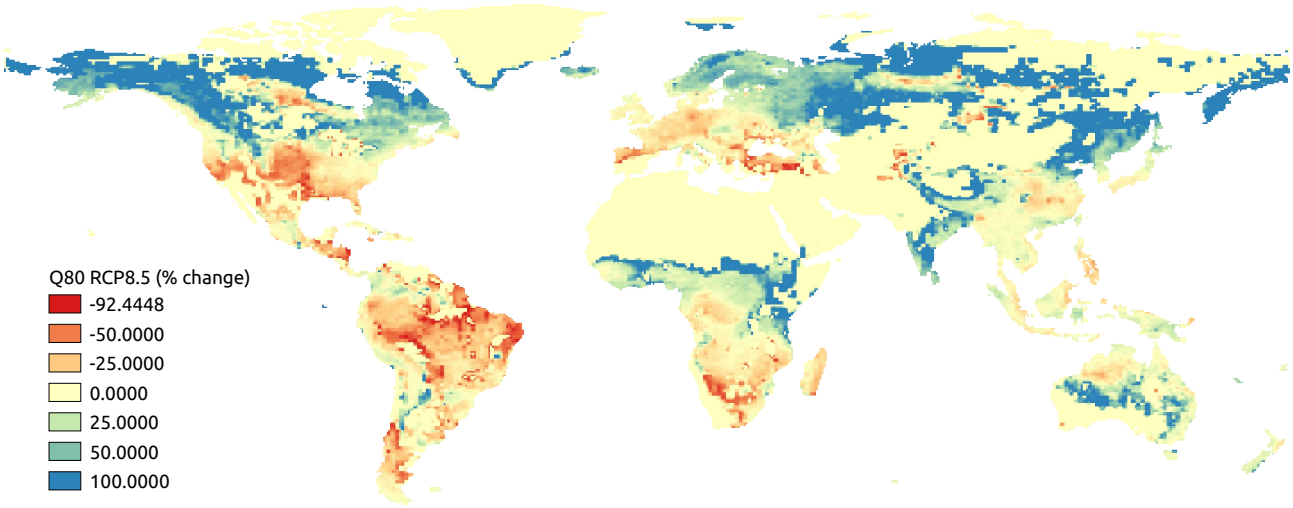


Figure C.2: Percentage difference in Q80 between RCP8.5 2050-70 and Baseline (2010-30) - (RCP8.5-BL)/BL x 100).

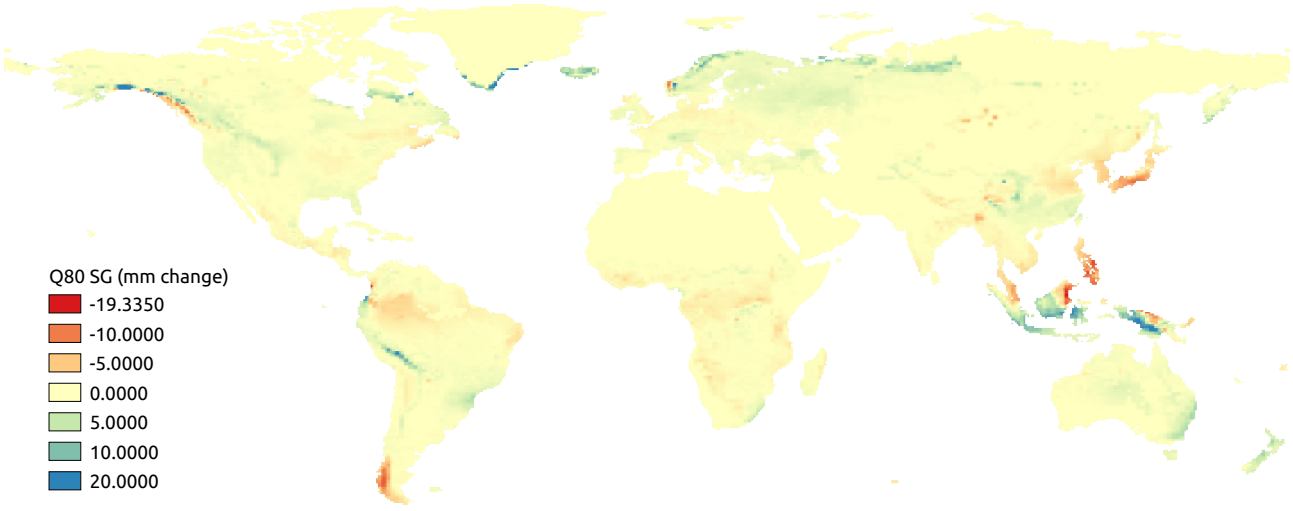


Figure C.3: Absolute (mm) difference in Q80 between SG 2050-70 and Baseline (2010-30) - SG-BL.

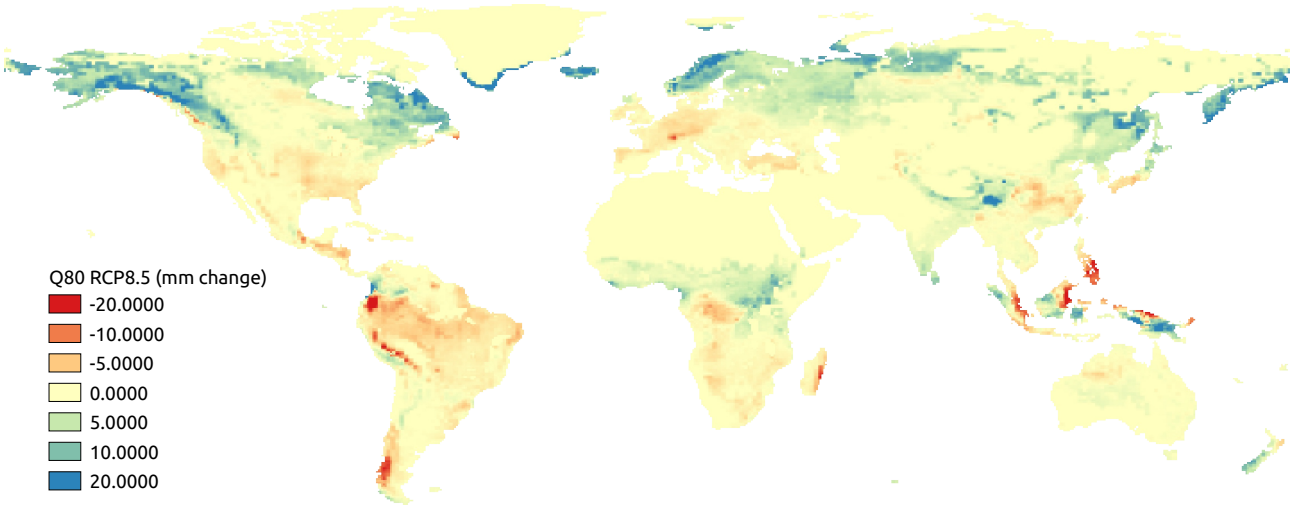


Figure C.4: Absolute (mm) difference in Q80 between RCP8.5 2050-70 and Baseline (2010-30) - RCP8.5-BL.

Appendix D

Standard deviation of daily precipitation

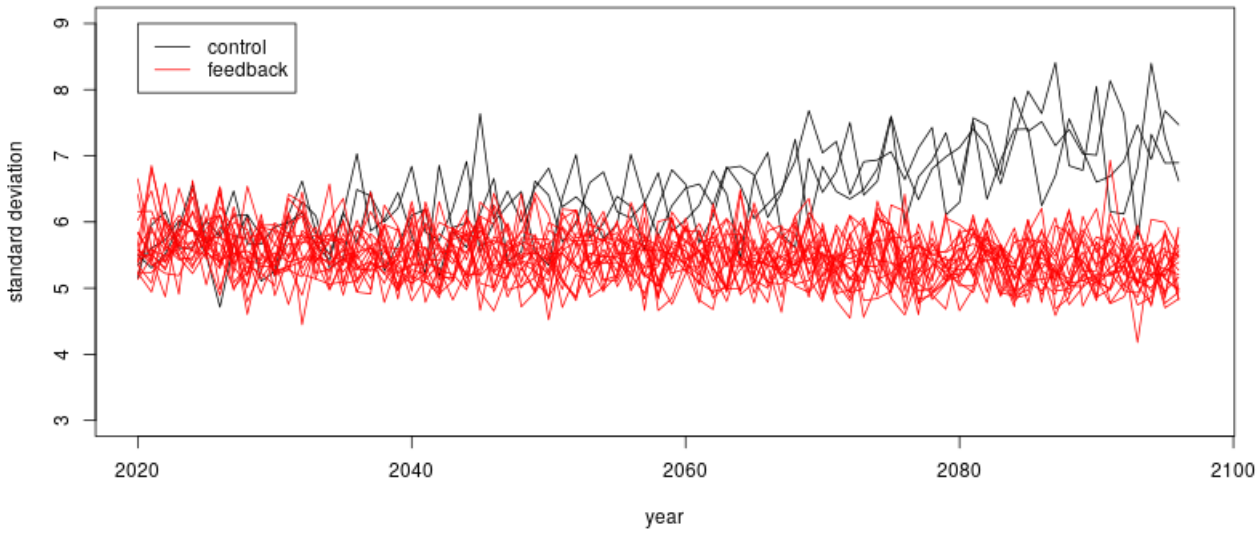


Figure D.1: Graph to show the standard deviation for each year in the daily total land precipitation for each of the 3 RCP8.5 and 20 SG ensemble members.

In order to examine the within year variation in precipitation between the two scenarios (climate change (RCP8.5) and solar geoengineering), the standard deviation of daily precipitation for each year was calculated. It can be seen that the standard deviation increases over time under RCP8.5 but remains more constant under SG. This suggests that more extremes in precipitation will occur under climate change and that the daily precipitation is much more varied than under SG.

Appendix E

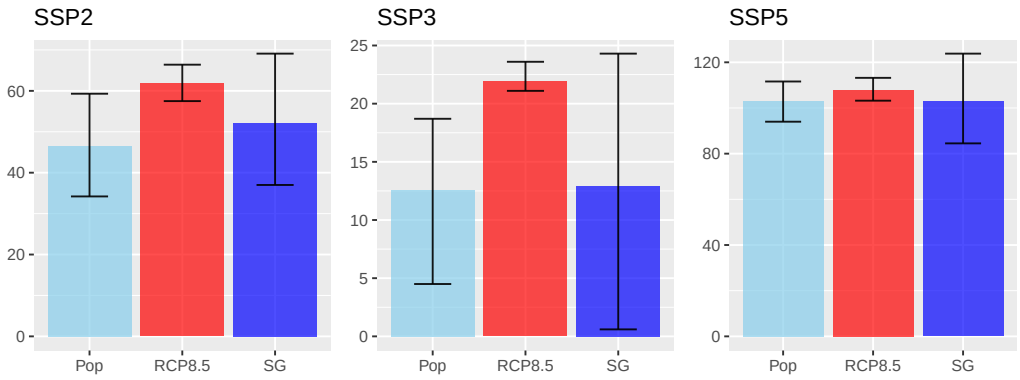
Power of the permutation test

Table E.1: Investigating the power of the permutation test, using a sample size of 20, 10 and 3 for the solar geoengineering group, including the median (minimum & maximum) of the 30 random sample sets of the 20 ensemble members for sample sizes of 10 and 3. The number of the 30 sample sets which were actually statistically significantly different are also shown to demonstrate how the power of the test and ability to find signifcant differences decreases with decreasing sample size.

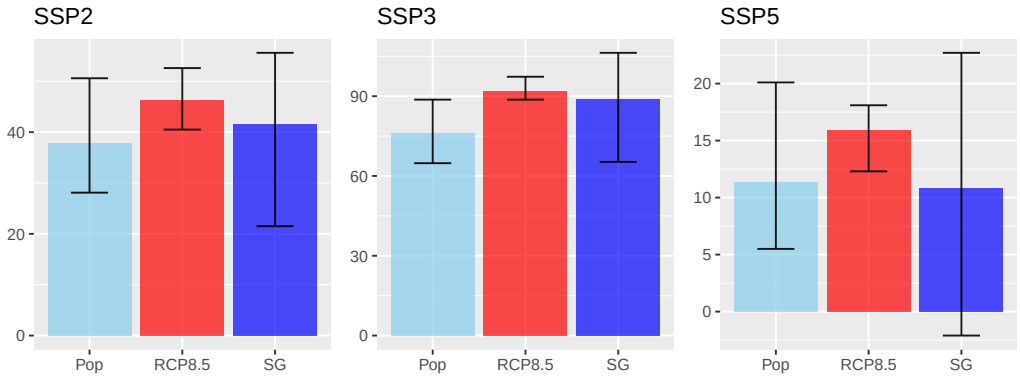
	SSP2			SSP3			SSP5		
sample size	20	10	3	20	10	3	20	10	3
Global	2037	2037.5 (2030 - 2040) n=30	2039 (2020 - 2043) n=30	2035	2034 (2031 - 2037) n=30	2037 (2028 - 2044) n=30	2042	2041 (2020 - 2045) n=30	2043 (2028 - 2048) n=30
South America	2038	2040 (2035 - 2044) n=30	2040 (2026 - 2052) n=9	2035	2036 (2033 - 2040) n=29	2039 (2035 - 2047) n=5	2040	2040 (2034 - 2048) n=30	2046 (2028 - 2050) n=9
Western Africa	2038	2038 (2037 - 2052) n=30	2040 (2036 - 2045) n=9	-	-	-	2021	2025 (2020 - 2048) n=26	2032 (2020 - 2036) n=7
Central America	2046	2064 (2026 - 2069) n=30	2064 (2045 - 2069) n=5	2065	2068 (2062 - 2071) n=30	2066 (2027 - 2071) n=9	2063	2069.5 (2046 - 2076) n=30	2053.5 (2026 - 2069) n=8
Eastern Africa	2035	2037 (2033 - 2038) n=30	2037 (2031 - 2039) n=9	2032	2035 (2026 - 2039) n=30	2030 (2025 - 2040) n=9	2033	2034 (2029 - 2036) n=30	2034 (2020 - 2036) n=9
Northern Africa	-	2041 (2037 - 2081) n=11	2042 (2038 - 2044) n=9	2044	2049 (2047 - 2052) n=30	-	2043	2037 (2022 - 2043) n=30	2027.5 (2021 - 2035) n=8
Middle Africa	2035	2033 (2024 - 2036) n=17	2029 (2024 - 2035) n=9	2036	2035 (2033 - 2038) n=30	2035 (2032 - 2040) n=8	2034	2025.5 (2021 - 2039) n=30	2031 (2023 - 2035) n=9
Northern America	2023	2027 (2021 - 2063) n=29	2035 (2024 - 2064) n=8	2027	2028 (2020 - 2036) n=30	2030 (2020 - 2034) n=7	2048	2048 (2022 - 2057) n=26	2051.5 (2023 - 2061) n=8
Eastern Asia	2035	2037 (2033 - 2040) n=29	2039 (2034 - 2048) n=9	-	2039 (2037 - 2041) n=8	2037 (2032 - 2040) n=5	2036	2037 (2033 - 2043) n=29	2036 (2033 - 2037) n=5
Southern Asia	2039	2042 (2037 - 2047) n=28	2036.5 (2031 - 2041) n=6	2031	2038 (2030 - 2042) n=30	2032 (2024 - 2037) n=9	2036	2035 (2031 - 2040) n=20	2034 (2025 - 2040) n=6
South -eastern Asia	2057	2062.5 (2057 - 2067) n=8	2060 (2054 - 2074) n=7	-	-	-	2065	2068 (2059 - 2072) n=21	-
Southern Europe	2038	2030 (2026 - 2041) n=17	2032.5 (2029 - 2056) n=4	2028	2025 (2022 - 2042) n=13	2028 (2025 - 2065) n=5	-	2041 (2033 - 2057) n=14	2074 (2065 - 2083) n=2
Australia and New Zealand	2053	2055 (2035 - 2062) n=19	2054 (2045 - 2060) n=3	-	-	2049 (2040 - 2052) n=4	-	2079 (2065 - 2086) n=14	2064 (2024 - 2078) n=9
Western Asia	2027	2028 (2023 - 2030) n=29	2029 (2025 - 2031) n=6	2027	2030 (2023 - 2040) n=30	2030 (2024 - 2033) n=9	2027	2027 (2023 - 2031) n=30	2034 (2028 - 2040) n=5

Appendix F

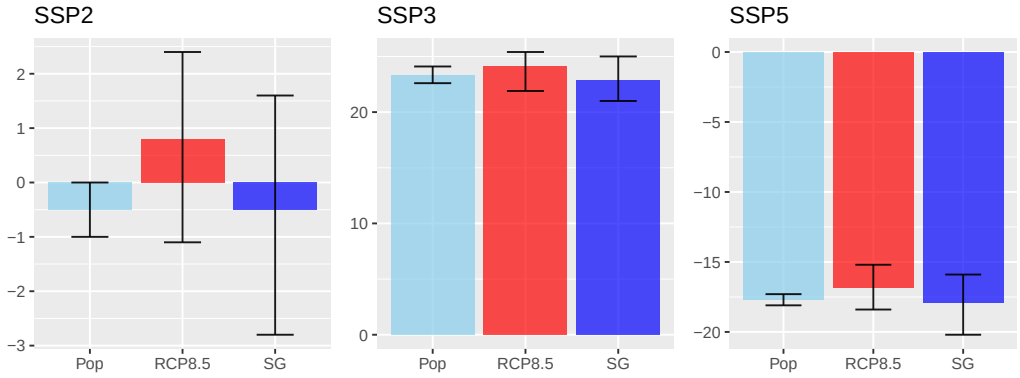
Water Scarcity projections by Sub-region



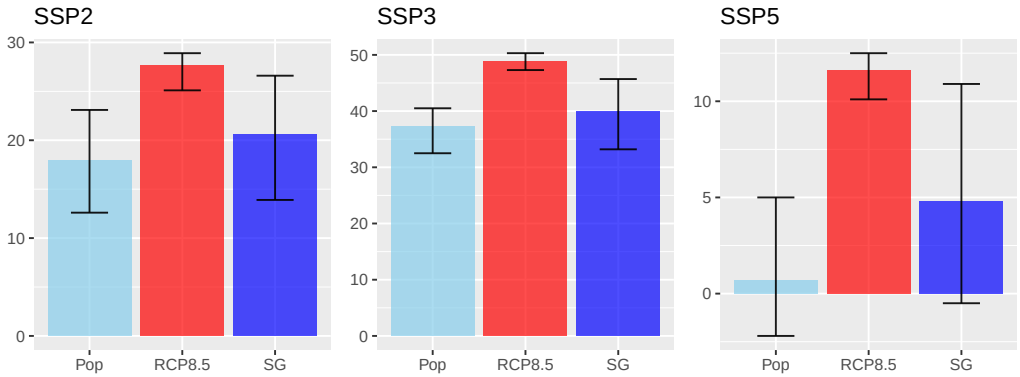
(a) North America



(b) Central America

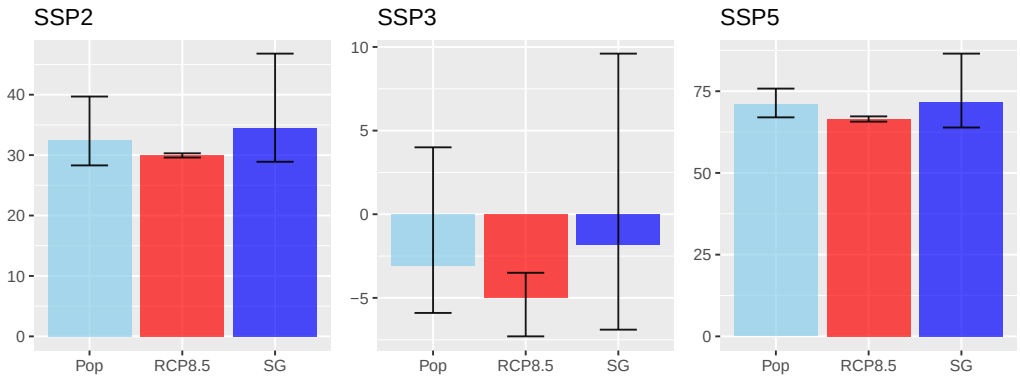


(c) Caribbean

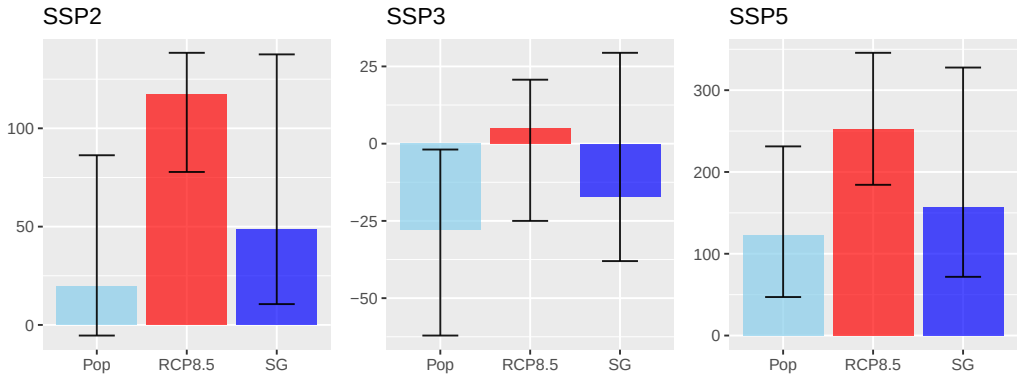


(d) South America

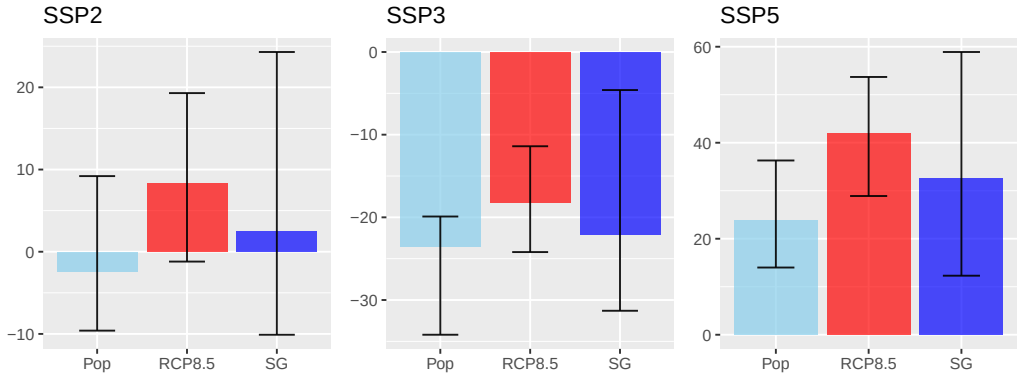
Figure F.1: Graph shows the percentage change in water scarcity for each Sub-region in the future (2050-70) under three scenarios (only change in population, scenario for RCP8.5 and scenario for SG) in comparison to the present day (2010-30).



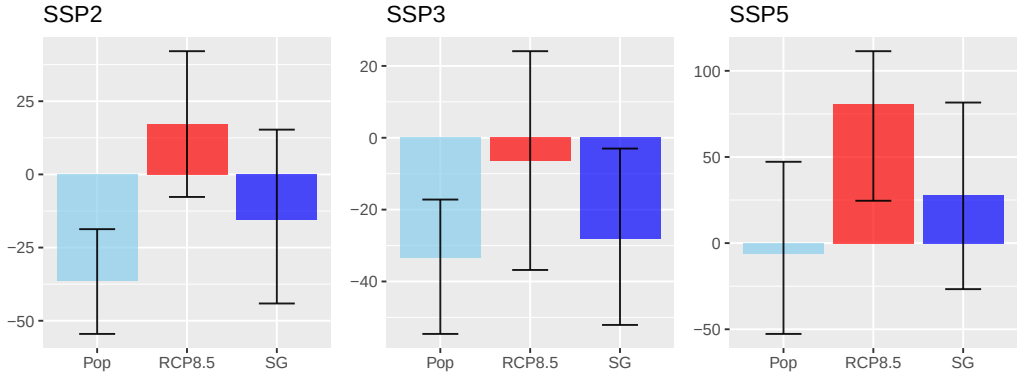
(a) Northern Europe



(b) Western Europe

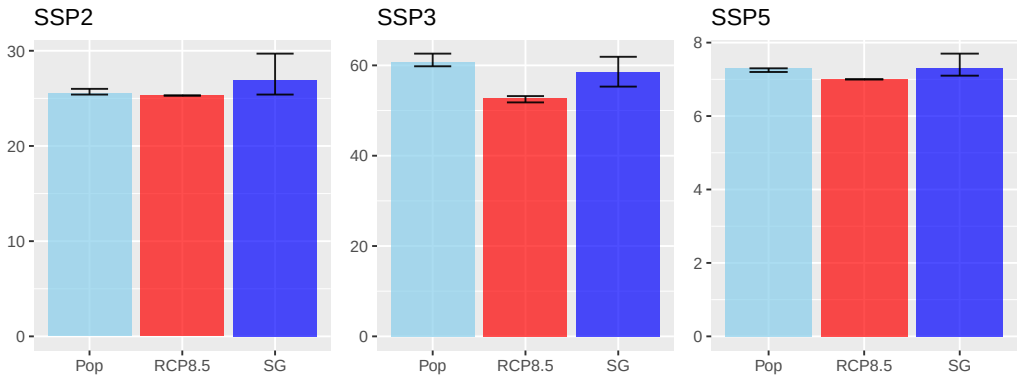


(c) Southern Europe

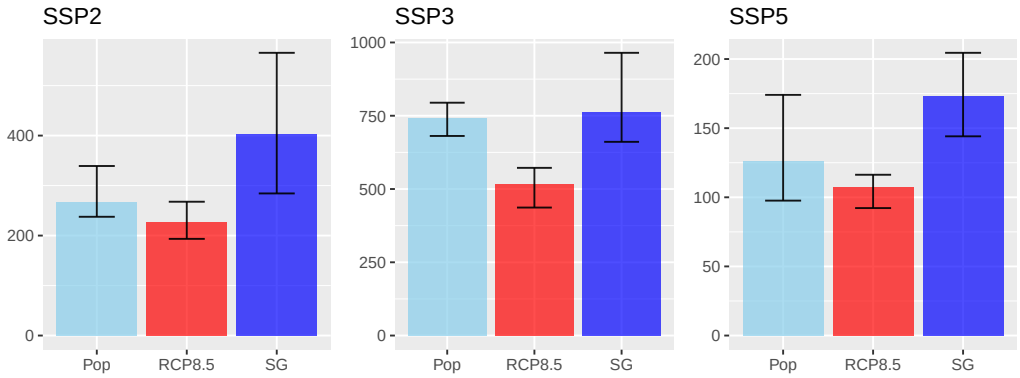


(d) Eastern Europe

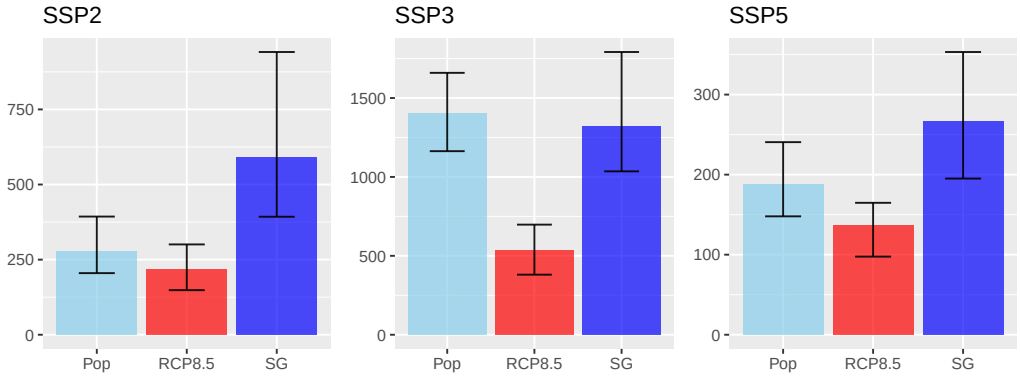
Figure F.2: Graph shows the percentage change in water scarcity for each Sub-region in the future (2050-70) under three scenarios (only change in population, scenario for RCP8.5 and scenario for SG) in comparison to the present day (2010-30).



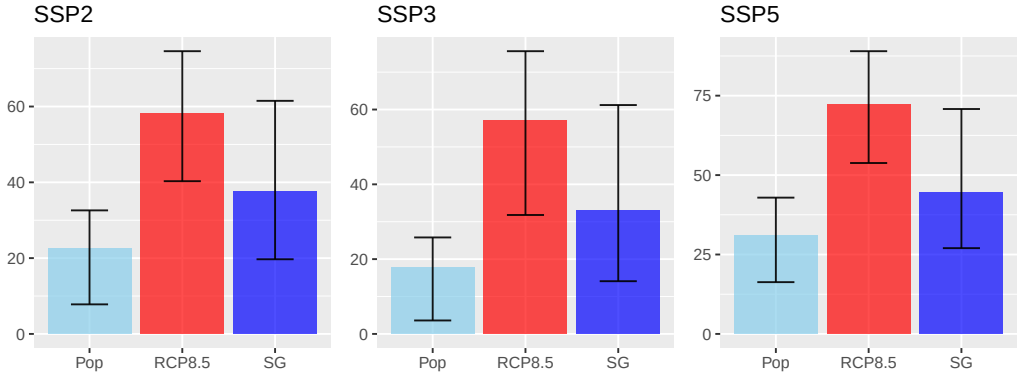
(a) Northern Africa



(b) Western Africa

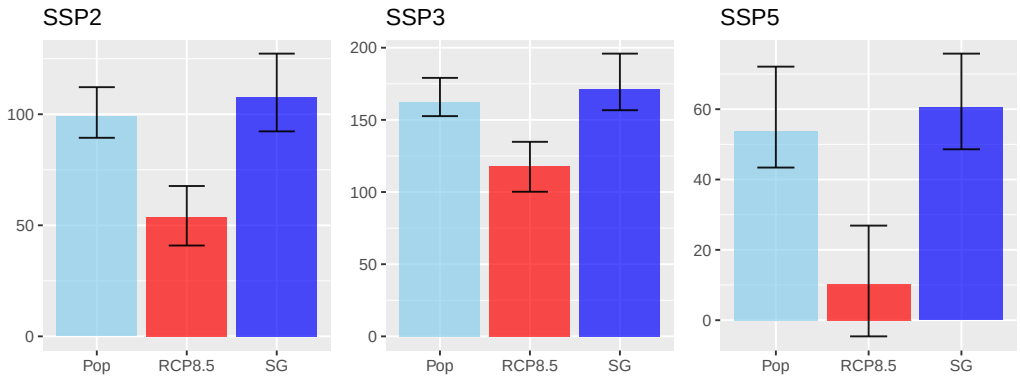


(c) Central Africa

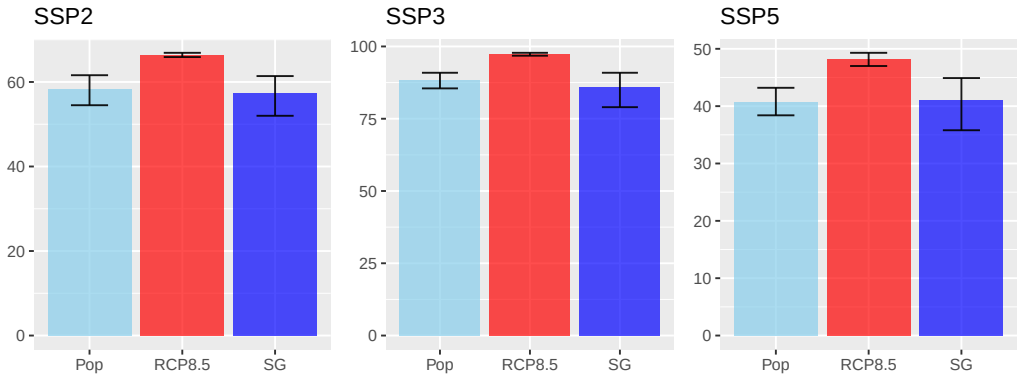


(d) Southern Africa

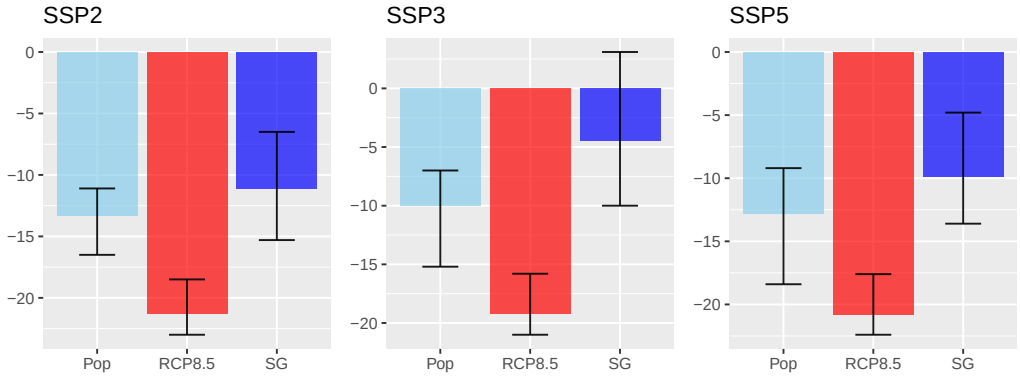
Figure F.3: Graph shows the percentage change in water scarcity for each Sub-region in the future (2050-70) under three scenarios (only change in population, scenario for RCP8.5 and scenario for SG) in comparison to the present day (2010-30).



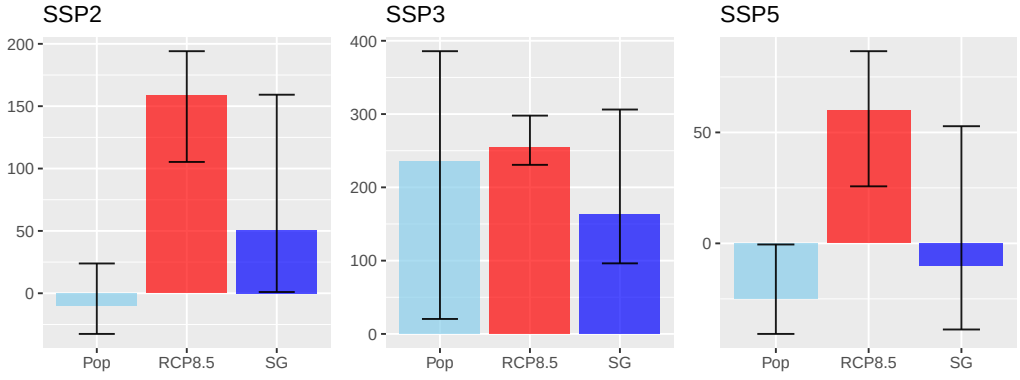
(a) Eastern Africa



(b) Western Asia

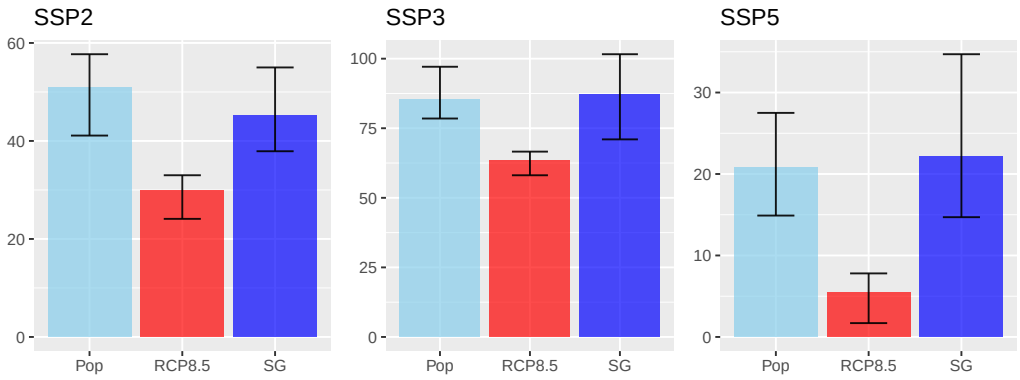


(c) Eastern Asia

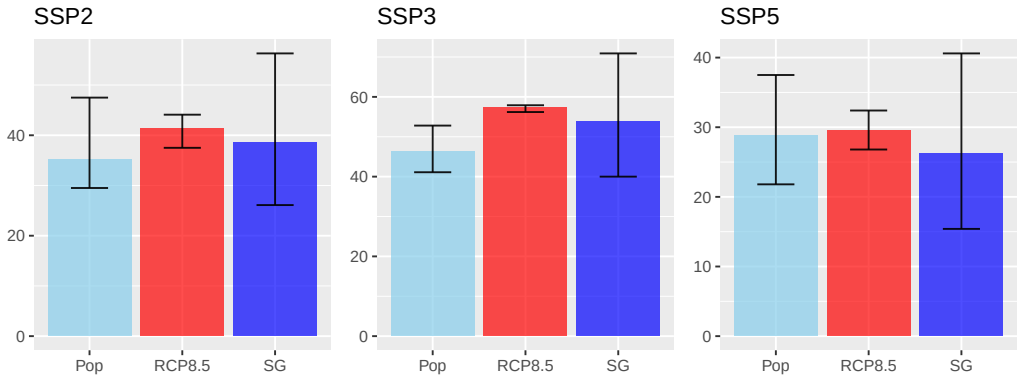


(d) Central Asia

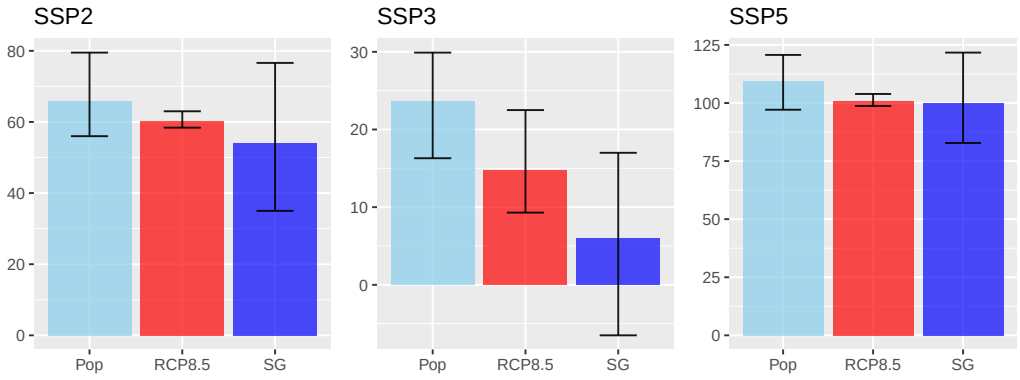
Figure F.4: Graph shows the percentage change in water scarcity for each Sub-region in the future (2050-70) under three scenarios (only change in population, scenario for RCP8.5 and scenario for SG) in comparison to the present day (2010-30).



(a) Southern Asia



(b) South-eastern Asia



(c) Australia and New Zealand

Figure F.5: Graph shows the percentage change in water scarcity for each Sub-region in the future (2050-70) under three scenarios (only change in population, scenario for RCP8.5 and scenario for SG) in comparison to the present day (2010-30).

Bibliography

Abbott, M., Bathurst, J., Cunge, J., O'connell, P., and Rasmussen, J. (1986a). An introduction to the european hydrological system—systeme hydrologique europeen,"she", 2: Structure of a physically-based, distributed modelling system. *Journal of hydrology*, 87(1-2):61–77.

Abbott, M. B., Bathurst, J. C., Cunge, J. A., O'Connell, P. E., and Rasmussen, J. (1986b). An introduction to the european hydrological system—systeme hydrologique europeen,"she", 1: History and philosophy of a physically-based, distributed modelling system. *Journal of hydrology*, 87(1-2):45–59.

Alcamo, J., Doll, P., Henrichs, T., Kaspar, F., Lehner, B., Rosch, T., and Siebert, S. (2003). Development and testing of the watergap 2 global model of water use and availability. *Hydrol. Sci. J.*, 48:317–337.

Alcamo, J., Flörke, M., and Märker, M. (2007). Future long-term changes in global water resources driven by socio-economic and climatic changes. *Hydrological Sciences Journal*, 52(2):247–275.

Allen, M. R. and Ingram, W. J. (2002). Constraints on future changes in climate and the hydrologic cycle. *Nature*, 419(6903):228–232.

Alley, W. M. (1984). The palmer drought severity index: limitations and assumptions. *Journal of Applied Meteorology and Climatology*, 23(7):1100–1109.

Andreadis, K. M., Clark, E. A., Wood, A. W., Hamlet, A. F., and Lettenmaier, D. P. (2005). Twentieth-century drought in the conterminous united states. *Journal of Hydrometeorology*, 6(6):985–1001.

Andrews, T. and Forster, P. M. (2008). Co2 forcing induces semi-direct effects with consequences for climate feedback interpretations. *Geophysical Research Letters*, 35(4).

Andrews, T., Forster, P. M., and Gregory, J. M. (2009). A surface energy perspective on climate change. *Journal of Climate*, 22(10):2557–2570.

Angel, R. (2006). Feasibility of cooling the earth with a cloud of small spacecraft near the inner lagrange point (l1). *Proceedings of the National Academy of Sciences*, 103(46):17184–17189.

Arino, O., Ramos Perez, J. J., Kalogirou, V., Bontemps, S., Defourny, P., and Van Bogaert, E. (2012). Global Land Cover Map for 2009 (GlobCover 2009). PANGAEA.

Arnell, N. W. (1999). A simple water balance model for the simulation of streamflow over a large geographic domain. *Journal of Hydrology*, 217(3):314–335.

Arnell, N. W. (2003). Effects of ipcc sres* emissions scenarios on river runoff: a global perspective. *Hydrology and Earth System Sciences Discussions*, 7(5):619–641.

Arnell, N. W. (2004). Climate change and global water resources: Sres emissions and socio-economic scenarios. *Global environmental change*, 14(1):31–52.

Arnell, N. W. and Lloyd-Hughes, B. (2014). The global-scale impacts of climate change on water resources and flooding under new climate and socio-economic scenarios. *Climatic change*, 122(1):127–140.

Arnell, N. W., van Vuuren, D. P., and Isaac, M. (2011). The implications of climate policy for the impacts of climate change on global water resources. *Global Environmental Change*, 21(2):592–603.

Arrhenius, S. (1896). Xxxi. on the influence of carbonic acid in the air upon the temperature of the ground. *The London, Edinburgh, and Dublin Philosophical Magazine and Journal of Science*, 41(251):237–276.

Aswathy, V., Boucher, O., Quaas, M., Niemeier, U., Muri, H., Mülmenstädt, J., and Quaas, J. (2015). Climate extremes in multi-model simulations of stratospheric aerosol and marine cloud brightening climate engineering. *Atmospheric Chemistry and Physics*, 15(16):9593–9610.

Azose, J. J., Ševčíková, H., and Raftery, A. E. (2016). Probabilistic population projections with migration uncertainty. *Proceedings of the National Academy of Sciences*, 113(23):6460–6465.

Bala, G., Caldeira, K., and Nemani, R. (2010). Fast versus slow response in climate change: implications for the global hydrological cycle. *Climate dynamics*, 35(2-3):423–434.

Bala, G., Duffy, P., and Taylor, K. (2008). Impact of geoengineering schemes on the global hydrological cycle. *Proceedings of the National Academy of Sciences*, 105(22):7664–7669.

Barrett, S. (2014). Solar geoengineering's brave new world: Thoughts on the governance of an unprecedented technology.

Bartholomé, E. and Belward, A. S. (2005). Glc2000: a new approach to global land cover mapping from earth observation data. *International Journal of Remote Sensing*, 26(9):1959–1977.

Beaulieu, E., Lucas, Y., Viville, D., Chabaux, F., Ackerer, P., Goddéris, Y., and Pierret, M.-C. (2016). Hydrological and vegetation response to climate change in a forested mountainous catchment. *Modeling Earth Systems and Environment*, 2(4):1–15.

Bellenger, H., Guilyardi, É., Leloup, J., Lengaigne, M., and Vialard, J. (2014). Enso representation in climate models: From cmip3 to cmip5. *Climate Dynamics*, 42(7):1999–2018.

Berkovitch, N., Ginzburg, P., and Orenstein, M. (2010). Concave plasmonic particles: broad-band geometrical tunability in the near-infrared. *Nano letters*, 10(4):1405–1408.

Best, M., Pryor, M., Clark, D., Rooney, G., Essery, R., Ménard, C., Edwards, J., Hendry, M., Porson, A., Gedney, N., et al. (2011). The joint uk land environment simulator (jules), model description–part 1: energy and water fluxes. *Geoscientific Model Development*, 4(3):677–699.

Beven, K. and Binley, A. (1992). The future of distributed models: model calibration and uncertainty prediction. *Hydrological processes*, 6(3):279–298.

Beven, K. J. (2012). *Rainfall-runoff modelling: the primer*. John Wiley & Sons.

Beven, K. J. and Kirkby, M. J. (1979). A physically based, variable contributing area model of basin hydrology/un modèle à base physique de zone d'appel variable de l'hydrologie du bassin versant. *Hydrological Sciences Journal*, 24(1):43–69.

Bierkens, M. F. (2015). Global hydrology 2015: State, trends, and directions. *Water Resources Research*, 51(7):4923–4947.

Birner, T. and Bönisch, H. (2011). Residual circulation trajectories and transit times into the extratropical lowermost stratosphere. *Atmospheric Chemistry and Physics*, 11(2):817.

Black, R., Bennett, S. R., Thomas, S. M., and Beddington, J. R. (2011). Climate change: Migration as adaptation. *Nature*, 478(7370):447–449.

Bluth, G. J., Doiron, S. D., Schnetzler, C. C., Krueger, A. J., and Walter, L. S. (1992). Global tracking of the so2 clouds from the june, 1991 mount pinatubo eruptions. *Geophysical Research Letters*, 19(2):151–154.

Boettcher, M. and Schäfer, S. (2017). Reflecting upon 10 years of geoengineering research: Introduction to the crutzen+ 10 special issue. *Earth's Future*, 5(3):266–277.

Bonan, G. B., Lawrence, P. J., Oleson, K. W., Levis, S., Jung, M., Reichstein, M., Lawrence, D. M., and Swenson, S. C. (2011). Improving canopy processes in the community land model version 4 (clm4) using global flux fields empirically inferred from fluxnet data. *Journal of Geophysical Research: Biogeosciences*, 116(G2).

Bonan, G. B., Oleson, K. W., Vertenstein, M., Levis, S., Zeng, X., Dai, Y., Dickinson, R. E., and Yang, Z.-L. (2002). The land surface climatology of the community land model coupled to the ncar community climate model. *Journal of climate*, 15(22):3123–3149.

Bondeau, A. (2007). Modelling the role of agriculture for the 20th century global terrestrial carbon balance. *Global Change Biol.*, 13:679–706.

Borzì, I., Bonaccorso, B., and Fiori, A. (2019). A modified ihacres rainfall-runoff model for predicting the hydrologic response of a river basin connected with a deep groundwater aquifer. *Water*, 11(10):2031.

Boyer, C., Chaumont, D., Chartier, I., and Roy, A. G. (2010). Impact of climate change on the hydrology of st. lawrence tributaries. *Journal of hydrology*, 384(1-2):65–83.

Brühl, C., Lelieveld, J., Crutzen, P., Tost, H., and Stier, P. (2012). The role of carbonyl sulphide as a source of stratospheric sulphate aerosol and its impact on climate. *Atmospheric Chemistry & Physics*, 12(3).

Budyko, M. I. (1977). *Climatic changes*. American Geophysical Union.

Butchart, N. (2014). The brewer-dobson circulation. *Reviews of geophysics*, 52(2):157–184.

Casey (2017). How do i convert specific humidity to relative humidity? https://earthscience.stackexchange.com/questions/2360/how-do-i-convert-specific-humidity-to-relative-humidity. Date accessed: 27.06.17.

Cheng, W., MacMartin, D. G., Dagon, K., Kravitz, B., Tilmes, S., Richter, J. H., Mills, M. J., and Simpson, I. R. (2019). Soil moisture and other hydrological changes in a stratospheric aerosol geoengineering large ensemble. *Journal of Geophysical Research: Atmospheres*, 124(23):12773–12793.

Clapp, R. B. and Hornberger, G. M. (1978). Empirical equations for some soil hydraulic properties. *Water resources research*, 14(4):601–604.

Clark, M. P., Kavetski, D., and Fenicia, F. (2011). Pursuing the method of multiple working hypotheses for hydrological modeling. *Water Resources Research*, 47(9).

Collatz, G. J., Ball, J. T., Grivet, C., and Berry, J. A. (1991). Physiological and environmental regulation of stomatal conductance, photosynthesis and transpiration: a model that includes a laminar boundary layer. *Agricultural and Forest meteorology*, 54(2-4):107–136.

Collatz, G. J., Ribas-Carbo, M., and Berry, J. (1992). Coupled photosynthesis-stomatal conductance model for leaves of c4 plants. *Functional Plant Biology*, 19(5):519–538.

Corzo Perez, G., Van Huijgevoort, M., Voß, F., and Van Lanen, H. (2011). On the spatio-temporal analysis of hydrological droughts from global hydrological models. *Hydrology and Earth System Sciences*, 15(9):2963–2978.

Cosby, B., Hornberger, G., Clapp, R., and Ginn, T. (1984). A statistical exploration of the relationships of soil moisture characteristics to the physical properties of soils. *Water resources research*, 20(6):682–690.

Crawford, N. H. and Linsley, R. K. (1966). Digital simulation in hydrology'stanford watershed model iv. *Department of Civil Engineering: Technical report.*

Crutzen, P. J. (1976). The possible importance of cso for the sulfate layer of the stratosphere. *Geophysical research letters*, 3(2):73–76.

Crutzen, P. J. (2002). Geology of mankind. *Nature*, 415(6867):23–23.

Crutzen, P. J. (2006). Albedo enhancement by stratospheric sulfur injections: a contribution to resolve a policy dilemma? *Climatic change*, 77(3):211–220.

Curry, C. L., Sillmann, J., Bronaugh, D., Alterskjaer, K., Cole, J. N., Ji, D., Kravitz, B., Kristjánsson, J. E., Moore, J. C., Muri, H., et al. (2014). A multimodel examination of climate extremes in an idealized geoengineering experiment. *Journal of Geophysical Research: Atmospheres*, 119(7):3900–3923.

Da-Allada, C., Baloïtcha, E., Alamou, E., Awo, F., Bonou, F., Pomalegni, Y., Biao, E., Obada, E., Zandagba, J., Tilmes, S., et al. (2020). Changes in west african summer monsoon precipitation under stratospheric aerosol geoengineering. *Earth's Future*, 8(7):e2020EF001595.

Dagon, K. and Schrag, D. P. (2016). Exploring the effects of solar radiation management on water cycling in a coupled land–atmosphere model. *Journal of Climate*, 29(7):2635–2650.

Dagon, K. and Schrag, D. P. (2019). Quantifying the effects of solar geoengineering on vegetation. *Climatic Change*, 153(1):235–251.

Dai, A. (2019). The climate data guide: Palmer drought severity index (pdsi). `https://climatedataguide.ucar.edu/climate-data/palmer-drought-severity-index-pdsi`. National Center for Atmospheric Research Staff (Eds). Last modified 12 Dec 2019.

Damkjaer, S. and Taylor, R. (2017). The measurement of water scarcity: Defining a meaningful indicator. *Ambio*, 46(5):513–531.

De Fries, R., Hansen, M., Townshend, J., and Sohlberg, R. (1998). Global land cover classifications at 8 km spatial resolution: the use of training data derived from landsat imagery in decision tree classifiers. *International Journal of Remote Sensing*, 19(16):3141–3168.

Deardorff, J. W. (1978). Efficient prediction of ground surface temperature and moisture, with inclusion of a layer of vegetation. *Journal of Geophysical Research: Oceans*, 83(C4):1889–1903.

De'ath, G., Fabricius, K. E., Sweatman, H., and Puotinen, M. (2012). The 27–year decline of coral cover on the great barrier reef and its causes. *Proceedings of the National Academy of Sciences*, 109(44):17995–17999.

Dickinson, R. E. (1984). Modeling evapotranspiration for three-dimensional global climate models. *Climate processes and climate sensitivity*, 29:58–72.

Döll, P. and Lehner, B. (2002). Validation of a new global 30-min drainage direction map. *Journal of Hydrology*, 258(1-4):214–231.

Dunn, S. and Mackay, R. (1995). Spatial variation in evapotranspiration and the influence of land use on catchment hydrology. *Journal of Hydrology*, 171(1-2):49–73.

Dykema, J. A., Keith, D., and Keutsch, F. (2016). Improved aerosol radiative properties as a foundation for solar geoengineering risk assessment. *Geophysical Research Letters*, 43(14):7758–7766.

Edwards, D. C. and McKee, T. B. (1997). *Characteristics of 20th century drought in the United States at multiple time scales*. PhD thesis, Colorado State University. Libraries.

Falkenmark, M., Berntell, A., Jägerskog, A., Lundqvist, J., Matz, M., and Tropp, H. (2007). *On the verge of a new water scarcity: a call for good governance and human ingenuity*. Stockholm International Water Institute (SIWI).

Falkenmark, M. and Molden, D. (2008). Wake up to realities of river basin closure. *International journal of water resources development*, 24(2):201–215.

Falkenmark, M. and Rockström, J. (2004). *Balancing water for humans and nature: the new approach in ecohydrology*. Earthscan.

Farese, P. (2012). Technology: How to build a low-energy future. *Nature*, 488(7411):275–277.

Farquhar, G. D., von Caemmerer, S. v., and Berry, J. A. (1980). A biochemical model of photosynthetic co 2 assimilation in leaves of c 3 species. *Planta*, 149(1):78–90.

Fekete, B. M., Vörösmarty, C. J., and Grabs, W. (1999). Global, composite runoff fields based on observed river discharge and simulated water balances. Global Runoff Data Centre Koblenz.

Feng, S. and Fu, Q. (2013). Expansion of global drylands under a warming climate. *Atmospheric Chemistry and Physics*, 13(19):10081–10094.

Field, C. B., Barros, V., Stocker, T. F., and Dahe, Q. (2012). *Managing the risks of*

extreme events and disasters to advance climate change adaptation: special report of the intergovernmental panel on climate change. Cambridge University Press.

Field, C. B. and Mach, K. J. (2017). Rightsizing carbon dioxide removal. *Science*, 356(6339):706–707.

Fleig, A. K., Tallaksen, L. M., Hisdal, H., and Demuth, S. (2006). A global evaluation of streamflow drought characteristics. *Hydrology and Earth System Sciences*, 10(4):535–552.

Flynn, C. M. and Mauritsen, T. (2020). On the climate sensitivity and historical warming evolution in recent coupled model ensembles. *Atmospheric Chemistry and Physics*, 20(13):7829–7842.

Fox, A. (2019). This sulfur-spewing russian volcano is turning sunsets purple. `https://www.sciencemag.org/news/2019/09/sulfur-spewing-russian-volcano-turning-sunsets-purple`. Date accessed: 12.08.20.

Freeze, R. A. and Harlan, R. (1969). Blueprint for a physically-based, digitally-simulated hydrologic response model. *Journal of Hydrology*, 9(3):237–258.

Friberg, J., Martinsson, B. G., Andersson, S. M., and Sandvik, O. S. (2018). Volcanic impact on the climate-the stratospheric aerosol load in the period 2006-2015. *Atmospheric Chemistry and Physics*, 18(15):11149–11169.

Fromm, M., Lindsey, D. T., Servranckx, R., Yue, G., Trickl, T., Sica, R., Doucet, P., and Godin-Beekmann, S. (2010). The untold story of pyrocumulonimbus. *Bulletin of the American Meteorological Society*, 91(9):1193–1210.

Frumhoff, P. C. and Stephens, J. C. (2018). Towards legitimacy of the solar geoengineering research enterprise. *Phil. Trans. R. Soc. A*, 376(2119):20160459.

Fuss, S., Canadell, J. G., Peters, G. P., Tavoni, M., Andrew, R. M., Ciais, P., Jackson, R. B., Jones, C. D., Kraxner, F., Nakicenovic, N., et al. (2014). Betting on negative emissions. *Nature climate change*, 4(10):850–853.

Gardiner, S. M. (2011). Some early ethics of geoengineering the climate: a commentary on the values of the royal society report. *Environmental Values*, 20(2):163–188.

Gattuso, J.-P., Mach, K. J., and Morgan, G. (2013). Ocean acidification and its impacts: an expert survey. *Climatic Change*, 117(4):725–738.

GeoMIP (2020). The geoengineering model intercomparison project website. `http://climate.envsci.rutgers.edu/GeoMIP/`. Date accessed: 20.09.20.

Ghiggi, G., Humphrey, V., Seneviratne, S. I., and Gudmundsson, L. (2019). Grun: an observation-based global gridded runoff dataset from 1902 to 2014. *Earth System Science Data*, 11(4):1655–1674.

Gidden, M., Riahi, K., Smith, S., Fujimori, S., Luderer, G., Kriegler, E., van Vuuren, D. P., van den Berg, M., Feng, L., Klein, D., et al. (2019). Global emissions pathways under different socioeconomic scenarios for use in cmip6: a dataset of harmonized emissions trajectories through the end of the century. *Geoscientific model development discussions*, 12(4):1443–1475.

Gilleland, E. and Katz, R. W. (2016). extRemes 2.0: An extreme value analysis package in R. *Journal of Statistical Software*, 72(8):1–39.

Glienke, S., Irvine, P. J., and Lawrence, M. G. (2015). The impact of geoengineering on vegetation in experiment g1 of the geomip. *Journal of Geophysical Research: Atmospheres*, 120(19):10–196.

Gosling, S., Taylor, R., Arnell, N., and Todd, M. (2011). A comparative analysis of projected impacts of climate change on river runoff from global and catchment-scale hydrological models. *Hydrology and Earth System Sciences*, 15(1):279–294.

Gosling, S. N. and Arnell, N. W. (2011). Simulating current global river runoff with a global hydrological model: model revisions, validation, and sensitivity analysis. *Hydrological Processes*, 25(7):1129–1145.

Gosling, S. N. and Arnell, N. W. (2016). A global assessment of the impact of climate change on water scarcity. *Climatic Change*, 134(3):371–385.

Gosling, S. N., Bretherton, D., Haines, K., and Arnell, N. W. (2010). Global hydrology modelling and uncertainty: running multiple ensembles with a campus grid. *Philosophical Transactions of the Royal Society of London A: Mathematical, Physical and Engineering Sciences*, 368(1926):4005–4021.

Govindasamy, B. and Caldeira, K. (2000). Geoengineering earth's radiation balance to mitigate co2-induced climate change. *Geophysical Research Letters*, 27(14):2141–2144.

GRDC (2020). The global runoff data base. `https://www.bafg.de/GRDC/EN/01_GRDC/grdc_node.html`. The Global Runoff Data Centre, 56068 Koblenz, Germany. Date accessed: 02.02.21.

Gregory, J. and Webb, M. (2008). Tropospheric adjustment induces a cloud component in co2 forcing. *Journal of Climate*, 21(1):58–71.

Guenther, A., Jiang, X., Heald, C. L., Sakulyanontvittaya, T., Duhl, T., Emmons, L., and Wang, X. (2012). The model of emissions of gases and aerosols from nature version 2.1 (megan2. 1): an extended and updated framework for modeling biogenic emissions. *Geoscientific Model Development*, 5(6):1471–1492.

Guimberteau, M., Ducharne, A., Ciais, P., Boisier, J.-P., Peng, S., De Weirdt, M., and Verbeeck, H. (2014). Testing conceptual and physically based soil hydrology schemes against observations for the amazon basin. *Geoscientific Model Development*, 7(3):1115–1136.

Haddeland, I., Clark, D. B., Franssen, W., Ludwig, F., Voß, F., Arnell, N. W., Bertrand, N., Best, M., Folwell, S., Gerten, D., et al. (2011). Multimodel estimate of the global terrestrial water balance: setup and first results. *Journal of Hydrometeorology*, 12(5):869–884.

Hanasaki, N., Fujimori, S., Yamamoto, T., Yoshikawa, S., Masaki, Y., Hijioka, Y., Kainuma, M., Kanamori, Y., Masui, T., Takahashi, K., et al. (2013). A global water scarcity assessment under shared socio-economic pathways–part 2: Water availability and scarcity. *Hydrology and Earth System Sciences*, 17(7):2393–2413.

Hanasaki, N., Kanae, S., Oki, T., Masuda, K., Motoya, K., Shirakawa, N., Shen, Y., and Tanaka, K. (2008). An integrated model for the assessment of global water resources–part 1: Model description and input meteorological forcing. *Hydrology and Earth System Sciences*, 12(4):1007–1025.

Hansen, G. and Cramer, W. (2015). Global distribution of observed climate change impacts. *Nature Climate Change*, 5(3):182–185.

Harris, B. (2008). The potential impact of super-volcanic eruptions on the earth's atmosphere. *Weather*, 63(8):221–225.

Hayes, M. J. (2000). Revisiting the spi: clarifying the process.

Haywood, J. M., Jones, A., Bellouin, N., and Stephenson, D. (2013). Asymmetric forcing from stratospheric aerosols impacts sahelian rainfall. *Nature Climate Change*, 3(7):660–665.

Heckendorn, P., Weisenstein, D., Fueglistaler, S., Luo, B. P., Rozanov, E., Schraner, M., Thomason, L. W., and Peter, T. (2009). The impact of geoengineering aerosols on stratospheric temperature and ozone. *Environmental Research Letters*, 4(4):045108.

Held, I. M. and Soden, B. J. (2006). Robust responses of the hydrological cycle to global warming. *Journal of climate*, 19(21):5686–5699.

Heyen, D., Horton, J., and Moreno-Cruz, J. (2019). Strategic implications of counter-geoengineering: Clash or cooperation? *Journal of Environmental Economics and Management*, 95:153–177.

Hodgkins, G. A. and Dudley, R. W. (2006). Changes in the timing of winter–spring streamflows in eastern north america, 1913–2002. *Geophysical Research Letters*, 33(6).

Hoekstra, A. Y. and Mekonnen, M. M. (2012). The water footprint of humanity. *Proceedings of the national academy of sciences*, 109(9):3232–3237.

Hoekstra, A. Y., Mekonnen, M. M., Chapagain, A. K., Mathews, R. E., and Richter, B. D. (2012). Global monthly water scarcity: blue water footprints versus blue water availability. *PloS one*, 7(2):e32688.

Horton, R. E. (1945). Erosional development of streams and their drainage basins; hydrophysical approach to quantitative morphology. *Geological society of America bulletin*, 56(3):275–370.

Hosking, J. R. (1990). L-moments: Analysis and estimation of distributions using linear combinations of order statistics. *Journal of the Royal Statistical Society: Series B (Methodological)*, 52(1):105–124.

Houghton, J. (2005). Reports on progress in physics. *Global warming*, 68:1343–1403.

Howey, D. A. (2012). Policy: a challenging future for cars. *Nature Climate Change*, 2(1):28–29.

Huber, M. and Knutti, R. (2012). Anthropogenic and natural warming inferred from changes in earth's energy balance. *Nature Geoscience*, 5(1):31–36.

Hudon, C., Armellin, A., Gagnon, P., and Patoine, A. (2010). Variations in water temperatures and levels in the st. lawrence river (québec, canada) and potential implications for three common fish species. *Hydrobiologia*, 647(1):145–161.

Hunger, M. and Döll, P. (2008). Value of river discharge data for global-scale hydrological modeling. *Hydrology and Earth System Sciences*, 12(3):841–861.

Hurrell, J. W., Holland, M. M., Gent, P. R., Ghan, S., Kay, J. E., Kushner, P. J., Lamarque, J.-F., Large, W. G., Lawrence, D., Lindsay, K., et al. (2013). The community earth system model: a framework for collaborative research. *Bulletin of the American Meteorological Society*, 94(9):1339–1360.

IPCC (2020). Home page: Intergovernmental panel on climate change. `http://www.ipcc.ch/`. Date accessed: 20.09.20.

Irvine, P. J. and Keith, D. W. (2020). Halving warming with stratospheric aerosol geoengineering moderates policy-relevant climate hazards. *Environmental Research Letters*, 15(4):044011.

Irvine, P. J., Kravitz, B., Lawrence, M. G., Gerten, D., Caminade, C., Gosling, S. N., Hendy, E. J., Kassie, B. T., Kissling, W. D., Muri, H., et al. (2017). Towards a comprehensive climate impacts assessment of solar geoengineering. *Earth's Future*, 5(1):93–106.

Jevrejeva, S., Moore, J., Grinsted, A., Matthews, A., and Spada, G. (2014). Trends and acceleration in global and regional sea levels since 1807. *Global and Planetary Change*, 113:11–22.

Jinnah, S., Nicholson, S., Morrow, D. R., Dove, Z., Wapner, P., Valdivia, W., Thiele, L. P., McKinnon, C., Light, A., Lahsen, M., et al. (2019). Governing climate engineering: a proposal for immediate governance of solar radiation management. *Sustainability*, 11(14):3954.

Jones, A. C., Haywood, J. M., Dunstone, N., Emanuel, K., Hawcroft, M. K., Hodges, K. I., and Jones, A. (2017). Impacts of hemispheric solar geoengineering on tropical cyclone frequency. *Nature Communications*, 8(1):1–10.

Jones, P. W. (1999). First-and second-order conservative remapping schemes for grids in spherical coordinates. *Monthly Weather Review*, 127(9):2204–2210.

Joo, E., Zeri, M., Hussain, M. Z., DeLucia, E. H., and Bernacchi, C. J. (2017). Enhanced evapotranspiration was observed during extreme drought from miscanthus, opposite of other crops. *Gcb Bioenergy*, 9(8):1306–1319.

Kalidindi, S., Bala, G., Modak, A., and Caldeira, K. (2015). Modeling of solar radiation management: a comparison of simulations using reduced solar constant and stratospheric sulphate aerosols. *Climate Dynamics*, 44(9-10):2909–2925.

Keilman, N. (2020). Uncertainty in population forecasts for the twenty-first century.

Keith, D. W. (2000). Geoengineering the climate: History and prospect. *Annual review of energy and the environment*, 25(1):245–284.

Keith, D. W. (2010). Photophoretic levitation of engineered aerosols for geoengineering. *Proceedings of the National Academy of Sciences*, 107(38):16428–16431.

Keith, D. W., Holmes, G., Angelo, D. S., and Heidel, K. (2018). A process for capturing co2 from the atmosphere. *Joule*, 2(8):1573–1594.

Keutsch Group (2020). Scopex. `https://www.keutschgroup.com/scopex`. Date accessed: 24.03.20.

Keyantash, J. (2018). The climate data guide: Standardized precipitation index (spi). `https://climatedataguide.ucar.edu/climate-data/standardized-precipitation-index-spi`. National Center for Atmospheric Research Staff (Eds). Last modified 07 Aug 2018.

Khlebtsov, N. G. and Dykman, L. A. (2010). Optical properties and biomedical applications of plasmonic nanoparticles. *Journal of Quantitative Spectroscopy and Radiative Transfer*, 111(1):1–35.

Kleidon, A., Kravitz, B., and Renner, M. (2015). The hydrological sensitivity to global warming and solar geoengineering derived from thermodynamic constraints. *Geophysical Research Letters*, 42(1):138–144.

Kravitz, B., Caldeira, K., Boucher, O., Robock, A., Rasch, P. J., Alterskjær, K., Bou Karam, D., Cole, J. N. S., Curry, C. L., Haywood, J. M., Irvine, P. J., Ji, D., Jones, A., Kristjánsson, J. E., Lunt, D. J., Moore, J. C., Niemeier, U., Schmidt, H.,

Schulz, M., Singh, B., Tilmes, S., Watanabe, S., Yang, S., and Yoon, J.-H. (2013a). Climate model response from the geoengineering model intercomparison project (geomip). *Journal of Geophysical Research: Atmospheres*, 118:8320–8332.

Kravitz, B., Forster, P. M., Jones, A., Robock, A., Alterskjær, K., Boucher, O., Jenkins, A. K., Korhonen, H., Kristjánsson, J. E., Muri, H., et al. (2013b). Sea spray geoengineering experiments in the geoengineering model intercomparison project (geomip): Experimental design and preliminary results. *Journal of Geophysical Research: Atmospheres*, 118(19):11–175.

Kravitz, B. and MacMartin, D. G. (2020). Uncertainty and the basis for confidence in solar geoengineering research. *Nature Reviews Earth & Environment*, 1(1):64–75.

Kravitz, B., MacMartin, D. G., Visioni, D., Boucher, O., Cole, J. N., Haywood, J., Jones, A., Lurton, T., Nabat, P., Niemeier, U., et al. (2020). Comparing different generations of idealized solar geoengineering simulations in the geoengineering model intercomparison project (geomip). *Atmospheric Chemistry and Physics Discussions*, pages 1–31.

Kravitz, B., Rasch, P. J., Forster, P. M., Andrews, T., Cole, J. N., Irvine, P. J., Ji, D., Kristjánsson, J. E., Moore, J. C., Muri, H., et al. (2013c). An energetic perspective on hydrological cycle changes in the geoengineering model intercomparison project. *Journal of Geophysical Research: Atmospheres*, 118(23).

Kravitz, B., Robock, A., Boucher, O., Schmidt, H., Taylor, K. E., Stenchikov, G., and Schulz, M. (2011). The geoengineering model intercomparison project (geomip). *Atmospheric Science Letters*, 12(2):162–167.

Kravitz, B., Robock, A., Tilmes, S., Boucher, O., English, J. M., Irvine, P. J., Jones, A., Lawrence, M. G., MacCracken, M., Muri, H., et al. (2015). The geoengineering model intercomparison project phase 6 (geomip6): Simulation design and preliminary results. *Geoscientific Model Development*, 8(10):3379–3392.

Kremser, S., Thomason, L. W., von Hobe, M., Hermann, M., Deshler, T., Timmreck, C., Toohey, M., Stenke, A., Schwarz, J. P., Weigel, R., et al. (2016). Stratospheric aerosol—observations, processes, and impact on climate. *Reviews of Geophysics*, 54(2):278–335.

Krinner, G., Viovy, N., de Noblet-Ducoudré, N., Ogée, J., Polcher, J., Friedlingstein, P., Ciais, P., Sitch, S., and Prentice, I. C. (2005). A dynamic global vegetation model

for studies of the coupled atmosphere-biosphere system. *Global Biogeochemical Cycles*, 19(1).

Kummu, M., Ward, P. J., de Moel, H., and Varis, O. (2010). Is physical water scarcity a new phenomenon? global assessment of water shortage over the last two millennia. *Environmental Research Letters*, 5(3):034006.

Latham, J. (1990). Control of global warming? *Nature*, 347(6291):339–340.

Lawrence, D. M., Fisher, R. A., Koven, C. D., Oleson, K. W., Swenson, S. C., Bonan, G., Collier, N., Ghimire, B., van Kampenhout, L., Kennedy, D., et al. (2019). The community land model version 5: Description of new features, benchmarking, and impact of forcing uncertainty. *Journal of Advances in Modeling Earth Systems*, 11(12):4245–4287.

Lawrence, D. M. and Slater, A. G. (2008). Incorporating organic soil into a global climate model. *Climate Dynamics*, 30(2-3):145–160.

Lawrence, D. M., Thornton, P. E., Oleson, K. W., and Bonan, G. B. (2007). The partitioning of evapotranspiration into transpiration, soil evaporation, and canopy evaporation in a gcm: Impacts on land–atmosphere interaction. *Journal of Hydrometeorology*, 8(4):862–880.

Lawrence, P. J. and Chase, T. N. (2007). Representing a new modis consistent land surface in the community land model (clm 3.0). *Journal of Geophysical Research: Biogeosciences*, 112(G1).

Le Quéré, C., Jackson, R. B., Jones, M. W., Smith, A. J., Abernethy, S., Andrew, R. M., De-Gol, A. J., Willis, D. R., Shan, Y., Canadell, J. G., et al. (2020). Temporary reduction in daily global co 2 emissions during the covid-19 forced confinement. *Nature Climate Change*, pages 1–7.

Lehner, B. and Döll, P. (2004). Development and validation of a global database of lakes, reservoirs and wetlands. *Journal of hydrology*, 296(1-4):1–22.

Li, F., Zeng, X., and Levis, S. (2012). A process-based fire parameterization of intermediate complexity in a dynamic global vegetation model. *Biogeosciences*, 9(7):2761–2780.

Li, H., Huang, M., Wigmosta, M. S., Ke, Y., Coleman, A. M., Leung, L. R., Wang, A., and Ricciuto, D. M. (2011). Evaluating runoff simulations from the community land

model 4.0 using observations from flux towers and a mountainous watershed. *Journal of Geophysical Research: Atmospheres*, 116(D24).

Liang, X., Lettenmaier, D. P., Wood, E. F., and Burges, S. J. (1994). A simple hydrologically based model of land surface water and energy fluxes for general circulation models. *J. Geophys. Res.*, 99:14 415–14 428.

Liu, J., Yang, H., Gosling, S. N., Kummu, M., Flörke, M., Pfister, S., Hanasaki, N., Wada, Y., Zhang, X., Zheng, C., et al. (2017). Water scarcity assessments in the past, present, and future. *Earth's future*, 5(6):545–559.

Liu, X., Easter, R. C., Ghan, S. J., Zaveri, R., Rasch, P., Shi, X., Lamarque, J.-F., Gettelman, A., Morrison, H., Vitt, F., et al. (2012). Toward a minimal representation of aerosols in climate models: Description and evaluation in the community atmosphere model cam5. *Geoscientific Model Development*, 5(3):709.

LLNL (2013). Cmip5 - coupled model intercomparison project phase 5 - overview. `https://pcmdi.llnl.gov/mips/cmip5/`. Date accessed: 24.08.20.

Lloyd-Hughes, B. and Saunders, M. A. (2002). A drought climatology for europe. *International Journal of Climatology: A Journal of the Royal Meteorological Society*, 22(13):1571–1592.

Lockwood, J. (2009). The climate of the earth. In Hewitt, C. N. and Jackson, A. V., editors, *Atmospheric Science for Environmental Scientists*, chapter 1, pages 1–25. Wiley-Blackwell.

Long, J. C. and Shepherd, J. G. (2014). The strategic value of geoengineering research. *Global environmental change*, 1:757–770.

Luhr, J. F., Carmichael, I. S., and Varekamp, J. C. (1984). The 1982 eruptions of el chichón volcano, chiapas, mexico: mineralogy and petrology of the anhydritebearing pumices. *Journal of Volcanology and Geothermal Research*, 23(1-2):69–108.

Lunt, D. J., Ridgwell, A., Valdes, P. J., and Seale, A. (2008). "sunshade world": A fully coupled gcm evaluation of the climatic impacts of geoengineering. *Geophysical Research Letters*, 35(12).

MacDougall, A. H., Frölicher, T. L., Jones, C. D., Rogelj, J., Matthews, H. D., Zickfeld, K., Arora, V. K., Barrett, N. J., Brovkin, V., Burger, F. A., et al. (2020). Is there

warming in the pipeline? a multi-model analysis of the zero emissions commitment from co 2. *Biogeosciences*, 17(11):2987–3016.

Mackenzie, R. (2009). Stratospheric chemistry and ozone depletion. In Hewitt, C. N. and Jackson, A. V., editors, *Atmospheric Science for Environmental Scientists*, chapter 8, pages 198–217. Wiley-Blackwell.

MacMartin, D. G., Irvine, P. J., Kravitz, B., and Horton, J. B. (2019). Technical characteristics of a solar geoengineering deployment and implications for governance. *Climate Policy*, 19(10):1325–1339.

MacMartin, D. G., Ricke, K. L., and Keith, D. W. (2018). Solar geoengineering as part of an overall strategy for meeting the 1.5 c paris target. *Phil. Trans. R. Soc. A*, 376(2119):20160454.

Madronich, S., Tilmes, S., Kravitz, B., MacMartin, D. G., and Richter, J. H. (2018). Response of surface ultraviolet and visible radiation to stratospheric so2 injections. *Atmosphere*, 9(11):432.

Manabe, S. (1969). Climate and the ocean circulation: I. the atmospheric circulation and the hydrology of the earth's surface. *Monthly Weather Review*, 97(11):739 – 774.

Marcos, M. and Amores, A. (2014). Quantifying anthropogenic and natural contributions to thermosteric sea level rise. *Geophysical Research Letters*, 41(7):2502–2507.

Marx, A., Kumar, R., Thober, S., Rakovec, O., Wanders, N., Zink, M., Wood, E. F., Pan, M., Sheffield, J., and Samaniego, L. (2018). Climate change alters low flows in europe under global warming of 1.5, 2, and 3 c. *Hydrology and Earth System Sciences*, 22(2):1017–1032.

Matthews, H. D. and Solomon, S. (2013). Irreversible does not mean unavoidable. *Science*, 340(6131):438–439.

McCabe, G. J., Wolock, D. M., and Austin, S. H. (2017). Variability of runoff-based drought conditions in the conterminous united states. *International Journal of Climatology*, 37(2):1014–1021.

McCormick, M. P., Thomason, L. W., and Trepte, C. R. (1995). Atmospheric effects of the mt pinatubo eruption. *Nature*, 373(6513):399.

McKee, T. B., Doesken, N. J., Kleist, J., et al. (1993). The relationship of drought

frequency and duration to time scales. In *Proceedings of the 8th Conference on Applied Climatology*, volume 17, pages 179–183. Boston.

Meehl, G. A., Senior, C. A., Eyring, V., Flato, G., Lamarque, J.-F., Stouffer, R. J., Taylor, K. E., and Schlund, M. (2020). Context for interpreting equilibrium climate sensitivity and transient climate response from the cmip6 earth system models. *Science Advances*, 6(26):eaba1981.

Meigh, J. R., McKenzie, A. A., and Sene, K. J. (1999). A grid-based approach to water scarcity estimates for eastern and southern africa. *Water Resour. Manage.*, 13:85–115.

Mekonnen, M. M. and Hoekstra, A. Y. (2016). Four billion people facing severe water scarcity. *Science advances*, 2(2):e1500323.

Meybeck, M., Kummu, M., and Dürr, H. (2013). Global hydrobelts and hydroregions: improved reporting scale for water-related issues? *Hydrology and Earth System Sciences*, 17(3):1093–1111.

Mills, M., Langford, A., O'Leary, T., Arpag, K., Miller, H., Proffitt, M., Sanders, R., and Solomon, S. (1993). On the relationship between stratospheric aerosols and nitrogen dioxide. *Geophysical research letters*, 20(12):1187–1190.

Mills, M. J., Richter, J. H., Tilmes, S., Kravitz, B., MacMartin, D. G., Glanville, A. A., Tribbia, J. J., Lamarque, J.-F., Vitt, F., Schmidt, A., et al. (2017). Radiative and chemical response to interactive stratospheric sulfate aerosols in fully coupled cesm1 (waccm). *Journal of Geophysical Research: Atmospheres*, 122(23).

Mills, M. J., Schmidt, A., Easter, R., Solomon, S., Kinnison, D. E., Ghan, S. J., Neely, R. R., Marsh, D. R., Conley, A., Bardeen, C. G., et al. (2016). Global volcanic aerosol properties derived from emissions, 1990–2014, using cesm1 (waccm). *Journal of Geophysical Research: Atmospheres*, 121(5):2332–2348.

Mishra, A. K. and Singh, V. P. (2010). A review of drought concepts. *Journal of hydrology*, 391(1-2):202–216.

Mitchell, D. L. and Finnegan, W. (2009). Modification of cirrus clouds to reduce global warming. *Environmental Research Letters*, 4(4):045102.

Molle, F. (2002). *The closure of the Chao Phraya River Basin in Thailand: Its causes, consequences and policy implications*. IWMI.

Moore, R. (1985). The probability-distributed principle and runoff production at point and basin scales. *Hydrological Sciences Journal*, 30(2):273–297.

Moore, R. (2007). The pdm rainfall-runoff model. *Hydrology and Earth System Sciences Discussions*, 11(1):483–499.

Moss, R. H., Edmonds, J. A., Hibbard, K. A., Manning, M. R., Rose, S. K., Van Vuuren, D. P., Carter, T. R., Emori, S., Kainuma, M., Kram, T., et al. (2010). The next generation of scenarios for climate change research and assessment. *Nature*, 463(7282):747–756.

Mulvany, T. J. (1851). On the use of self-registering rain and flood gauges in making observations of the relations of rainfall and flood discharges in a given catchment. *Proceedings of the institution of Civil Engineers of Ireland*, 4:19–31.

NASA (2019). Raikoke erupts. `https://www.earthobservatory.nasa.gov/images/145226/raikoke-erupts`. Date accessed: 12.08.20.

NCEI (2021). Definition of drought. `https://www.ncdc.noaa.gov/monitoring-references/dyk/drought-definition`. National Centers for Environmental Information, National Oceanic and Atmospheric Administration. Date accessed: 02.03.21.

Nehrbass-Ahles, C., Shin, J., Schmitt, J., Bereiter, B., Joos, F., Schilt, A., Schmidely, L., Silva, L., Teste, G., Grilli, R., Chappellaz, J., Hodell, D., Fischer, H., and Stocker, T. (2020). Abrupt co2 release to the atmosphere under glacial and early interglacial climate conditions. *Science*, 369(6506):1000–1005.

New Scientist (2009). Hacking the planet: The only climate solution left? `https://www.newscientist.com/article/mg20126973.600-hacking-the-planet-the-only-climate-solution-left/?full=true`. Date accessed: 23.06.17.

Niemeier, U., Schmidt, H., Alterskjær, K., and Kristjánsson, J. (2013). Solar irradiance reduction via climate engineering: Impact of different techniques on the energy balance and the hydrological cycle. *Journal of Geophysical Research: Atmospheres*, 118(21):11–905.

Nijssen, B., O'Donnell, G. M., Lettenmaier, D. P., Lohmann, D., and Wood, E. F. (2001). Predicting the discharge of global rivers. *Journal of Climate*, 14(15):3307–3323.

Niu, G.-Y., Yang, Z.-L., Dickinson, R. E., and Gulden, L. E. (2005). A simple topmodel-based runoff parameterization (simtop) for use in global climate models. *Journal of Geophysical Research: Atmospheres*, 110(D21).

NOAA (2020). 2019 was 2nd hottest year on record for earth say noaa, nasa. `https://www.noaa.gov/news/2019-was-2nd-hottest-year-on-record-for-earth-say-noaa-nasa`. Date accessed: 12.06.17.

Odoulami, R. C., New, M., Wolski, P., Guillemet, G., Pinto, I., Lennard, C., Muri, H., and Tilmes, S. (2020). Stratospheric aerosol geoengineering could lower future risk of 'day zero'level droughts in cape town. *Environmental Research Letters*, 15(12):124007.

Oki, T., Agata, Y., Kanae, S., Saruhashi, T., Yang, D., and Musiake, K. (2001). Global assessment of current water resources using total runoff integrating pathways. *Hydrological Sciences Journal*, 46(6):983–995.

Oleson, K., Lawrence, D., Bonan, G., Drewniak, B., Huang, M., Koven, C., Levis, S., Li, F., Riley, W., Subin, Z., Swenson, S., Thornton, P., Bozbiyik, A., Fisher, R., Kluzek, E., Lamarque, J.-F., Lawrence, P., Leung, L., Lipscomb, W., Muszala, S., Ricciuto, D., Sacks, W., Sun, Y., Tang, J., and Yang, Z.-L. (2013). Technical description of version 4.5 of the community land model (clm). `https://www.cesm.ucar.edu/models/cesm1.2/clm/CLM45_Tech_Note.pdf`. National Center for Atmospheric Research, Boulder, CO.

O'Neill, B. C., Kriegler, E., Riahi, K., Ebi, Kristie, L., Hallegatte, S., Carter, T. R., Mathur, R., and van Vuuren, D. P. (2014). A new scenario framework for climate change research: the concept of shared socioeconomic pathways. *Climatic Change*, 122:387–400.

Oppenheimer, C. (2002). Limited global change due to the largest known quaternary eruption, toba ∼74 kyr bp? *Quaternary Science Reviews*, 21(14-15):1593–1609.

Oppenheimer, C. (2003). Climatic, environmental and human consequences of the largest known historic eruption: Tambora volcano (indonesia) 1815. *Progress in physical geography*, 27(2):230–259.

Oreskes, N. and Conway, E. M. (2011). *Merchants of doubt: How a handful of scientists obscured the truth on issues from tobacco smoke to global warming*. Bloomsbury Publishing USA.

Pacifici, M., Foden, W. B., Visconti, P., Watson, J. E., Butchart, S. H., Kovacs, K. M., Scheffers, B. R., Hole, D. G., Martin, T. G., Akçakaya, H. R., et al. (2015). Assessing species vulnerability to climate change. *Nature Climate Change*, 5(3):215–224.

Pandolfi, J. M., Connolly, S. R., Marshall, D. J., and Cohen, A. L. (2011). Projecting coral reef futures under global warming and ocean acidification. *science*, 333(6041):418–422.

Parker, A. and Irvine, P. J. (2018). The risk of termination shock from solar geoengineering. *Earth's Future*, 6(3):456–467.

Pascale, S., Kapnick, S. B., Delworth, T. L., and Cooke, W. F. (2020). Increasing risk of another cape town "day zero" drought in the 21st century. *Proceedings of the National Academy of Sciences*, 117(47):29495–29503.

Peters, G. P. and Geden, O. (2017). Catalysing a political shift from low to negative carbon. *Nature Climate Change*, 7(9):619–621.

Pitari, G., Aquila, V., Kravitz, B., Robock, A., Watanabe, S., Cionni, I., Luca, N. D., Genova, G. D., Mancini, E., and Tilmes, S. (2014). Stratospheric ozone response to sulfate geoengineering: Results from the geoengineering model intercomparison project (geomip). *Journal of Geophysical Research: Atmospheres*, 119(5):2629–2653.

Rampino, M., Self, S., and Stothers, R. (1988). Volcanic winters: Annual review of earth and planetary science, v. 16.

Rampino, M. R. and Self, S. (1992). Volcanic winter and accelerated glaciation following the toba super-eruption. *Nature*, 359(6390):50.

Rasch, P. J., Crutzen, P. J., and Coleman, D. B. (2008a). Exploring the geoengineering of climate using stratospheric sulfate aerosols: The role of particle size. *Geophysical Research Letters*, 35(2).

Rasch, P. J., Tilmes, S., Turco, R. P., Robock, A., Oman, L., Chen, C.-C. J., Stenchikov, G. L., and Garcia, R. R. (2008b). An overview of geoengineering of climate using stratospheric sulphate aerosols. *Philosophical Transactions of the Royal Society of London A: Mathematical, Physical and Engineering Sciences*, 366(1882):4007–4037.

Reynolds, J. L. (2021). Is solar geoengineering ungovernable? a critical assessment of governance challenges identified by the intergovernmental panel on climate change. *Wiley Interdisciplinary Reviews: Climate Change*, 12(2):e690.

Reynolds, J. L. and Horton, J. B. (2020). An earth system governance perspective on solar geoengineering. *Earth System Governance*, page 100043.

Reynolds, J. L., Parker, A., and Irvine, P. (2016). Five solar geoengineering tropes that have outstayed their welcome. *Earth's Future*, 4(12):562–568.

Richter, J. H., Tilmes, S., Mills, M. J., Tribbia, J. J., Kravitz, B., MacMartin, D. G., Vitt, F., and Lamarque, J.-F. (2017). Stratospheric dynamical response and ozone feedbacks in the presence of so2 injections. *Journal of Geophysical Research: Atmospheres*, 122(23):12–557.

Rijsberman, F. R. (2006). Water scarcity: fact or fiction? *Agricultural water management*, 80(1-3):5–22.

Riley, W., Subin, Z., Lawrence, D., Swenson, S., Torn, M., Meng, L., Mahowald, N., and Hess, P. (2011). Barriers to predicting changes in global terrestrial methane fluxes: analyses using clm4me, a methane biogeochemistry model integrated in cesm. *Biogeosciences*, 8(7):1925–1953.

Ripple, W. J., Smith, P., Haberl, H., Montzka, S. A., McAlpine, C., and Boucher, D. H. (2014). Ruminants, climate change and climate policy. *Nature Climate Change*, 4(1):2–5.

Robock, A. (2000). Volcanic eruptions and climate. *Reviews of geophysics*, 38(2):191–219.

Robock, A. (2008). 20 reasons why geoengineering may be a bad idea. *Bulletin of the Atomic Scientists*, 64(2):14–18.

Robock, A. and Mao, J. (1995). The volcanic signal in surface temperature observations. *Journal of Climate*, 8(5):1086–1103.

Robock, A., Marquardt, A., Kravitz, B., and Stenchikov, G. (2009). Benefits, risks, and costs of stratospheric geoengineering. *Geophysical Research Letters*, 36(19).

Robock, A. and Matson, M. (1983). Circumglobal transport of the el chichón volcanic dust cloud. *Science*, 221(4606):195–197.

Robock, A., Oman, L., and Stenchikov, G. L. (2008). Regional climate responses to geoengineering with tropical and arctic so2 injections. *Journal of Geophysical Research: Atmospheres*, 113(D16101).

Rockström, J., Falkenmark, M., Karlberg, L., Hoff, H., Rost, S., and Gerten, D. (2009). Future water availability for global food production: the potential of green water for increasing resilience to global change. *Water Resources Research*, 45(7).

Rockström, J., Schellnhuber, H. J., Hoskins, B., Ramanathan, V., Schlosser, P., Brasseur, G. P., Gaffney, O., Nobre, C., Meinshausen, M., Rogelj, J., et al. (2016). The world's biggest gamble. *Earth's Future*, 4(10):465–470.

Rollins, A., Thornberry, T., Watts, L., Yu, P., Rosenlof, K., Mills, M., Baumann, E., Giorgetta, F., Bui, T., Höpfner, M., et al. (2017). The role of sulfur dioxide in stratospheric aerosol formation evaluated by using in situ measurements in the tropical lower stratosphere. *Geophysical research letters*, 44(9):4280–4286.

Rust, W., Holman, I., Bloomfield, J., Cuthbert, M., and Corstanje, R. (2019). Understanding the potential of climate teleconnections to project future groundwater drought. *Hydrology and Earth System Sciences*, 23(8):3233–3245.

Saft, M., Western, A. W., Zhang, L., Peel, M. C., and Potter, N. J. (2015). The influence of multiyear drought on the annual rainfall-runoff relationship: An a ustralian perspective. *Water Resources Research*, 51(4):2444–2463.

Samir, K. and Lutz, W. (2017). The human core of the shared socioeconomic pathways: Population scenarios by age, sex and level of education for all countries to 2100. *Global Environmental Change*, 42:181–192.

Santer, B. D., Bonfils, C., Painter, J. F., Zelinka, M. D., Mears, C., Solomon, S., Schmidt, G. A., Fyfe, J. C., Cole, J. N., Nazarenko, L., et al. (2014). Volcanic contribution to decadal changes in tropospheric temperature. *Nature Geoscience*, 7(3):185–189.

Santer, B. D., Painter, J. F., Mears, C. A., Doutriaux, C., Caldwell, P., Arblaster, J. M., Cameron-Smith, P. J., Gillett, N. P., Gleckler, P. J., Lanzante, J., et al. (2013). Identifying human influences on atmospheric temperature. *Proceedings of the National Academy of Sciences*, 110(1):26–33.

Santer, B. D., Po-Chedley, S., Zelinka, M. D., Cvijanovic, I., Bonfils, C., Durack, P. J., Fu, Q., Kiehl, J., Mears, C., Painter, J., et al. (2018). Human influence on the seasonal cycle of tropospheric temperature. *Science*, 361(6399).

Schewe, J., Heinke, J., Gerten, D., Haddeland, I., Arnell, N. W., Clark, D. B., Dankers, R., Eisner, S., Fekete, B. M., Colón-González, F. J., et al. (2014). Multimodel assessment of

water scarcity under climate change. *Proceedings of the National Academy of Sciences*, 111(9):3245–3250.

Schultz, M. G., Akimoto, H., Bottenheim, J., Buchmann, B., Galbally, I. E., Gilge, S., Helmig, D., Koide, H., Lewis, A. C., Novelli, P. C., et al. (2015). The global atmosphere watch reactive gases measurement network. *Elementa*, 3.

Schulzweida, U. (2019). Cdo user guide. `https://code.mpimet.mpg.de/projects/cdo/embedded/cdo.pdf`. Date accessed: 20.03.19.

Scripps Institution of Oceanography (2021). The keeling curve. `https://scripps.ucsd.edu/programs/keelingcurve/`. Last accessed: 28.03.21.

SCS (1987). Soil mecahnics level 1. module 3. usda textural classification study guide. `https://www.wcc.nrcs.usda.gov/ftpref/wntsc/H&H/training/soilsOther/soil-USDA-textural-class.pdf`. United States Department of Agriculture, Soil Conservation Service.

Seeley, J. T., Lutsko, N. J., and Keith, D. W. (2020). Designing a radiative antidote to co2. *Geophysical Research Letters*, page e2020GL090876.

Seftor, C. (2020). Nasa animates world path of smoke and aerosols from australian fires. `https://www.nasa.gov/feature/goddard/2020/nasa-animates-world-path-of-smoke-and-aerosols-from-australian-fires`. Date accessed: 24.08.20.

Sellers, P., Randall, D., Collatz, G., Berry, J., Field, C., Dazlich, D., Zhang, C., Collelo, G., and Bounoua, L. (1996). A revised land surface parameterization (sib2) for atmospheric gcms. part i: Model formulation. *Journal of climate*, 9(4):676–705.

Sheng, J.-X., Weisenstein, D. K., Luo, B.-P., Rozanov, E., Stenke, A., Anet, J., Bingemer, H., and Peter, T. (2015). Global atmospheric sulfur budget under volcanically quiescent conditions: Aerosol-chemistry-climate model predictions and validation. *Journal of Geophysical Research: Atmospheres*, 120(1):256–276.

Shepherd, J. G. (2009). *Geoengineering the climate: science, governance and uncertainty*. Royal Society.

Sherman, L. (1949). The unit hydrograph method. *Physics of the Earth*, pages 514–525.

Shukla, S. and Wood, A. W. (2008). Use of a standardized runoff index for characterizing hydrologic drought. *Geophysical research letters*, 35(2).

Sillmann, J., Kharin, V., Zhang, X., Zwiers, F., and Bronaugh, D. (2013). Climate extremes indices in the cmip5 multimodel ensemble: Part 1. model evaluation in the present climate. *Journal of Geophysical Research: Atmospheres*, 118(4):1716–1733.

Simpson, I., Tilmes, S., Richter, J., Kravitz, B., MacMartin, D., Mills, M., Fasullo, J., and Pendergrass, A. G. (2019). The regional hydroclimate response to stratospheric sulfate geoengineering and the role of stratospheric heating. *Journal of Geophysical Research: Atmospheres*, 124(23):12587–12616.

Smith, C. J., Forster, P. M., Allen, M., Fuglestvedt, J., Millar, R. J., Rogelj, J., and Zickfeld, K. (2019). Current fossil fuel infrastructure does not yet commit us to 1.5 c warming. *Nature communications*, 10(1):1–10.

Smith, K. A. (2015). *Investigating Uncertainty in Global Hydrology Modelling*. PhD thesis, University of Nottingham.

SOCCOM (2020). What is an earth system model (esm)? `https://soccom.princeton.edu/content/what-earth-system-model-esm`. Date accessed: 02.02.21.

Solomon, S., Plattner, G.-K., Knutti, R., and Friedlingstein, P. (2009). Irreversible climate change due to carbon dioxide emissions. *Proceedings of the national academy of sciences*, 106(6):1704–1709.

Solow, A. R. (2013). Global warming: A call for peace on climate and conflict. *Nature*, 497(7448):179–180.

Sood, A. and Smakhtin, V. (2015). Global hydrological models: a review. *Hydrological Sciences Journal*, 60(4):549–565.

SRMGI (2021). Decimals fund. `https://www.srmgi.org/decimals-fund/`. Solar Radiation Management Governance Initiative. Last accessed 20 Mar 2021.

Srokosz, M. A. and Bryden, H. L. (2015). Observing the atlantic meridional overturning circulation yields a decade of inevitable surprises. *Science*, 348(6241):1255575.

Stocker, T. (2014). *Climate Change 2013: The Physical Science Basis: Working Group I contribution to the Fifth Assessment Report of the Intergovernmental Panel on Climate Change*. Cambridge University Press.

Subin, Z. M., Riley, W. J., and Mironov, D. (2012). An improved lake model for climate simulations: Model structure, evaluation, and sensitivity analyses in cesm1. *Journal of Advances in Modeling Earth Systems*, 4(1).

Sun, Y., Gu, L., and Dickinson, R. E. (2012). A numerical issue in calculating the coupled carbon and water fluxes in a climate model. *Journal of Geophysical Research: Atmospheres*, 117(D22).

Svoboda, T. (2012). The ethics of geoengineering: moral considerability and the convergence hypothesis. *Journal of Applied Philosophy*, 29(3):243–256.

Swann, A. L. (2018). Plants and drought in a changing climate. *Current Climate Change Reports*, 4(2):192–201.

Swenson, S. C. and Lawrence, D. (2012). A new fractional snow-covered area parameterization for the community land model and its effect on the surface energy balance. *Journal of geophysical research: Atmospheres*, 117(D21).

Takata, K., Emori, S., and Watanabe, T. (2003). Development of the minimal advanced treatments of surface interaction and runoff. *Global Planet. Change*, 8:209–222.

Teller, E., Wood, L., and Hyde, R. (1996). Global warming and ice ages: I. prospects for physics-based modulation of global change. Technical report, Lawrence Livermore National Lab.

Teuling, A. J., Van Loon, A. F., Seneviratne, S. I., Lehner, I., Aubinet, M., Heinesch, B., Bernhofer, C., Grünwald, T., Prasse, H., and Spank, U. (2013). Evapotranspiration amplifies european summer drought. *Geophysical Research Letters*, 40(10):2071–2075.

Theisen, O. M., Gleditsch, N. P., and Buhaug, H. (2013). Is climate change a driver of armed conflict? *Climatic change*, 117(3):613–625.

Tilmes, S., Fasullo, J., Lamarque, J.-F., Marsh, D. R., Mills, M., Alterskjær, K., Muri, H., Kristjánsson, J. E., Boucher, O., Schulz, M., Cole, J. N. S., Curry, C. L., Jones, A., Haywood, J., Irvine, P. J., Ji, D., Moore, J. C., Karam, D. B., Kravitz, B., Rasch, P. J., Singh, B., Yoon, J.-H., Niemeier, U., Schmidt, H., Robock, A., Yang, S., and Watanabe, S. (2013). The hydrological impact of geoengineering in the geoengineering model intercomparison project (geomip). *Journal of Geophysical Research: Atmospheres*, 118(19).

Tilmes, S., MacMartin, D. G., Lenaerts, J., Kampenhout, L. v., Muntjewerf, L., Xia, L.,

Harrison, C. S., Krumhardt, K. M., Mills, M. J., Kravitz, B., et al. (2020). Reaching 1.5 and 2.0°c global surface temperature targets using stratospheric aerosol geoengineering. *Earth System Dynamics*, 11(3):579–601.

Tilmes, S., Richter, J., Kravitz, B., MacMartin, D., Mills, M., Simpson, I., Glanville, A., Fasullo, J., Phillips, A., Lamarque, J., Tribbia, J., Edwards, J., Mickelson, S., and Gosh, S. (2018). Cesm1(waccm) stratospheric aerosol geoengineering large ensemble (glens) project. *Bulletin of the American Meteorological Society*, in press.

Trenberth, K. E. and Dai, A. (2007). Effects of mount pinatubo volcanic eruption on the hydrological cycle as an analog of geoengineering. *Geophysical Research Letters*, 34(15).

Tukey, J. W. (1965). *Restoring the Quality of our Environment: Report of The Environmental Pollution Panel President's Science Advisory Committee*. The White House.

UCAR (2020). Geoengineering large ensemble output fields list. `http://www.cesm.ucar.edu/experiments/cesm1.2/GLE/GLENS_output_fields/`. Date accessed: 16.06.20.

UNFCCC (2020a). Conference of the parties (cop). `https://unfccc.int/process/bodies/supreme-bodies/conference-of-the-parties-cop`. Date accessed: 20.09.20.

UNFCCC (2020b). What is the paris agreement? `https://unfccc.int/process-and-meetings/the-paris-agreement/what-is-the-paris-agreement`. Date accessed: 20.09.20.

United Nations, S. D. (2019). Standard country or area codes for statistical use (m49): Geographic regions. `https://unstats.un.org/unsd/methodology/m49/`. Date accessed: 20.03.19.

UoL (2019). 3rd international workshop on stratospheric sulfur and its role in climate (ssirc): Raikoke volcanic aerosol plume. `https://eu.eventscloud.com/ehome/200197691/Raikoke/`. University of Leeds, Date accessed: 12.08.20.

UoOxford (2017). What is geoengineering? `http://www.geoengineering.ox.ac.uk/what-is-geoengineering/what-is-geoengineering/`. Date accessed: 21.06.17.

Van Huijgevoort, M., Hazenberg, P., Van Lanen, H., Teuling, A., Clark, D., Folwell, S., Gosling, S., Hanasaki, N., Heinke, J., Koirala, S., et al. (2013). Global multimodel

analysis of drought in runoff for the second half of the twentieth century. *Journal of Hydrometeorology*, 14(5):1535–1552.

Van Huijgevoort, M., Van Lanen, H., Teuling, A., and Uijlenhoet, R. (2014). Identification of changes in hydrological drought characteristics from a multi-gcm driven ensemble constrained by observed discharge. *Journal of Hydrology*, 512:421–434.

Van Loon, A. and Laaha, G. (2015). Hydrological drought severity explained by climate and catchment characteristics. *Journal of hydrology*, 526:3–14.

Van Loon, A. F. (2015). Hydrological drought explained. *Wiley Interdisciplinary Reviews: Water*, 2(4):359–392.

Van Loon, A. F., Tijdeman, E., Wanders, N., Van Lanen, H. J., Teuling, A., and Uijlenhoet, R. (2014). How climate seasonality modifies drought duration and deficit. *Journal of Geophysical Research: Atmospheres*, 119(8):4640–4656.

Van Loon, A. F. and Van Lanen, H. A. (2013). Making the distinction between water scarcity and drought using an observation-modeling framework. *Water Resources Research*, 49(3):1483–1502.

Van Renssen, S. (2012). The greenhouse-gas gang. *Nature Climate Change*, 2(3):143–144.

van Vuuren, D. P., Edmonds, J., Kainuma, M., Riahi, K., Thomson, A., Hibbard, K., Hurtt, G. C., Kram, T., Krey, V., Lamarque, J.-F., Masui, T., Meinshausen, M., Nakicenovic, N., J, S. S., and K, R. S. (2011). The representative concentration pathways: an overview. *Climatic change*, 109(1-2):5.

Veldkamp, T. I. E., Zhao, F., Ward, P. J., De Moel, H., Aerts, J. C., Schmied, H. M., Portmann, F. T., Masaki, Y., Pokhrel, Y., Liu, X., et al. (2018). Human impact parameterizations in global hydrological models improve estimates of monthly discharges and hydrological extremes: a multi-model validation study. *Environmental Research Letters*, 13(5):055008.

Verzano, K., Bärlund, I., Flörke, M., Lehner, B., Kynast, E., Voß, F., and Alcamo, J. (2012). Modeling variable river flow velocity on continental scale: Current situation and climate change impacts in europe. *Journal of Hydrology*, 424-425:238–251.

Vicente-Serrano, S. M., Beguería, S., and López-Moreno, J. I. (2010). A multiscalar

drought index sensitive to global warming: the standardized precipitation evapotranspiration index. *Journal of climate*, 23(7):1696–1718.

Visioni, D., MacMartin, D. G., Kravitz, B., Tilmes, S., Mills, M. J., Richter, J. H., and Boudreau, M. P. (2019). Seasonal injection strategies for stratospheric aerosol geoengineering. *Geophysical Research Letters*, 46(13):7790–7799.

Visioni, D., Simpson, I. R., MacMartin, D. G., Richter, J. H., Kravitz, B., and Lee, W. (2020). Reduced poleward transport due to stratospheric heating under geoengineering.

Vörösmarty, C. J., Green, P., Salisbury, J., and Lammers, R. B. (2000). Global water resources: vulnerability from climate change and population growth. *science*, 289(5477):284–288.

Vörösmarty, C. J., Moore, B., Grace, A. L., Gildea, M. P., Melillo, J. M., Peterson, B. J., Rastetter, E. B., and Steudler, P. A. (1989). Continental scale models of water balance and fluvial transport: an application to south america. *Global biogeochemical cycles*, 3(3):241–265.

Wada, Y., Van Beek, L., and Bierkens, M. F. (2011a). Modelling global water stress of the recent past: on the relative importance of trends in water demand and climate variability. *Hydrology and Earth System Sciences*, 15(12):3785–3808.

Wada, Y., Van Beek, L., Viviroli, D., Dürr, H. H., Weingartner, R., and Bierkens, M. F. (2011b). Global monthly water stress: 2. water demand and severity of water stress. *Water Resources Research*, 47(7).

Wada, Y., Wisser, D., and Bierkens, M. (2014). Global modeling of withdrawal, allocation and consumptive use of surface water and groundwater resources. *Earth System Dynamics*, 5(1):15.

Wei, L., Ji, D., Miao, C., and Moore, J. C. (2018). Global streamflow and flood response to stratospheric aerosol geoengineering. *Atmospheric Chemistry and Physics Discussions*.

Wells, N., Goddard, S., and Hayes, M. J. (2004). A self-calibrating palmer drought severity index. *Journal of climate*, 17(12):2335–2351.

Wieding, J., Stubenrauch, J., and Ekardt, F. (2020). Human rights and precautionary principle: Limits to geoengineering, srm, and ipcc scenarios. *Sustainability*, 12(21):8858.

Wigley, T. M. (2006). A combined mitigation/geoengineering approach to climate stabilization. *Science*, 314(5798):452–454.

Williams, P. I. and Baltensperger, U. (2009). Particulate matter in the atmosphere. In Hewitt, C. N. and Jackson, A. V., editors, *Atmospheric Science for Environmental Scientists*, chapter 7, pages 168–197. Wiley-Blackwell.

WMO (2006). Technical regulations, volume iii: Hydrology. `https://library.wmo.int/index.php?lvl=notice_display&id=10700#.YA52zdanxuQ`.

Xia, L., Robock, A., Cole, J., Curry, C. L., Ji, D., Jones, A., Kravitz, B., Moore, J. C., Muri, H., Niemeier, U., et al. (2014). Solar radiation management impacts on agriculture in china: A case study in the geoengineering model intercomparison project (geomip). *Journal of Geophysical Research: Atmospheres*, 119(14):8695–8711.

Xu, Y., Lin, L., Tilmes, S., Dagon, K., Xia, L., Diao, C., Cheng, W., Wang, Z., Simpson, I., and Burnell, L. (2020). Climate engineering to mitigate the projected 21st-century terrestrial drying of the americas: a direct comparison of carbon capture and sulfur injection. *Earth System Dynamics*, 11(3):673–695.

Zaherpour, J., Gosling, S. N., Mount, N., Schmied, H. M., Veldkamp, T. I., Dankers, R., Eisner, S., Gerten, D., Gudmundsson, L., Haddeland, I., et al. (2018). Worldwide evaluation of mean and extreme runoff from six global-scale hydrological models that account for human impacts. *Environmental Research Letters*, 13(6):065015.

Zaherpour, J., Mount, N., Gosling, S. N., Dankers, R., Eisner, S., Gerten, D., Liu, X., Masaki, Y., Schmied, H. M., Tang, Q., et al. (2019). Exploring the value of machine learning for weighted multi-model combination of an ensemble of global hydrological models. *Environmental modelling & software*, 114:112–128.

Zargar, A., Sadiq, R., Naser, B., and Khan, F. I. (2011). A review of drought indices. *Environmental Reviews*, 19(NA):333–349.

Zelinka, M. D., Myers, T. A., McCoy, D. T., Po-Chedley, S., Caldwell, P. M., Ceppi, P., Klein, S. A., and Taylor, K. E. (2020). Causes of higher climate sensitivity in cmip6 models. *Geophysical Research Letters*, 47(1):e2019GL085782.

Zender, C. S., Bian, H., and Newman, D. (2003). Mineral dust entrainment and deposition (dead) model: Description and 1990s dust climatology. *Journal of Geophysical Research: Atmospheres*, 108(D14).

Zeng, X. and Decker, M. (2009). Improving the numerical solution of soil moisture–based richards equation for land models with a deep or shallow water table. *Journal of Hydrometeorology*, 10(1):308–319.

Zeng, X., Shaikh, M., Dai, Y., Dickinson, R. E., and Myneni, R. (2002). Coupling of the common land model to the ncar community climate model. *Journal of Climate*, 15(14):1832–1854.